

Solidification Behaviour and Microstructure
Evolution of Refractory Metals-Based Alloys
Under Rapid Solidification

LEANDRO MORAES FEITOSA

A thesis submitted to
THE UNIVERSITY OF LEICESTER
For the degree of
DOCTOR OF PHILOSOPHY

Department of Engineering
University of Leicester
2018

Solidification Behaviour and Microstructure Evolution of Refractory Metals-Based Alloys Under Rapid Solidification

Leandro Moraes Feitosa

Abstract

In this thesis, the solidification behaviour and microstructure evolution of Ta-Al-Fe, Nb-Al-Co, Nb-Al-Fe, Ta-Al-Ti and Nb-Si-Ti alloys rapidly solidified via arc melting, suspended droplet alloying and additive manufacturing techniques were examined. Loss of interfacial equilibrium resulted in an extended solute solubility with significant undercooling due to nucleation constraints, leading to unexpected phases.

For Ta-Al-Fe alloys, when Al < 10 at.% and Fe < 4 at.%, the peritectic reaction, $L+A_2 \rightarrow \sigma$, is suppressed and the eutectic, $L \rightarrow A_2 + \mu$, occurs with formation of a halo of μ on primary σ phase. For Co-rich Nb-Al-Co alloys, when Nb > 20 at.%, the quasi-peritectic reaction, $L+Co_2AlNb \rightarrow C36+CoAl$ does not occur, C36 and CoAl phases form through solid-state precipitation. A halo of C14 forms on primary CoAl but limited vice-versa. In Nb-Al-Fe alloys, failure to initiate coupled growth of $NbAl_3+C14$ leads to a two-phase halo of $C14+Nb_2Al$. The quasi-peritectic reaction, $L+Nb_2Al \rightarrow (Nb)+\mu$ is suppressed, forming the eutectic $Nb_2Al+\mu$ instead. The ternary eutectic, $L+C14+Nb_2Al \rightarrow \mu$, is limited with μ forming primarily. For Ti-Al-Ta alloys, the quasi-peritectic reactions, $L+\beta \rightarrow \alpha+\sigma$ and $L+\sigma \rightarrow \alpha+\kappa$, occur at a very narrow window; good agreement for γ and ϵ phases is found with non-equilibrium formation of ϵ .

For additive manufactured Nb-Si-Ti alloys, an increase in scanning speed led to microstructure refinement. Due to elemental additions, Nb_3Si is suppressed with formation of $Nb_{ss}+Nb_5Si_3$. C15 Laves phase formed when Cr > 5 at.%, with HfO_2 when Hf is added. For Ti > 22 at.% and Si > 18 at.%, a Ti-rich Nb_5Si_3 forms due to rejection of Ti solute. Hot isostatic pressing and heat treatment led to crystal structure changes, densification and phase coarsening. Diffusion and local super-saturation led to the split of Nb_{ss} into an energetically stable and homogeneous Ti_{ss} phase.

Acknowledgements

I would like to thank my sponsor, CNPq, and the Ministry of Education in Brazil for their financial support of my studies during these three years. Although our country has been passing through difficult situations, they have kept their support throughout the whole duration of my PhD.

I would like to thank my PhD supervisor, Professor Hongbiao Dong, who has guided me and helped during this time, always supporting me and providing me with his utmost confidence to achieve my best performance. I also thank my industrial supervisor, Neil D'Souza, from Rolls-Royce plc, who has also helped me in many ways and for his contribution and partnership to our international publications.

I would like to thank my friends and partners in this research group, Adam Allen, Andrew Douglas and Huan Qian, who have always contributed with my work and had given me a lot of support for this study. Our technicians, lecturers and professors who have provided great support, which have made several analyses possible to be concluded in time.

I also thank our partners Yunlong Lee and Professor Xin Lin from the Northwestern Polytechnical University, in Xi'an, Chin, for their hospitality and help in producing our additive manufactured alloys.

Finally, and most importantly, I would like to thank God for his help, patience and strength to achieve my goals. Another special thanks go to my parents, Nilson Feitosa and Ádima Moraes, my sister Lorena Feitosa, and my wife Simone Ferreira Ribas, who have supported me every day during this study and have given me emotional support to continue, even from an enormous distance, and without whom I would not be where I am.

To all of you who helped me come to this point, I'm very grateful!

"A wise man can learn more from a foolish question than a fool can learn from a wise answer."

Bruce Lee

List of Publications

[1] N. D'Souza, B. Kantor, G.D. West, L.M. Feitosa, H.B. Dong. Key aspects of carbide precipitation during solidification in the Ni-base superalloy, MAR M002. Journal of Alloys and Compounds, vol. 702, 2017, p. 6-12.

DOI: 10.1016/j.jallcom.2017.01.104

[2] N. D'Souza, L.M. Feitosa, G.D. West, N.G. Jones, H.B. Dong. Effects of solute trapping on solidification path in Ta-rich Ta-Al-Fe ternary alloys under rapid freezing. Journal of Alloys and Compounds, vol. 698, 2017, p. 375-383.

DOI: 10.1016/j.jallcom.2016.12.149

[3] L.M. Feitosa, N. D'Souza, G.D. West, H.B. Dong. Solidification reaction sequence of Co-rich Nb-Al-Co alloys. Metallurgical and Materials Transactions A, vol. 48, 2017, p. 3814-3822.

DOI: 10.1007/s11661-017-4138-2

[4] N. D'Souza, L.M. Feitosa, G.D. West, H.B. Dong. Halo formation during solidification of refractory metal aluminide ternary systems. Metallurgical and Materials Transactions A, 2018, p. 1-13.

DOI: 10.1007/s11661-018-4519-1

[5] L.M. Feitosa, A. Allen, A. Douglas, H. Qian, H.B. Dong. Microstructure Evolution of the Nb-18Si-24Ti-5Cr-5Al-2Mo Alloy Produced via Laser Additive Manufacturing METAL 2017, Conference Proceedings p. 1615-1618.

ISBN: 978-80-87294-79-6

List of Conference Presentations

- [1] A.C. Douglas, A. Allen, H. Qian, L.M. Feitosa, H.B. Dong, X. Lin, W. Huang. Laser additive manufacturing of niobium silicide-based composites, in Proceedings of “Beyond Nickel-Based Superalloys II”, ECI Symposium Series, Cambridge, 2016. Oral Presentation.
- [2] L.M. Feitosa, A. Allen, A. Douglas, H. Qian, H.B. Dong. Microstructure evolution of the Nb-18Si-24Ti-5Cr-5Al-2Mo alloy produced via laser additive manufacturing, in Proceedings of “Metal 2017”, Brno, 2017. Oral Presentation.
- [3] L.M. Feitosa, A. Allen, H. Qian, A. Douglas, H.B. Dong, X. Lin, W. Huang. Analysis of the solidification behaviour of Nb-Si-Ti alloys produced by Laser Additive Manufacturing, in Proceedings of the “5th Decennial International Conference on Solidification Processing”, Old Windsor, 2017. Oral Presentation.
- [4] N. D’Souza, L.M. Feitosa, G.D. West, N.G. Jones, H.B. Dong. Effects of Solute Trapping on Solidification Path of Ta-Al-Fe and Nb-Al-Fe Ternary Alloys under Rapid Freezing, in Proceedings of the “5th Decennial International Conference on Solidification Processing”, Old Windsor, 2017. Oral Presentation.
- [5] L.M. Feitosa, N. D’Souza, G.D. West, H.B. Dong. Halo Formation in Nb-Al-Co and Nb-Al-Fe Ternary Alloys, in Proceedings of the “5th Decennial International Conference on Solidification Processing”, Old Windsor, 2017. Poster presentation.
- [6] L.M. Feitosa, A. Allen, A. Douglas, H. Qian, H.B. Dong. Thermal Analysis Validation of the Solidification Sequence of a High Chromium Niobium-Based Alloy Produced via Additive Manufacturing, in Proceedings of “Recent Applications of Thermal Analysis and Calorimetry”, Belfast, 2018. Oral Presentation.

Table of Contents

List of Figures	X
List of Tables	XIX
Nomenclature	XXII
Chapter 1 Introduction	1
1.1. Justification	1
1.2. Objectives	3
1.3. Thesis structure	3
Chapter 2 Refractory metals-based ternary alloys	5
2.1. Solidification behaviour of refractory metals-based alloys	5
2.1.1. The peritectic invariant reaction	7
2.1.2. Crystal growth during peritectic reaction	9
2.1.3. Peritectic solidification of binary alloys	9
2.1.4. Banding structures formed during peritectic reaction	12
2.1.5. Island Bands formed during peritectic reaction	13
2.1.6. Peritectic Couple Growth	13
2.2. A ternary Ta-Al-Fe system	15
2.3. A ternary Co-Al-Nb system	17
2.4. A ternary Nb-Al-Fe system	18
2.5. A ternary Ta-Al-Ti system	20
2.6. A ternary Nb-Si-Ti system	23
2.7. Halo defect formation	26

Chapter 3	NbSi-based alloys for high temperature applications	31
3.1.	Turbine blades and Ni-base alloys	31
3.2.	Materials beyond Ni-based alloys	33
3.2.1.	Microstructure of Nb-Si composites.....	34
3.2.2.	Mechanical properties of Nb-based composites.....	38
3.2.2.1.	Fracture toughness.....	38
3.2.2.2.	Creep	40
3.2.2.3.	Oxidation.....	42
3.2.3.	The role of main alloying elements in Nb-Si alloys	44
Chapter 4	Processing methods for high temperature alloys	47
4.1.	Laser additive manufacturing of Nb-based alloys	48
4.1.1.	An introduction to additive manufacturing.....	49
4.1.2.	Advantages of additive manufacturing processing over traditional manufacturing.....	50
4.1.3.	Restrictions of additive manufacturing production	52
4.1.4.	Production costs	53
4.1.5.	Metallic materials used for additive manufacturing	54
4.1.6.	Coatings used for Nb-Si alloys	55
4.2.	Processing methods of refractory metals-based alloys	57
4.2.1.	Suspended Droplet Alloying	57
4.2.1.1.	Introduction	57
4.2.1.2.	Method description.....	58
4.2.2.	Arc melting	61
4.2.2.1.	Introduction	61
4.2.2.2.	Method description.....	62

Chapter 5	Experimental Procedures	64
5.1.	Casting processes	64
5.2.	Additive manufacturing processing	65
5.2.1.	Additive manufacturing parameters	67
5.2.2.	Scanning strategy	68
5.3.	Post processing techniques	70
5.3.1.	Hot Isostatic Pressing	70
5.3.2.	Heat Treatment	72
5.4.	Microstructural analysis	73
5.4.1.	Specimens preparation	73
5.4.2.	Materials characterisation	73
Chapter 6	Solidification sequences and structures of rapidly solidified cast refractory metals-based ternary alloys	75
6.1.	Ta-Al-Fe system	75
6.2.	Nb-Al-Co system	89
6.2.1.	Class I - Ternary eutectic reaction	90
6.2.2.	Class II - Quasi-Peritectic reaction	95
6.2.3.	Class III - Peritectic reaction	101
6.3.	Nb-Al-Fe system	103
6.3.1.	Three-phase reaction	105
6.3.2.	Class I – Ternary eutectic reaction	107
6.3.3.	Class II – Quasi-Peritectic reaction	112
6.3.4.	Class III – Ternary Peritectic reaction	115
6.4.	Ta-Al-Ti system	118
6.4.1.	Three-phase reaction	119

6.4.2.	Class II – Quasi-Peritectic reaction.....	121
6.5.	Halo formation on ternary systems alloys	134
6.5.1.	Ta-Al-Fe alloys analysis	134
6.5.2.	Nb-Al-Co alloys analysis.....	139
6.5.3.	Nb-Al-Fe alloys analysis	144
6.5.4.	General discussion.....	146
Chapter 7	Solidification sequences and microstructure evolution of additive manufactured NbSi-based alloys	152
7.1.	NbSi-based alloys results.....	152
7.1.1.	Nb-15Si-22Ti-14Cr-2Al-2Hf-2V.....	153
7.1.2.	Nb-15Si-22Ti-2Cr-2Al-2Hf-2V.....	163
7.1.3.	Nb-18Si-24Ti-5Cr-5Al-2Mo.....	171
7.1.4.	Nb-22Si-26Ti-6Cr-2Al-3Hf	183
Chapter 8	Conclusions and Future Work.....	190
8.1.	Cast refractory metals-based alloys conclusions	190
8.2.	AM processed NbSi-based alloys conclusions.....	193
8.3.	Future Work	193
References.....	195

List of Figures

Figure 1 - Temperature and pressure variation across the different sections of a turbine engine. LPC and HPC correspond to low and high-pressure compressors, respectively. HPT, IPT and LPT correspond to high, intermediate and low pressure turbines, respectively [4].	1
Figure 2 - Peritectic solidification diagram. [31]	8
Figure 3 - Peritectic solidification. Adapted from [32]	8
Figure 4 - Liquid-solid diffusion during peritectic reaction. [31]	9
Figure 5 - Binary diagram of Fe-Ni. Adapted from [35] and [36]	10
Figure 6 - Possible microstructures formed during peritectic solidification. [34]	11
Figure 7 - Schematic of solidification morphologies in alloy castings [37].	11
Figure 8 - Peritectic diagram in terms of nucleation temperatures. [31]	12
Figure 9 - Models of peritectic solidification as described, (a) first and (b) second model. [42]	15
Figure 10 - Computed liquidus projection of Ta-Al-Fe. [21, 30]	16
Figure 11 - Calculated liquidus projection of Nb-Al-Co ternary system. [27, 29]	17
Figure 12 - Liquidus projection of Nb-Al-Fe system. [26]	20
Figure 13 - Liquidus projection of Ta-Al-Ti system. [30, 66]	22
Figure 14 - Calculated liquidus projection of the Nb-Si-Ti system. Adapted from [73].	24
Figure 15 - Isothermal section at 1200°C for Nb-Si-Ti system [73].	25
Figure 16 - Schematic illustration for formation of halos in a binary system, (a) Role of nucleation undercooling, where α phase is a good nucleant for β phase, but β phase is not a good nucleant for α phase in equiaxed solidification, (b) Directional solidification showing the undercooling at the growing tips of the halo phase and that required for coupled planar eutectic growth, (c) Schematic	

evolution of the secondary phase morphology in the inter-dendritic region and the existence of a lateral composition gradient.	29
Figure 17 - Turbofan Trent 800 from Rolls Royce. [86]	31
Figure 18 - Usage of materials in a jet engine. [90].....	32
Figure 19 - Example of Nb-silicide turbine blade. [7, 9].....	34
Figure 20 - Nb-Si binary phase diagram. [9, 107, 108].....	35
Figure 21 - Microstructures of a DS alloys annealed at 1773K for 500 h: (a) Nb–17.5Si at 10 mm/h and (b) Nb–10Ti–17.5Si at 10 mm/h (at.%). [1, 113].....	37
Figure 22 - Longitudinal microstructure of an Nb-Si-Ti-Al-Cr-Hf alloy during (a) transient zone and (b) steady-state growth. Adapted from [105].....	38
Figure 23 - Fracture toughness of directionally solidified Nb-Si alloys. [116] ...	39
Figure 24 – Secondary creep behaviour of an Nb-silicide comparing with a MASC alloy, and the creep goal hoped to be achieved. [9].....	41
Figure 25 - Variation of material loss with temperature for an Nb-Ti-Al-Cr-V alloy in oxygen at 1 atm exposed during 60, 120 and 180 minutes between 800°C and 1400°C. [123]	43
Figure 26 - Schematic of power feeding processing LSF [144].....	50
Figure 27 - A simplified illustration of the staircase effect during laser additive manufacturing; where T_L refers to the thickness of layer. [147].....	52
Figure 28 - Unit production cost for additive and traditional manufacturing; (a) against production volume and (b) against product complexity or customisation. Adapted from [154-158].	53
Figure 29 - Nb-silicide cyclic oxidation behaviour. [7].....	56
Figure 30 - Schematic drawing of the SDA processing method. Adapted from [179].	59
Figure 31 - Wire feedstock meeting at the laser beam focus point creating a molten pool. Adapted from [179].	60
Figure 32 - Schematic illustration of the physical stages of melting and solidification via SDA. [180].....	60

Figure 33 - A typical electric arc furnace [203].	63
Figure 34 - MITR YXQM-0.4 L ball mill used in the mixture of elemental powders.	65
Figure 35 - Containers for the alloyed powders to be blown at the nozzles.	66
Figure 36 - LSF-SI600A model laser additive manufacturing machine used for the experiments.....	67
Figure 37 - LAM processed alloys in shape of bars; (a) regular sized samples and (b) shortest and tallest samples. Dimensions vary, but usually 10-20 cm x 2-3cm x 1 cm.	68
Figure 38 - Scanning patterns selected for the AM process; (a) unidirectional, (b) snake and (c) cross-snake.	69
Figure 39 - Typical mechanism for hot isostatic pressing [206].....	71
Figure 40 - HIP machine used for the experiment.....	71
Figure 41 - Characteristic X-ray produced upon interaction with specimen. Adapted from [209].....	74
Figure 42 - Alloy compositions plotted on the Gibbs triangle corresponding to, (a) liquidus projection, (b) solidus projection [21].....	76
Figure 43 - BEI corresponding to S1, (a) low magnification, (b) high magnification.	77
Figure 44 - BEI corresponding to S2, (a) low magnification, (b) high magnification; and to S3 (c) low magnification, (d) high magnification.	78
Figure 45 - Measured composition of solid phases present in S1, S2 and S3 plotted on (a) liquidus and (b) solidus projections, including phase boundaries with decreasing temperature [21].	79
Figure 46 - BEI corresponding to S4, (a) low magnification and (b) high magnification.....	80
Figure 47 - Measured composition of solid phases present in S4 plotted on (a) liquidus and (b) solidus projections, including phase boundaries with decreasing temperature [21].	81

Figure 48 - BEI corresponding to S5, (a) low magnification, (b) high magnification; and to S6 (c) low magnification, (d) high magnification.	85
Figure 49 - Measured compositions of solid phases present in S5 and S6 plotted on (a) liquidus and (b) solidus projections, including phase boundaries with decreasing temperature [21].	87
Figure 50 - (a) Liquidus projection [27], (b) Isothermal section at 1200°C with superimposed limits of solute solubility at 800°C [18].	90
Figure 51 - BEI of microstructure corresponding to S1, (a) low and (b) high magnification; and to S2, (c) low and (d) high magnification.	91
Figure 52 - X-ray diffraction patterns, (a) S1, (b) S2.	92
Figure 53 - Isothermal sections at 1200°C and 800°C, showing the phase boundaries in relation to the compositions in the different phases for S1 and S2 [18].	93
Figure 54 - (a) BEI for S3, (b) low magnification BEI for S4, (c) high magnification BEI for S4.	96
Figure 55 – (a) Isothermal sections at 1250°C and 800°C, showing the phase boundaries in relation to the compositions in the different phases for S3 and S4 [18]; (b) Liquidus projection illustrating path traversed by the liquid composition during freezing in S4 [27].	97
Figure 56 - (a) low magnification BEI for S5, (b) low magnification BEI for S6, (c) high magnification BEI for S5, (d) high magnification BEI for S6.	100
Figure 57 - Isothermal sections at 1250°C and 800°C [18], showing the phase boundaries in relation to the compositions in the different phases for S5 and S6.	100
Figure 58 - (a) low magnification BEI for S7, (b) high magnification BEI for S7.	101
Figure 59 - (a) low magnification BEI for S8, (b) high magnification BEI for S8.	102

Figure 60 - Isothermal sections at 1250°C and 800°C, showing the phase boundaries in relation to the compositions in the different phases for S7 and S8 [18].	103
Figure 61 - (a) Liquidus projection, (b) Isothermal section at 1300°C with superimposed limits of solute solubility at 1000°C [26]. The compositions in this study are superimposed in the figures.	104
Figure 62 - BEI of microstructure corresponding to S1, (a) low magnification, (b) high magnification.	105
Figure 63 - BEI of microstructure corresponding to S2.	106
Figure 64 - Isothermal sections at 1300°C and superimposed solute solubility at 1000°C, showing the phase boundaries in relation to the compositions in the different phases for S1 and S2. Dotted lines show tie-lines from [26].	107
Figure 65 - BEI of microstructure corresponding to S3, (a) low magnification, (b) high magnification.	108
Figure 66 - Isothermal sections at 1300°C and superimposed solute solubility at 1000°C, showing the phase boundaries in relation to the compositions in the different phases for S3 and S4. Dotted lines show tie-lines from [26].	109
Figure 67 - BEI of microstructure corresponding to S4, (a) low magnification, (b) high magnification.	109
Figure 68 - High magnification image of S4 showing in detail the ternary eutectic formation.	110
Figure 69 - BEI of microstructure corresponding to S5, (a) low magnification, (b) high magnification.	112
Figure 70 - BEI of microstructure corresponding to S6, (a) low magnification, (b) high magnification.	112
Figure 71 - Isothermal sections at 1300°C and superimposed solute solubility at 1000°C, showing the phase boundaries in relation to the compositions in the different phases for S5 and S6. Dotted lines show tie-lines from [26].	114
Figure 72 - BEI of microstructure corresponding to S7, (a) low magnification, (c) high magnification; and S8, (b) low magnification, (d) high magnification.	116

Figure 73 - Isothermal sections at 1300°C and superimposed solute solubility at 1000°C, showing the phase boundaries in relation to the compositions in the different phases for S7 and S8. Dotted lines show tie-lines from [26].	117
Figure 74 - (a) Liquidus projection, (b) Solidus projection with superimposed limits of solute solubility at 1350°C [28, 30, 63]. The compositions in this study are superimposed in the figures.	119
Figure 75 - BEI of microstructure corresponding to S1, (a) low magnification, (b) high magnification.	119
Figure 76 - Solidus projection and superimposed solute solubility at 1350°C, showing the phase boundaries in relation to the compositions in the different phases for S1 [30].	120
Figure 77 - BEI of microstructure corresponding to S2, (a) low magnification, (b) high magnification.	121
Figure 78 - Solidus projection and superimposed solute solubility at 1350°C, showing the phase boundaries in relation to the compositions in the different phases for S2 [30].	123
Figure 79 - BEI of microstructure corresponding to S3, (a) low magnification, (b) high magnification.	124
Figure 80 - Solidus projection and superimposed solute solubility at 1350°C, showing the phase boundaries in relation to the compositions in the different phases for S3 [30].	126
Figure 81 - BEI of microstructure corresponding to S4, (a) low magnification, (b) high magnification.	126
Figure 82 - Detailed high magnification BEI of S4.	128
Figure 83 – Solidus projection and superimposed solute solubility at 1350°C, showing the phase boundaries in relation to the compositions in the different phases for S4 [30].	130
Figure 84 - Low magnification BEI of microstructure corresponding to S5.	131
Figure 85 - High magnification BEI of microstructure corresponding to S5, (a) Ta-rich side, and (b) Ti-rich side.	131

Figure 86 - Solidus projection and superimposed solute solubility at 1350°C, showing the phase boundaries in relation to the compositions in the different phases for S5 [30].	133
Figure 87 - BEI's for S1, (a) low magnification, (b) high magnification, and (c) liquidus projection and (d) solidus projections at Ta-rich end. Also included are phase boundaries with decreasing temperature and the measured composition in the phases. Adapted from [21, 30].	136
Figure 88 - BEI's corresponding to S2, (a) low magnification, (b) high magnification, and (c) liquidus projection and (d) solidus projections at Ta-rich end. Also included are phase boundaries with decreasing temperature and the measured composition in the phases. Adapted from [21, 30].	138
Figure 89 - BEI's corresponding to S3, (a) low magnification, (b) and (c) high magnification, and (d) liquidus projection and (e) isothermal sections showing phase boundaries with decreasing temperature, with the measured phases compositions included. Adapted from [18, 27, 218].	140
Figure 90 - BEI's corresponding to S4, (a) low magnification, (b) and (c) high magnification, and (d) liquidus projection and (e) isothermal sections showing phase boundaries with decreasing temperature, with the measured phases compositions included. Adapted from [18, 27, 218].	143
Figure 91 - BEI's corresponding to S5, (a) low magnification, (b) and (c) high magnification, and (d) liquidus projection and isothermal sections showing phase boundaries with decreasing temperature in the Al-rich end, including phases measured compositions. Adapted from [26, 219, 220].	146
Figure 92 - Liquid and solid interfacial equilibrium during solidification.	147
Figure 93 - Schematic of ternary diagram illustrating the liquid and solid compositions during eutectic growth, $L \rightarrow \alpha + \beta$, as a function of the undercooling. Adapted from [20].	148
Figure 94 – Liquidus projection of ternary Nb-Si-Ti [70-72].	152
Figure 95 - BEI of Nb-15Si-22Ti-14Cr-2Al-2Hf-2V as-formed alloy, (a) low magnification and (b) high magnification.	153

Figure 96 - XRD pattern for the as-formed Nb-15Si-22Ti-14Cr-2Al-2Hf-2V alloy.	155
Figure 97 - BEI of Nb-15Si-22Ti-14Cr-2Al-2Hf-2V alloy after HIP process, (a) low magnification and (b) high magnification.....	157
Figure 98 - BEI of Nb-15Si-22Ti-14Cr-2Al-2Hf-2V alloy after heat treatment process, (a) low magnification and (b) high magnification.....	158
Figure 99 - Isothermal section at 1500°C for the Nb-Ti-Cr system, showing the likely position of the C15 Laves phase composition [224].	159
Figure 100 - DSC curve analysis of heat treated Nb-15Si-22Ti-14Cr-2Al-2Hf-2V alloy at 1500°C.....	160
Figure 101 - Microstructure evolution of Nb-15Si-22Ti-14Cr-2Al-2Hf-2V alloy from as-formed to HIP process to heat treatment stages.....	162
Figure 102 - BEI of as-formed Nb-15Si-22Ti-2Cr-2Al-2Hf-2V alloy, (a) low magnification and (b) high magnification.....	163
Figure 103 - XRD pattern for the as-formed Nb-15Si-22Ti-2Cr-2Al-2Hf-2V alloy.	164
Figure 104 - BEI of Nb-15Si-22Ti-2Cr-2Al-2Hf-2V alloy after HIP process, (a) low magnification and (b) high magnification.....	166
Figure 105 - BEI of the centre of Nb-15Si-22Ti-2Cr-2Al-2Hf-2V alloy after heat treatment, (a) low magnification and (b) high magnification.	167
Figure 106 - BEI of the edge of Nb-15Si-22Ti-2Cr-2Al-2Hf-2V alloy after heat treatment, (a) low magnification and (b) high magnification.	169
Figure 107 - Microstructure evolution of Nb-15Si-22Ti-2Cr-2Al-2Hf-2V alloy from as-formed to HIP process to heat treatment stages.	170
Figure 108 - BEI of as-formed Nb-18Si-24Ti-5Cr-5Al-2Mo alloy, (a) low magnification and (b) high magnification.....	171
Figure 109 - Isothermal section at 1200°C with measured compositions of phases present in the Nb-18Si-24Ti-5Cr-5Al-2Mo alloy [73]. Solid triangle and square represent Nb ₅ Si ₃ phase; solid circle represents solid solution phase.....	173

Figure 110 - BEI of HIP processed Nb-18Si-24Ti-5Cr-5Al-2Mo alloy, (a) low magnification and (b) high magnification.....	174
Figure 111 - BEI of Nb-18Si-24Ti-5Cr-5Al-2Mo alloy after heat treatment, (a) low magnification and (b) high magnification.....	176
Figure 112 - Detail of formation of Ti_{ss} phase.....	178
Figure 113 - XRD pattern for Nb-18Si-24Ti-5Cr-5Al-2Mo alloy, (a) as-formed, (b) HIP processed and (c) heat treated.	180
Figure 114 - Microstructure evolution of Nb-18Si-24Ti-5Cr-5Al-2Mo alloy from as-formed to HIP process to heat treatment stages.	182
Figure 115 - BEI of as-formed Nb-22Si-26Ti-6Cr-2Al-3Hf alloy, (a) low magnification and (b) high magnification.....	183
Figure 116 - XRD pattern for the as-formed Nb-22Si-26Ti-6Cr-2Al-3Hf.....	185
Figure 117 - BEI of HIP processed Nb-22Si-26Ti-6Cr-2Al-3Hf alloy, (a) low magnification and (b) high magnification.....	185
Figure 118 - BEI of Nb-22Si-26Ti-6Cr-2Al-3Hf alloy after heat treatment, (a) low magnification and (b) high magnification.....	187
Figure 119 - Microstructure evolution of Nb-22Si-26Ti-6Cr-2Al-3Hf alloy from as-formed to HIP process to heat treatment stages.	189

List of Tables

Table 1 - Equilibrium transformations and invariant reactions in the Nb and Ti-rich corner of Nb-Si-Ti system [70, 73, 76].	26
Table 2 - Difference between conventional manufacturing and additive manufacturing in terms of many production aspects. [145, 146]	51
Table 3 - Mechanical properties comparison for a range of Ni, Ti and Co-based alloys in terms of processing methods [171-175].	55
Table 4 - The comparison between wire-feed system and powder-feed system.	58
Table 5 - Parameters of laser used in the LAM processing of alloys.	67
Table 6 - Selection of compositions (in at.%) for AM processed alloys.	68
Table 7 - Parameters used during HIP process.	72
Table 8 - List of samples, elemental composition, condition and observed phases in the microstructure of Ta-Al-Fe samples.	75
Table 9 - Average measured compositions (in at.%) of phase present in S1, S2 and S3.	78
Table 10 - Average measured compositions (in at.%) of phase present in S4.	82
Table 11 - Average measured compositions (in at.%) of phase present in S5 and S6.	86
Table 12 - List of samples, elemental composition and observed phases in the microstructure of Nb-Al-Co samples.	89
Table 13 - Average composition (in at.%) of phases present in S1 and S2.	92
Table 14 - Average composition (in at.%) of phases present in S3 and S4.	95
Table 15 - Average composition (in at.%) of phases present in S5 and S6.	98
Table 16 - Average composition (in at.%) of phases present in S7.	101
Table 17 - Average composition (in at.%) of phases present in S8.	102

Table 18 - Nominal measured compositions of the alloys studied (in at. %) and phases expected according to liquidus projection.	103
Table 19 - Average measured composition (in at.%) of phases present in S1 and S2.....	106
Table 20 - Average composition (in at.%) of phases present in S3.....	108
Table 21 - Average composition (in at.%) of phases present in S5 and S6. ...	113
Table 22 - Average composition (in at.%) of phases present in S7 and S8. ...	115
Table 23 - Nominal measured compositions of the alloys studied (in at. %) and phases expected according to liquidus projection.	118
Table 24 - Average measured composition (in at.%) of phases present in S1.	120
Table 25 - Average measured composition (in at.%) of phases present in S2.	122
Table 26 - Average measured composition (in at.%) of phases present in S3.	124
Table 27 - Average measured composition (in at.%) of phases present in S4.	127
Table 28 - Comparison between nominal and measured composition (in at.%) for S5.....	130
Table 29 - Average measured composition (in at.%)of phases present in S5.	132
Table 30 - List of samples, elemental composition and observed phases in the microstructure. “p” denotes primary phase.....	134
Table 31 - Average composition (in at.%) of phases with standard deviation in S1 and S2.....	139
Table 32 - Average composition of phases (in at.%) with standard deviation in S3 and S4.....	144
Table 33 - Average composition of phases with standard deviation in S5 (in at. %).	145

Table 34 - Average compositions (in at.%) of phases present in Nb-15Si-22Ti-14Cr-2Al-2Hf-2V alloy.	153
Table 35 - Range of temperature for the suggested solidification path of Nb-15Si-22Ti-14Cr-2Al-2Hf-2V alloy.	155
Table 36 - Average composition (in at.%) of phases present in HIP processed Nb-15Si-22Ti-14Cr-2Al-2Hf-2V alloy.	157
Table 37 - Average composition (in at.%) of phases present in heat treated Nb-15Si-22Ti-14Cr-2Al-2Hf-2V alloy.....	160
Table 38 – Average composition (in at.%) of phases present in Nb-15Si-22Ti-2Cr-2Al-2Hf-2V alloy.	165
Table 39 - Average composition (in at.%) of phases present in HIP processed Nb-15Si-22Ti-2Cr-2Al-2Hf-2V alloy.....	166
Table 40 - Average composition (in at.%) of phases present in the heat treated Nb-15Si-22Ti-2Cr-2Al-2Hf-2V alloy.....	168
Table 41 – Average composition (in at.%) of phases in the as-formed Nb-18Si-24Ti-5Cr-5Al alloy.	172
Table 42 - Average compositions (in at.%) of phases present in Nb-18Si-24Ti-5Cr-5Al-2Mo alloy after HIP process.....	175
Table 43 – Average measured compositions of phases present in Nb-18Si-24Ti-5Cr-5Al-2Mo alloy after heat treatment.	177
Table 44 - Diffusivity of Ti and Nb solute as a function of Nb content and temperature.....	179
Table 45 - Average composition (in at.%) of phases present in as-formed Nb-22Si-26Ti-6Cr-2Al-3Hf alloy.	184
Table 46 - Average composition (in at.%) of phases present in HIP processed Nb-22Si-26Ti-6Cr-2Al-3Hf alloy.....	186
Table 47 - Average composition (in at.%) of phases present in heat treated Nb-22Si-26Ti-6Cr-2Al-3Hf alloy.	188

Nomenclature

AM	Additive Manufacturing
BCC	Body-Centered Cubic
BCT	Boettinger-Coriell-Trivedi
BEI	Back-scattered Image
CAD	Computer Aided Design
CNC	Computer Numeric Control
DLF	Direct Laser Fabrication
DLF	Direct Laser Fabrication
DLS	Directional Laser Sintering
DS	Directional Solidification
DSC	Differential Scanning Calorimetry
EAF	Electric Arc Furnace
EDS	Energy Dispersive Spectroscopy
FCC	Face-Centered Cubic
FEG	Field Emission Gun
FIB	Focus Ion Beam
FZ	Floating Zone
HIP	Hot Isostatic Pressing
HT	Heat Treatment
ID	Inter-Dendritic
LAM	Laser Additive Manufacturing
LSF	Laser Solid Forming
MASC	Metal and Silicide Composite

PCG	Peritectic Coupled Growth
PVD	Physical Vapour Deposition
RM	Refractory Metal
RMIC	Refractory Metal-Intermetallic Composites
SDA	Suspended Droplet Alloying
SDD	Silicon Drift Detector
SEM	Scanning Electron Microscope
TBC	Thermal Barrier Coating
TET	Turbine Entry Temperature
TMK	Trivedi-Magnin-Kurz
XRD	X-ray Diffraction

Chapter 1 Introduction

1.1. Justification

Ni-based superalloys are getting to their limits when it comes to working temperature, as they have approached temperatures near the melting temperature [1]. Throughout the past years, improvements in casting and composition have increased the working temperature by 125°C, to approximately 1150°C, even with the use of thermal barrier coating (TBC). Temperatures beyond this will be very difficult to achieve, since the melting temperature of these advanced alloys can reach about 1350°C [2, 3]. Figure 1 shows the variation of temperature and pressure in the different sections of a turbine engine [4].

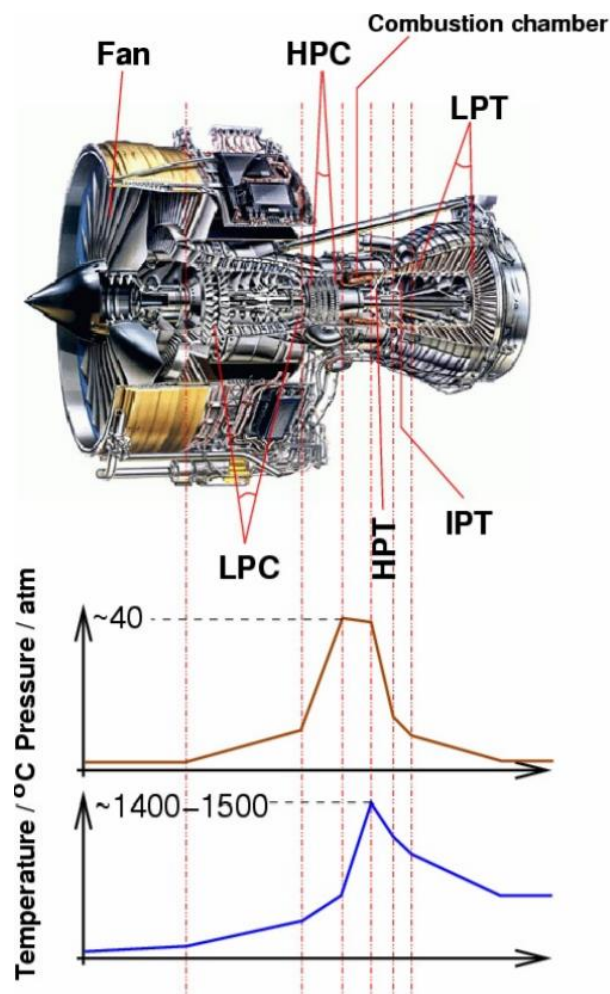


Figure 1 - Temperature and pressure variation across the different sections of a turbine engine. LPC and HPC correspond to low and high-pressure compressors, respectively. HPT, IPT and LPT correspond to high, intermediate and low pressure turbines, respectively [4].

New refractory metals-based ternary alloys are being investigated as alternate candidate materials to Ni-base alloys. These systems contain a refractory metal (RM) with aluminium (Al) being part of the composition, and a third reinforcing metal (namely X), thus potential candidates for static components in gas turbines, such as discs. Its notation refers as [5]:

- RM refers to refractory metals, and they are required to provide high temperature capability and generally show solid solution hardening;
- Al provides the formation of a protective oxide layer that ensures good oxidation resistance;
- X usually refers to a transition metal, which confers high temperature strength, such as Fe, Ti and Ta.

Examples of these systems are Nb-Al-Ru and Nb-Al-Pd, where the ordered B2 precipitates present in the disordered A2 matrix constitute the strengthening phase. This principle is similar to that in Ni-base alloys, where the ordered γ' (L1₂) precipitate in the disordered A1 FCC matrix provides the high temperature strength, while the matrix is ductile [6].

Niobium silicide-based composites, in the application of gas turbine blades, promise significant efficiency improvements compared to current Ni-based alloys [7]. Higher temperature capability would allow engines to run at higher temperatures, increasing their efficiency [8]. These composites possess lower density and high strength, due to the presence of ceramic phases as Nb₅Si₃ and/or Nb₃Si combined with Nb_{ss} phase, given that lower mass would also increase engine efficiency, which is one of the main reasons for its use. [9, 10]. Additions of alloying elements such as Al, Ti, Cr, Hf, V and Mo into the composition of Nb-silicide alloys seek a balance of properties to produce a composite useful in applications at high temperatures [11-13].

The high promise of Nb-silicide based alloys combined with the manufacturing processes based on additive manufacturing methods have been proven to be highly innovative, as it opens a new window of opportunities for efficiency, the reduction of energy consumption and the waste of raw materials [14].

1.2. Objectives

The main objectives of this thesis include: (a) a review of current developments in the production of refractory metals alloys based on niobium silicide systems, focusing on the analysis of results obtained for the novel additive manufacturing process when compared to cast processed alloys; and (b) the validation of the behaviour of refractory metals-based cast alloys under conditions far from equilibrium, as this will dictate whether these alloys could potentially be used in high temperature applications due to their high melting temperature capabilities.

Two specific objectives can be drawn:

- 1) The analysis of the solidification sequence of Nb- and Ta-based ternary alloys processed by rapid solidification techniques, which will provide a validation of the liquidus and solidus projections as well as of the isothermal sections obtained under equilibrium conditions.
- 2) The analysis of the solidification sequence and the microstructure evolution of NbSi-based alloys processed via an additive manufacturing technique, which will provide a comparison between previously studied alloys processed via traditional routes and the novel additive manufacturing process for high temperature applications. This will lead to a validation of phase equilibria obtained under equilibrium conditions, the analysis of the effect of alloying elements and the change in microstructure caused by post processing methods, such as hot isostatic pressing and heat treatment.

1.3. Thesis structure

It is well understood that high temperature Ni-based alloys for jet engine application are reaching their limits, and further improvements are necessary. New classes of materials are suggested in order to provide a high temperature capability higher than that of Ni-based alloys. In these engine parts, both static and dynamic loadings are observed.

Ternary alloys based on refractory metals alloys are being investigated for static loading applications (such as engine case and vanes), with focus on the formation of intermetallic phases, which is of interest in achieving the properties needed for these materials. A thorough analysis of these alloys is presented in Chapter 2.

High pressure turbine blades are subjected to dynamic loading at high temperature and are sought to be replaced by lighter materials with higher temperature capability. For these applications, niobium silicide-based alloys have been under investigation in the past years, and a review of the recent progress in developing the new materials are presented in Chapter 3.

Although much is yet to be understood about these different alloys, a detailed study of how the solidification path takes place during freezing in addition to the invariant reactions has been carried out, with focus on peritectic and quasi-peritectic reactions.

An extended analysis of experimental procedures is given in Chapter 4, with an introduction to the novel additive manufacturing process to high temperature alloys. Chapter 5 shows the choice of parameters for each technique, with details on how the alloys have been produced.

Chapter 6 and 7 present a detailed analysis of the results obtained for the refractory metals-based cast ternary alloys and the additive manufactured alloys, respectively. Each subsection shows the perspective of results for individual alloys systems.

Finally, the overall conclusions and the suggestions for future work are presented in Chapter 8.

Chapter 2 Refractory metals-based ternary alloys

Many ternary systems of this type are under investigation, though much is yet to be understood, which require the use of experimental ternary diagrams, liquidus projections and isothermal sections that are being developed to assist on this matter [6].

Addition of Al on these systems aims to improve the oxidation behaviour with the formation of a continuous layer of Al_2O_3 . Other intermetallic phases as the Laves phase has also been identified as promising phases for structural applications [15, 16], since they show high strength at temperatures above 1000°C , although they show brittle behaviour at room temperature [16].

Additions of Ta are important in promoting a ternary Laves phase, with hexagonal C14 structure [16]. Past investigations show that when Ta is added to the Fe_3Al aluminide, there is an unexpected formation of a Heusler-type ternary phase in addition to the formation of the $(\text{Fe,Al})_2\text{Ta}$ Laves phase [17]. The Heusler-type phase is also observed when Nb is added to the alloy system, where the formation of Co_2AlNb occurs [18].

2.1. Solidification behaviour of refractory metals-based alloys

In ternary systems, additional aspects need to be considered when addressing the solidification path. During primary phase growth, there is an added degree of freedom, different to binary systems. Therefore, an extent of back-diffusion within the solid might be caused due to the path traversed by the liquid composition on the liquidus surface, which then dictates the evolution of solid phase fraction, and in ternary systems determine where the liquid composition intersects the monovariant line that marks the end of primary freezing if all the liquid has not been consumed [19]. From that, two cases are developed;

- (a) If there is a transition in the monovariant line across the liquidus surface while proceeding to lower temperatures, then the path followed by the liquid composition will dictate the nature of the three-phase reaction that will result (eutectic, peritectic, etc.) [20].
- (b) Two of the three monovariant lines emanating from the invariant point will enclose the liquidus surface of the primary phase. The path traversed by the liquid will determine which of these two monovariant lines the liquid composition will intersect at the end of primary freezing. Also in some cases suppression of the four-phase invariant reaction, $L + \alpha \rightarrow \beta + \gamma$ might also occur [5, 21].

Both points will have a role on the subsequent invariant reactions, whether it will occur and on the subsequent three-phase reactions or not. In a binary system for an invariant reaction with two phases and liquid (L, α, β) [22];

- Eutectic – The three phases grow simultaneously and are co-incident along a line, where the compositions in the phases follow the tie-line ($L \rightarrow \alpha + \beta$). Apart from the tie-line, the primary growth of separated two phases will occur as, $L \rightarrow \alpha$ and $L \rightarrow \beta$ respectively.
- Peritectic – Phases also co-incident along a line, where the reaction takes place ($L + \alpha \rightarrow \beta$). This is controlled by diffusion in the liquid which leads to the formation of a rim of peritectic β phase across primary α and is given by the two reactions, $L \rightarrow \beta$ and $\alpha \rightarrow L$. Due to limited diffusion in the solid, the subsequent peritectic transformation is inhibited and growth of β occurs through primary freezing as, $L \rightarrow \beta$ [23].

The understanding of peritectic reactions and/or invariant four-phase reactions will be of great help during the analysis of the solidification path of the alloys. These invariant reactions encountered for the ternary systems involving four phases (L, α, β, γ). In this case, co-incident of all phases will only occur at a point, nucleation of the third solid phase will necessarily occur on one of the two existing solid phases and growth of this third phase must involve a three-phase reaction [22];

- Class I, ternary eutectic reaction – This reaction comprises of a formation of three different solids directly from the liquid, $L \rightarrow \alpha + \beta + \gamma$. Due to limited

diffusion and freezing over a range of temperature, this reaction can occur as two separate eutectics.

- Class II, quasi-peritectic reaction – After primary freezing and following a monovariant reaction, the Class II reaction can take place when not all liquid has been consumed, and the consumption of one solid gives place to the formation of two new solids, $L + \alpha \rightarrow \beta + \gamma$.
- Class III, ternary peritectic reaction – The ternary peritectic occurs from the consumption of two phases formed primarily, eutectically or peritectically into a new third phase, $L + \alpha + \beta \rightarrow \gamma$. Similarly to the binary case, this reaction is very limited, and it can occur into separate reactions, e.g. $L \rightarrow \alpha + \gamma$, $L + \beta \rightarrow \gamma$ or even primary formation, $L \rightarrow \gamma$, when the phases are surrounded at lower temperatures.

It is highly important that the sequence of solidification of these alloys is understood, which will dictate the final microstructure and the heat treatment to be used, if any. Equilibrium conditions may not always be constant in these systems, so a careful study is needed to identify phases and invariant reactions present in the alloys, since diffusion, solubility and solidification rate may cause deviations from the expected sequence. During this study, four ternary systems are being considered under investigation: Nb-Al-Co, Nb-Al-Fe, Ta-Al-Ti and Ta-Al-Fe. The diagrams for these systems will be presented. The phases and the reactions present in each diagram are present elsewhere [18, 24-30].

2.1.1. The peritectic invariant reaction

The peritectic reaction occurs when, during solidification, a liquid phase reacts with a solid phase to produce a second solid phase, generally an intermetallic phase, and is defined as $\alpha + L \rightarrow \beta$, in a peritectic composition C_p of the solid β , at a peritectic temperature T_p , as shown in Figure 2. C_α and C_L are related to the composition of the solid α and the peritectic liquid during the transformation, respectively, and define the range of composition for a peritectic alloy.

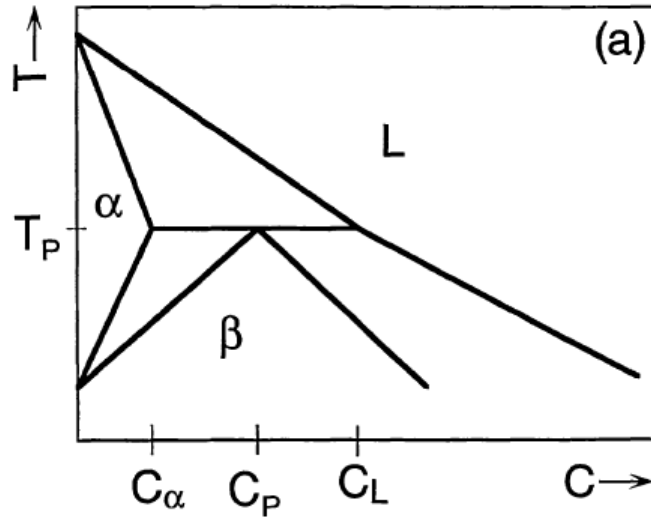


Figure 2 - Peritectic solidification diagram. [31]

A rim of β phase tends to be formed around the solid α phase as the solidification takes place, as shown in the synchrotron X-ray analysis in Figure 3.

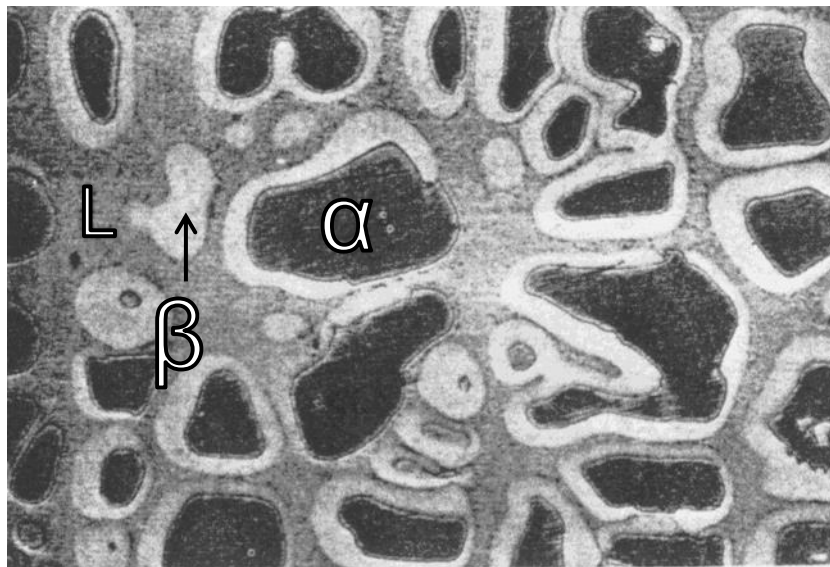


Figure 3 - Peritectic solidification. Adapted from [32]

For binary systems, the peritectic reaction is observed to occur at a specific temperature T_p , and for ternary or higher order alloys, at a range of temperatures along the invariant line where a tie-triangle is formed, in which the three phases coexist.

2.1.2. Crystal growth during peritectic reaction

As stated by Kerr et al. [31], the growth of a peritectic β phase can be identified in three stages: (i) the reaction, due to the interaction between the solid α and the liquid (L) (seen in Figure 3); (ii) the transformation, by the thickening of β phase through solid state diffusion; and (iii) solidification of β from the liquid to the β layer. Figure 4 presents a schematic diagram of this process.

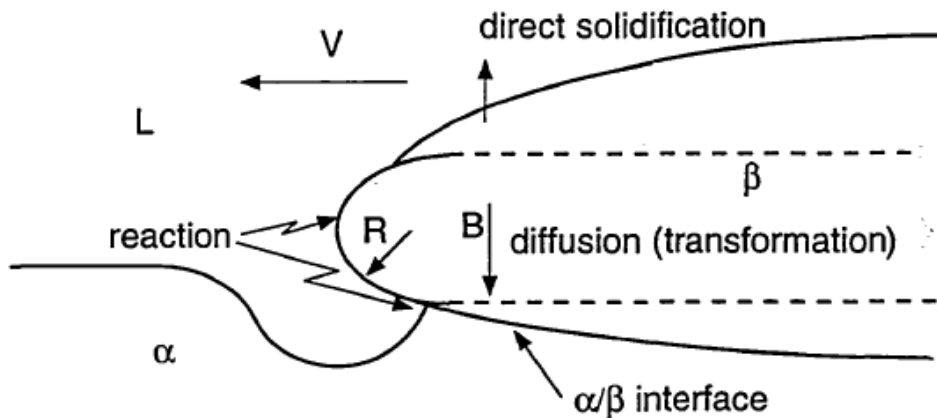


Figure 4 - Liquid-solid diffusion during peritectic reaction. [31]

In the three phase equilibrium junction, the surface energy is expected to be balanced, as stated by Hillert [23]. Thus, dissolution and re-solidification of α occurs during growth of β , which is driven by the compositional difference.

2.1.3. Peritectic solidification of binary alloys

The peritectic solidification in binary alloys, as for Fe-Ni used here for exemplification, is given by $L + \delta (\text{Fe}) \rightarrow \gamma (\text{Fe,Ni})$, as shown in the Fe-Ni binary diagram in Figure 5. These alloys are often used in a range of 4-5 atomic (at.) % Ni [33].

For a composition between C_δ and C_γ , as shown in Figure 5, a lamellar peritectic coupled growth (PCG) was observed to be originated under plane front conditions. Dobler et al.[34] found that for a G/V of $1.8 \times 10^9 \text{ K.s/m}^2$ (G being thermal gradient and V the solidification rate), the local composition for the lamellar growth was between 3.9 and 4.3 at.% Ni, and for the lower limit of 3.9 at.%, preferred low-energy interfaces were found between the solid phases,

forming short wavelength $1-\lambda$ oscillatory instabilities ($1-\lambda$ referring to the lateral wavelength corresponding to the lamellar spacing λ).

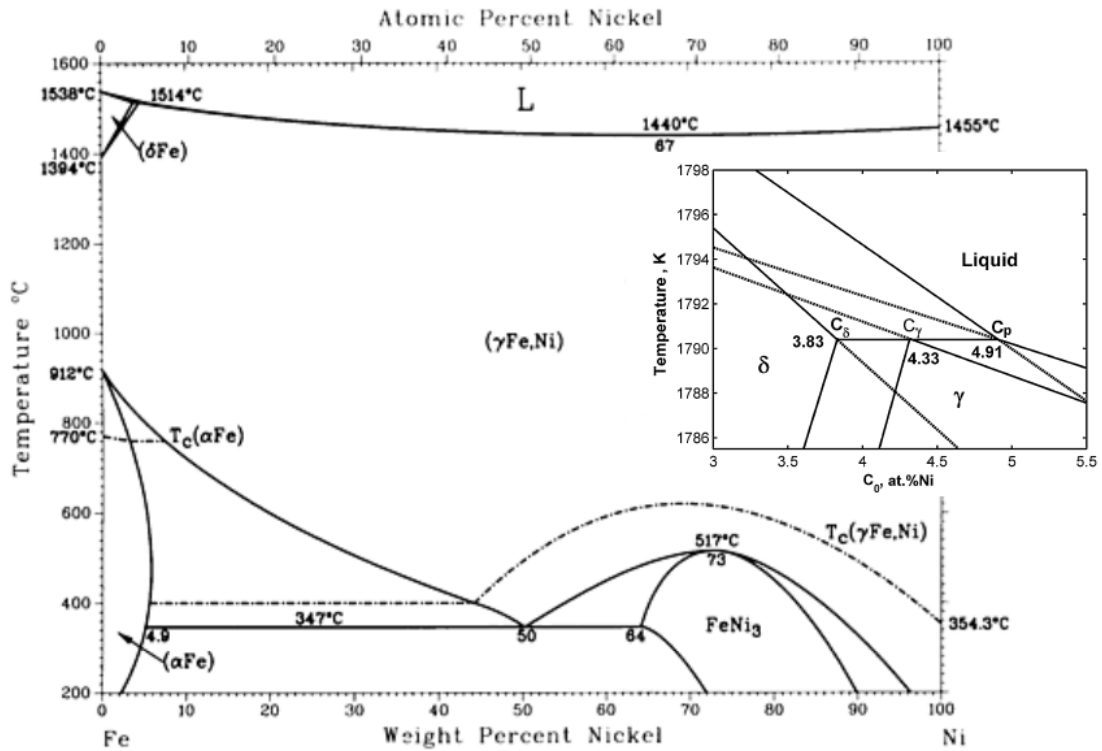


Figure 5 - Binary diagram of Fe-Ni. Adapted from [35] and [36].

At lower compositions, cells of peritectic formation can be present. On the other hand, for the upper limit of 4.3 at.%, no preference was found in the interface of growth of the lamellar structure, which forms a random maze-like structure. In this case, with the composition near C_γ , a transformation occurs from the oscillatory characteristic into fibres. Below composition C_δ , a plane front of δ phase is formed, and at higher concentrations, a planar γ phase appears. Figure 6 shows the structure relationship with the varying Ni composition.

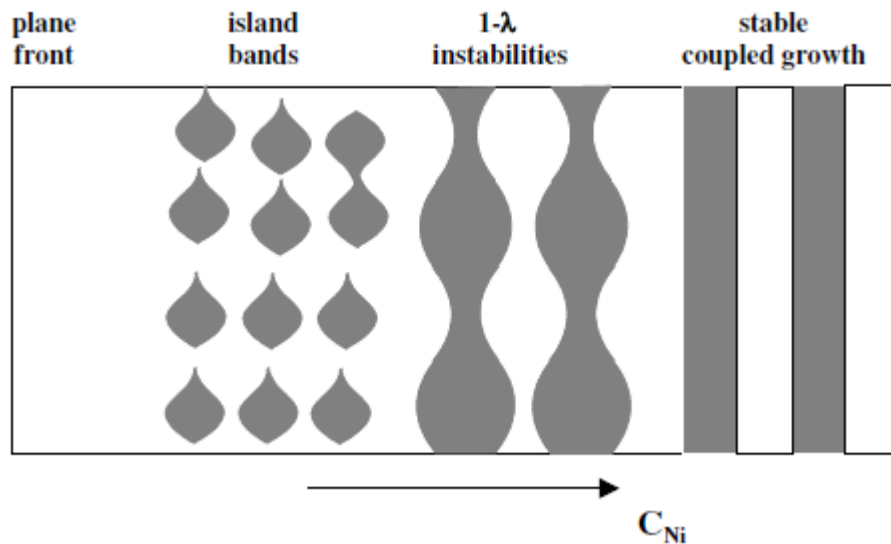


Figure 6 - Possible microstructures formed during peritectic solidification. [34]

Even with the necessary conditions for the stable couple growth, its formation is not spontaneous, and a transition from the oscillatory structure is often present. Due to the micro-segregation during this transition, island bands can also be present in the solidification [34]. The change in front of solidification is widely debated and can vary from alloy to alloy, however a general overview of different velocities and temperature gradients during casting is given in Figure 7 [37].

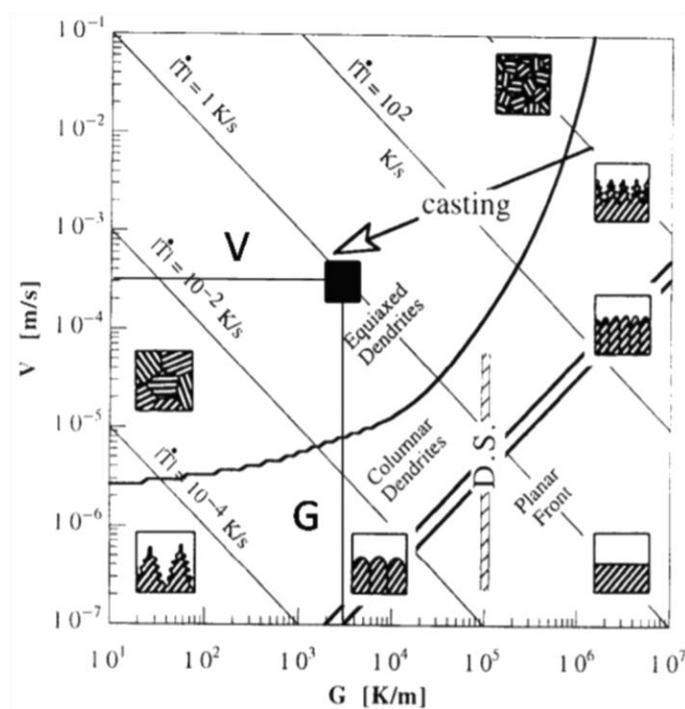


Figure 7 - Schematic of solidification morphologies in alloy castings [37].

2.1.4. Banding structures formed during peritectic reaction

The formation of band structures is given by the presence of unstable fronts of growth when high velocity of solidification provokes oscillatory instabilities, which are formed by the transition from the dendritic/cellular front to plane fronts of growth during solidification. High velocity bands are usually formed by a single phase, while low velocity bands can be formed by the presence of two phases of an unstable peritectic growth. The study of band formations in peritectic solidification is yet to be improved as many details remain unknown, and these formations are largely dependent on the nucleation sites through the liquid.

A model of band formations has been proposed by Trivedi [38], considering an alloy of composition C_0 under stable planar front growth, with $\Delta G > 0$, as presented in Figure 8.

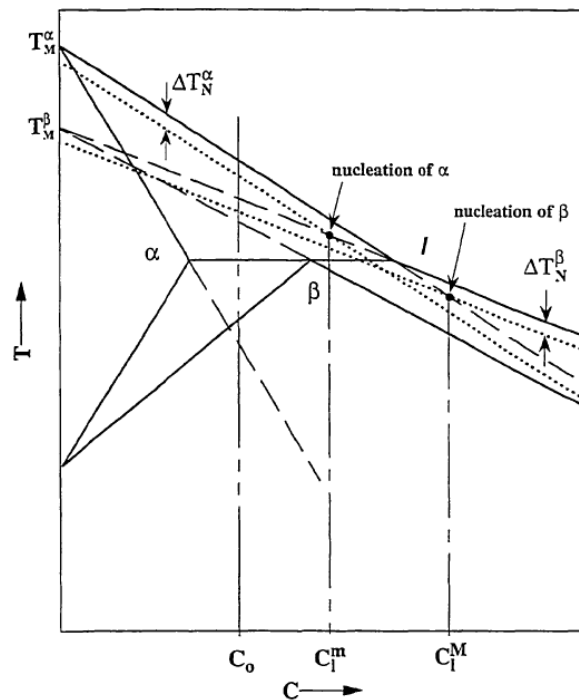


Figure 8 - Peritectic diagram in terms of nucleation temperatures. [31]

Under controlled growth and nominal composition C_0 , α phase nucleates with a solid composition C_1^m , achieving a steady state. Metastable β can be formed if the liquid reaches the composition C_1^M , given by the crossover of α liquidus in its metastable form with the nucleation temperature of β , given by β liquidus minus the undercooling of formation of β -phase (ΔT_N^β), when the solid composition is higher than C_0 .

With a local composition higher than C_0 , the solid temperature reaches the nucleation point of β phase, where the liquid has composition C_1^M . After that, there is a recalescence that elevates the local temperature high enough for nucleation of α , and this generates a cycle of solidification, which leads to the formation of a banding structure [32, 34, 38].

Banding structures usually appear in the microstructure of low temperature alloys, although they can appear in the Fe-Ni according to the solidification parameters, and they act as nucleant for the formation of PCG [35].

2.1.5. Island Bands formed during peritectic reaction

From phase-field simulations, Lo et al. [32] have mentioned that the island morphology is formed when the volume fraction of peritectic phase is low, and for a balanced fraction of primary and peritectic phases bands formations are favoured. This means that, for a given range of composition, there exists a microstructure selection, for a given G/V . From those simulations, microstructures of peritectic phases as island bands in a primary phase matrix were obtained, as well as primary phase islands in a peritectic matrix, although neither seems to have been fully formed experimentally.

The undercooling is responsible for the islands nucleation in the solid-liquid interface, and the transition from bands to island banding occurs due to solute redistribution.

2.1.6. Peritectic Couple Growth

In directional solidification, low temperature gradients of binary alloys facilitate the primary phase formation with a dendritic or plate-like front, followed by the peritectic phase. Recent studies have been carried out, trying to achieve an ordered directional coupled structure, as that obtained for eutectic alloys.

Boettinger [39] has studied the peritectic coupled growth of directional solidified Sn-Cd at different G/V ratios, and applying the Jackson-Hunt [40] model for eutectic growth, assuming that the growth occurred as a lamellar structure, it was found that the peritectic structure is dependent on ΔT and lamellar spacing, λ .

Chalmers [41] has pointed out that in a composition range between C_α and C_p , two solids can form from the liquid in a coupled growth characteristic at T_p , if plane front conditions are found.

The PCG is characterised as the simultaneous growth of phases δ and γ side by side, for the Fe-Ni system, sharing a weak diffusion between them, towards the liquid. Island banding can appear for some conditions, mainly by nucleation in the intercellular grooves, forming isolated island of solid phase.

Feng et al. [42] found that PCG was originated directly from the planar δ phase. From that, two models were proposed as follows;

- (a) The first model considers the diffusion of solute from the primary solid to the liquid, which generates a solute concentration followed by an undercooling. From that undercooling, the γ phase may nucleate and form island bands, which initiate the couple growth. Based on this, the formation of PCG from the δ bands was given by the fact that the small distances between the γ nuclei can allow the δ phase to squeeze through and form the couple growth, at a steady velocity [32, 38].
- (b) The second model is proposed based on the influence of the peritectic reaction. Given the undercooling achieved similar to the first model, if γ phase does not reach the necessary requirements for nucleation, the planar growth of δ phase can turn into a cellular front growth, which will extend into the liquid. The region below the tips may reach the temperature of peritectic reaction T_p and can decrease rapidly, therefore a small fraction of γ will form, which can cause solidification of γ directly from the remaining liquid into the δ spaces to start the couple growth. Figure 9 represents both proposed models [42].

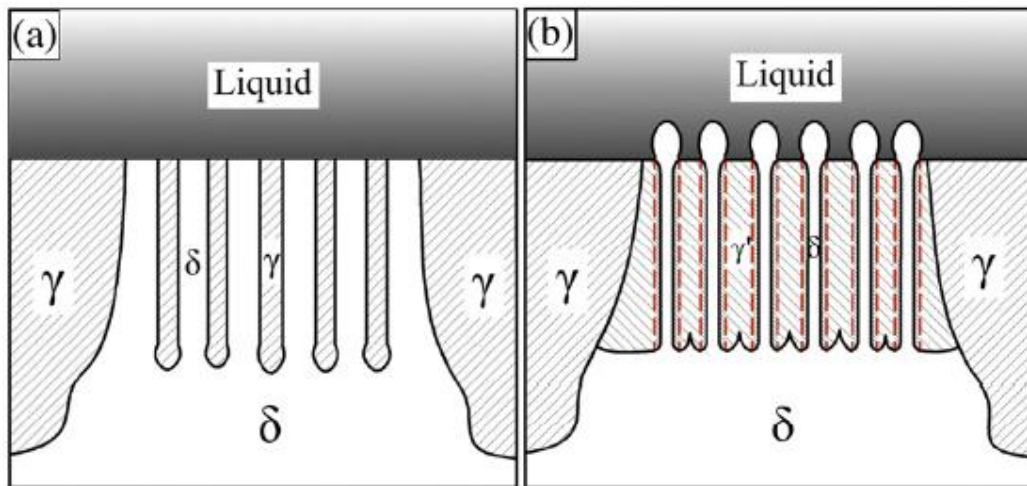


Figure 9 - Models of peritectic solidification as described, (a) first and (b) second model. [42]

Vandyoussefi et al. [43] have succeeded in producing a coupled growth microstructures in the centre of specimens of Fe-Ni alloys with $C_0 = 4.49$ at. %Ni, for G/V between 0.8×10^9 and 1.3×10^9 K.s/m². It was found that the Ni content through the phases attained values very close to their equilibrium conditions. Specimens with lower Ni content formed various two-phase morphologies rather than oriented coupled growth, with δ phase at the centre and γ ferrite at the edge, and with some observed transitions of cells, oscillatory formations and planar front.

2.2. A ternary Ta-Al-Fe system

When normal solidification is observed, it is commonly assumed that the solid/liquid interface is under equilibrium conditions, even though there is a limitation to diffusion [44]. However, an “added degree of freedom” exists for a ternary system during primary freezing due to the additional pure phase present, and depending on the diffusion in the solid, the path followed by the liquid composition will dictate the amounts of phases present [45]. Large cooling rates might be encountered during freezing due to high melting point and superheat. When this occurs, extended solute solubility occurs accompanied by significant deviations from the expected freezing sequence [46-48].

Therefore, to understand the solidification path in these alloys under rapid freezing conditions, Ta-Al-Fe system alloys, shown in Figure 10 with compositions in the Ta-rich corner will be selected in order to evaluate how the

different primary phases, the uni-variant eutectic and peritectic reaction and the invariant Class II invariant reactions vary under non-equilibrium conditions.

A possible use of ternary system based on Ta-Al-Fe for high temperature applications is on the Ta-rich corner. The main intermetallic phases reported for this region are the A2-type σ phase (Ta_2Al), which has a tetragonal crystal structure (D_{8h}) and μ phase ($TaFe$ or Ta_6Fe_7), which has a rhombohedral structure [21]. The Ta-Al-Fe ternary system has been studied recently by Ghosh [49], based on data previously reported [50, 51]. Although, the main composition range that was targeted by his study has been limited to the Fe-rich regions; with Al additions < 35 at.% Al and Ta additions < 50 at.%.

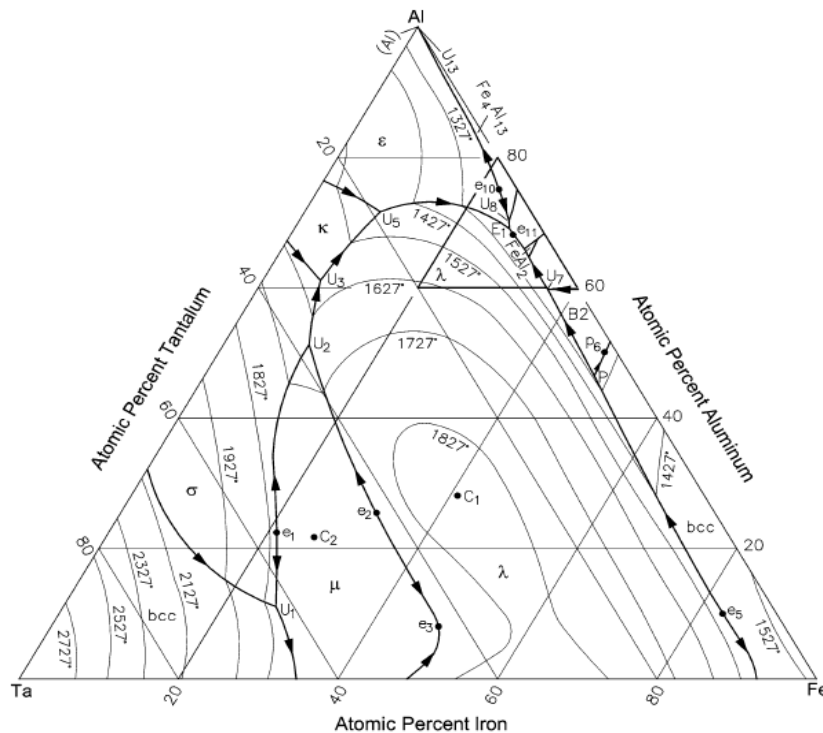


Figure 10 - Computed liquidus projection of Ta-Al-Fe. [21, 30]

Furthermore, isothermal sections at 1000°C have been studied that report on the stability of μ and λ (C14 Laves) phases that were observed in the binary systems for these compositions ranges [52]. Moreover, some compositions in the Ta-rich corner have been considered, where the primary freezing of σ , μ and A2 (Ta) phases was observed.

2.3. A ternary Co-Al-Nb system

Unlike the Ta-Al-Fe, the Co-Al-Nb system is of significant interest for the understanding of the stability of different types of the Laves phase. This is because all three types of Laves phase; hexagonal C14 and C36 as well as cubic C15 are stable in the binary Co-Nb system [53, 54].

It is unlikely that solidification will terminate at the invariant point and in this study invariant reactions in the Nb-rich and Co-rich corners of the Co-Al-Nb ternary system involving the Laves and Heusler phase will be investigated, which involves Class I, Class II and Class III reactions. The computed liquidus projection to be used in this investigation is presented in Figure 11 [27].

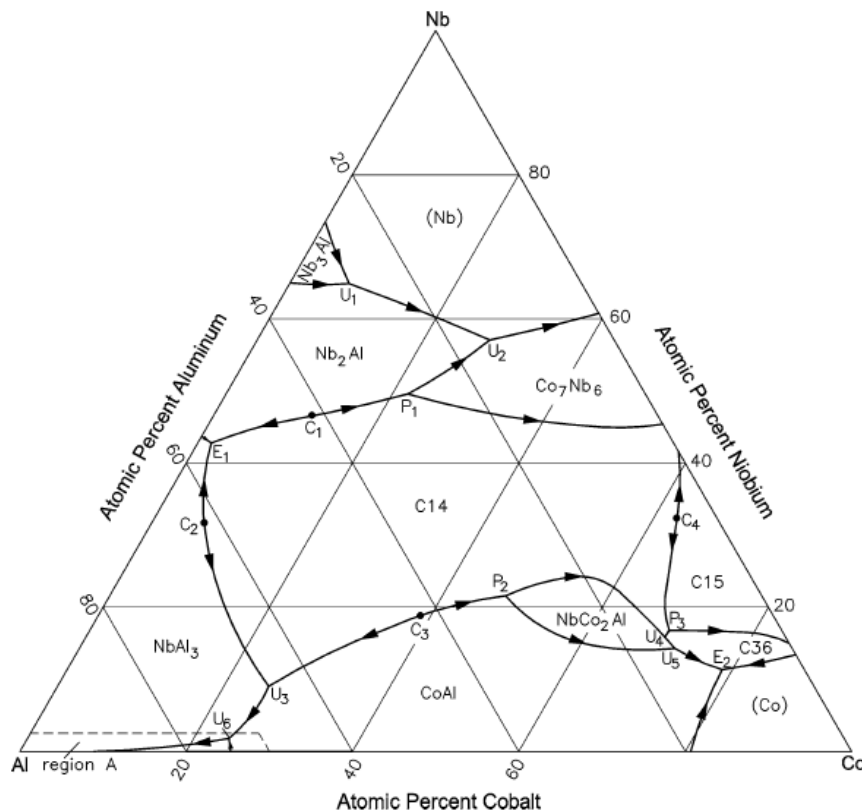


Figure 11 - Calculated liquidus projection of Nb-Al-Co ternary system. [27, 29]

The development in this study will be given in three-fold:

- (1) α -Co, C36, CoAl phases in Co-rich corner - An analysis of primary freezing of Co and CoAl phases and subsequent [Co + C36] and [CoAl + C36] eutectics and the ternary eutectic [Co + C36 + CoAl]. The emphasis will be on measurement of the solubility limits in the various phases.

- (2) C14, Co₂AlNb, C36, CoAl phases in Co-rich corner – The focus will be on primary freezing of C14 and subsequent eutectic reaction preceding the Class II reaction, $L + \text{Co}_2\text{AlNb} \rightarrow \text{C36} + \text{CoAl}$. Specifically, the analysis of isothermal projections and the tie-triangle evolution with reducing temperature. The implications of a possible solid-state reaction leading to nucleation and growth of the CoAl phase will be considered.
- (3) C14, Nb₂Al, Co₇Nb₆ in Nb-rich corner – The focus will be on primary freezing of C14 and subsequent eutectic reaction preceding the Class III reaction, $L + \text{C14} + \text{Nb}_2\text{Al} \rightarrow \text{Co}_7\text{Nb}_6$. The nature of the three-phase reaction following the invariant reaction will be identified and the solubility limits in the different phases will be determined.

2.4. A ternary Nb-Al-Fe system

It is known that Ta is an important alloying addition to Fe-Al, as it forms the ternary Laves phase, with hexagonal C14 structure [15-17, 21]. Recent investigations indicate that in addition to the formation of the (Fe,Al)₂Ta Laves phase, when Ta is added to Fe₃Al, there is the unexpected formation of the Heusler-type phase [5, 17]. Another ternary, the Co-Al-Nb alloy system exists, in which both the ternary Laves phase as well as the Heusler phase, Co₂AlNb occur [18, 27]. Similarly, the system Nb-Al-Fe presents C14 (Fe,Al)₂Nb, where intermetallic phases of the type NbAl₃ and Nb₂Al are present [55].

In ternary systems there are some additional aspects that need to be considered while addressing the solidification path. During primary phase growth, unlike in binary systems an added degree of freedom exists [44, 45]. Therefore, the path traversed by the liquid composition on the liquidus surface will be contingent on micro-segregation, which will not only dictate the evolution of solid-fraction, but importantly determine where the liquid composition intersects the monovariant line that marks the end of primary freezing if all the liquid has not been consumed [19, 22].

In an invariant reaction involving four phases (L, α , β , γ), co-incidence of all phases will only occur at a point. However, nucleation at a point is difficult, and nucleation of a third solid phase will necessarily occur on one of the two existing

solid phases and growth of this third phase must involve a three-phase reaction [23]. Therefore, solidification cannot terminate at the invariant point [5].

During rapid freezing, deviation from equilibrium can occur, generating non-equilibrium structures and anomalous formations. One type of anomaly is the formation of a halo of one or two phases around a primary dendrite [56]. Sundquist et al. [57] have proposed a requirement of undercooling for the equilibrium nucleation to take place. Kofler [58] and Gigliotti et al. [59] have highlighted the importance of the growth velocity as well as the solute content.

According to Gigliotti et al. [59] during coupled eutectic growth studies, after primary freezing, a secondary phase can nucleate prior to the leading phase of the binary eutectic when re-nucleation does not take place. A larger halo formation signals the presence of a poor nucleant, given the inability to re-nucleation following primary freezing.

This study will be developed in a four-fold analysis:

- (1) Three-phase reactions, involving the liquid, C14 Laves, Nb₂Al and μ phases – samples S1 and S2: an analysis of primary freezing of C14 and μ phase, that occur at temperature of approximately 1650°C and 1550°C respectively [26], followed by the subsequent eutectic ($L \rightarrow \text{Nb}_2\text{Al} + \mu$) and peritectic ($L + \text{C14} \rightarrow \mu$) invariant reaction;
- (2) Formation of phases C14, Nb₂Al and NbAl₃ – samples S3 and S4, with high Al contents: following the primary formation of C14 and NbAl₃ phases (formed from the liquid at around 1540°C [26]), a detailed analysis will be given in the eutectic (C14 + Nb₂Al) reaction for S3 and the formation of a eutectic halo prior to the occurrence of the Class I reaction in S4, or ternary peritectic reaction, that forms the (NbAl₃ + C14 + Nb₂Al) structure;
- (3) Phases (Nb), Nb₂Al and μ in the Nb-rich corner– samples S5 and S6: here, the focus will be given to the peritectic formation of Nb₂Al and the subsequent Class II quasi-peritectic reaction $L + \text{Nb}_2\text{Al} \rightarrow (\text{Nb}) + \mu$, predicted under equilibrium conditions, following the primary formation of the solid solution (Nb) phase, from the liquid at approximately from 1650°C up to 2100°C according to the liquidus projection [26].

Moreover, the observance of suppression of the Class II reaction followed by solute trapping of Al in (Nb) phase and deviation of the reaction sequence predicted for equilibrium conditions.

- (4) Phases Nb₂Al, C14 and μ – samples S7 and S8: following primary freezing of C14 phase, a closer examination will be made to evaluate the formation of the Class III ternary peritectic reaction L + C14 + Nb₂Al → μ , following the eutectic formation of C14 + Nb₂Al, and its limitation regarding the limited diffusion with decreasing temperature.

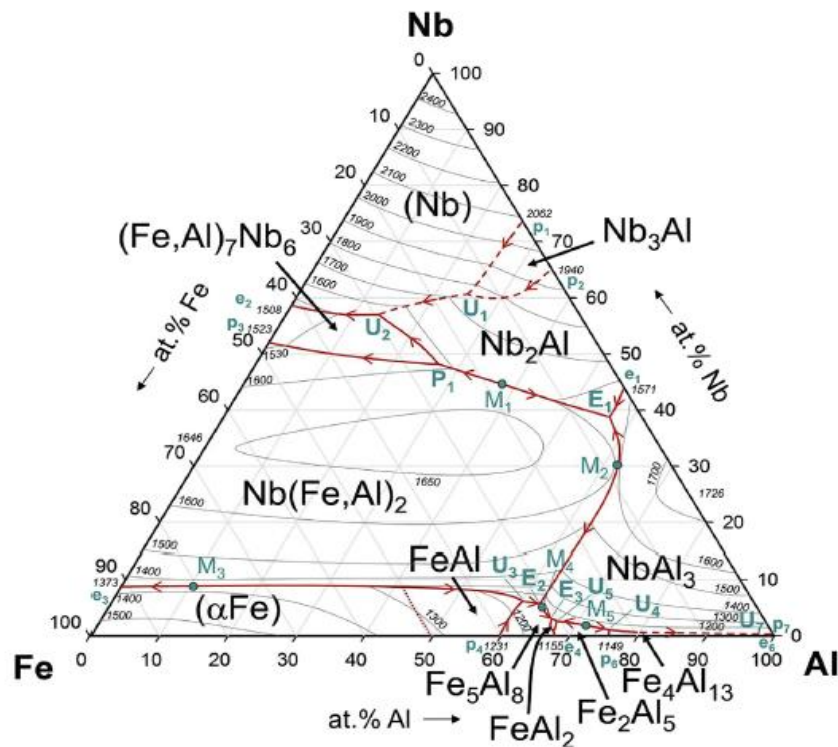


Figure 12 - Liquidus projection of Nb-Al-Fe system. [26]

The liquidus projection, seen in Figure 12, will be used in addition to the solidus isothermal projections, in order to evaluate the solidification path and phases expected during freezing under equilibrium conditions, and to observe how solubility of the phase regions change with decreasing temperature.

2.5. A ternary Ta-Al-Ti system

Refractory metal alloys, such as those based on the Ta-Al-Ti system, have been considered as potential candidates for high temperature use in structural

applications, as it is the case for high strength, demanding applications in jet turbine engines [60, 61]. These alloys have attracted interest due to the grain-refinement strengthening effect of Ta in titanium aluminides [61, 62] (usually described as γ -TiAl) and have been the target of many studies [24, 25, 28, 63-65] from the past decades in order to gather a more comprehensible knowledge on various aspects of microstructure stability, processing and post-processing effects on the final properties of these alloys based on the analysis of liquid state to room temperature.

The use of Ta and Nb as alloying elements has proven to be of high importance to binary TiAl alloys, due to an increase in stiffness and oxidation resistance at high temperature, besides providing room temperature strength. Additions of Ta up to 25 at.% are commonly used for aerospace materials, substituting Ti atoms, providing a final microstructure of a reinforcing σ (tetragonal $D8_b$ type Ta_2Al intermetallic, containing 51-81 at.% of Ta) embedded in a γ -TiAl matrix (tetragonal $L1_0$ type intermetallic) [28, 64].

However, these alloys can present significant segregation problems during casting, which is due to the prominent partition characteristic of the ternary system, the slow diffusion of Ta and the evolution of γ phase as a peritectic product [25, 60, 64].

Recent developments of phase diagrams for this system have been presented by Witusiewicz et al. [66], where there is the presentation of a solidus projection and a liquidus projection (shown in Figure 13) in addition to isothermal sections. Previous studies on this system have developed similar results regarding phase diagrams [67-69].

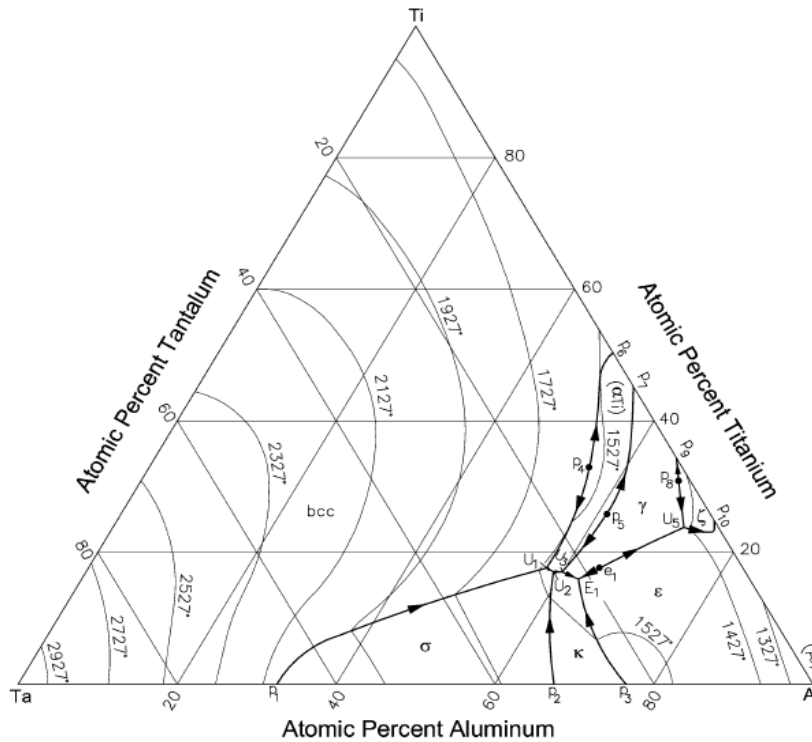


Figure 13 - Liquidus projection of Ta-Al-Ti system. [30, 66]

A thorough analysis of this system is yet to be presented, regarding liquidus temperatures, invariant reactions, and partition of elements. This work focuses on presenting the findings for rapid solidification circumstances, and will involve the following aspects;

- (1) Peritectic reactions – The formation of γ phase via $L + \alpha \rightarrow \gamma$, by the consumption of the low temperature hexagonal α Ti can occur at temperatures as high as 1775 K [66]. Formation of peritectic σ phase is also observed via $L + \beta \rightarrow \sigma$, when the cubic BCC β Ti (that forms a continuous solid solution with Ta) is consumed at 2347 K; the high temperature β phase is decomposed into α by solid state transformation under equilibrium conditions [30, 61]. For the Al-rich corner, there is formation of a tetragonal $D0_{22}$ -type intermetallic $TaAl_3$, denoted as ϵ , via $L + K \rightarrow \epsilon$.
- (2) Class II invariant reactions – These four-phase reactions involve the consumption of β to promote a eutectic formation of $\alpha + \sigma$, via $L + \beta \rightarrow \alpha + \sigma$, that occurs at 1770 K, and the consumption of σ to promote formation of $\alpha + \kappa$, at temperature close to 1755 K [66]. Phase κ is an intermediate cubic intermetallic compound, denoted from $Ta_{39}Al_{69}$. The implications of

rapid solidification on the solidification sequence will be analysed with the use of the solidus projection.

2.6. A ternary Nb-Si-Ti system

Although most of current review studies focus on properties of Nb-Si binary composites, it is important to highlight that this system is usually applied as a means to obtaining multi-component alloys, which calls for the addition of a third major element. The use of Ti is widely spread through the Nb-Si research community, due to its role when added to these alloys, as mentioned in the previous section.

The addition of Ti in relatively large amounts pushes the Nb-silicide composites to a ternary system rather than a binary, which is why it is important to have a fair understanding of the phase equilibria for this system. Moreover, this understanding will help with prediction of the solidification path with which the alloy will follow, depending on its composition. The prediction of final phases and transformations is very important when multi-element alloys are studied, since every property might change for different combination of phases formed.

The liquidus projection was first built by Bewlay et al. [70] when studying Nb-rich and Ti-rich ternary Nb-Si-Ti alloys, and later assessed by Jing et al. [71] by experimental analysis. Thermodynamic models of this system have been carried out by Liang et al. [72] and later by Geng et al. [73], which showed a small divergence from the liquidus projection obtained empirically, in terms of the $\text{Nb}_5\text{Si}_3/\text{Ti}_5\text{Si}_3$ peritectic surface.

However, given the range of divergence of empirical projection, the calculated version of the ternary phase diagram for liquidus projection will be used, which is shown in Figure 14 [73].

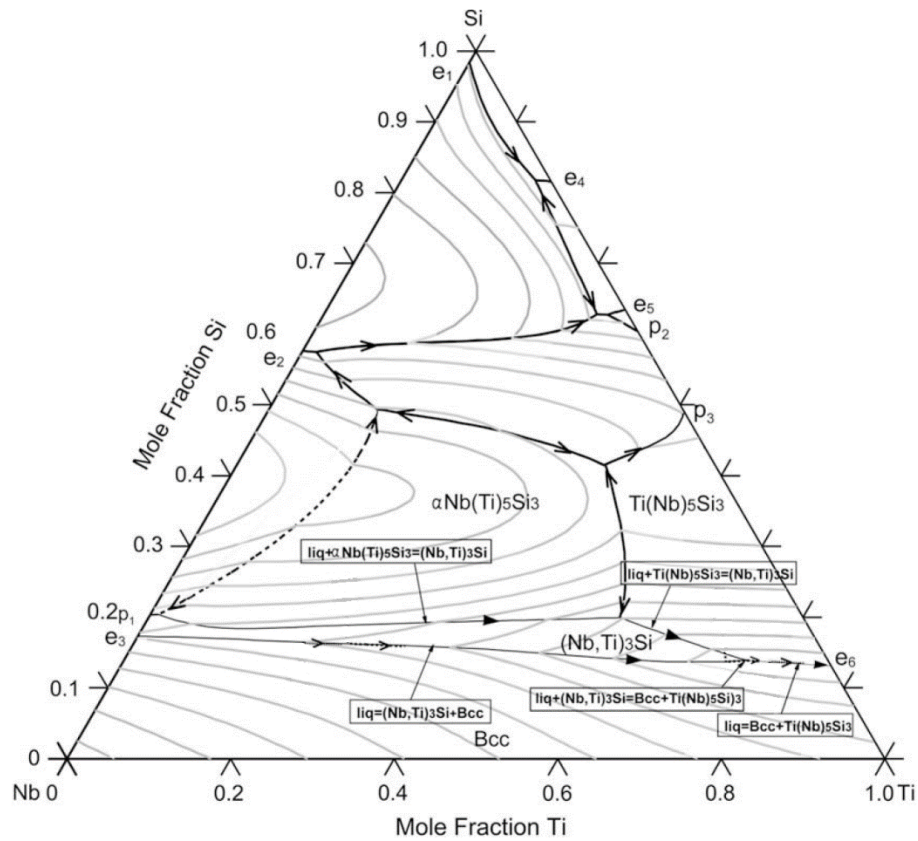


Figure 14 - Calculated liquidus projection of the Nb-Si-Ti system. Adapted from [73].

As important as analysing the solidification sequence and the phases to be formed from the liquids projection, solidus projections serve as an auxiliary method of predicting the final phases under equilibrium, or when this is not possible, isothermal sections which are held for long periods of time at high temperature.

Isothermal sections present phase regions that depend on the composition of the alloys. Because of diffusion process and the influence of alloying elements, it is important to assess how equilibrium phases change with temperature, which will also affect heat treatment temperature selection.

In the case of Nb-silicide alloys, an important transformation is the transformation of Nb_3Si into Nb_5Si_3 , which is very slow. Furthermore, the Nb_3Si phase is usually present in as-cast microstructures, and it takes temperatures as high as $1500^\circ C$ and long holding times to be dissolved.

Bewlay et al. [74] have built solidus projections at 1150 , 1320 , 1340 , 1350 and $1500^\circ C$ for Nb-rich and Ti-rich alloys. Liquid is still present for Ti-rich alloys above

1320°C, which change drastically within the temperature range given. Zhao et al. [75] and Geng et al. [73] obtained isothermal projections at 1000, 1150 and 1200°C, which proved to be consistent with that predicted by Bewlay. For as-cast studies, it is important to carry out analysis when all liquid has been consumed, which is why the projection at 1200°C has been chosen to represent the following studies, showed in Figure 15.

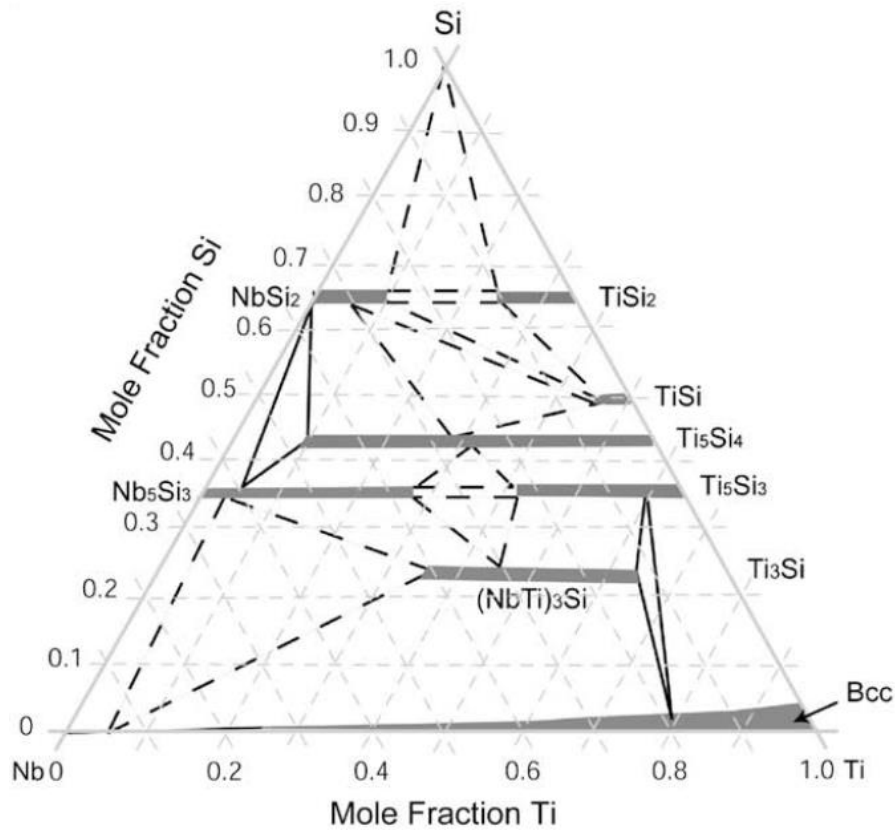


Figure 15 - Isothermal section at 1200°C for Nb-Si-Ti system [73].

For high temperature application, a focus is given to Ti-rich Nb-based alloys, and the list of transformations and invariant reactions present in the Nb and Ti-rich corner are shown in [70]. Table 1 shows the reaction sequences and temperatures for the Nb-Ti-Si system.

Table 1 - Equilibrium transformations and invariant reactions in the Nb and Ti-rich corner of Nb-Si-Ti system [70, 73, 76].

Transformation		Temperature (°C)
<i>Three-phase reaction</i>		
p1	$L + Nb(Ti)_5Si_3 \rightarrow Ti(Nb)_5Si_3$	2130
p2	$L + Nb(Ti)_5Si_3 \rightarrow Nb(Ti)_3Si$	1975
e1	$L \rightarrow BCC + Nb(Ti)_3Si$	1915
e2	$L \rightarrow BCC + Ti(Nb)_5Si_3$	1330
<i>Four-phase reaction</i>		
U1	$L + Nb(Ti)_5Si_3 \rightarrow Nb(Ti)_3Si + Ti(Nb)_5Si_3$	1600-1650
U2	$L + Nb(Ti)_3Si \rightarrow BCC + Ti(Nb)_5Si_3$	1350

The notation of BCC phase is related to the solid solution phase where (Nb,Ti,Si) form one phase with the same structure, regardless of the major element. The same applies for the silicide phases, where the element in parentheses is the element in solid solution within that said phase, as in Nb(Ti)₅Si₃.

Because of this, a range of same-structure phases can be formed for varying compositions, which will cause a deviation of stoichiometry. That can be seen in the isothermal section in Figure 15, where a same compound can form different components with same structure and different amounts of Ti, Si or Nb can be present, which is characterised as a phase region.

Moreover, four-phase reactions are also observed for these alloys, when liquid is still present. These reactions consume one phase to form two new phases and are denominated as quasi-peritectic reactions. More details about these reactions will be discussed in Chapter 6.

2.7. Halo defect formation

The formation of a halo or growth of a secondary phase around the primary phase and thereby precluding coupled growth is a common occurrence in off-eutectic alloy compositions [59]. One of the possible processing methods for manufacture of components is via the liquid route, as it involves extension of a well-established

technology that permits components to be produced in a single stage process. However, in liquid-solid phase transformations, alloy compositions are restricted by the occurrence of appropriate phase equilibria that is dictated by thermodynamic as well as kinetic considerations. The latter specifically plays a key role in the evolution of phase morphologies for eutectic or near-eutectic compositions, such as in in-situ composites, where fine coupled eutectic structures are desirable over coarser dendritic structures (or halos) for superior mechanical properties [77]. Therefore, it becomes important to study the conditions under which the fine-structure coupled eutectic prevails over the coarser dendritic structures or halos during solidification.

In equiaxed solidification, halo formation has been interpreted on the basis of non-reciprocal nucleation [57]. This can be illustrated in Figure 16(a), β phase nucleates on α phase with undercooling, $\Delta T_{\beta\alpha}$, but α phase nucleation on primary β requires a greater undercooling, $\Delta T_{\alpha\beta}$. Therefore, when a hyper-eutectic alloy of nominal composition, C_2 is cooled from the liquid state, β phase forms from the liquid and on cooling to $T_{\alpha\beta}$, α phase nucleates at an undercooling, $\Delta T_{\alpha\beta}$. α phase grows around β phase as a halo. Subsequent growth of α phase returns the liquid composition back to C_e and release of latent heat results in the liquid temperature reaching T_e , when coupled eutectic growth occurs thereafter. The implicit assumption therefore is that coupled eutectic growth only occurs at a unique composition, C_e [57]. It follows therefore that the size of the halo around the primary phase increases with increasing nucleation undercooling, i.e. deviation of the liquid composition from C_e .

However, it has been shown that coupled growth can in fact occur over a composition-temperature region, referred to as the coupled zone [78]. In this case the selection of the morphology, i.e. halo (primary growth of secondary phase) or coupled eutectic is determined by the growth undercooling or growth kinetics. The halo phase will grow around the primary solid, if it grows at lower undercooling (or greater tip temperature) compared with the eutectic front for a given velocity. This is illustrated in Figure 16(b).

For growth of the secondary phase as halo around the primary phase and corresponding to the liquid composition, $C_{\infty 1}$; the undercooling below the eutectic

temperature is determined from the α liquidus extension and is given by, $\Delta T_{\alpha 1}$. If β phase forms from liquid composition, $C_{\infty 1}$, the undercooling for growth of β phase must be calculated with respect to its equilibrium liquidus temperature and is given by, $[\Delta T_{\alpha 1} + \Delta T_{\beta 1}]$, where $\Delta T_{\beta 1}$ is the undercooling calculated with respect to the eutectic temperature, T_e , as shown in Figure 16(b).

The growth velocity of β phase (V) can be calculated from the local undercooling [79]. On the other hand, if plane front coupled eutectic growth occurs, then it must do so with an undercooling, $\Delta T_{\alpha 1} = \Delta T_{e1}$ below the eutectic temperature and with a velocity, V' [40]. Therefore, for a given undercooling below the eutectic temperature, $\Delta T_{\alpha 1} = \Delta T_{e1} = m_{\alpha}(C_e - C_{\infty 1})$, where m_{α} (liquidus slope of α phase) < 0 . Here C_e is the invariant eutectic composition. A halo of β phase forms around primary α phase if, $V > V'$, while coupled eutectic growth occurs if $V < V'$ [80]. If a halo forms, then progressive growth of β phase results in depletion of solute B in the liquid and consequently the liquid composition shifts progressively to $C_{\infty 2}$, $C_{\infty 3}$, ..., where, $C_{\infty 1} > C_{\infty 2} > C_{\infty 3} > \dots$, as in Figure 16(b).

At each successive liquid composition, there will be a decrease in equilibrium liquidus temperature for β phase. This in turn results in decreased undercooling for continued halo growth, which in turn results in a lower growth velocity, V . Therefore, at a certain liquid composition, $C_{\infty i}$, $V < V'$ and consequently coupled eutectic growth will be established in the liquid. This must result in the development of a lateral composition gradient in the liquid perpendicular to the growth direction, as indicated in Figure 16(b) [80, 81]. The evolution of the microstructure, i.e. growth of halo phase or coupled eutectic is schematically illustrated in Figure 16(c).

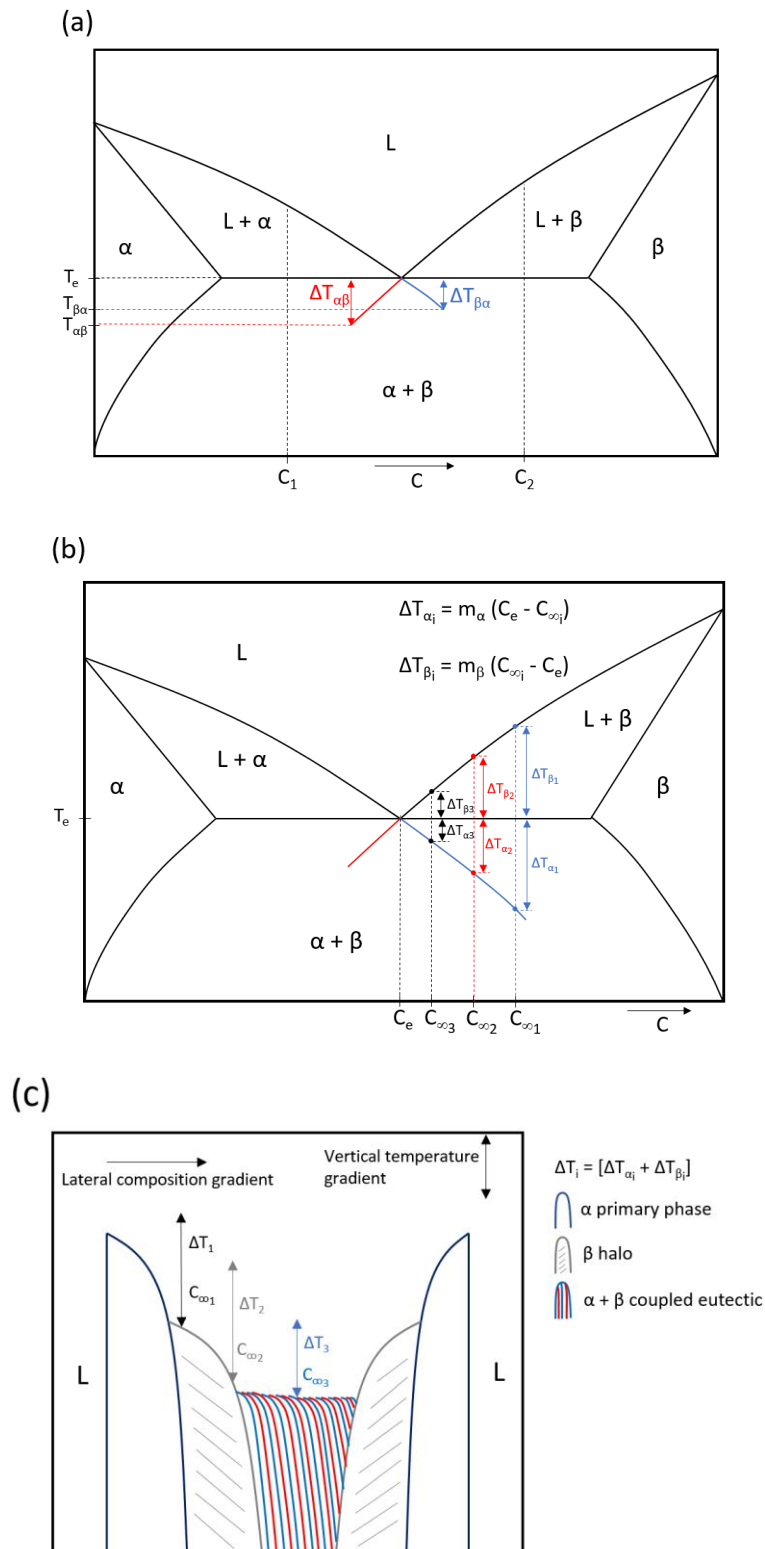


Figure 16 - Schematic illustration for formation of halos in a binary system, (a) Role of nucleation undercooling, where α phase is a good nucleant for β phase, but β phase is not a good nucleant for α phase in equiaxed solidification, (b) Directional solidification showing the undercooling at the growing tips of the halo phase and that required for coupled planar eutectic growth, (c) Schematic evolution of the secondary phase morphology in the inter-dendritic region and the existence of a lateral composition gradient.

The formation of halos in binary systems under conditions of directional solidification have been well documented and temperature composition maps have been established for a range of alloy systems where the secondary phase grows as a halo phase and precluding coupled eutectic growth [5, 22, 81-85]. However, there are fewer investigations in ternary systems, where additional constraints occur.

- First, in ternary systems during primary growth the liquid composition unlike in the case of the binary case, is determined by a kinetic model [30]. Therefore, it is not straightforward to determine $\Delta T_{\alpha 1}$.
- Second, in ternary systems de-stabilisation of one or both phases can occur since the partitioning of the third element will not be the same in both phases and a long-range diffusion layer is built-up [16, 78].

Accordingly, section 6.5 will focus on some select compositions in the Ta-Al-Fe, Nb-Al-Co and Nb-Al-Fe ternary systems produced by the arc melting process.

Chapter 3 NbSi-based alloys for high temperature applications

3.1. Turbine blades and Ni-base alloys

The gas turbine engine, as shown in Figure 17, is one of the most important parts of an aircraft, as it is responsible for providing the necessary thrust for the plane to take off. Fuel and air must be combined in a calculated amount, in order to provide an ignition followed by the liberation of gases at high temperature and pressure [86].

This process occurs firstly through the compression of air, generally in two stages: the low and the high frequency compressor. A combustor then mixes fuel and air to cause an ignition. A turbine extracts the mechanical work from hot gases, with the spinning of the blades, and drives the compressor by a shaft [77, 86]. Many variants of this engine are possible, being common the use of a fan, as a low compressor, in front of the engine, known as turbofan. Figure 17 shows a typical turbofan, produced by Rolls Royce plc., the Trent 800 [86, 87].

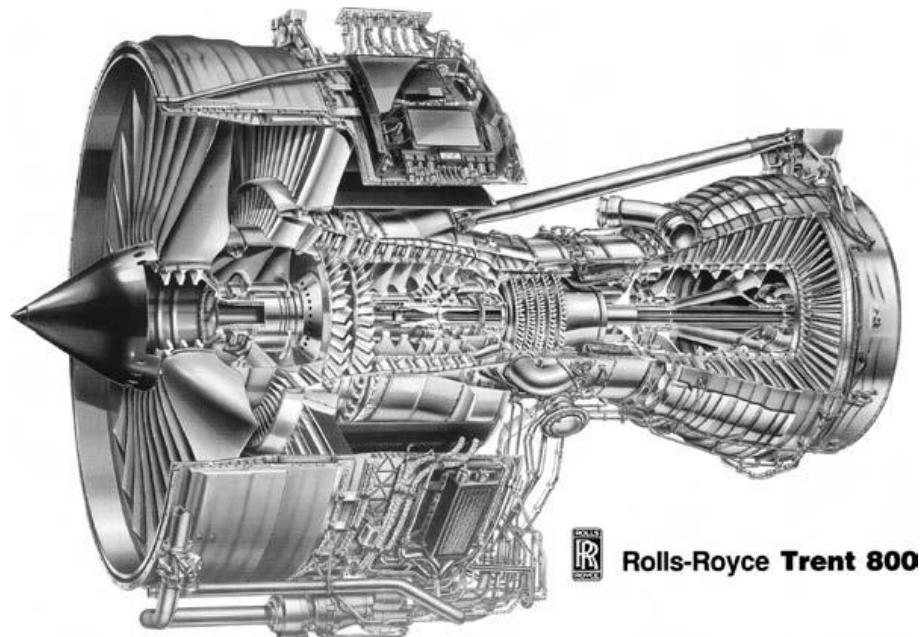


Figure 17 - Turbofan Trent 800 from Rolls Royce. [86]

The choice of the alloys used in the parts of an engine is based on the temperature that the material will have to support. The materials choice for these equipment must be very strict, since they are submitted to high temperatures, which may cause failures or damages to the various parts of the engine [2, 7, 9]. In the hottest sections of the engine, where the combustion occurs, nickel-based (Ni-based) single-crystal superalloys are currently in use, as these alloys maintain their excellent mechanical properties at temperatures near the melting temperature (approximately 70% of the melting temperature). All properties of Ni-based superalloys submitted to high temperatures will depend on the addition of elements as well as the phases formed. Titanium, steel and aluminium alloys can be used in the cooler sections of the engine, due to their light weight and the fact that the environment is not as severe, which is why simpler polycrystalline materials with lower melting temperature can be used. Figure 18 shows, in general, the usage of materials in an engine [7, 88, 89].

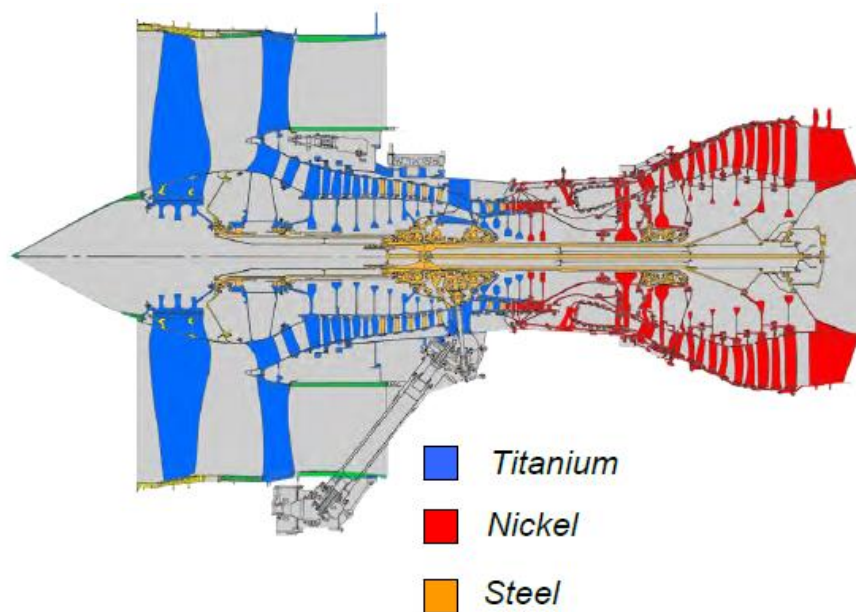


Figure 18 - Usage of materials in a jet engine. [90]

The Ni-based superalloys can support severe work conditions, as corrosive atmospheres, high temperature and high loads. Among their properties, it can be highlighted the high creep resistance and high mechanical properties. This is relevant, since the temperature in which gases enter the turbine, known as Turbine Entry Temperature (TET) is high. The higher the TET the more effective the engine will be, and this shows the need for capable materials, such as these

superalloys [87, 91]. The TET has been increased by about 700°C, from the earliest engines from the decade of 1940 to today's engines [86].

The use of Ni-based superalloys is then justified by their advantages on creep, oxidation resistance, and low mechanical deformation at high temperatures, when submitted at high loads in service, which is due to the FCC structure, as it is ductile and tough [87, 91, 92]. This is observed due to the presence of ordered γ' ($L1_2$) precipitate in the disordered A1 FCC matrix that provides the high temperature strength, while the matrix is ductile. Also, the beneficial role of Al is to impart oxidation resistance through the formation of a continuous protective layer of Al_2O_3 [93-95].

The change of composition over the years has affected the formation of the oxide layer, which has not accompanied the evolution and development of new alloys. Instead, an increasing number of studies about coating technologies are being carried out, in order to obtain better oxidation resistance and improve the alloy's life span [86, 87].

3.2. Materials beyond Ni-based alloys

A new family of high temperature materials is being developed, with properties such as high melting temperature, low density, high oxidation resistance and high temperature strength, for the use in gas turbine applications. Refractory metals have been considered for that, such as niobium (Nb) and molybdenum (Mo), since they have wide solubility of adding elements [11, 96-98].

Nb alloys have a lower density and higher ductility at room temperature, when compared with Mo alloys. Their high temperature oxidation resistance depends on the intermetallic phase formed by the refractory metal-intermetallic composites (RMIC). Among other properties, Nb becomes a better choice for the application of turbine engines [9].

The melting temperature of silicide composites can pass 1750°C, with a working temperature for turbine blades made of these composites reaching 1350°C. A weight reduction can lead to less difficulties to cool down the blades, which is

achieved with the use of the low-density alloys based on the formation of such silicides.

A typical Nb-silicide composite is strengthened by an intermetallic phase, usually Nb_3Si or Nb_5Si_3 in a fraction of 0.55, besides the matrix phase consisting of Nb solid solution. In some composites with Cr additions, the $NbCr_2$ Laves phase can be present in a fraction of about 0.10, which improves the oxidation resistance, by reducing oxygen diffusion, and forming a protective layer of oxide in the alloy's surface. A typical composition of Nb-silicide alloys contains Ti, Hf, Cr, Al, V, Mo and Si, and the effects of these elements will be explored so an alloy with synergy of properties can be developed [7, 9, 99-102].

The design of a blade must be taken very strictly, in order to balance the properties and the requirements needed for its operation. Density and elastic modulus play an important role on thermal and mechanical design of the blades. Figure 19 shows an example of an NbSi-based alloy turbine blade.



Figure 19 - Example of Nb-silicide turbine blade. [7, 9]

3.2.1. Microstructure of Nb-Si composites

The microstructure characteristic of a typical (or desired) Nb-silicide is formed of a Nb solid solution, defined hereafter as $(Nb,Ti)_{ss}$ or simply Nb_{ss} and a variety of brittle silicides with different structures, such as α , β , γ - M_5Si_3 and/or M_3Si , with M

being Ti or Nb. According to equilibrium conditions, the eutectic reaction form from the liquid into $Nb_{ss} + Nb_3Si$, to a eutectoid into $Nb_{ss} + Nb_5Si_3$, although the phase Nb_3Si can be still present at room temperature due to its low kinetic decomposition [12, 103-106]. It was found that Ti and Zr can increase the velocity of decomposition of Nb_3Si by as much as 10% [98, 107]. Figure 20 presents a binary phase diagram of Nb-Si in the region of use for high temperature applications.

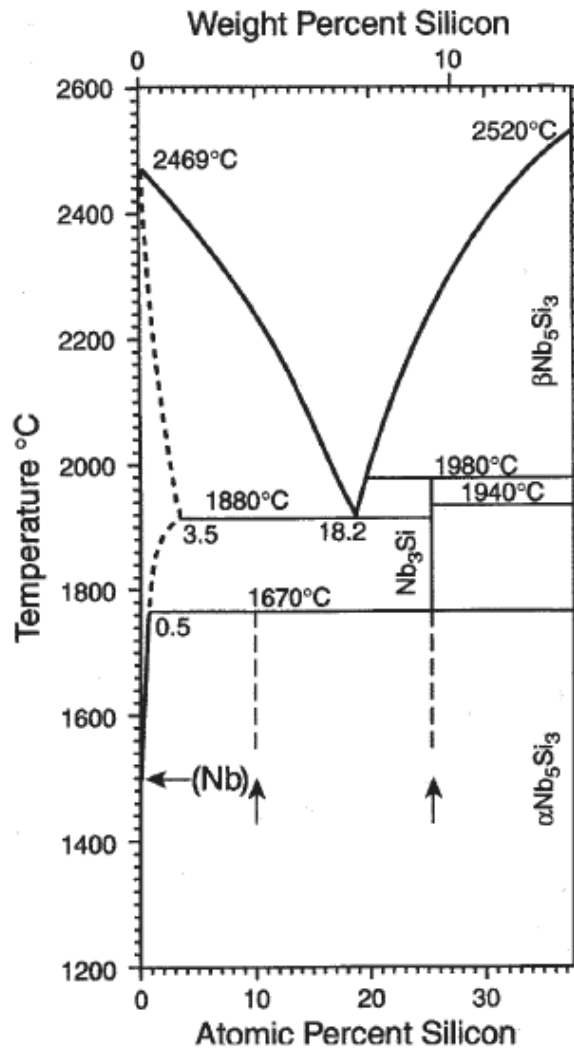


Figure 20 - Nb-Si binary phase diagram. [9, 107, 108]

From the binary diagram in Figure 20, it is possible to see that Nb_3Si is stable between 1700°C and 1980°C, and Nb_5Si_3 possess a melting temperature of about 2520°C and it can be decomposed in α , β or γ crystal structures [109].

The silicides α - and β - Nb_5Si_3 have a tetragonal crystal structure, similar to the silicide Nb_3Si . A third silicide γ - Nb_5Si_3 is commonly formed, with hexagonal

structure, by a metastable transformation [99, 108]. Other important phase can be present when Cr is added, forming Cr_2Nb , the C14 or C15 Laves phase, which improves the oxidation behaviour of these alloys when present in a volume fraction lesser than 10 at.% of Cr [7, 9, 110].

A fully lamellar structure is very difficult to obtain, as the formation from the liquid necessarily forms a structure of $\text{Nb}_{\text{SS}} + (\text{Nb}_{\text{SS}}/\text{Nb}_5\text{Si}_3)$ [Figure 21(b)]. A full transformation of the Nb_3Si into Nb_5Si_3 can be achieved by the use of solution heat treatments during long periods of time, and by the use of alloying elements that can increase the kinetics of this transformation [1, 106]. The lamellar structure has a good stability at high temperature, contrary to the usual spheroidisation of the lamellae during long exposure times [106].

A variety of ternary alloys based on Nb-Si-X systems are being studied, and it has been noted that the eutectic transformation can occur in a large range of compositions. Mo addition influences the high temperature strength of these silicides [2, 7, 9, 98].

DS alloys present higher mechanical properties than cellular alloys due to the higher fracture toughness provided by the Nb ductile plates embedded on a brittle matrix. The solidification rate affects directly the microstructure development of Nb-Si alloys. Higher rates tend to promote finer discontinuous Nb_{SS} phase, whilst lower rates tend to promote a lamellar structure. The silicide Nb_3Si grows faster than Nb_{SS} phase [7, 111].

Limited growth rates during DS are preferred to avoid the coarsening of the silicides particles by solid-state diffusion [112]. DS structures provide better mechanical performance during service, which is due to the columnar orientation of the silicide phase, being more resistant to mechanical deformation, since equiaxed microstructure would facilitate grain sliding at higher temperatures applications [105, 112].

Figure 21 shows a typical lamellar structure provided by directional solidification of an annealed Nb-silicide alloy. Segregation can be observed, usually caused by high cooling rates.

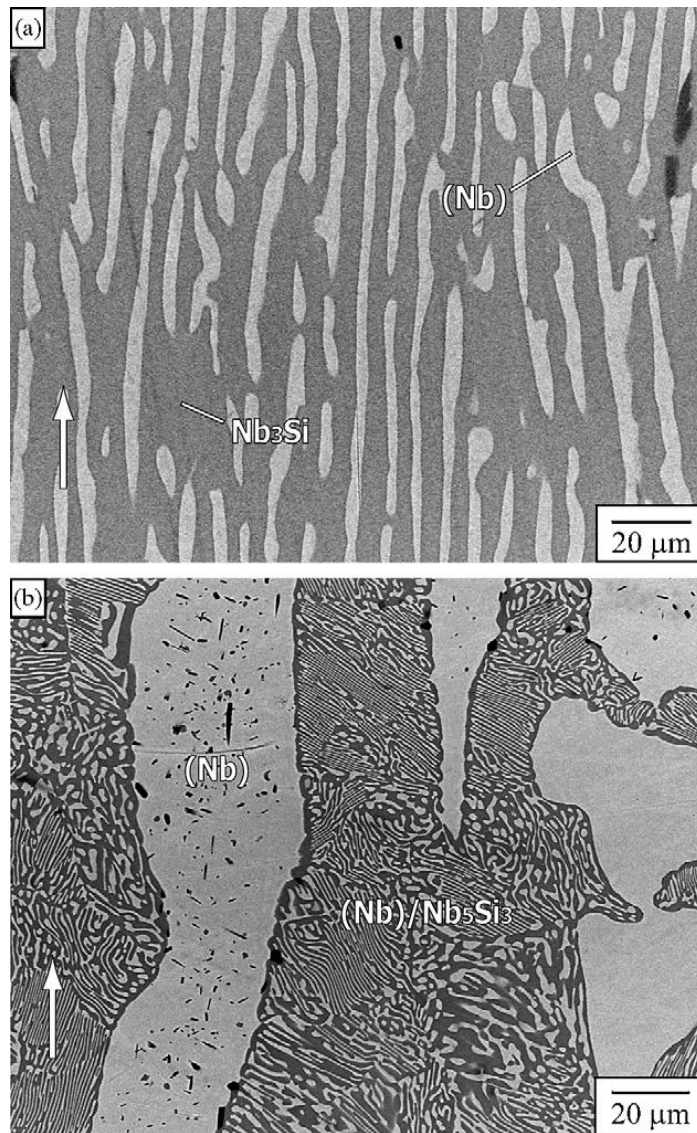


Figure 21 - Microstructures of a DS alloys annealed at 1773K for 500 h: (a) Nb-17.5Si at 10 mm/h and (b) Nb-10Ti-17.5Si at 10 mm/h (at.%). [1, 113]

DS of in-situ Nb-Si composites with Ti, Al, Cr and Hf additions can produce various microstructures. Kang et al. [105] have encountered in their studies the presence of Nb_{ss} , β -(Nb,Ti)₅Si₃ and γ -(Nb,Ti)₅Si₃ phases and the presence of particles of HfO₂, which is formed by oxidation during solidification.

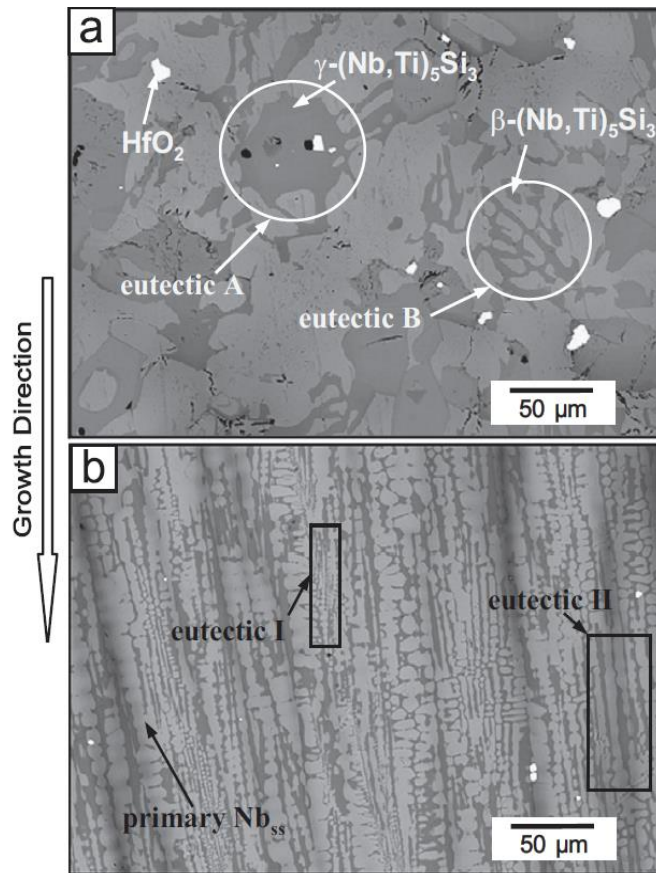


Figure 22 - Longitudinal microstructure of an Nb-Si-Ti-Al-Cr-Hf alloy during (a) transient zone and (b) steady-state growth. Adapted from [105]

The microstructure obtained by Kang [105] is shown in Figure 22. Figure 22(a) shows a Nb-silicide in a section of initial transient zone, where the phases mentioned can be seen with two types of Nb_{SS}/(Nb,Ti)₅Si₃ eutectics. Eutectic A contains a central phase γ -(Nb,Ti)₅Si₃ surrounded by Nb_{SS}, and eutectic B shows islands of Nb_{SS} primary phase in a fine β -(Nb,Ti)₅Si₃ matrix. In steady-state growth [Figure 22(b)], a more oriented structure can be seen, where two types of eutectics are also present. Eutectic I presents a fine two-phase growth, while eutectic II presents coarser phases.

3.2.2. Mechanical properties of Nb-based composites

3.2.2.1. Fracture toughness

Fracture toughness is the ability of the material to tolerate damage through crack propagation, and this plays a key role for structural pieces and for high temperature applications. For Nb-Si alloys, a minimum of $\sim 20 \text{ MPa}\cdot\text{m}^{1/2}$ is

required for turbine blades application [103, 114, 115]. The difficulty for Nb-silicide alloys is to balance high fracture toughness with other mechanical properties and oxidation resistance, thus making its development very difficult to be achieved. Figure 23 shows the fracture toughness of a series of Nb-Si alloys and the goal expected to be achieved for these alloys to be applied at high temperatures.

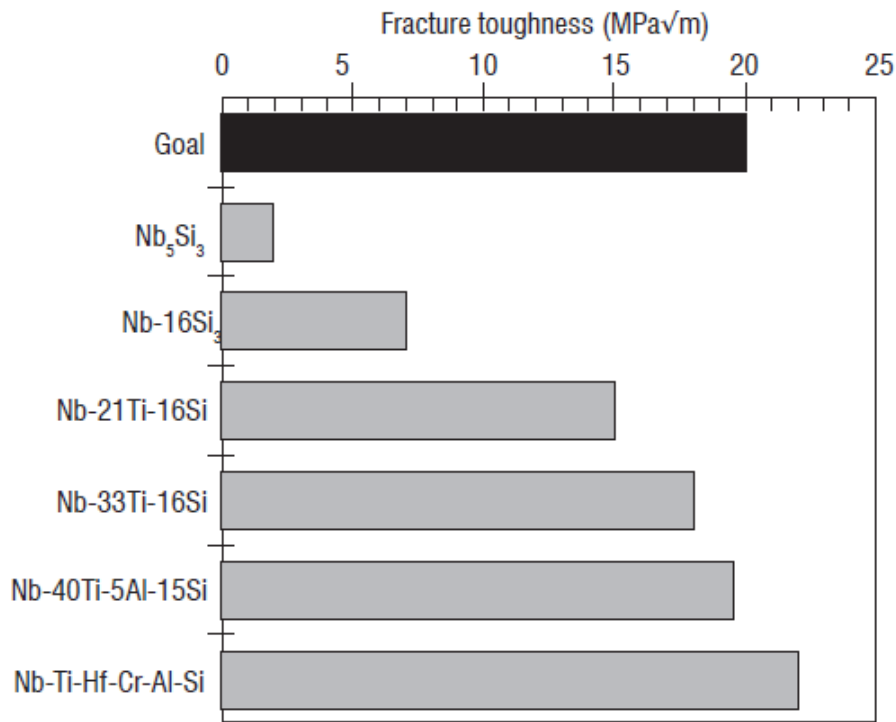


Figure 23 - Fracture toughness of directionally solidified Nb-Si alloys. [116]

Huang et al. [112] found that a directional solidified multi-component Nb-silicide in-situ presented room temperature fracture toughness 58.6% higher, for a solidification growth rate of 5 mm/h, when compared with an arc-melted sample of the same composition, which proves the favourability of directional solidification.

Kang et al. [105] measured the fracture toughness of Nb-Si-Ti alloys with Hf and Cr additions during a transient zone and steady-state growth, and they found an increase from ~9 to ~14 MPa.m^{1/2}, which shows that a oriented structure can deflect better the crack growth during service.

The control of the microstructure has proved to play a key role for fracture toughness, since the presence of lamellar oriented structures provides higher performance, given the occurrence of cracks deflection in the reinforcing silicide

phases [1, 117, 118]. Moreover, the rate of solidification can alter these properties when directional solidification is used, showing results in the range of $\sim 15 \text{ MPa}\cdot\text{m}^{1/2}$ [1]. The addition of Ga proved to increase the fracture toughness to values as high as $24 \text{ MPa}\cdot\text{m}^{1/2}$ [119].

The failure mode in these alloys can occur by rupture of the primary ductile Nb_{ss} phase or by the fracture of the brittle silicide phases [120]. The method of processing and the alloying elements addition show high importance in the process to improve the behaviour of toughening mechanisms.

3.2.2.2. Creep

It is noted that the creep is of crucial importance in the mechanical behaviour of a turbine blade, and even few stresses are able to provoke strain that compromise its use, since these components work with very tight tolerances [7, 121, 122].

Creep performance is still to be further studied for Nb-silicide alloys. In temperatures above 1000°C, the metallic phase has no significant influence in the creep resistance, but rather by the Nb diffusion into the Nb₅Si₃ phase [9].

The creep resistance of the Nb-silicide is still low for the same temperatures when compared with some single-crystal superalloy. The use of coatings can improve this behaviour, by protecting the blade from extremely oxidative environments and reducing the temperature that the alloy experiences in its surface. Figure 24 shows the comparison between an alloyed Nb-silicide and an early Nb metal and silicide composite (MASC) alloys, and the creep goal for applications at 1200°C and higher temperatures.

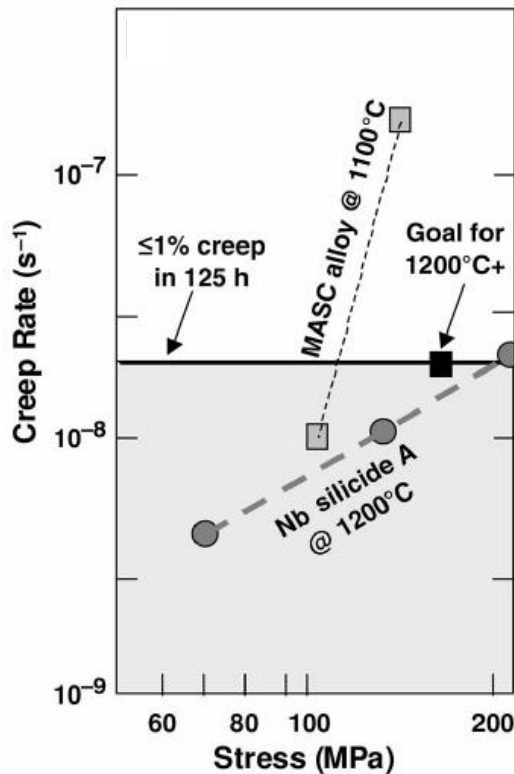


Figure 24 – Secondary creep behaviour of an Nb-silicide comparing with a MASC alloy, and the creep goal hoped to be achieved. [9]

The creep behaviour of Nb-Si composites was reported by Henshall et al. [121] and Subramanian et al. [122] in compression, in which a two-phase Nb/Nb₅Si₃ composite behaviour was studied at high temperatures.

The creep stresses used were below the compressive fracture strength of ~670 MPa at 1500°C, investigated at temperatures between 1100°C and 1400°C [122]. Nb₅Si₃ phase is expected to present a brittle behaviour, giving the ceramic nature of Si-based phases, and therefore a balance with the ductility of Nb_{ss} is hoped to occur. Henshall [121] concluded that a prediction of creep by numeric modelling in the steady state is not reliable, due to possible matrix cracking and assumptions regarding the microstructure. Furthermore, the creep deformation was found to occur by diffusion of Nb in Nb₅Si₃ through the grains [122], which causes the elongation and deformation of grain structures throughout the microstructure.

3.2.2.3. Oxidation

Extensive work has been done in defining oxidation resistance behaviour for Nb-Si alloys for high temperature application [104, 123]. A balance of properties is required for an acceptable oxidation resistance without sacrificing other properties, and thus the level of alloying must be controlled for that to occur. The inherent poor oxidation behaviour of Nb-silicides is due the fact of difficult formation of an adherent oxide layer in the alloy surface and to prevent oxygen diffusion [124-127].

It is noted that the use of Ti and Hf between a ratio of 1.8 and 2.1 improves the oxidation resistance, when Si levels are kept between 17 and 19 at%. Additions of Al and Cr have a beneficial role in oxidation resistance. Ge and B additions of up to 6 at.% can improve the oxidation behaviour [12, 100, 124].

Pesting oxidation, which is characterised as a disintegration due to oxidation, appears at intermediate temperatures (800 to 1200°C), and it is usually coupled with oxygen embrittlement. Sn addition is effective, but does not show a significant effect above 1200°C [124].

Geng et al. [124] have studied the effect of Mo, Ti and Hf additions on the oxidation resistance of Nb-silicides, and confirmed that additions of Ti suppressed the formation of Laves phase and reduced the fraction volume of Nb_{ss}, which caused a reduction in the oxidation resistance at 800°C. Also, the decrease of Mo content has shown to be beneficial, to levels not higher than 2 at.%. At 1200°C, Hf additions have increased the oxidation resistance of these alloys [96, 124, 125].

The oxidation of Nb-based alloys at low to intermediate temperatures, in the range of 700°C to 900°C, showed an extensive material loss, according to an early study made by Felten [128].

This was also shown when the formation of NbSi₂ was found at temperatures of 1538°C, due to the presence of silicate glass oxides [123]. Additions of Al are expected to cause the formation of an alumina layer at some extent, when the Al content agrees with the critical atom fraction (N) for these alloys, according to a model proposed by Wagner [129] in Equation 1:

$$N_{Al}^{crit} = \left(\frac{\pi g^*}{3} N_O^{(s)} \frac{D_O V_m}{D_{Al} V_{ox}} \right)^{\frac{1}{2}} \quad (1)$$

Where $N_O^{(s)}$ is the O solubility, D_O and D_{Al} the diffusivity of O and Al, V_m and V_{ox} the molar volume of the alloy and the oxide, and g^* the critical value of oxide volume.

If N_{Al} is less than the critical value, oxidation of Al is observed, and the protective layer of alumina is not formed. The diffusivity of O can be controlled by the addition of elements such as Cr and Ti, reducing the critical Al content to form a more protective layer [123].

Perkins and Meiers [123] have postulated that additions of Cr and V enhance the formation of an alumina external layer by reducing the O diffusivity. It was found that at temperatures higher than 1300°C, a continuous alumina layer was formed with lower loss of material, as shown in Figure 25.

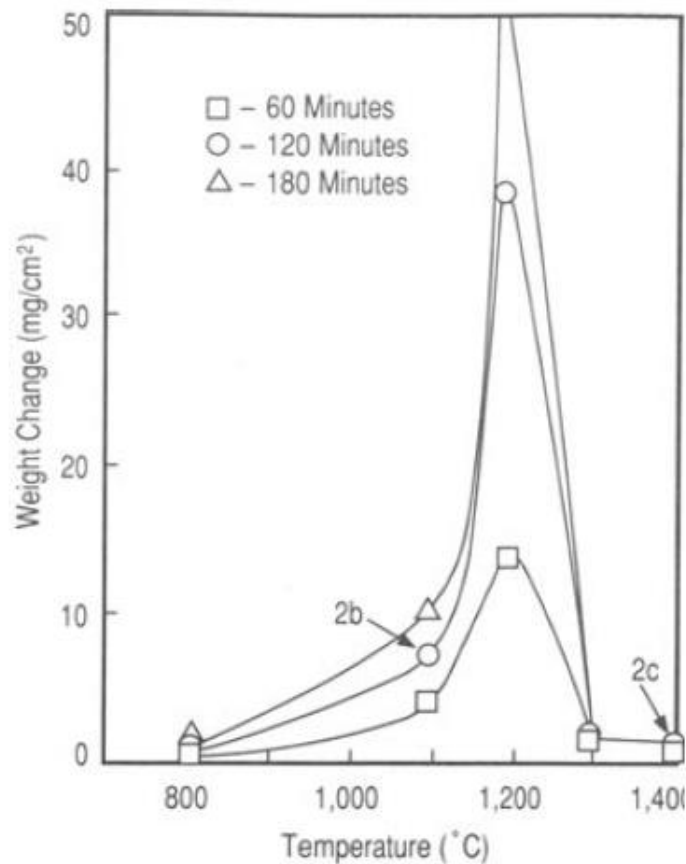


Figure 25 - Variation of material loss with temperature for an Nb-Ti-Al-Cr-V alloy in oxygen at 1 atm exposed during 60, 120 and 180 minutes between 800°C and 1400°C. [123]

These results show that an Nb-based alloy can attain acceptable oxidation properties, however mechanical properties might be sacrificed due to reducing ductility and fracture toughness caused by certain elemental additions.

To avoid this problem and to make it possible for Nb-based alloys to be used as structural materials, the use of high temperature coatings may be used. The effect of coatings will be detailed in section 4.1.6.

3.2.3. The role of main alloying elements in Nb-Si alloys

For a new family of materials to be introduced, it is necessary that these materials present good properties at high temperatures, such as high oxidation resistance, good creep performance and high strength. Nb-silicide based alloys are in constant development in order to achieve these properties in a long-term goal, as they still present insufficient oxidation resistance and toughness at room temperature, as previously discussed. The addition of alloying elements seeks a balance of properties to produce a composite useful in applications in high temperature [11, 13, 96, 99-101, 124, 125, 130, 131]. The role of alloying elements for specific properties of the Nb-silicide alloys may have been discussed in the previous sections, and this section aims to present a summary of the general impacts of the alloying elements.

- Aluminium

The role of Al addition is to improve fracture toughness and the oxidation resistance [99, 114], but it can also promote the formation of β -Nb₅Si₃ phase [119].

Al reduces the oxygen diffusivity and it forms a protective external Al-oxide layer to improve oxidation resistance [100].

- Titanium

Ti improves fracture toughness and the oxidation behaviour [99, 114]. Studies show that an alloy with Ti, Cr, Al, Mo after heat treatment carried at 1500°C for 100h led to the dissolution of Laves phase [107, 130].

Addition of Ti increase the kinetics of transformation from Nb_3Si to Nb_5Si_3 silicide, improving the fracture toughness through solution heat treatment. Unidirectional solidified microstructures show better mechanical properties, when compared with arc-melted alloys. Although Ti-containing alloys can present cellular microstructures, lamellar structures are preferable [1, 98, 107].

Ti additions to these alloys lead to the formation of larger Nb_{ss} particles, which can increase the fracture toughness and the ductility of the solid solution. In addition to this, directionally solidified Ti-containing alloys present higher strength in compression and tension, since the aligned composite presents an elevated mechanical resistance [1, 105-107, 113].

The concentration of Ti can also control the amount of β or γ - $(\text{Nb},\text{Ti})_5\text{Si}_3$ silicides. The silicide Ti_5Si_3 can also be formed when a high content of Ti is added. This Ti-silicide presents the same hexagonal crystal structure of the γ - Nb_5Si_3 , and when Ti_5Si_3 is present, the formation of β - Nb_5Si_3 is favoured [102].

- Chromium

Cr has a similar effect of the Al, as it improves fracture toughness due to solid solution strengthening and the oxidation behaviour [99, 114], and it promotes the formation of β - Nb_5Si_3 phase.

The addition of Cr in these alloys must be controlled, as it can reduce the mechanical properties and lower the melting temperature. Cr additions can also promote the formation of a protective layer of Cr-oxides which have varying adhesion levels [100, 110, 132].

- Hafnium

Hf can improve the room temperature strength and the oxidation behaviour of Nb-silicide based alloys [1, 99, 114]. The simultaneous addition of Hf and Sn decreases the Si content in the silicide phase. Hf stabilises the formation of the γ - Nb_5Si_3 [106], and furthermore, Hf and Sn can be effective to increase fracture toughness and improve peeling oxidation resistance [107].

- Tin

The addition of Sn increases the solubility of Si and lead to a reduction of Ti and Cr in the solid solution phase, which can then lead to formation of Si-rich Laves

phase at 1300°C [106, 107]. Sn also improves the pesting oxidation resistance at intermediate temperatures. The biggest disadvantage of Sn additions is the difficulty in controlling the composition due to vaporisation and the lowering melting temperature of the system [9].

- Molybdenum

Additions of Mo to Nb-silicide composites increase their melting temperature and strengthen the composite by solid solution strengthening [133], and affect negatively the oxidation resistance [99, 103].

It was also reported by Li et al. [106] that Mo additions increase the ductility of Nb-silicide alloys by leading to an eutectic reaction between Nb_{SS} and β-Nb₅Si₃, which is caused by the suppression of Nb₃Si phase [11, 119].

- Gallium

Ga has a limited solubility in Nb of about 1 at.% Ga at room temperature. Nb-Ga phases have similar crystal structures to those formed in Nb-Si systems [36, 119]. The addition of Ga to a near eutectic Nb-Si alloy has a similar effect of that observed by Al and Mo, suppressing Nb₃Si and promoting the formation of β-Nb₅Si₃ phase, which leads to an improvement in the mechanical properties.

The improvement of mechanical properties by Ga is given by the refinement of the microstructure, which increases the hardness and fracture toughness at room temperature. Additions of Ga are not commonly used, since it is an expensive element and it lowers the melting temperature of the alloys. For additive manufacturing use, this element is not usually available in powder form.

- Vanadium

Vanadium is observed to promote the formation of Nb₅Si₃ phase, and it substitutes Si atoms [100, 124], increasing the mechanical properties by solid solution strengthening, when added in small quantities, since it increases the price and does not present significant effects for high additions.

The addition of V can also control the formation of α-Nb₅Si₃ phase, which increases the yield strength at room temperature [101].

Chapter 4 Processing methods for high temperature alloys

The novel methods of processing by additive manufacturing (AM) via powdered metal feedstock have been developed to manufacture near net-shape pieces by laser deposition. These methods operate under the same principle, such as the Direct Laser Fabrication (DLF) and, more recently, the Laser Solid Forming (LSF) [134, 135]. The metal powder is fed into a laser beam that melts it under a substrate to form a component. Through CAD and CNC machining technology, a laser beam can be moved freely in space to build complex pieces in a sequence of layers, which characterises as one of the main advantages of these processes [136, 137]. Among the advantages of this process, the possibility of complex shapes has caught much of the attention, however this is not the only positive point.

For the suspended alloying droplet (SDA), different samples were synthesised by varying the ratio of wire feed rates. An alloy button is built by depositing a number of alloy droplets onto a substrate whilst maintaining a melt pool on the top of the sample. Metal wires are fed into the beam path and subsequently melt. The melting process initiates the formation of a droplet on the tip of each wire and eventually the droplet “pinches off”. As the droplet comes into contact with the copper substrate it spreads and is quenched rapidly to form a “splat”.

In electric arc melting processes, a high electric current is created between water cooled anode and cathode, melting the metallic charge inside the furnace chamber, which is then subject to solidification after the melt can be poured into a mould.

This chapter will describe in more details the procedures involved in fabricating the alloys used for this work, showing their characteristics, advantages, disadvantages and main uses, justifying the use of such techniques for this project.

4.1. Laser additive manufacturing of Nb-based alloys

A variety of processing methods can be used in Nb-Si composites, and due to its high reactivity, the use of ceramic moulds is limited. Investment cast, as used to Ni-based superalloys, is still not very used, given the difficulty of selecting materials for the high temperatures.

Among the processes used by researchers of Nb-Si composites, there is a focus to produce an in-situ lamellar composite. Directional solidification may be the main focus of current researches, in order to get higher fracture toughness.

Some types of DS can be addressed, such as the floating-zone processing (FZ), Czochralski, and Bridgman methods of directional solidification.

The FZ technique consists in a melting zone contained in a metal ingot, concentrating impurities at the end of the melt, thus eliminating the need for a crucible [2]. The Czochralski method is an induction method that allows the melt to levitate. As for the Bridgman method, being more common due to its easy control and use of a water-cooled copper plate rather than a ceramic one, and it allows the molten metal to solidify unidirectionally since the heat is extract from the bottom through the cooled plate [2, 103, 138].

Arc-melting is a common process used to produce small samples and it is capable of providing a variety of microstructure patterns to be studied. This process can also be followed by heat treatment, to ease micro-segregation and tensions from the solidification process and from the different cooling rates through the structure, such as the annealing treatment and ageing [10, 13, 100, 120, 139].

Directional Laser Sintering (DLS) and Physical Vapour Deposition (PVD) have also been used to produce Nb-Si alloys for high temperature application, as well as Hot Isostatic Pressing (HIP) [120, 140].

With the use of PVD techniques, the thickness of the laminates can be controlled, producing thin layers of Nb_{ss}/Nb₅Si₃ [141]. As for the DLS, it can be used to fabricate pre alloyed pieces, though tool and structural materials may be difficult to produce due to segregation and the cost of the process, and also for the drawback of providing powder material [120, 140]. The HIP process is also a form

to production by powder form, which is deposited into a mould and heated at high pressure in all directions, and then cooled with water. This process allows the piece to be produced in complex shapes, though the diffusion time required for the powder to consolidate can make the process unattractive [120].

4.1.1. An introduction to additive manufacturing

The technology for additive manufacturing (AM), or commonly known as 3D-printing, has been introduced many years ago by Charles W. Hull, where prototypes of objects were built by layer by layer printing assisted by computer-aided design (CAD). However, the development of projects based on this method had been ruled as non-feasible due to the high costs involved [142]. This cost barrier has drastically decreased over the years, with industrial use taken place nowadays, still at a small scale, over a wide range of materials.

The described laser process requires a substrate, which is usually a high temperature material, or even the existing component (in cases for in-situ rebuilding). A focused laser beam with pre-selected power is aimed onto the substrate to create a molten pool, with a constant flow rate of metallic powder being simultaneously directed at the beam through a nozzle. A computer numeric control (CNC) motion system assists the 3D movement of the substrate, which will create the final piece shape with the pre-programmed CAD model. As the substrate moves, the molten pool is dislocated, leaving a rapidly solidified layer behind [143].

The second step of this process involves the deposition of a following layer of metal on top of the initial layer, creating a wall structure. The repetition of this step is designated to form complex shapes by the movement of the laser beam, which controls the direction of the molten pool, and therefore the design of the shaped part without any mould or die [143]. Figure 26 shows the schematics of a powder feeding laser manufacturing technique, such as the LSF.

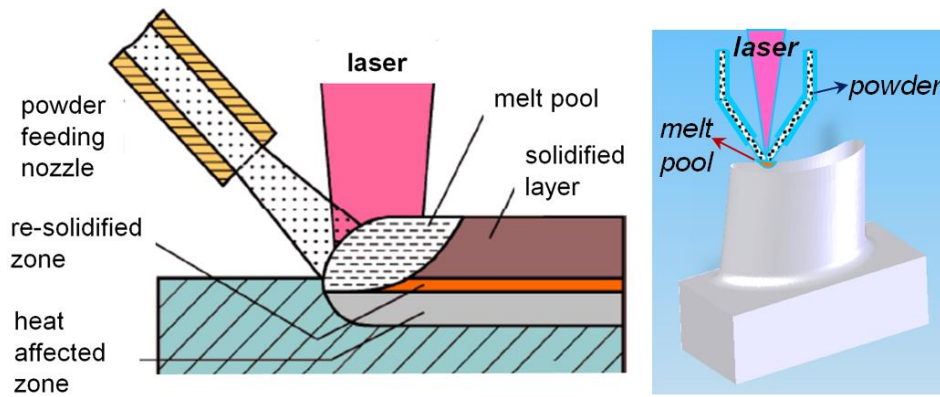


Figure 26 - Schematic of power feeding processing LSF [144].

Although highly capable, additive manufacturing machines have their shortcomings, which can be related to the cost of a production line, time consumption and post-processing. The speed of printing is of high importance and a key challenge for practical use in the metal manufacturing industries, due to the time spent during the set up (design of prototype, scanning speed of nozzle, power flow rate, power intensity, etc.), which accounts for most part of the production. This may put the use of AM techniques in question, when compared to traditional mass production methods. Besides, the size and the complexity of shape requires more planning and additional costs to the production of high technology products [14].

4.1.2. Advantages of additive manufacturing processing over traditional manufacturing

The ability of processing a near net-shape component without a mould, the good mix of the elements, reducing of waste material and diminishing micro-segregation are also some of the reason for this process to be investigated [134]. Though, it is important to outline that a dimension tolerance should be considered, as the efficiency varies according to the scan speed, and loss of material can be observed. It was noted that increasing the scanning speed increases the efficiency, since there is less material being fed [140].

A comparison of general aspects between conventional manufacturing techniques and additive manufacturing is given in Table 2 [145, 146].

Table 2 - Difference between conventional manufacturing and additive manufacturing in terms of many production aspects. [145, 146]

Aspect	Conventional manufacturing	AM
Equipment setup	Specific for each material and process	Adaptable, but require specific parameters
Reproducibility	High. Carried out in batches of up to thousands with small variations	Very. Requires good operator skills, but process is fairly automated
Production volume	Efficient for high numbers, reducing tooling cost and time	Best for low volume. High individual cost, but efficient for mid-range volume
Throughput	Increased batches, which give high initial costs	Buying new machines for simultaneous running
Machining	Always required	Usually required, but some processes produce excellent surface finishes
Heat treatment	Required for improving mechanical properties and ductility	Depends on the application. Usually reduces porosity and residual stress
Multi-material system	Not possible. Welding required	Some techniques are capable
Initial setup cost	Usually high, but reduced for high numbers	Machine prices are high
Raw material cost	High, but efficient for large batches	Depends on the material, but it requires a powder form material
Defining characteristic	Single design, high initial cost, high volume production and low part cost	Specific design, high initial cost, near net-shape formation, no use of moulds

The manufacturing processes based on AM methods have been proven to be highly innovative, as it opens a new window of opportunities for efficiency, the reduction of energy consumption and the waste of raw materials. It's worth mentioning that AM will hardly replace traditional manufacturing processes, but it will revolutionise many niche areas. This process allows consumers to rapidly repair and replace simple parts or mechanical pieces and enables mass customisation at low costs [142].

4.1.3. Restrictions of additive manufacturing production

Due to the layer-by-layer production associated with this process, the LAM process requires the use of complex 3D geometry design, which can be reduced into 2D steps forming a final complex and detailed shape [147].

To reduce costs and time spent with LAM processes, a redesign is usually studied in order to reduce heights or thickness of the pieces. As the layer-wise build up is done by steps, the geometric accuracy and resolution are of high importance. This is where the layer thickness can affect the roughness and surface quality, since this building process leads to the production of a “staircase effect” at angle and curved surfaces, as shown in Figure 27. Therefore, only an approximate contour of the final shape is produced [148, 149].

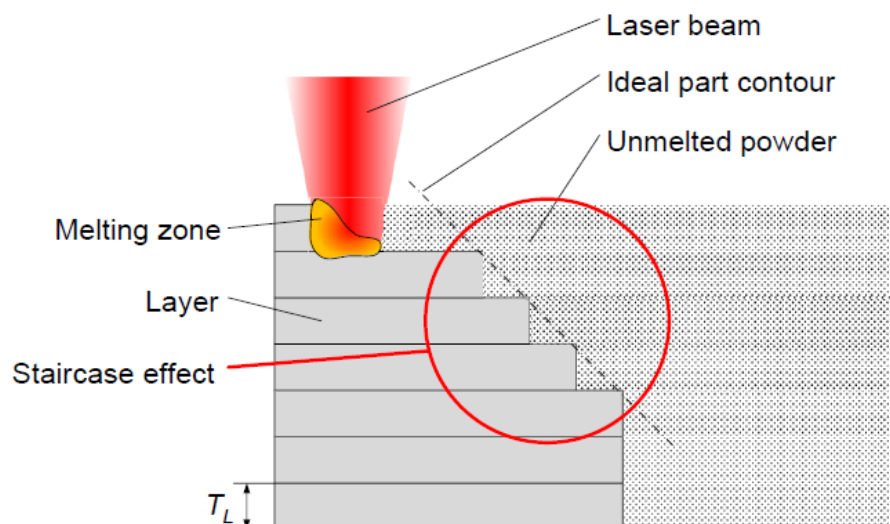


Figure 27 - A simplified illustration of the staircase effect during laser additive manufacturing; where T_L refers to the thickness of layer. [147]

4.1.4. Production costs

The barrier of production costs of pieces by the AM processes has still to be overcome. Many factors can contribute for the final price of AM parts, which can be related to the volume of production, the degree of complexity, the need for elements in powder form or the customisation of the parts [150].

Despite a greater efficiency by this method, costs involved with machine cost, energy consumption, set-up and build-up time and other indirect costs can cause a final cost higher than that of tradition routes [151, 152]. One example of this issue is given by Atzeni et al. [153], when showing that the conventional production of Al-base sintered alloys cost on average ten times less than the costs involved with AM formation.

Although, according to studies made on the costs in relation to the production volumes and complexity of parts, there is an insignificant change on the scale of economics of AM processes, when compared to the costs associated with conventional routes for the same parameters, as it is shown in Figure 28 [154-158].

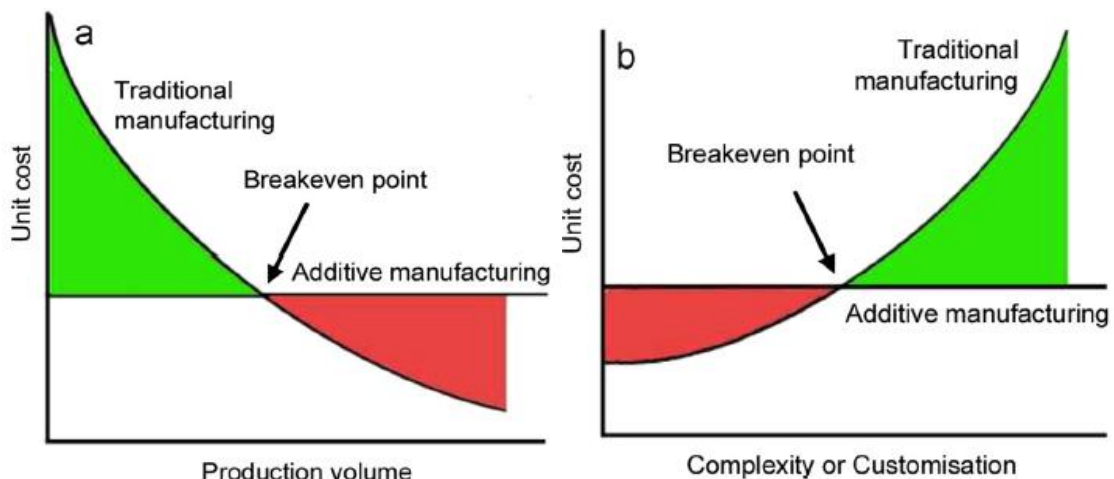


Figure 28 - Unit production cost for additive and traditional manufacturing; (a) against production volume and (b) against product complexity or customisation. Adapted from [154-158].

The position of the breakeven point places the AM process at a higher cost, which is directly related to the machining of final parts, material preparation and post processing methods for high quality finishing of the pieces [159-161].

From Figure 28, it is clear that AM methods are preferable when a small number of pieces are required to be produced, which is the case of replacement parts. When associated with a production line for an ongoing product, the traditional manufacturing shows to be much more economic and less time consuming [150]. Similarly, the degree of complexity has a significant impact, as pointed in Figure 28(b), as greater complexity will affect mostly the costs of traditional manufacturing due to the need of new design of moulds, tooling, operator times and certifications [150].

4.1.5. Metallic materials used for additive manufacturing

In early processes involving laser manufacturing, Co-based stellite alloys have been successfully built by two-dimensional laser cladding processes. These alloys were popular coating materials given the need for wear and corrosion resistance in harsh environments, and this process consisted of simultaneous injection, melting and rapid cooling of fine alloys onto steel surfaces [146].

Laser additive manufacturing based on direct energy deposition have also been used to produce medical grade CoCrMo alloys [162], where carbide precipitates are produced along with coarse columnar dendritic and finer equiaxed dendritic phases. Hazelhurst et al. [163] demonstrated the use of such alloys with parts 40% lighter and 60% more flexible than traditionally manufactured parts. Similarly, Monroy et al. [164] have produced dense parts using Selective Laser Melting, with porosities as low as 0.9% and averaging 5.77%. However, it is important to know the porosity size and distribution for an assessment of fatigue.

Fe-based alloys are widely produced materials by laser techniques, which is due to the great variety of materials for which it can be used, such as tool steels and stainless steels. For specific applications, alloys such as SS316, SAE4140 and H13 have shown high performance when compared to traditional routes, in terms of microstructure and strength for high complexity parts [165-168].

New high temperature alloys based on Ni, Ti and Nb are of extreme engineering interest, often applied for specialised systems, assemblies and aerospace applications. Recent researches have studied the production of Ti6Al4V alloys,

NiTi-shaped memory alloys and numerous studies on the prediction of microstructure and microstructure evolution, such as in this present study, as well as Ti-based materials for biomedical applications [169, 170]. The advantage of this process in producing these alloys is the ability to fine tune the composition to specific applications and to achieve the required properties.

Laser formed alloys have shown great promise in terms of mechanical properties for Ni, Ti and Co-based alloys before or after heat treatment, when compared to alloys produced by conventional methods, such as die casting, investment casting, wrought alloys, sand casting and powder metallurgy, as shown in Table 3 [171-175]. Such behaviour is expected to be reflected on Nb-based alloys.

Table 3 - Mechanical properties comparison for a range of Ni, Ti and Co-based alloys in terms of processing methods [171-175].

Alloy	Processing method	$\sigma_{0.2}$ (MPa)	σ_{UTS} (MPa)	δ (%)
IN 738	AM (HT)	1085±19	1238±12	21±2
	Wrought (HT)	1036	1240	12
	Cast (HT)	915	1100	5
Ti-6Al-4V	AM (thin wall)	1062	1157	6.2
	Wrought	965	1035	8
	Cast	890	1035	10
Stellite 6	AM (vertical)	751±16	1245±55	3.1±0.1
	Sand cast	541	834	1-2
	Investment cast	662	793	3
	Powder metallurgy	-	896	<1

4.1.6. Coatings used for Nb-Si alloys

An uncoated Nb-silicide alloy presents a high loss material, compared with Ni superalloys as cited previously, thus the use of coatings improves this behaviour. The goal is to decrease the loss of material in temperatures above 1300°C, while a superalloy is used at 1150°C. This relation is shown in Figure 29. Uncoated Nb-silicide needs improvement as for the demanding engine tests. The use of coatings will become permanent, as the dependency on them increases [7, 9].

As the role of coatings is of great importance, current studies have been developing coating in which the temperature of work can be up to 1370°C for 100h, which depends on the deposition and bonding process. Cracks can be present due to the different expansion behaviour and the fragile nature of the material, although the cracks do not propagate into the bulk, even up to temperature of 1430°C [9].

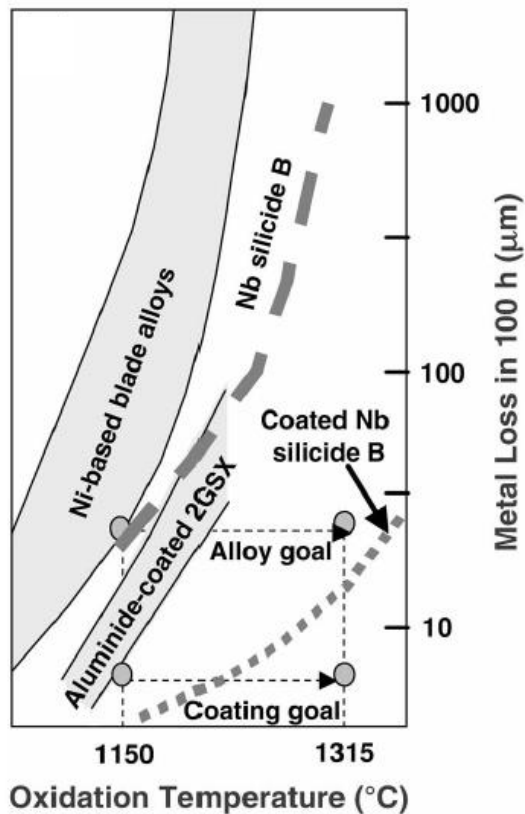


Figure 29 - Nb-silicide cyclic oxidation behaviour. [7]

A great concern regarding coating development is the prediction of possible failure that occur due to thermal fatigue, and once the external coat fails, the oxidation of the alloy may occur rapidly, as reported in early studies [123, 176].

The poor oxidation of Nb-silicides is due to the niobium oxides layer formation, which is not protective, due to easy penetration of oxygen. It is known that Al and Si based oxides can perform well at high temperatures [131, 177]. Suzuki et al. [178] have studied the effect of a NbSi₂ as a coat in Nb-silicides using molten salt, as a mean to form a layer of protective SiO₂. It was found that the layer was successful in preventing pest oxidation, though the deposition of this kind of coating remains restricted to lower temperature alloys.

4.2. Processing methods of refractory metals-based alloys

To derive the solidification path in the alloys under rapid freezing conditions, samples were produced using the following two methods:

- (i) Suspended Droplet Alloying (SDA) utilises a laser beam to melt elemental wire feedstock in order to produce a bulk alloy material sample. Compositionally different samples can be synthesised by varying the ratio of wire feed rates.
- (ii) Arc melting, which involved melting of elemental powders on a cooled Cu hearth.

4.2.1. Suspended Droplet Alloying

4.2.1.1. Introduction

This process allows the production of a small thin metallic button of various alloys with precise stoichiometry, which has been proved to be highly efficient in terms of cost and time when compared to traditional methodology for these types of exploratory processing, such as thin film deposition and diffusion multiples, which restrict the testing of alloys due specific layer thicknesses.

The SDA processing is based on the method of Direct Laser Fabrication (DLF), which is derived from additive manufacturing. The use of pre-mixed powder feedstock is generally used for this process, though specifically the SDA processing replaces the use of a powder feedstock into the use of a wire feedstock, in which there is no movement of the substrate. This allows the targeted composition to be achieved with more precision. A comparison between these two methods is presented in Table 4.

Table 4 - The comparison between wire-feed system and powder-feed system.

DLF powder-feed system	SDA wire-feed system
The waste of materials can be as high as 10-50%, as not all powder is melted	100% of the wired materials can be fed directly into the melting pool
An extra attention is needed to manage the over-sprayed powder	Less aggressive to the environment
Complex set-up system	Set-up system is simpler
Powder materials usually expensive	Low cost of wire materials
Elemental powder is available at a great extent	Wire compositions very limited

4.2.1.2. Method description

The wired material is melted by the direct contact with a laser beam, which produces a molten pool on top of the substrate. The droplets usually fall onto a substrate, producing a button-shaped alloy.

Given that the SDA process does not require the movement of the substrate, only the nozzle head is moved freely in vertical direction, which allows to an adjustment of the specimen height, while a cooled substrate is fixed. Thus, unlike the DLF or LSF methods, the SDA process is not classified as a net-shape processing since there is no need for a CAD file to be built beforehand.

For a wire feedstock to produce the target composition rapidly and accurately, there has to be a careful control of the feeding speed of the elemental wires being fed into the laser beam, which is protected with a non-reactive gas atmosphere to avoid oxidation, usually argon. A schematic drawing of this process is presented in Figure 30 [179].

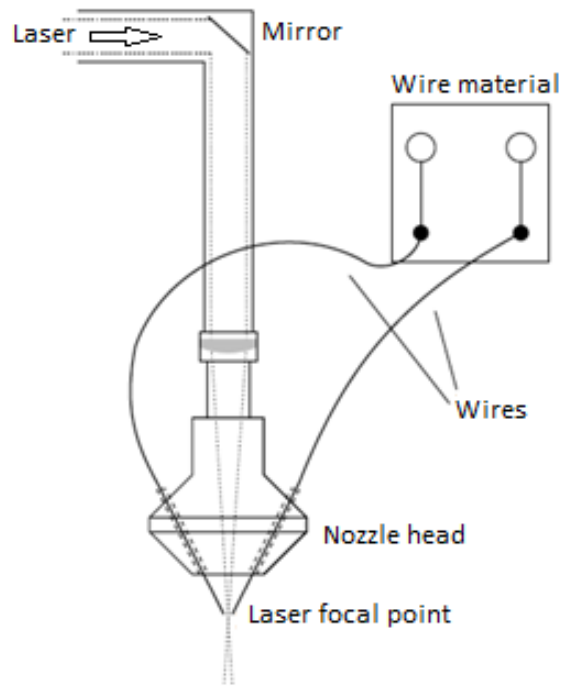


Figure 30 - Schematic drawing of the SDA processing method. Adapted from [179].

The wire feeder directs the wired materials into the nozzle head, where they will meet with each other at the laser beam focus point and melt. The droplet of material starts to grow as the laser beam energy increases through the wires, which is held by surface tension, and it eventually produces a droplet heavy enough to pinch-off the wire and drop onto the cooled substrate.

The droplet creates a molten pool onto the substrate, which allows the subsequent droplets to fall directly into it and undergo further mixing. This process can be carried out many times to produce cylinder-like materials or use the small droplet to produce a thin button, which can be used to study the effects of rapid (or splat) solidification, as is the case of the study for the Ta-Al-Fe alloys used in this project, schematically shown in Figure 31 [179].

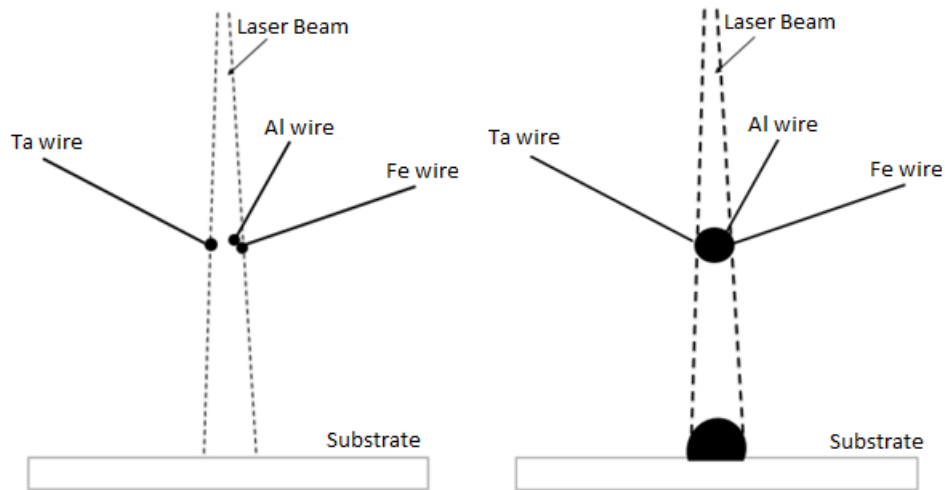


Figure 31 - Wire feedstock meeting at the laser beam focus point creating a molten pool.
Adapted from [179].

There are two physical stages involved in this process [180, 181]; (i) melting and pinching-off of the metal from the wire feedstock towards the cooled substrate, (ii) droplet impact and solidification, producing a solid deposit onto the substrate. Both cases are exemplified in Figure 32 [180].

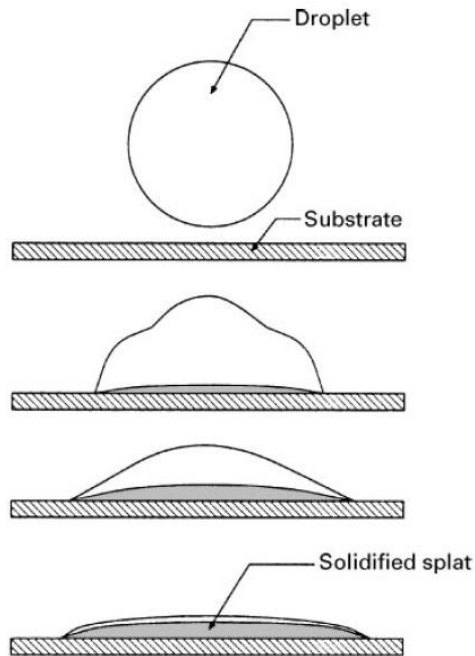


Figure 32 - Schematic illustration of the physical stages of melting and solidification via SDA.
[180]

The general idea of the impact of a droplet onto a solid surface has been studied from many points of view. It is a complex fluid dynamics and heat transfer issue,

given that after the droplet comes into contact with the substrate, there is a material spread and solidification [182, 183]. The determination of the solid phase thickness has also been widely studied and modelled [184-187].

Similarly, the analysis of deformation and solidification of droplets has also been presented by Madejski [184, 188], which considers that the droplet assumes the shape of a cylindrical button after impact, provided that the initial molten droplet falls with a spherical form, followed by simultaneous solidification. Later studies by San Marchi et al. [185] have also observed the effect of partial in-flight solidification.

4.2.2. Arc melting

4.2.2.1. Introduction

The electric arc furnace was invented by Paul Héroult, in 1889, and from the turn of the century new and cheaper technologies have made their way into the industry. Competitors like the Bessemer/Thomas converters and Siemens Martins furnaces had been target for the production of steels for high temperature [189, 190].

Since the introduction in 1905 and the increase in availability of cheap scrap steel products, the use of electric arc furnace (EAF) melting processing has been increasingly important for development of new and more efficient equipment capable of producing steels of the highest quality, to meet the demand for specified steels at the lowest possible cost [191].

Over the past century, an increased amount of research has contributed to the development of this technique, which include the improvement of the design electrode regulators [192-195], electrode and refractory consumption [196], refractory index control [197] and the aspects of power system loading and voltage flicker [198-200].

Lower electric energy consuming EAF have been in development since 1965, with enlarger capacity (up to 350 ton) [190]. The use of scrap has helped in the decreasing use of energy [190, 201].

The use of scrap metals is aimed to reuse most of ferrous alloys worldwide and refine them to special steels via the EAF processing. This is the case for newer EAF machines, such as the use of ultra-high-power furnaces, which are versatile and can transform all sorts of scrap metal to all types of steels. For modern EAF processes, 100% of all scrap metals, most commonly steels, is reused [190].

The EAF process can account for up to 3% of the electrical energy use in the industry worldwide, as it is classified as an energy-intensive process. However, this process can produce temperatures of up to 15,000°C in the electric arc, by convection and radiation, thus making it more favourable than other types of electrical routes of melting, since it is highly efficient in converting electrical energy into the melting heat [202, 203].

4.2.2.2. Method description

The design of electric arc furnaces is generally simple, in which there is the use of water cooled electrodes (anode and cathode), that when electric current is applied present the formation of an electric arc.

Most arc furnaces make use of alternate current, however since the decade of 1990 there has been an increased development in direct current furnaces, which use less energy [190]. A typical high capacity EAF is shown in Figure 33.

The current materials used as electrodes are artificial graphite-based materials, with water cooling in the late 1990's, aiming to decrease the consumption of the electrodes and reduce the amount of energy consumed [190].

A typical sequence of processing undertaken in an EAF, can be summarised in four main points [203];

- **Charging:** depending on the grade of the targeted metal, a close analysis is carried out regarding the amount and the quality of scrap or the elemental additions of powder metals being used. A residual melt can be present, which usually serves as a heat reservoir and can accelerate the melting process.
- **Melting:** As the electric arc is initiated, there is melting of the outside layers of scrap or powder metals which progresses into the bulk as the

arc grows. The use of burners can be added at this stage to promote the burning of the scrap or powder pile. Oxygen is also used to provide an oxidising environment and form a slag.

- **Superheating:** After melting of the scrap or the powder metal is completed, there can be the occurrence of hot spots generated from radiation. To reduce this effect, there is a decrease in the electric arc length.
- **Tapping:** After the molten metal achieved the required temperature, the EAF tilts into position for tapping, where the metal is drained from the furnace.

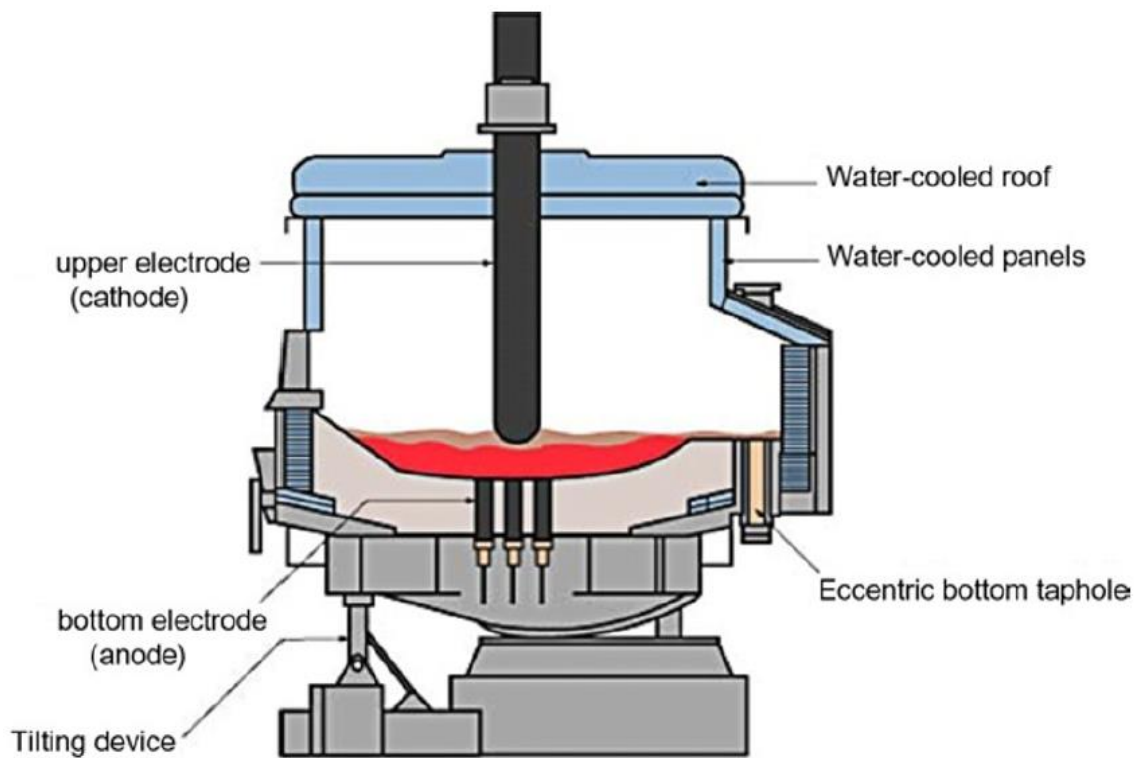


Figure 33 - A typical electric arc furnace [203].

Chapter 5 Experimental Procedures

5.1. Casting processes

Cast refractory metals-based alloys such as Ta-Al-Fe, Nb-Al-Fe, Nb-Al-Co and Ta-Al-Ti were produced in the University of Cambridge via two processing techniques, suspended droplet alloying and electric arc melting, which have already been introduced in Chapter 4.

For the suspended droplet alloying, compositionally different samples were synthesised by varying the ratio of wire feed rates. An alloy button is built by depositing a number of alloy droplets onto a substrate whilst maintaining a melt pool on the top of the sample. Al, Co and Ta wires are fed into the beam path and subsequently melt. The melting process initiates the formation of a droplet on the tip of each wire and eventually the droplet “pinches off”. As the droplet comes into contact with the copper substrate it spreads and is quenched rapidly to form a “splat”.

For the cooling rates for these splats solids are estimated to be in the region of 10^3 K/s. The laser beam was then fired in continuous wave mode and the wire feeders were activated. The bespoke alloy synthesis system utilised was manufactured by Renishaw plc. and was fitted with a 1000W fibre laser with a wavelength of 630 – 680nm.

The laser beam was introduced into the atmosphere-controlled chamber through a fused silica window. Within this atmosphere-controlled chamber oxygen levels were kept at 10 ppm during processing with an additional flow of shielding gas from the copper nozzle at a rate of 3 L/min over the alloy material during synthesis

For arc melting processes, small ingots of each alloy, weighing ~ 40 g, were cast via arc melting on a water-cooled hearth in an evacuated and argon backfilled atmosphere. Elemental metals, with purity $\geq 99.9\%$, were used as the feedstock and to minimise the loss of Al during the melting process, the alloys were fabricated in a two-step procedure. A binary alloy was created from the refractory

and transition metals, which was subsequently melted with pure Al to create the final ingot. To increase the homogeneity of both the binary and ternary alloys, at least two re-melting operations were used at each stage in between which, the ingots were physically inverted on the hearth.

5.2. Additive manufacturing processing

The alloys were prepared by the LAM processing method at the Northwestern Polytechnical University in Xi'an, China, with a main protective experimental cabinet for argon use. Pure elemental powders (Nb, Si, Ti, Al, Hf, V, Mo and Cr) have been obtained from Sigma Aldrich with size of 200 and 100 mesh, which is equivalent to approximately 74 to 149 μm , respectively.

The alloyed powders were prepared by weighing out the individual elemental powders by electronic balance and then dried for 3 hours at 120°C, following grinding for 2 hours using a MITR YXQM-0.4 L ball mill, shown in Figure 34.



Figure 34 - MITR YXQM-0.4 L ball mill used in the mixture of elemental powders.

The resulting powders were then filtered to help ensure an even distribution in powder size and poured into the containers typed DPSF-2, presented in Figure 35, to be blown into the laser beam at the end nozzles. An inert gas such as argon is used to feed the powders.



Figure 35 - Containers for the alloyed powders to be blown at the nozzles.

The powders have been selectively melted by the laser onto a preheated titanium base plate. The preheating has been used to reduce residual stress in the base plate. A laser scanning speed of 600 to 900 mm/min was used to reduce the grain size as it will be demonstrated in the results presented in Chapter 7.

An LSF-SI600A model laser additive manufacturing machine, located at the State Key Laboratory of Solidification Processing, consisted of a CW CO₂ laser (CP4000) with 4 kW mean power capacity, a five-axis numerical control table, inert atmosphere chamber (oxygen content lower than 100 ppm), and the powder feeders with a coaxial nozzle. The equipment is shown in Figure 36.



Figure 36 - LSF-SI600A model laser additive manufacturing machine used for the experiments.

5.2.1. Additive manufacturing parameters

The choice of parameter used for the LAM processing is listed in Table 5. The resulting materials from the LAM have been obtained in shapes of tall bars onto a Ti base substrate, as presented in Figure 37.

Table 5 - Parameters of laser used in the LAM processing of alloys.

Parameter	Value
Laser model	LSF-SI600A
Laser power	3.0 kW
Distance from substrate	15 mm
Spot size	6.0 mm
Build overlap	30%
Powder flow rate	6.0 L/min
Scan speed	600 - 900 mm/min

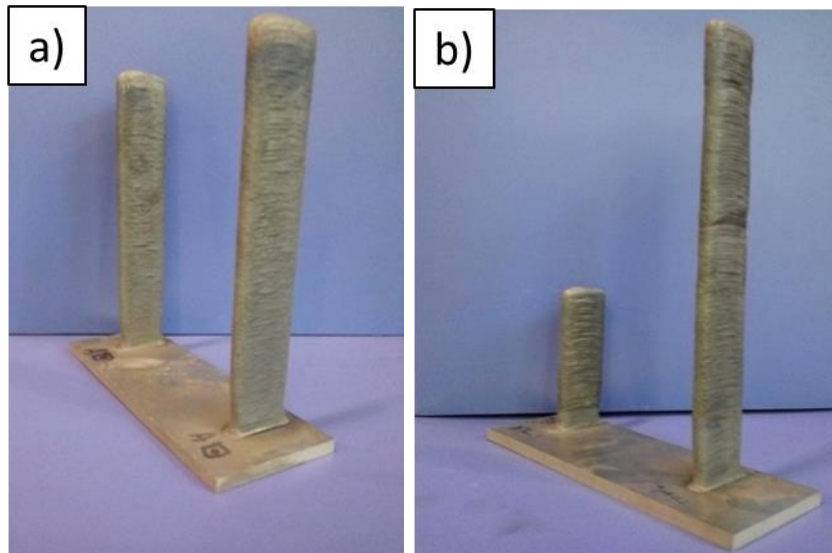


Figure 37 - LAM processed alloys in shape of bars; (a) regular sized samples and (b) shortest and tallest samples. Dimensions vary, but usually 10-20 cm x 2-3cm x 1 cm.

5.2.2. Scanning strategy

Different alloys have been selected to processing via the AM method. The choice of compositions has been made on previous studies via arc melting, which can provide a significant insight on the different and advantages of each process, and in the end produce a record of necessary improvements and requirements for each process. The chosen compositions (in at.%) are presented in Table 6.

Table 6 - Selection of compositions (in at.%) for AM processed alloys.

Alloy	Nb	Ti	Si	Al	Cr	Hf	V	Mo
A [110]	Bal.	22	15	2	14	2	2	-
B [110]	Bal.	22	15	2	2	2	2	-
C [125]	Bal.	24	18	5	5	-	-	2
D [140]	Bal.	26	22	2	6	3	-	-

The AM processing has been done using different scanning patterns, aiming to provide different mechanical properties, reduce thermal stresses during cooling and provide a complete study the effect of these different strategies of laser scanning on the processed alloys. Three different patterns have been selected, which are shown in Figure 38 and described as follows;

- Unidirectional pattern: This pattern follows a simple scan in only one direction of the plan (x, y). The molten powder is deposited on the substrate in a +x line, returning to the origin and moving in the y direction to a new line of deposition. This process is repeated layer by layer and produces the highest thermal stresses, as the second deposition layer will occur on top of an already cooled material.
- Snake pattern: This pattern is named after the “S” shaped movement of a snake, and in this case the laser is scanned laterally in both +x and -x directions. This produces a better equilibrium of heat dispersion onto the deposited material as the additional layers are added.
- Cross-snake pattern: This pattern presents movement in all directions of the (x, y) plane. The first layer of material is scanned with a snake pattern deposition in the x direction (as described previously), followed by second layer deposited in both +y and -y directions. This pattern is expected to produce the least thermal stress and distribute heat more equally throughout the material surface.

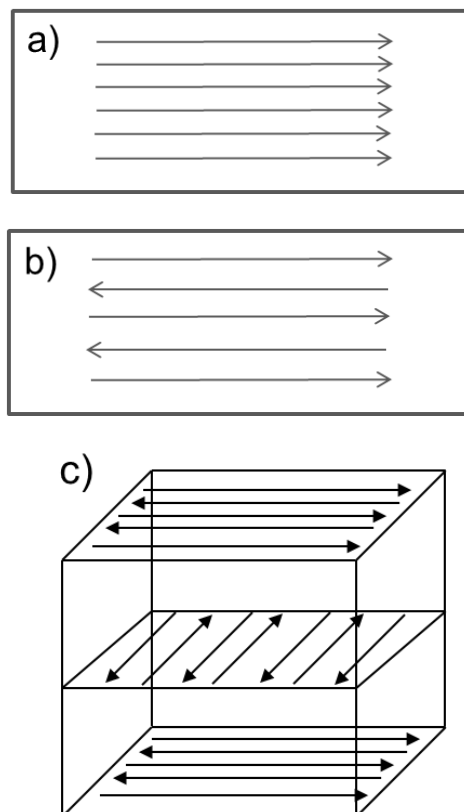


Figure 38 - Scanning patterns selected for the AM process; (a) unidirectional, (b) snake and (c) cross-snake.

5.3. Post processing techniques

Regardless of the method of processing used for the fabrication of an alloy, post processing will usually accompany the final steps of the production line. Materials rarely exhibit the desired properties or microstructure without post processing techniques. These techniques aim to improve the material properties by inducing phase transformation, microstructural changes and by removing unwanted parts or features of the alloy, such as porosity or impurities.

The parameters to be used are determined by a detailed analysis of the material in question and a design of required properties. The post processing used for the NbSi-based alloys in this study will be discussed in the following sections.

5.3.1. Hot Isostatic Pressing

The laser solid forming processing, due to its large cooling rate, induces significant residual stress for the solid metals and large contraction after cooling produces internal porosity, which then damage the required properties for materials produced via this method. A post-processing of pressing is therefore used, in order to work around this problem, and it consists of using Hot Isostatic Pressing (HIP) treatment, so that porosity and gases within the microstructure can be reduced to a minimum.

The HIP process subjects the alloys to high temperatures and high pressures applied by an inert gas, such as argon or helium. These are dependent on the alloy system, with a temperature below the melting temperature of the alloy in question [204].

This process aims to reduce the internal porosity. This can occur in ways such as trapping of atmospheric gas or shrinkage during solidification, which are detrimental to the material performance. Pores can act as sites for crack initiation and propagation, increasing the possibility of fatigue and reducing ductility [205]. The mechanism for HIP is dependent on the solubility of the trapped gas in the alloy and on the position of the porosity, and a typical mechanism is shown in Figure 39.

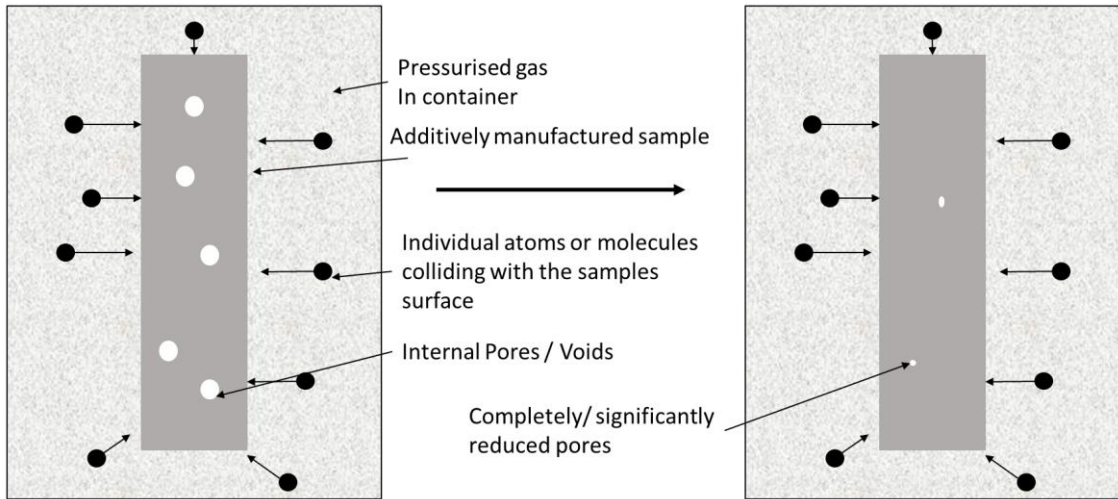


Figure 39 - Typical mechanism for hot isostatic pressing [206].

For the HIP process, the Ti substrate bases have been removed from the alloys. The model number and manufacturer of the HIP machine used for this experiment is and EPSI model V0 15197, shown in Figure 40 shows the HIP machine.



Figure 40 - HIP machine used for the experiment.

Table 7 presents the parameters used during the HIP processing of additive manufactured alloys. The alloys have then been cleaned and analysed, followed by the heat treatment process.

Table 7 - Parameters used during HIP process.

Parameter	Value
Heating/Cooling rate	10°C/min
Temperature	1200°C
Pressure	150 MPa
Dwell time	6h

5.3.2. Heat Treatment

Heat treatment is a common process used in the metallurgy industry. Cooling rates involved during primary production are rarely close to equilibrium conditions. This leads to changes in phases formations and volume fraction expected, also deviating the suggested solidification sequence from phase diagrams [207].

A single stage heat treatment elevates a material to a higher temperature, close to liquidus, for a period of time. Increased temperature leads to solid state diffusion, allowing an alloy to reach its equilibrium state. The length of time and temperature used vary significantly for different materials and the desired properties.

Aluminium alloys, for example, are subjected to different heat treatments, and different temper, some of which are 0, T6 and T7. This causes precipitates to grow at different rates and contribute differently towards the yield strength of the material [208].

In addition to HIP processing, the heat treatment of NbSi-based alloys has been done at a temperature of 1500°C for a dwell time of 1 hour in a directional solidification furnace under vacuum. Argon gas has been injected in the furnace chamber twice before evacuation had been completed. Cooling has occurred inside the furnace to room temperature.

5.4. Microstructural analysis

5.4.1. Specimens preparation

The alloys produced have been cut off from the substrate plate into small pieces of approximately 5 to 8 mm thick, using an ATM Brilliant 220 precision cutter, and were mounted in conductive Bakelite in a Struers CitoPress 1.

The resulting samples were ground using 80, 240, 400, 600 and 1200 grit SiC papers followed by polishing pads with diamond past of 6 and 1 μm for metallographic analysis.

5.4.2. Materials characterisation

All scanning electron microscopy (SEM) was performed using a dual beam (FEI Nova 600 Nanolab), Focused Ion Beam (FIB)/ Field Emission Gun Scanning Electron Microscope (FEG-SEM) and Philips XL 30 environmental scanning electron microscope (ESEM). Back-scattered electron images (BEI) were collected using a retractable solid-state back-scatter detector using high (20 kV) electron beam accelerating voltages for enhanced compositional contrast and working distance of 10 mm.

Chemical analysis was undertaken in this system at 20 kV using Energy Dispersive Spectroscopy (EDS) using an Octane super 60 mm² Silicon Drift Detector (SDD) from EDAX. EDS spectrum were collected using INCA and Aztec software to assess sample compositional homogeneity. From these scans regions for collecting comparative spectra were defined and these were collected for 120 s live time.

Figure 41 schematically shows the generation of EDX signal upon interaction with the specimen surface. As the electron beam penetrates the surface, the interaction volume from which the X-ray signal is detected increases, therefore it is worth mentioning the effect of volume averaging when analysing phases with fine morphology.

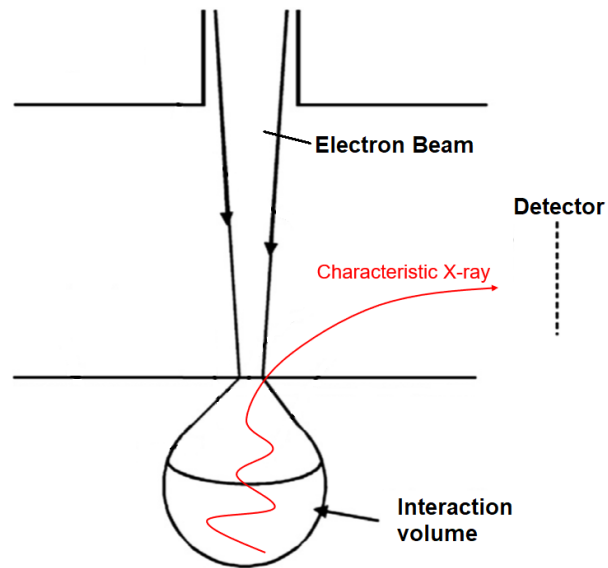


Figure 41 - Characteristic X-ray produced upon interaction with specimen. Adapted from [209]

Phase identification was undertaken using an Empyrean (PANalytical) X-ray diffractometer. The system used Co as the anode material and was operated at 40 kV with a tube current of 40 mA. Spectra were collected in the scan range (20 to 120°) corresponding to 2h with a 0.013° step size.

Chapter 6 Solidification sequences and structures of rapidly solidified cast refractory metals-based ternary alloys

6.1. Ta-Al-Fe system

The different compositions investigated for this system are plotted in Figure 42, presenting the liquidus projection and solidus projections, and the nominal compositions with expected and observed phases (identified by the use of the phase diagrams and isothermal sections) have been measured by EDS and are listed in Table 8.

Table 8 - List of samples, elemental composition, condition and observed phases in the microstructure of Ta-Al-Fe samples.

Sample	Composition (at. %)			Method of Manufacture	Equilibrium Phases	Observed Phases
	Ta	Al	Fe			
S1	86.8	7.3	5.9	Arc Melting	A2 + σ	A2 + μ
S2	80.2	9.8	10.0	Arc Melting	A2 + σ	A2 + μ
S3	78.1	10.2	11.7	Arc Melting	A2 + σ + μ	A2 + μ
S4	75.0	17.4	7.6	Arc Melting	σ	A2 + σ + μ
S5	81.6	11.2	7.2	Splat	A2 + σ	A2 + μ
S6	80.5	6.9	12.6	Splat	A2 + σ	A2 + μ

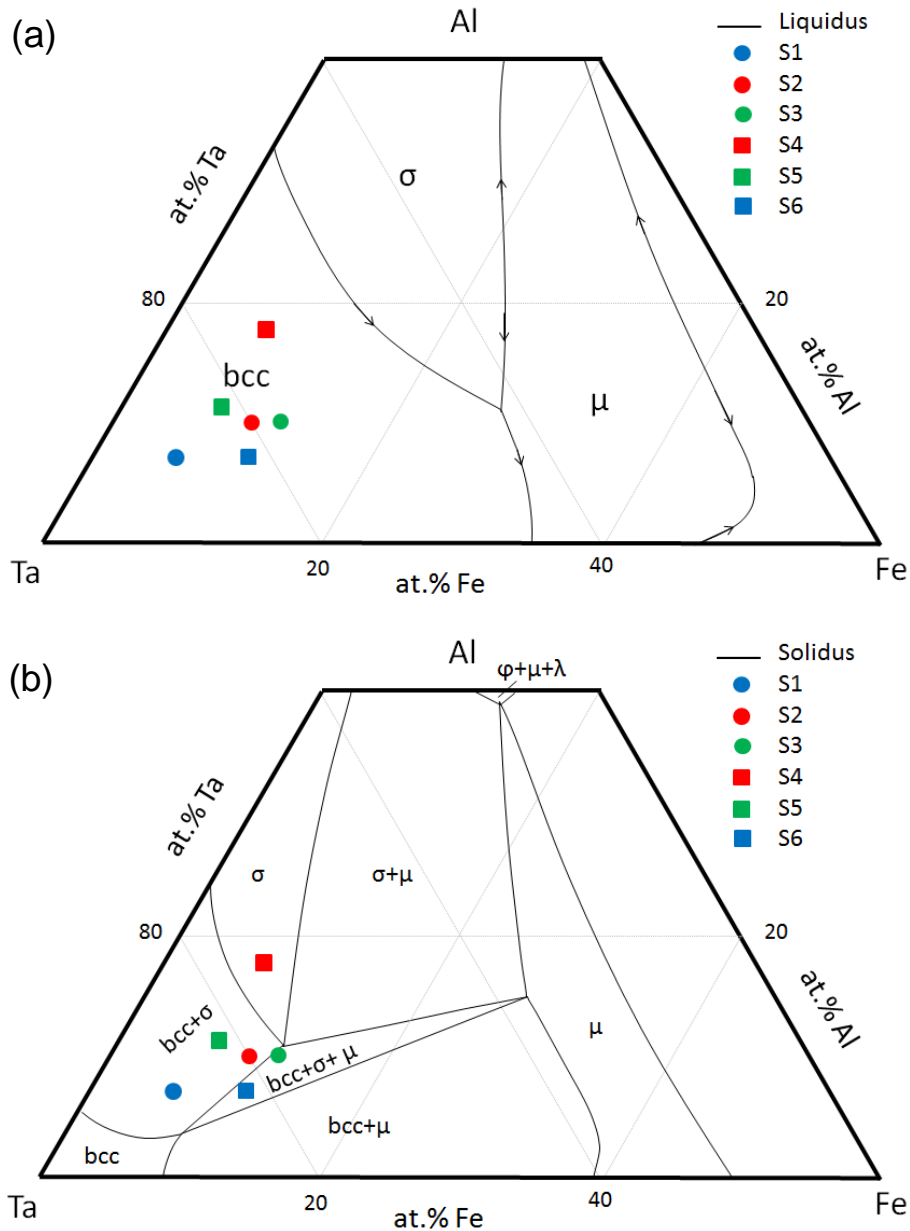


Figure 42 - Alloy compositions plotted on the Gibbs triangle corresponding to, (a) liquidus projection, (b) solidus projection [21].

Samples S1 and S2 are expected to undergo the peritectic reaction after primary freezing of phase A2, $L \rightarrow A2$ and $L + A2 \rightarrow \sigma$ (when all liquid is consumed), while S3, due to a lesser content of Ta, is expected to undergo the 4-phase invariant reaction, following the solidification path: $L \rightarrow A2$, $L + A2 \rightarrow \sigma$, $L + \sigma \rightarrow A2 + \mu$, which can be seen in the liquidus and solidus projections in Figure 42. The observed phases, however, did not show the presence of σ phase for any of these three alloys.

Figure 43 presents the low and high magnification back-scattered electron images (BEI's) of S1.

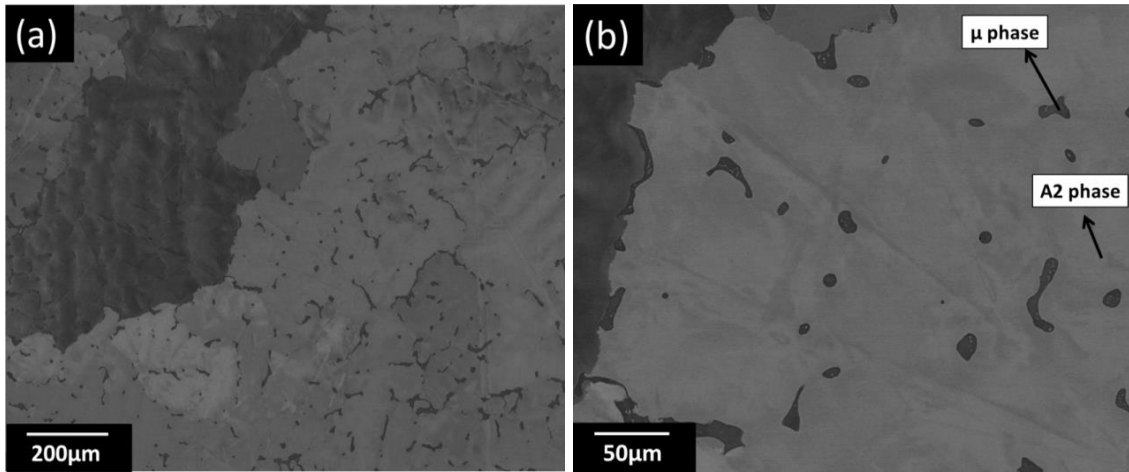
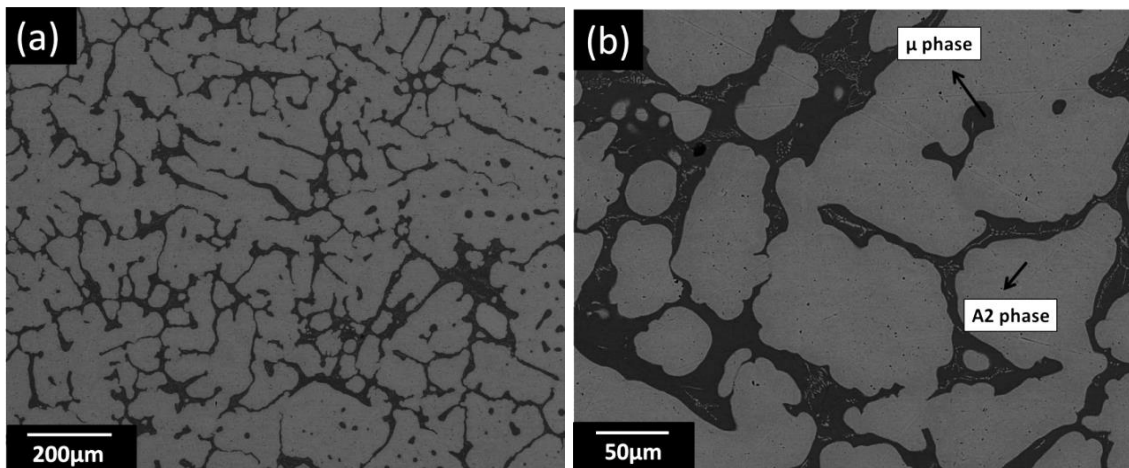


Figure 43 - BEI corresponding to S1, (a) low magnification, (b) high magnification.

It can be observed a primary dendritic formation of A2 phase with a sporadic and acicular inter-dendritic region, which is corresponding to the eutectic formation. The measured composition (in at.%) of the phases observed is presented in Table 9.

Figure 44 presents the microstructure observed for S2 and S3. The measure composition (in at.%) of the phases observed for these alloys is presented in Table 9.



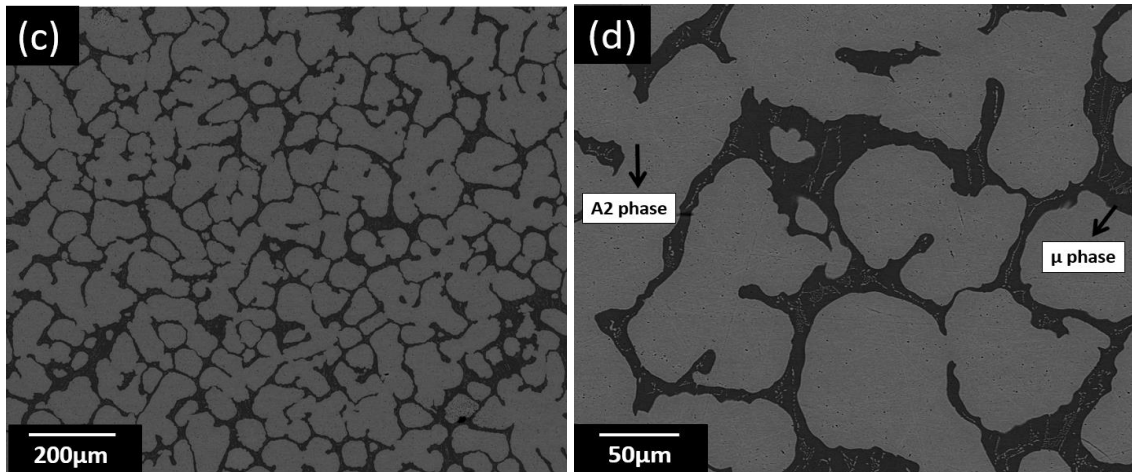


Figure 44 - BEI corresponding to S2, (a) low magnification, (b) high magnification; and to S3 (c) low magnification, (d) high magnification.

Samples S2 and S3 present a very similar structure, with a primary dendritic phase in a large extent across the microstructure. As seen in Figure 44, the composition of μ phase lies on the single-phase boundary in the solidus projection. The morphology observed for the A2 + μ eutectic is primarily divorced, but within μ phase a lamellar morphology is also noticed.

Table 9 - Average measured compositions (in at.%) of phase present in S1, S2 and S3.

Sample	Phase	%Ta	%Al	%Fe
S1	A2	89.4	6.8	3.8
	μ	57.2	13.5	29.3
S2	A2	88.4	7.5	4.1
	μ	56.0	15.7	28.3
S3	A2	87.2	8.5	4.4
	μ	56.1	15.5	28.4

The solid composition of the different phases is plotted in the liquidus and solidus projection in Figure 45, which also includes the positions of the phase boundaries at lower temperature for S1, S2 and S3 (same colour represents the same phase, while the shapes for phases of different samples follows that of the nominal composition).

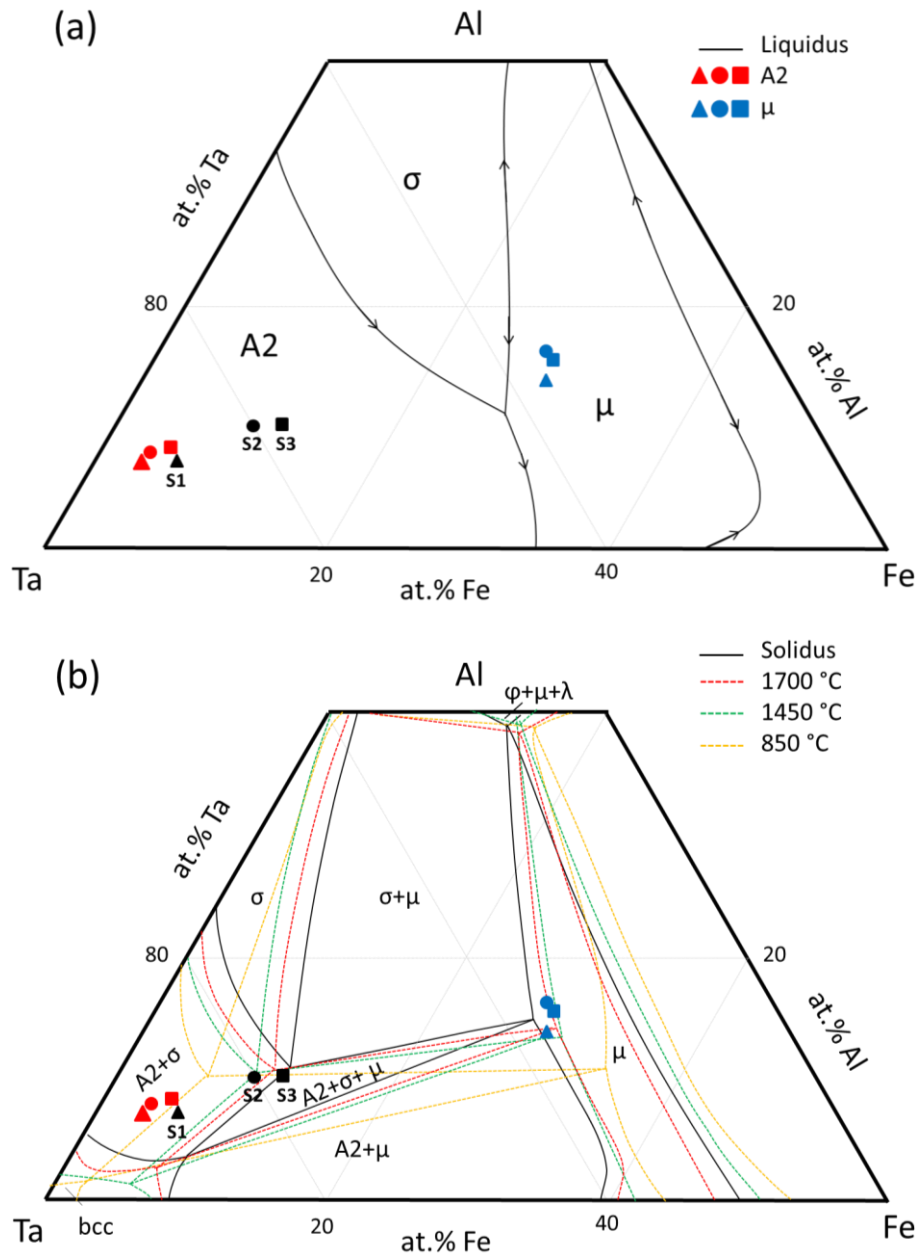


Figure 45 - Measured composition of solid phases present in S1, S2 and S3 plotted on (a) liquidus and (b) solidus projections, including phase boundaries with decreasing temperature [21].

Knowing that σ phase has its stability increased for higher Al concentration, it is important to have a closer look at the composition range beyond where the formation of σ phase is not suppressed, given that possibility.

For this to be investigated, a new composition that is progressively enriched in Al and lower in Fe has been made, namely S4, such that the nominal composition is increasingly remote from the A2 - μ valley in the liquidus projection. The

expected solidification sequence in this case is; $L \rightarrow A2$ and $L + A2 \rightarrow \sigma$ (when all liquid is consumed).

The low and high magnification back-scattered electron images (BEI's) for this alloy are presented in Figure 46, while the solid composition in the different phases is plotted in the liquidus and solidus projection in Figure 47.

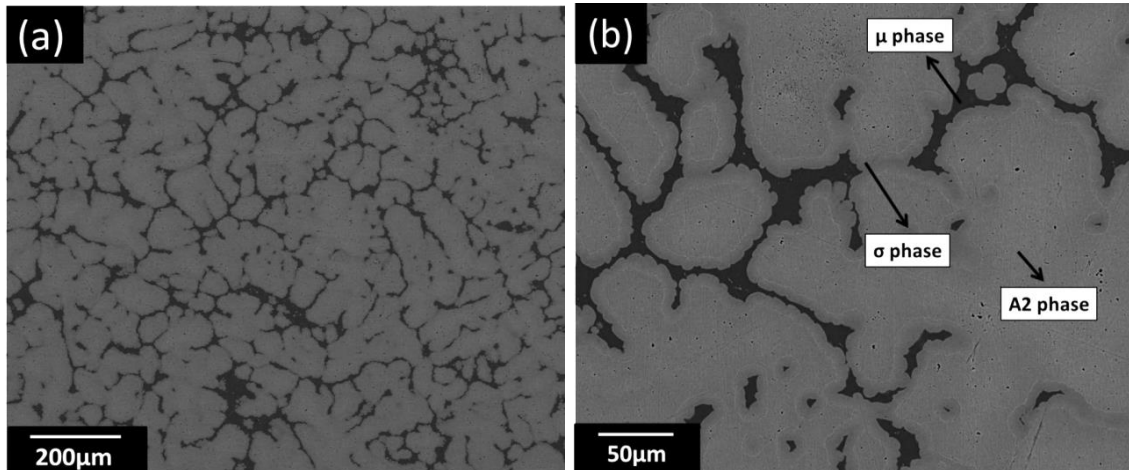


Figure 46 - BEI corresponding to S4, (a) low magnification and (b) high magnification.

The primary A2 phase is formed with dendritic pattern from the liquid, represented as $L \rightarrow A2$. As observed for the previous alloys, there exists an extended solubility of primarily Al and to a lesser extent Fe in A2.

Within the inter-dendritic region there is the distinct formation of a “grey” σ phase that forms a rim continuously across the dendrite. The measured compositions of σ phase lie on the boundary of the single phase-field in the solidus projection observed in Figure 47.

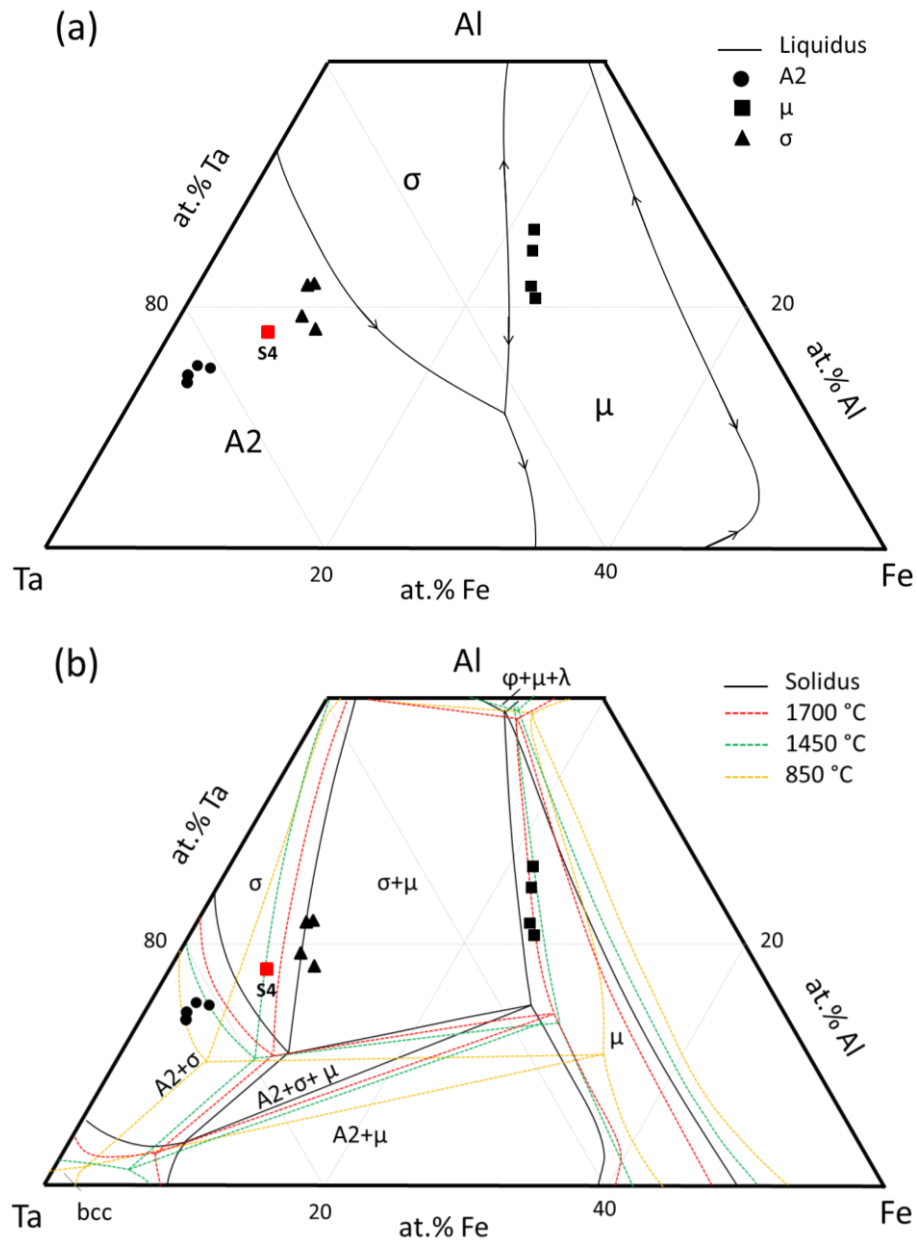


Figure 47 - Measured composition of solid phases present in S4 plotted on (a) liquidus and (b) solidus projections, including phase boundaries with decreasing temperature [21].

The formation of σ phase occurs via peritectic reaction, $L + A2 \rightarrow \sigma$, which initiates at the solid/liquid interface and can be represented as two separate reactions; $L \rightarrow \sigma$ and $A2 \rightarrow L$ [23, 31]. The subsequent peritectic transformation, governed by diffusion through the solid, is rarely completed and instead it occurs via primary deposition of σ phase, through $L \rightarrow \sigma$. Here the liquid composition leaves the liquidus curve and traverses the σ -liquidus surface, while the solid composition traverses the solidus surface.

Solidification terminates with the eutectic reaction, $L \rightarrow \sigma + \mu$, which forms with a divorced morphology. The composition of the “dark” μ phase lies on the boundary of the single-phase field in the solidus projection. The average measured compositions of the phases observed is presented in Table 10.

Table 10 - Average measured compositions (in at.%) of phase present in S4.

Sample	Phase	%Ta	%Al	%Fe
S4	A2	81.3	15.0	3.7
	σ	70.1	20.2	9.0
	μ	53.2	23.7	23.3

From these results, the following key points can be drawn:

- (i) It is observed that within the primary dendritic A2 phase there is an extended solubility of Al formed primarily to a lesser extent, and this cannot be accounted for by changes in solute solubility during cooling.
- (ii) There is a change in the observed solidification path from that predicted from the liquidus and solidus projections under equilibrium condition. For samples that contain lower Al and higher Fe concentrations, such as S1, S2 and S3, suppression of the peritectic reaction ($L + A2 \rightarrow \sigma$) is noticed and a new eutectic reaction ($L \rightarrow A2 + \mu$) occurs following primary freezing of A2. Therefore, the 4-phase invariant reaction is not observed for S3.
- (iii) For S4, which contains higher Al and lower Fe contents, the peritectic reaction is observed. The reaction is then followed by the eutectic reaction $L \rightarrow \sigma + \mu$.

The extended solubility of A2 can then occur if the nucleation of σ phase is suppressed and that the primary solid is continuously deposited during freezing of A2. The liquid and solid compositions consequently traverse the metastable extensions of the liquidus and solidus surfaces respectively. This suppression is reasonable if significant crystallographic mismatch exists between the two phases; which in this case are the disordered bcc (A2) and the tetragonal, σ phases [210].

Given that the solubility limits of up to 9 at.% of Al and 4 at.% of Fe in A2 for samples S1, S2 and S3, the solute concentrations traversing the metastable solidus should exhibit a concentration gradient within primary A2, which is not consistent with microstructural analysis, as back-diffusion is not sufficient to eliminate these solute gradients entirely.

Furthermore, a decrease in the solubility of Al and Fe is noticed in A2 at lower temperatures, thus the extended solubility of Al and Fe cannot be accounted for by changing solute solubility during cooling below the solidus. However, with increasing Al concentration, even though an extended solubility of Al exists within A2, nucleation and growth of σ phase occurs via the peritectic reaction, as observed for S4.

Following the approach in [20], given the negligible composition gradient in A2, a tie-line can be plotted by joining the nominal composition of S4 and the solid composition in the liquidus projection in Figure 47(a). This line then intersects the A2 - σ peritectic valley and it explains the occurrence of the peritectic reaction observed.

Therefore, the absence of the peritectic reaction in samples S1, S2 and S3 can be explained with regarding the primary freezing, which is related to the extended solubility of Al and Fe in the primary A2 phase. Similarly, a tie-line can be drawn for S1, S2 and S3 joining the nominal alloy composition and the solid compositions in the liquidus projection in Figure 45(a).

Based on that, two important findings can be suggested;

- (a) The line extended for the nominal and solid compositions does intersect the A2 - σ peritectic valley. Thus, if the eutectic reaction $L \rightarrow A2 + \mu$ was to occur following primary freezing of A2, this line would have to intersect the A2 - μ eutectic valley instead.
- (b) From the analysis of the solidus projection, for the compositions of samples S2 and S3, the composition of μ phase lies adjacently to the vertex of the tie-triangle corresponding to the 4-phase invariant reaction involving μ phase. This is true, given the fact that when the eutectic

reaction occurs, the composition of μ phase should lie beneath this vertex along the single-phase boundary.

These points corroborate that the eutectic reaction can only be possible if shift towards “north-west” (upwards and leftwards) of the valley is assumed. In this case, a change for the A2 - σ peritectic and A2 - μ eutectic valleys in the liquidus projection and for the vertex corresponding to μ phase in the 4-phase invariant reaction, $L + \sigma \rightarrow A2 + \mu$ in the solidus projection. This shift in peritectic and eutectic valleys as well as the extended solubility of Al and Fe in A2 phase is a clear proof of the decrease in solute partitioning during primary freezing, which also shows the loss of interfacial equilibrium during primary solidification.

For samples prepared by arc melting, the thickness chosen is related to the maximum height of solidification, and this occurs due to the transverse movement of the arc along the bar, which will present high cooling rates if the samples have small diameters.

Given the solidification path deviation from equilibrium, which might be attributed to the rapid cooling rates, the use of the splat quenching technique has been experimented for thinner samples to investigate this phenomenon.

With compositions close to S1, S2 and S3, to provide comparison, a similar solidification path followed from the liquidus and solidus projections can be expected. The composition of two new samples (S5 and S6) has been presented in Table 8.

For both S5 and S6, a very fine dendritic microstructure is observed, which is consistent with the splat quenching method. The microstructure for these alloys can be seen in Figure 48.

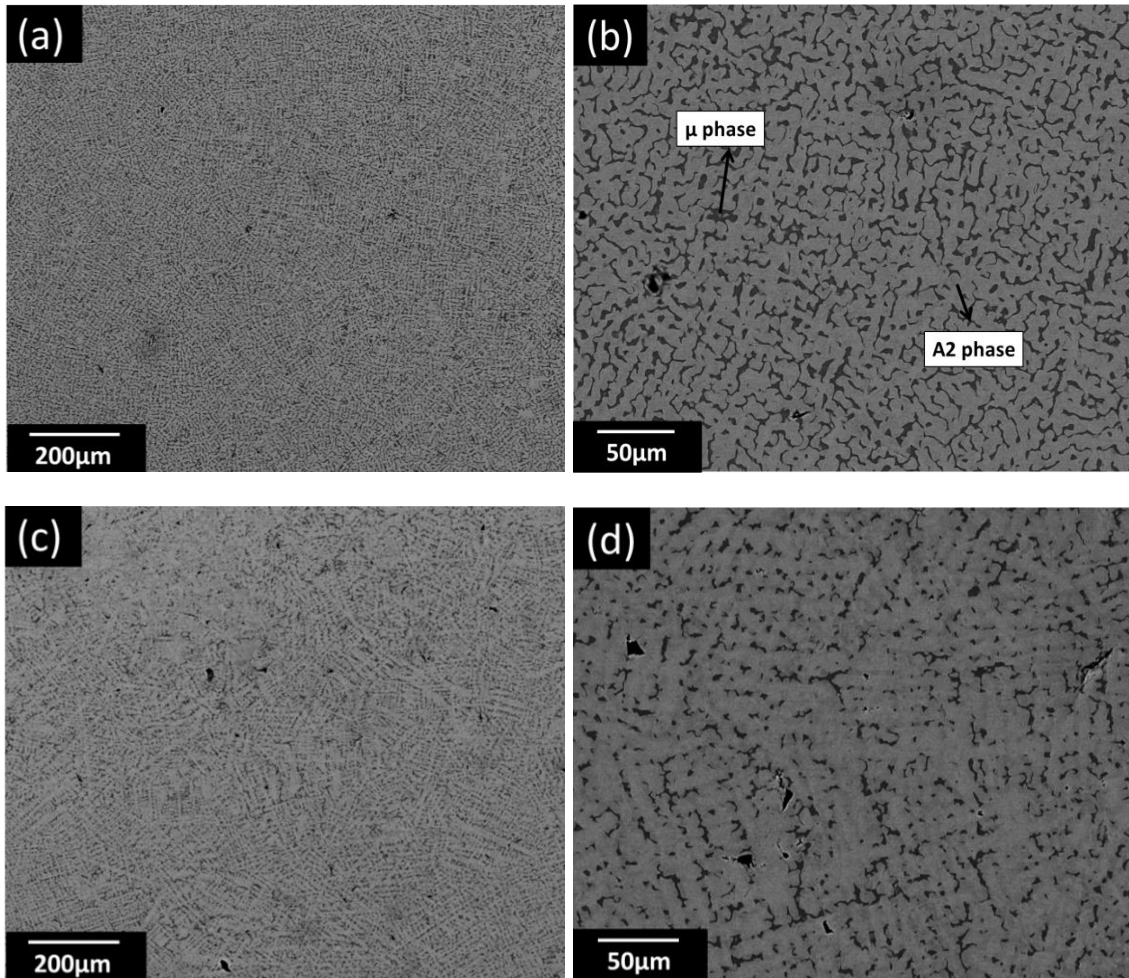


Figure 48 - BEI corresponding to S5, (a) low magnification, (b) high magnification; and to S6 (c) low magnification, (d) high magnification.

From EDS measurements, it is found that the primary phase is A2 (Table 11) and an extended solubility of Al and Fe solutes exists in A2. Primary freezing can therefore be represented as; $L \rightarrow A2$.

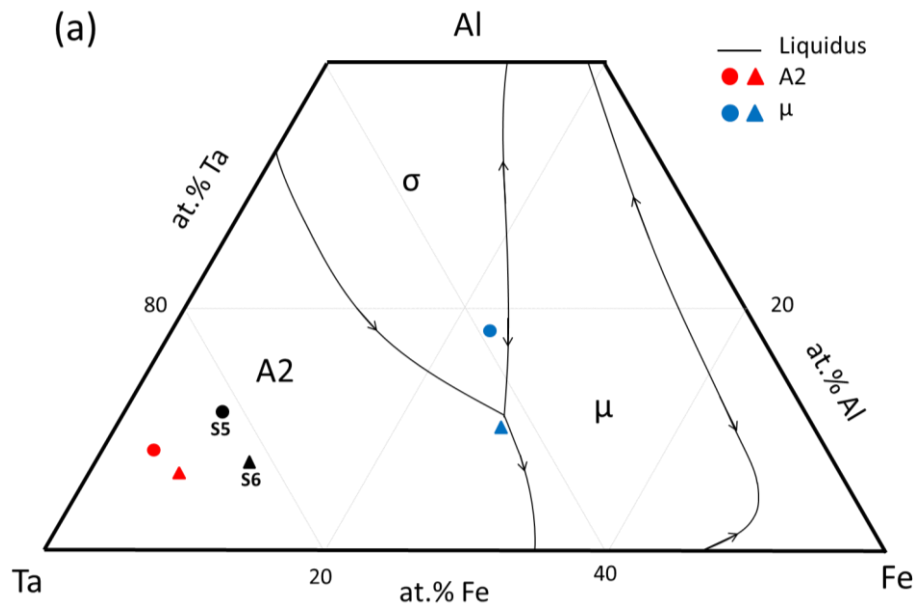
The composition measured at various locations within the inter-dendritic region is presented in Table 11, which corresponds to μ phase. Moreover, it is noticed the compositions of μ phase lie beyond the single phase-field in the solidus projection, as shown in Figure 49, and cannot be accounted for by changing solubility with decreasing temperature. The formation of μ phase follows the eutectic reaction, $L \rightarrow A2 + \mu$, with a divorced morphology.

Table 11 - Average measured compositions (in at.%) of phase present in S5 and S6.

Sample	Phase	%Ta	%Al	%Fe
S5	A2	87.6	6.1	6.3
	μ	63.0	8.9	28.2
S6	A2	88.0	8.4	3.7
	μ	59.0	18.2	22.9

Therefore, it can be confirmed that with increasing cooling rate, there is also extended solubility of primarily formed Ta in μ phase corresponding to the eutectic reaction.

The deviation from interfacial equilibrium occurs due to freezing at high cooling rates, where the characteristic distance $\delta \ll D_L/V$, where “V” is the interface migration rate and D_L is the solute diffusivity at the interface [24]. Qualitatively, this phenomenon can be understood by the fact that, when the copper-cooled hearth is maintained at a fixed temperature ($\sim 100^\circ\text{C}$), a higher melt superheat will result in a high thermal gradient, thus increasing cooling rates during the initial stages of solidification, at approximately 10 mm up the diameter of the bar.



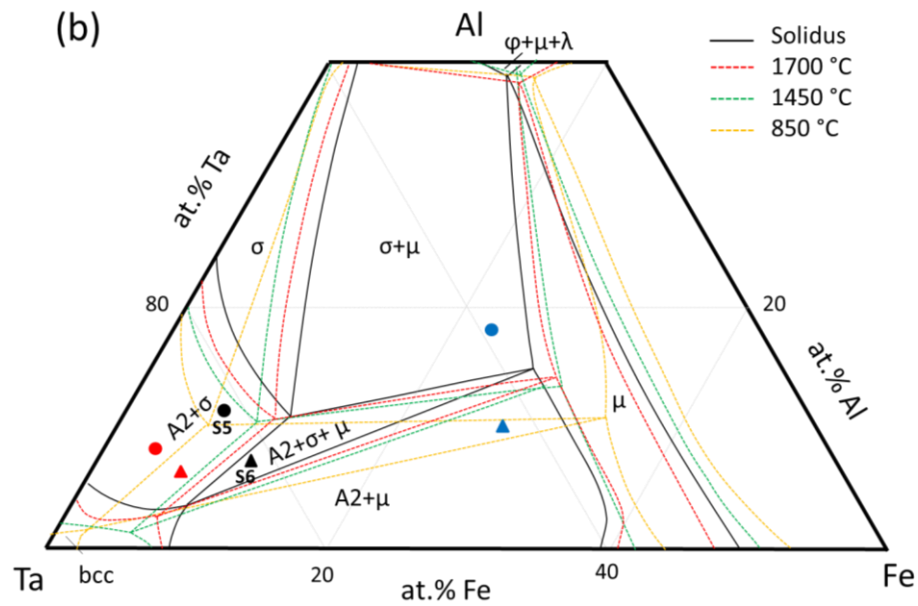


Figure 49 - Measured compositions of solid phases present in S5 and S6 plotted on (a) liquidus and (b) solidus projections, including phase boundaries with decreasing temperature [21].

By examining the liquidus projection in [21], the liquidus temperature for the different alloys can be approximately ascertained. When the primary phase was A2, the liquidus temperatures were in the range of 2400 to 2600°C, while for σ as the primary phase, liquidus temperatures were in the range of 1800 to 1900°C. This increased superheat of $\sim 600^\circ\text{C}$ can qualitatively account for greater cooling rates for the compositions with higher liquidus temperature.

For the case of S4, the composition of σ phase lies close to the boundary of the solidus projection, with no extended solubility and which is consistent with this argument, which was confirmed during primary freezing of A2 is obtained from the splat cooling experiments.

For sample S6, if an extended line is drawn by joining the A2 composition and nominal composition, it intersects the A2 - μ eutectic valley. Beside the extended solubility of Al and Fe in A2, there is also extended solubility of Ta in the composition of μ phase.

For S5, however, the extended line intersects the A2 - σ peritectic valley. Here, the extended solubility of Al and Fe in A2 is also observed, but the composition of μ phase shows extended solubility of both Ta and Al solutes.

It must be noticed that the change in solute composition during cooling within μ phase cannot account for this extension in solute solubility, as the $A2 + \mu / \mu$ phase boundary shifts towards higher Fe, not Ta nor Al. Therefore, the increased cooling rate proportioned by splat quenching additionally leads to a non-equilibrium freezing during the eutectic $L \rightarrow A2 + \mu$, trapping of Ta and Al within μ phase.

If the condition $\Delta G = [G_S - G_L] < 0$, per mole of solid is satisfied, there exists a range of solid compositions that can be formed from the liquid under non-equilibrium, given the rapid cooling.

For the case of metallic systems, interfacial attachment kinetics is infinitely rapid and consuming all of ΔG for migration of the interface from the effects of solute trapping [211]. However, unlike binary phase diagrams, where the partition coefficient (k) is fixed at a given temperature during primary freezing, this is differently for ternary systems, since an added degree of freedom exists.

Regardless of this observation and given the range of compositions within $A2$ and μ phase observed in Figure 47, it can be clearly seen that an extended solubility of Al and Fe exists, and this significantly exceeds the boundaries of the solidus projection during primary freezing of $A2$.

For the eutectic morphology observed in S2 and S3, it can be noticed that while the initial $A2 + \mu$ is divorced, a distinct lamellar morphology is observed within μ phase remote from the primary dendrite lobes. At the end of primary $A2$ freezing, nucleation of μ phase will occur on the dendrite lobes and not within the bulk liquid.

During the eutectic freezing, there is growth of $A2$ and μ phases independently of each other, given as primary growth, $L \rightarrow A2$ and $L \rightarrow \mu$. However, if μ phase completely grows around the primary $A2$ solid, further eutectic growth necessarily requires nucleation of $A2$. This is the possible reason for the observance of lamellar morphology within μ phase in the inter-dendritic region. Furthermore, as the lamellar morphology is located in the middle of the inter-dendritic region, it is formed in the terminal stages of solidification.

A similar situation is observed for sample S4, where following the peritectic reaction a rim of σ phase forms around A2 and subsequently isolates A2 from the liquid, as shown in Figure 46(b). The following peritectic transformation involves solid-state diffusion through σ phase, which is restricted. This gives a primary growth of σ phase, $L \rightarrow \sigma$, where the liquid composition traverses the σ liquidus before intersecting the $\sigma - \mu$ eutectic valley and resulting in the eutectic reaction, $L \rightarrow \sigma + \mu$.

6.2. Nb-Al-Co system

Alloys with eight different compositions were prepared for the investigation of this system and its different reactions. The compositions are superimposed in the liquidus projection [Figure 50(a)] and solidus projections [Figure 50(b)], and the nominal compositions with expected and observed phases are listed in Table 12.

Table 12 - List of samples, elemental composition and observed phases in the microstructure of Nb-Al-Co samples.

Sample	Composition (at. %)			Observed Phases
	Nb	Co	Al	
S1	9.9	78.5	11.6	Co + C36 + CoAl
S2	10.0	68.4	21.6	Co + C36 + CoAl
S3	23.3	46.1	22.6	C14 + Co ₂ AlNb
S4	24.5	49.1	26.4	C14 + Co ₂ AlNb
S5	19.4	58.5	22.1	Co ₂ AlNb + C36 + CoAl
S6	15.0	58.5	26.5	Co ₂ AlNb + C36 + CoAl
S7	58.0	14.8	27.2	Nb ₂ Al + Co ₇ Nb ₆
S8	46.1	18.1	35.8	Co ₇ Nb ₆ + C14 + Nb ₂ Al

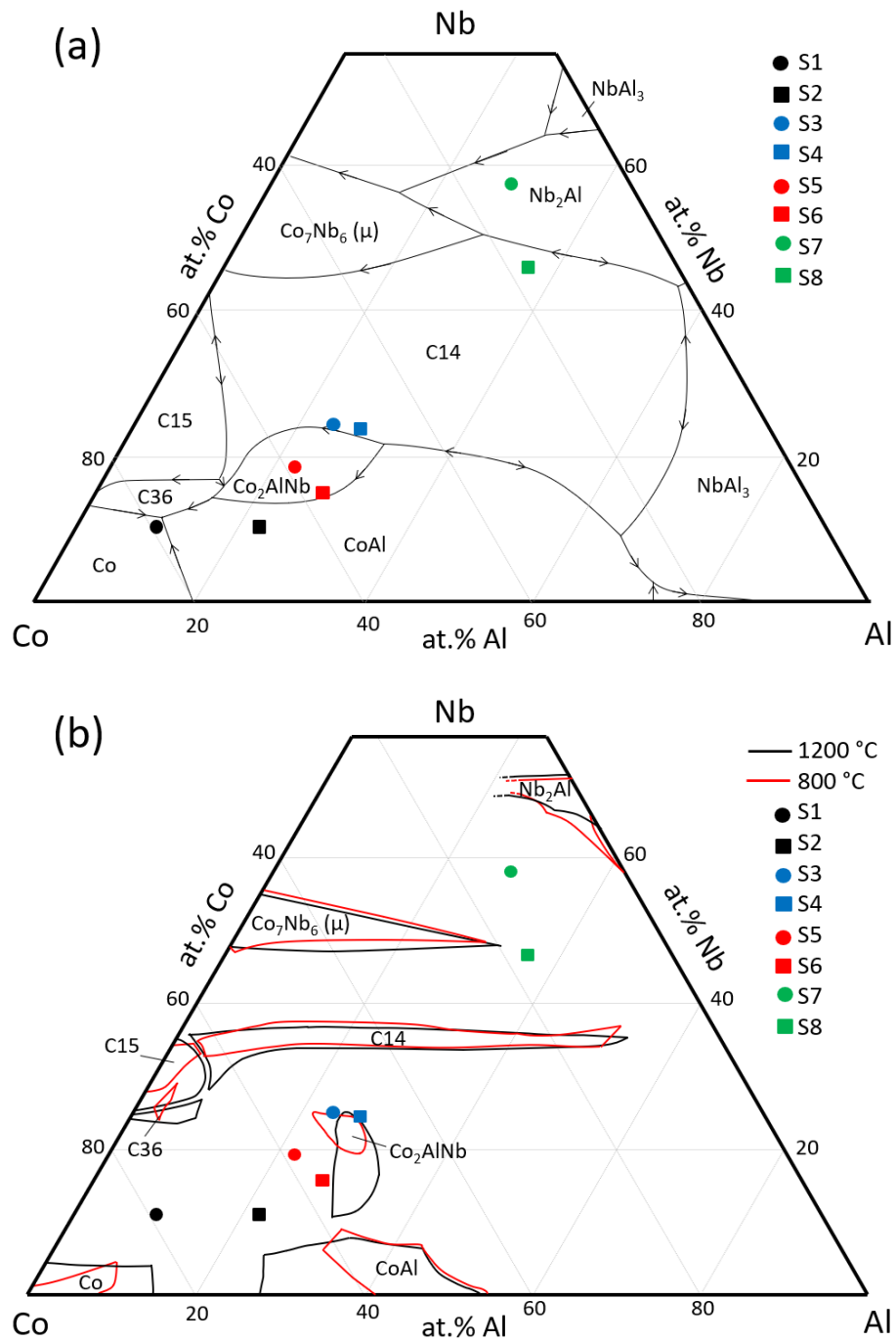


Figure 50 - (a) Liquidus projection [27], (b) Isothermal section at 1200°C with superimposed limits of solute solubility at 800°C [18].

6.2.1. Class I - Ternary eutectic reaction

Figure 51 presents a low and high magnification back-scattered electron images (BEI) corresponding to S1 and S2. For the case of sample S1, phases α -Co,

CoAl and C36 are expected in the as-cast microstructure. The composition of the constitute α -Co of primary dendrites (grey) is presented in Table 13.

The morphology of the eutectic (α -Co + C36) is of lamellar characteristic, which is indicating a cooperative growth, with C36 being the bright phase. The sporadic CoAl (dark) phase is formed as the ternary eutectic, as observed in the high magnification BEI in Figure 51(b). Owing to the scale of the microstructure and to prevent volume averaging [212], composition measurements were restricted to within α -Co phase.

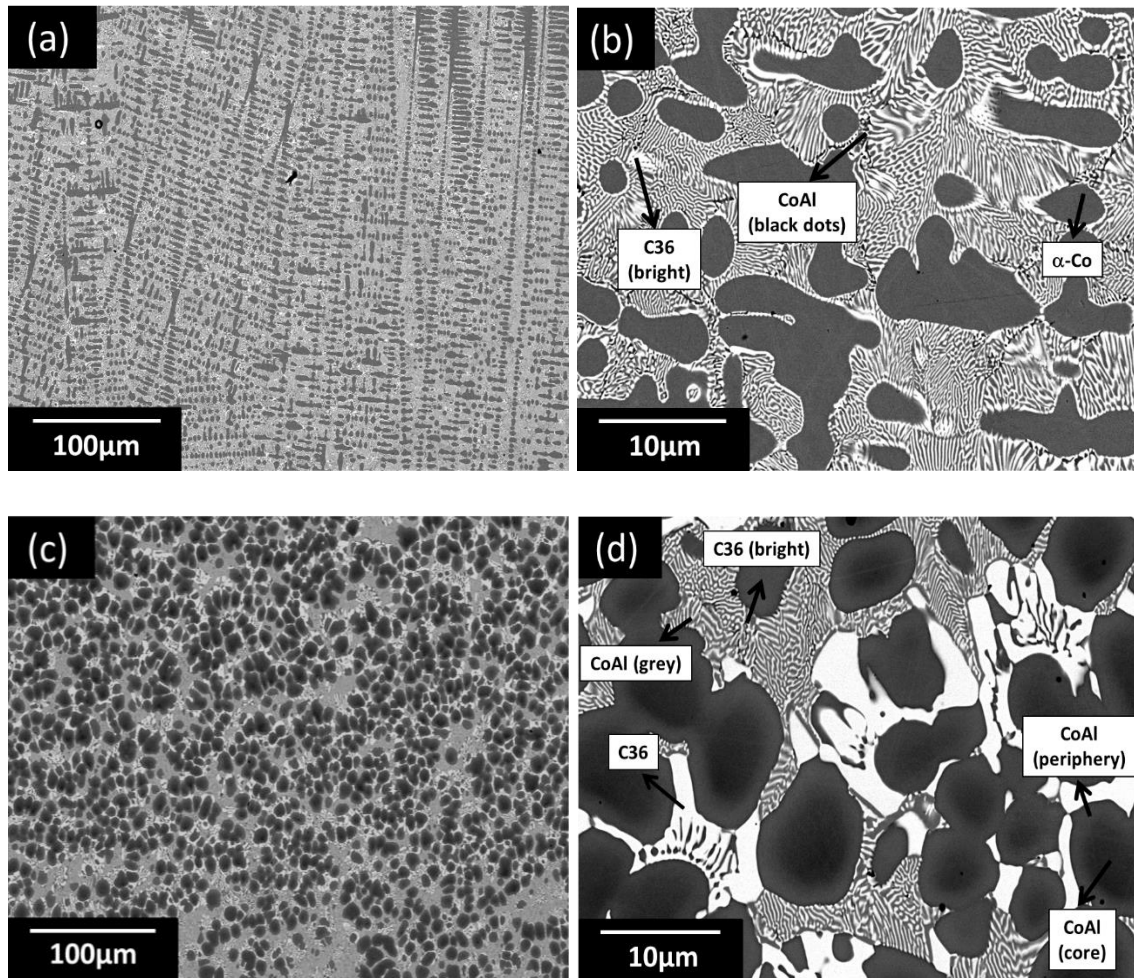


Figure 51 - BEI of microstructure corresponding to S1, (a) low and (b) high magnification; and to S2, (c) low and (d) high magnification.

Furthermore, in order to definitively confirm the presence of the ternary eutectic in S2 to justify the comparison to the tie-triangle, since it was not possible to ascertain whether α -Co forms as the ternary eutectic in S2, given the gradation

in contrast within CoAl in the BEI, X-ray diffraction was carried out to identify the phases in both S1 and S2.

The XRD patterns for S1 and S2 are presented in Figure 52, from which it can unequivocally be confirmed that α -Co does occur as a ternary eutectic in S2, like in the case of S1.

Table 13 - Average composition (in at.%) of phases present in S1 and S2.

Phase	%Al	%Co	%Nb
α -Co (S1)	12.9	83.1	4.1
CoAl (Dark core S2)	32.1	62.1	5.8
CoAl (Periphery S2)	27.0	67.0	6.0
C36 (Coarse cellular S2)	6.5	69.9	23.7

It is clear that, unlike in the case of the phase CoAl, there is a negligible micro-segregation within either α -Co or C36 phases. The measured compositions are plotted in the isothermal section at 1200°C in Figure 53 [94]. Also, given that changes in solute solubility can occur during cooling in the solid phase, an isothermal section at 800°C is also included in Figure 53 [94].

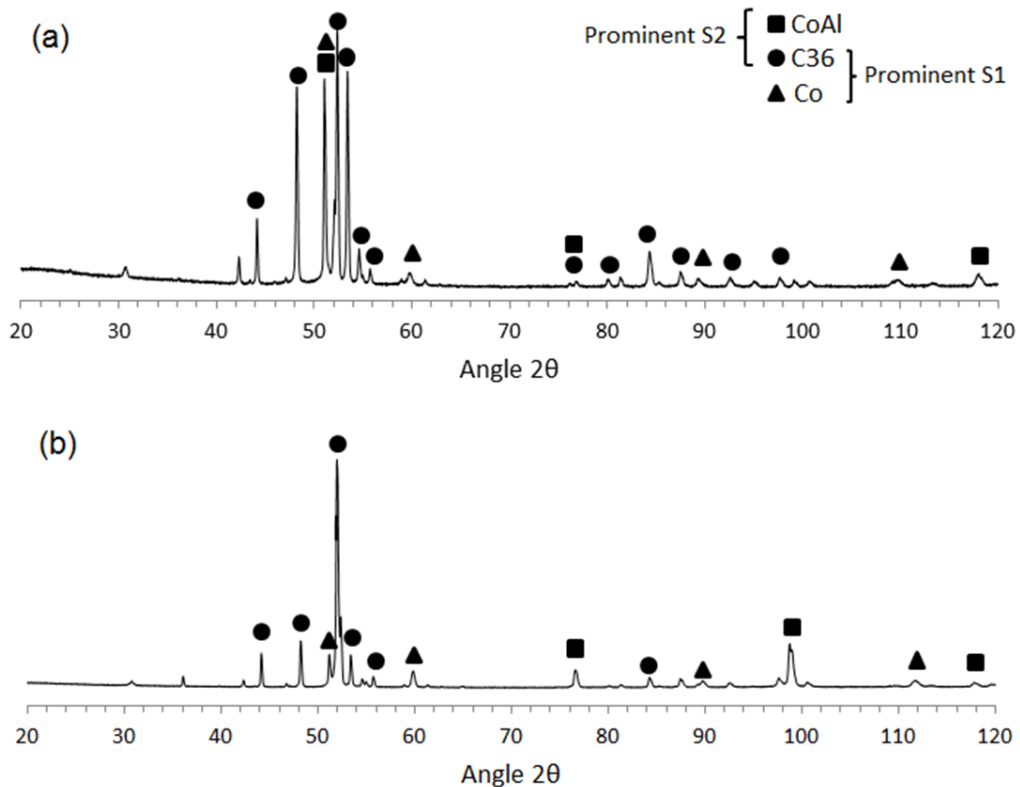


Figure 52 - X-ray diffraction patterns, (a) S1, (b) S2.

Both the α -Co and C36 measured compositions are in good agreement with the respective vertices in the tie-triangle in the isothermal section at 1200°C, but this is not so in the case of CoAl. Since this concerns the freezing path, it is important to consider isothermal sections that are close to where freezing would terminate, since isothermal sections constructed at lower temperatures correspond to fully heat-treated conditions where there can be appreciable changes in solute solubility. Therefore, in this case we merely compare our measured compositions with those represented by tie lines or tie triangles in the relevant isothermal sections.

Accordingly, for alloys S1 and S2, the isothermal section at 1200°C was used, while the isothermal section at 1250°C will be used for alloys S3 to S6, as these were higher melting alloys. While the Nb composition in both the dendrite core and periphery is similar to that in the isothermal section, the measured composition shows a higher Al (and lower Co) concentration. Further comparison with the isothermal section at 800°C shows that α -Co is super-saturated in Al. The absence of micro-segregation in primary α -Co also precludes micro-segregation during subsequent eutectic freezing, $L \rightarrow \alpha\text{-Co} + \text{C36}$. The solidus temperature for the ternary reaction is 1220°C [27].

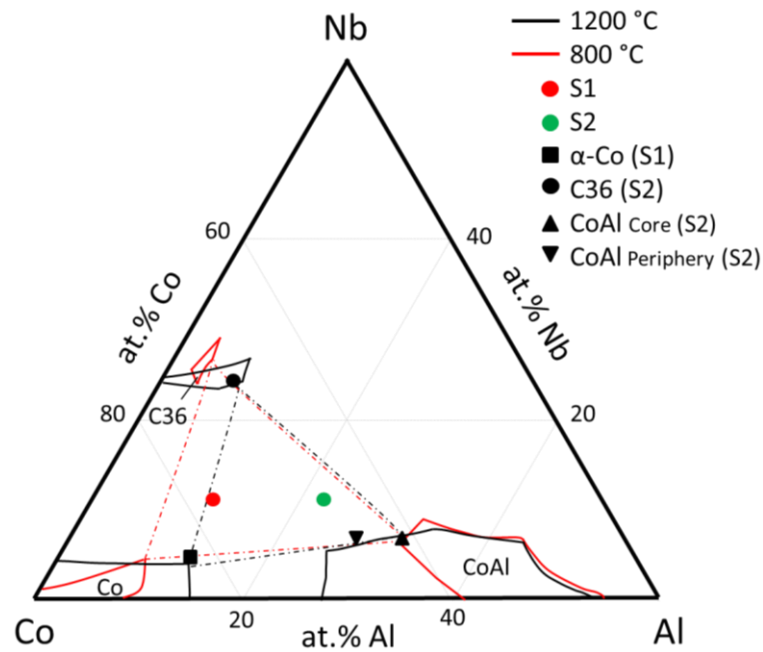


Figure 53 - Isothermal sections at 1200°C and 800°C, showing the phase boundaries in relation to the compositions in the different phases for S1 and S2 [18].

Since the measured composition within primary α -Co is also in good agreement with the corresponding vertex in the tie-triangle at 1200°C, it can therefore be concluded that this composition of α -Co also corresponds to that at the onset of freezing of the ternary eutectic. In the case of CoAl being the primary phase in S2 and where appreciable micro-segregation exists, the dendrite core composition is in good agreement with the vertex of the tie-triangle, while the dendrite periphery instead is super-saturated in Co (depleted in Al). The changing composition from dendrite core to periphery arises from coring (micro-segregation) during solidification and arising from limited solute solubility.

The absence of micro-segregation in primary α -Co also precludes micro-segregation during subsequent eutectic freezing, $L \rightarrow \alpha\text{-Co} + \text{C36}$. The solidus temperature for the ternary reaction lies between 1200 and 1250 °C [94]. Since the measured composition within primary α -Co is also in good agreement with the corresponding vertex in the tie-triangle in the isothermal section at 1200°C, it can therefore be concluded that the measured composition of α -Co corresponds to that at the onset of freezing of the ternary eutectic. Likewise, in the case of C36, where there exists a limited solid solute solubility, there should be a negligible composition gradient within this phase, as observed. Therefore, the composition of C36 within the coarse cellular eutectic also corresponds to that at the onset of the ternary eutectic reaction. This then determines two of the vertices of the tie-triangle.

The extent of the ternary eutectic is very limited [Figure 51(b)] and therefore terminal freezing occurs over a narrow temperature range. In this case, the liquid and solid compositions traverse the metastable liquidus and solidus lines below the invariant temperature. Freezing of the terminal eutectic can occur either as, $L \rightarrow \alpha\text{-Co} + \text{CoAl}$ or $L \rightarrow \text{C36} + \text{CoAl}$ (if α -Co is the primary phase – S1) or $L \rightarrow \text{CoAl} + \alpha\text{-Co}$ or $L \rightarrow \text{C36} + \alpha\text{-Co}$ (if CoAl is the primary phase – S2) and depends on which phase the ternary phases nucleates on. From the microstructure, it is difficult to determine which of the cases is likely. Following from the preceding arguments, it is clear that the ternary eutectic cannot freeze at a single temperature, albeit it will freeze over a narrow temperature range, as a three-phase reaction.

6.2.2. Class II - Quasi-Peritectic reaction

The images presented in Figure 54 correspond to BEI's from S3 and S4 respectively. In both cases primary freezing constitutes C14 and the measured compositions are presented in Table 14.

There is negligible micro-segregation observed within the primary C14 phase. In S3, there is very sporadic existence of the second phase and solidification is dominated by primary freezing. The terminal liquid is then consumed by the peritectic reaction, $L + C14 \rightarrow Co_2AlNb$ with compositions given in Table 14.

Table 14 - Average composition (in at.%) of phases present in S3 and S4.

Phases	%Al	%Co	%Nb
C14 (S3)	22.3 ± 0.61	44.4 ± 0.92	33.3 ± 0.31
C14 (S4)	25.3 ± 0.23	43.1 ± 0.26	31.6 ± 0.06
Co ₂ AlNb (S3)	26.1 ± 0.76	51.4 ± 0.93	22.5 ± 0.43
Co ₂ AlNb (S4)	27.8 ± 0.35	51.1 ± 0.25	21.1 ± 0.45

On the other hand, in the case of S4 in Figure 54(b), Co₂AlNb exists as two distinct morphologies, which is exemplified in Figure 54(c). The composition of the primary C14 phase and the coarse Co₂AlNb morphology have been measured and reported in Table 14. The fine acicular morphology of Co₂AlNb precludes composition measurement owing to volume averaging effects.

The tie-line joining the compositions corresponding to C14 and Co₂AlNb is represented in Figure 55(a) referring to the isothermal sections at 1250°C and 800°C [94]. In both cases it is clearly shown that the compositions in the two phases do not lie at the boundary of their respective single-phase regions at 1250°C. This indicates negligible diffusion in the solid during subsequent cooling to lower temperatures.

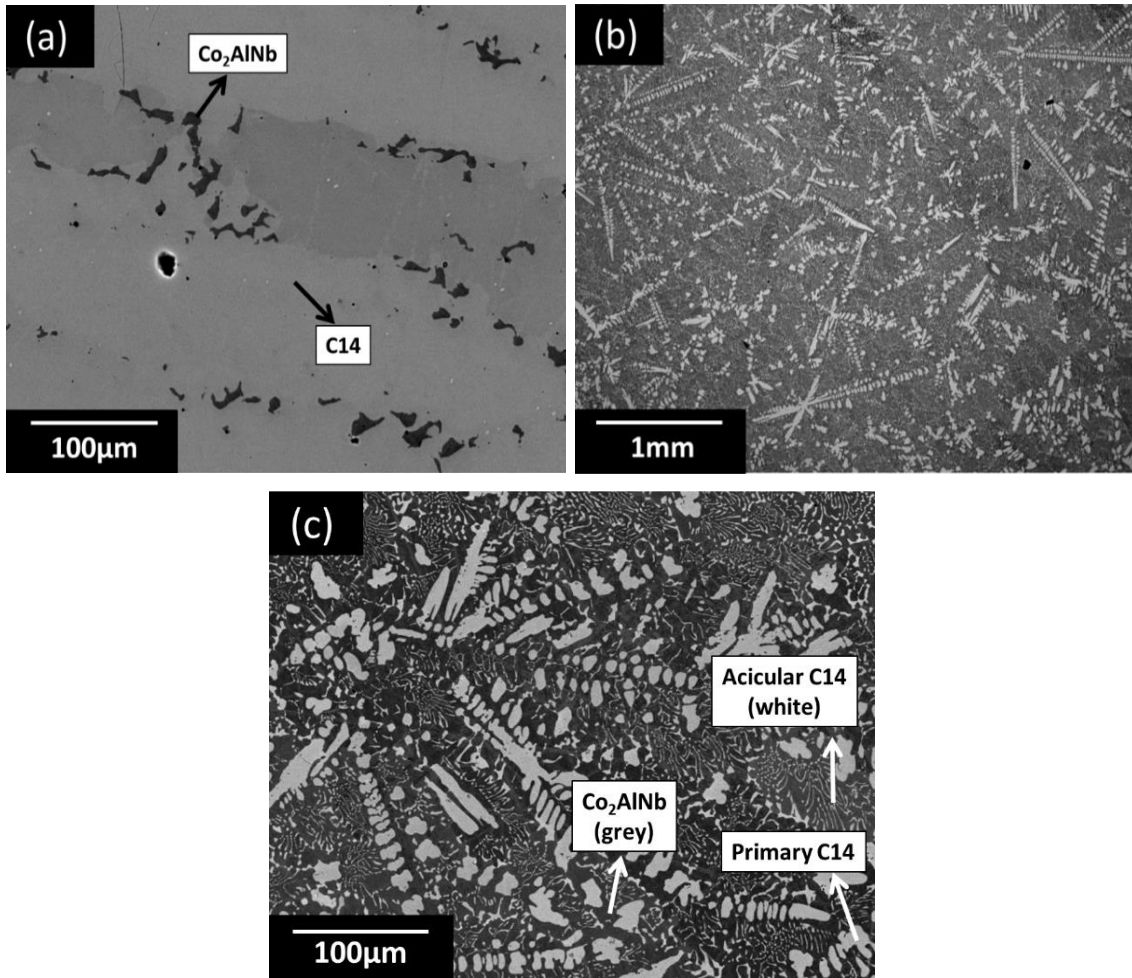
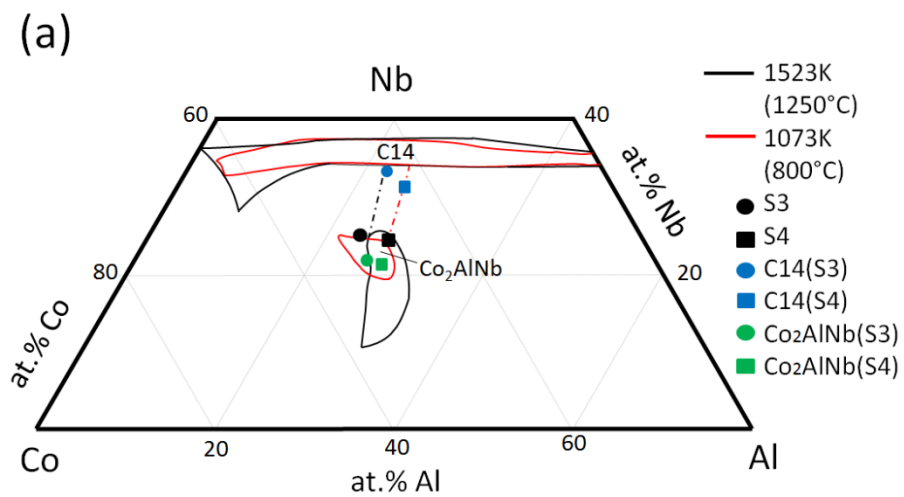


Figure 54 - (a) BEI for S3, (b) low magnification BEI for S4, (c) high magnification BEI for S4.



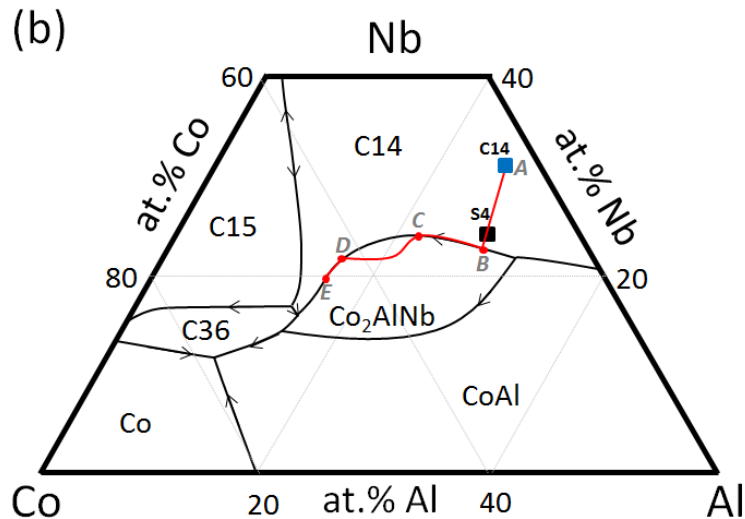


Figure 55 – (a) Isothermal sections at 1250°C and 800°C, showing the phase boundaries in relation to the compositions in the different phases for S3 and S4 [18]; (b) Liquidus projection illustrating path traversed by the liquid composition during freezing in S4 [27].

In case of S3 and S4, initial primary freezing of C14 is followed by the peritectic reaction, $L + C14 \rightarrow Co_2AlNb$. Since the peritectic transformation that follows the peritectic reaction never goes to conclusion, the liquid composition leaves the peritectic valley and traverses the Co_2AlNb liquidus surface and in S3 freezing terminates through primary solidification of Co_2AlNb [23, 31].

In case of S4, a similar situation is encountered, but with a difference. The peritectically formed Co_2AlNb phase is labelled “grey” in Figure 54(c), like in the case of S3. However, if all the liquid has not been consumed during primary freezing of Co_2AlNb (governed by back-diffusion in the solid), the liquid composition will re-intersect the C14 – Co_2AlNb valley. However, the C14 – Co_2AlNb valley in the liquidus projection changes from peritectic to eutectic with decreasing temperature, i.e. for Al < 20 at. % and Nb < 20 at. %, the valley is eutectic in nature [27].

Consequently, the re-intersection of the liquid composition with the C14 – Co_2AlNb valley results in the eutectic reaction, $L \rightarrow C14 + Co_2AlNb$. The path traversed by the liquid composition during freezing of S4 is schematically illustrated in the liquidus projection in Figure 55(b). Here, AB refers to primary freezing of C14, BC corresponds to the peritectic reaction and incomplete peritectic transformation, CD refers to primary freezing of Co_2AlNb and DE represents the terminal eutectic reaction, when all liquid is consumed at E.

Since the peritectically formed Co_2AlNb has isolated the prior C14 primary phase from the liquid, the eutectic reaction requires re-nucleation of C14, but this will occur on Co_2AlNb . It is this “re-nucleated” C14 phase growing as the (C14 + Co_2AlNb) eutectic that exhibits the acicular-type morphology. A similar phenomenon has also been observed in the Fe-Al-Nb ternary system, where following primary freezing of Nb and followed by the peritectic reaction, $\text{L} + \text{Nb} \rightarrow \text{Nb}_2\text{Al}$, the class II reaction, $\text{L} + \text{Nb}_2\text{Al} \rightarrow \text{Nb} + \mu$ requires nucleation of both these phases on Nb_2Al [26].

Figure 56 shows the microstructure for S5 and S6. In S6, there is also the existence of C36 (bright) and CoAl (dark) and the measured composition in these phases are given in Table 15.

The compositions are included in the isothermal section at 1250°C and 800°C , in Figure 57, from which it can be observed that good agreement is obtained in the case of Co_2AlNb with some deviation in C36 (4 % higher Co) with respect to the vertices of the tie-triangle.

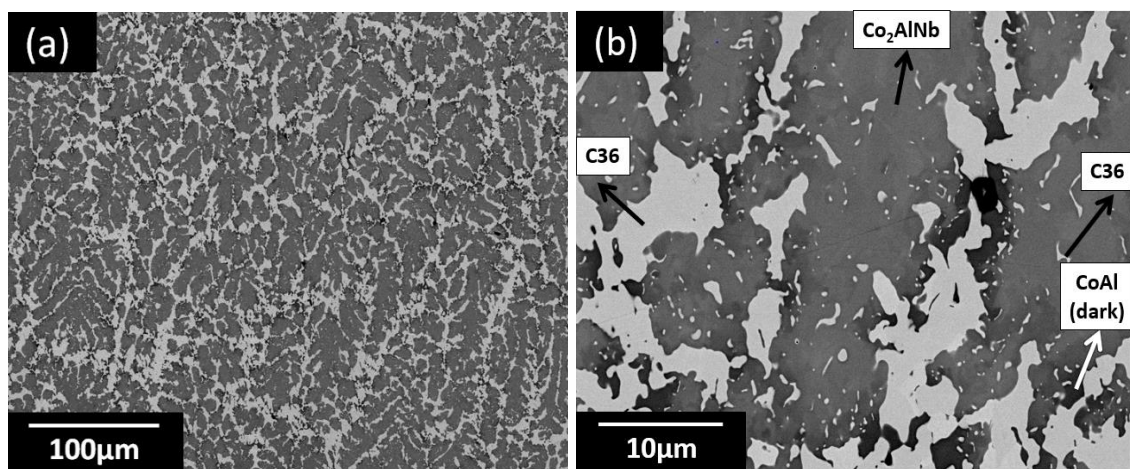
Table 15 - Average composition (in at.%) of phases present in S5 and S6.

Phases	%Al	%Co	%Nb
Co_2AlNb (S5)	27.4 ± 0.10	52.5 ± 0.13	20.1 ± 0.17
Co_2AlNb (S6)	30.8 ± 0.36	54.3 ± 0.10	14.9 ± 0.36
C36 (S5)	9.9 ± 0.44	64.3 ± 0.62	25.8 ± 0.22
C36 (S6)	6.9 ± 0.21	69.3 ± 0.24	23.8 ± 0.41
CoAl (S5)	27.9 ± 1.38	64.0 ± 2.48	8.2 ± 1.10
CoAl (S6)	27.7 ± 0.75	65.0 ± 1.65	7.4 ± 0.94

However, significant deviation exists in the case of CoAl. This is not unexpected, since micro-segregation is observed within CoAl. The line joining the composition of Co_2AlNb and the nominal composition in S6 intersects the Co_2AlNb - C36 eutectic valley. Therefore, primary freezing will be followed by the eutectic reaction, $\text{L} \rightarrow \text{Co}_2\text{AlNb} + \text{C36}$. Beyond the invariant temperature, CoAl must nucleate, and it can be observed that CoAl nucleates on the Co_2AlNb dendrite lobes [Figure 56(b)]. The growth of the (C36 + CoAl) eutectic occurs with a divorced morphology and corresponding to, $\text{L} \rightarrow \text{C36} + \text{CoAl}$.

However, in the case of S5 a distinctly different microstructure is observed. There is evidence of precipitation of C36 within the primary Co_2AlNb phase and the (C36 + CoAl) morphology is markedly different to that observed in S6. The measured compositions are also plotted in Figure 57. From the isothermal section at 1250°C it is clear that the Class II reaction is not expected to occur, since the nominal composition falls outside the tie-triangle. A lower concentration of Nb in Co_2AlNb is required for the Class II reaction to occur, as is the case of S6. Therefore, it follows that CoAl precipitates through a solid-state reaction. The composition of Co_2AlNb lies on the boundary of the single-phase region, however there is the distinct super-saturation of Al in C36 at 1250°C and more so at 800°C .

From the isothermal section at 1250°C it appears that freezing should terminate with the $\text{L} \rightarrow \text{Co}_2\text{AlNb} + \text{C36}$ eutectic reaction. However, it is clear that within primary Co_2AlNb , there is precipitation of C36 in the solid-state, which constitutes the flaky morphology in the primary phase [Figure 56(b)]. This conclusion is further corroborated by the fact that the straight line joining the Co_2AlNb composition and the nominal composition in the isothermal section at 1250°C does not intersect the $\text{Co}_2\text{AlNb} - \text{C36}$ eutectic valley, as would have been required for the eutectic reaction. Such a construction would have intersected the $\text{Co}_2\text{AlNb} - \text{C36}$ eutectic valley, had the Al super-saturated $[\text{Co}_2\text{AlNb}]_{\text{ss}}$ composition been used instead. This therefore clearly indicates solid-state precipitation of C36 within Co_2AlNb via the reaction, $[\text{Co}_2\text{AlNb}]_{\text{ss}} \rightarrow \text{Co}_2\text{AlNb} + \text{C36}$.



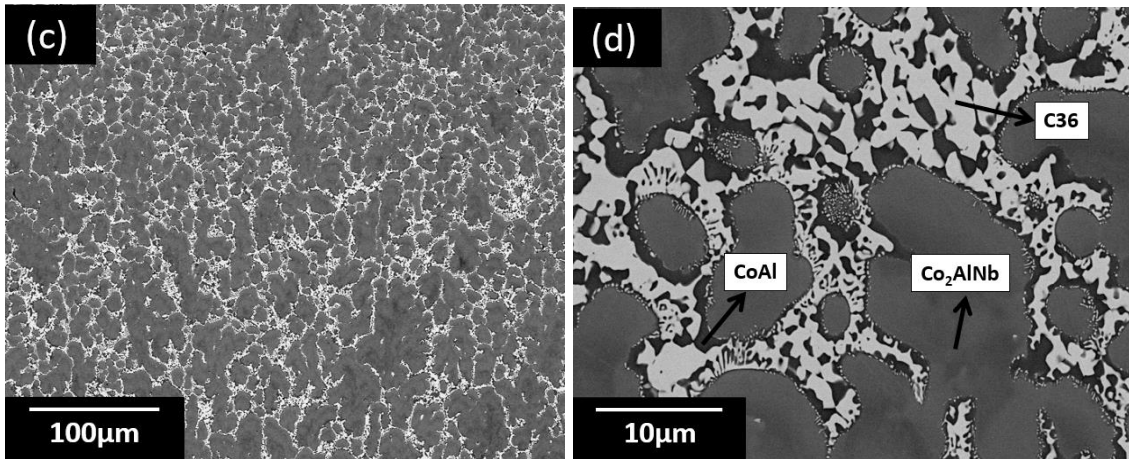


Figure 56 - (a) low magnification BEI for S5, (b) low magnification BEI for S6, (c) high magnification BEI for S5, (d) high magnification BEI for S6.

The microstructure in the primary phase therefore constitutes to Co_2AlNb + C36 and the measured composition of the primary phase is not $[\text{Co}_2\text{AlNb}]_{\text{ss}}$. Additionally, CoAl is also present in the microstructure. From the isothermal section at 800°C it is clear that C36 is super-saturated in Al and therefore resulting in the solid precipitation of CoAl via, $[\text{C36}]_{\text{ss}} \rightarrow \text{C36} + \text{CoAl}$. The solid-state precipitation of CoAl within C36 clearly accounts for the difference between the microstructures in S5 and S6, where in the latter CoAl forms as a divorced eutectic with C36 through a eutectic reaction.

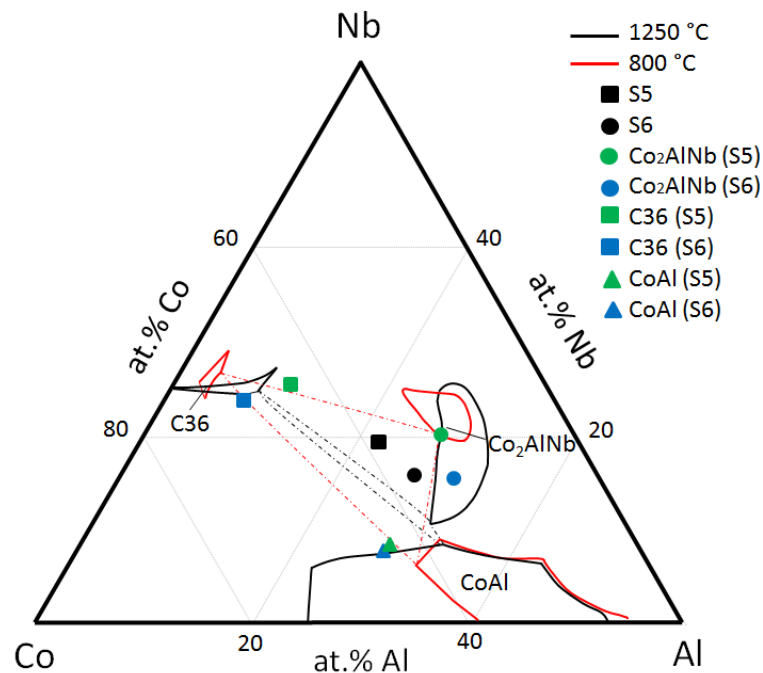


Figure 57 - Isothermal sections at 1250°C and 800°C [18], showing the phase boundaries in relation to the compositions in the different phases for S5 and S6.

6.2.3. Class III - Peritectic reaction

Figure 58(a) and Figure 58(b) are low and high magnification BEI images that corresponding to S7. Primary freezing initiates with Nb₂Al and followed by the eutectic reaction, $L \rightarrow \text{Nb}_2\text{Al} + \text{Co}_7\text{Nb}_6$. The eutectic forms with a divorced morphology. The measured compositions for the two phases are presented in Table 16.

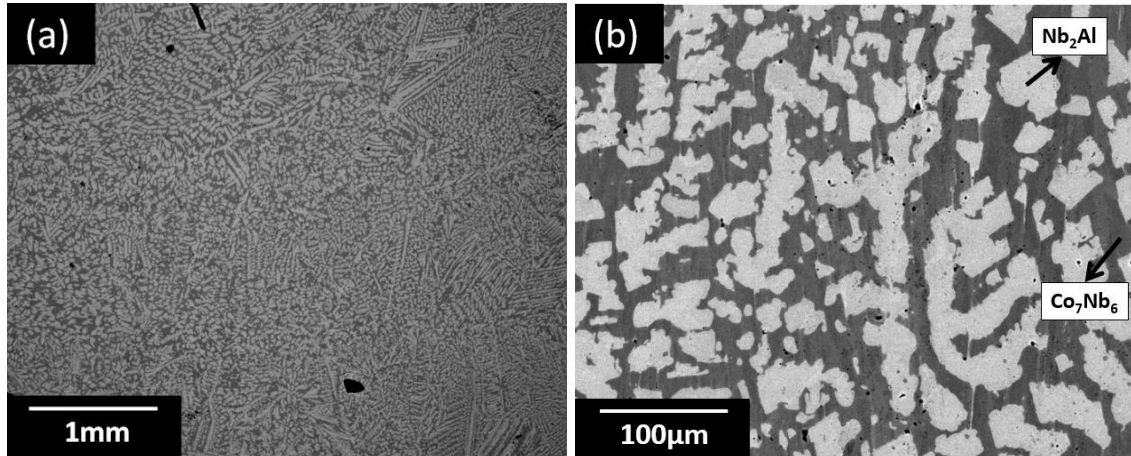


Figure 58 - (a) low magnification BEI for S7, (b) high magnification BEI for S7.

The tie-line showing the measured compositions is represented in the isothermal sections at 1250°C and 800°C, presented in Figure 60, and in both cases the composition of the two phases lie on their phase boundaries.

Table 16 - Average composition (in at.%) of phases present in S7.

Phases	%Al	%Co	%Nb
Nb ₂ Al	26.7 ± 0.34	6.30 ± 0.30	67.2 ± 0.61
Co ₇ Nb ₆	28.5 ± 0.70	23.3 ± 0.70	48.2 ± 0

Figure 59(a) and Figure 59(b) are low and high magnification BEI images that corresponding to S8, where C14, Nb₂Al and Co₇Nb₆ are the expected phases in the as-cast microstructure. The primary phase is C14, with the lath-type morphology, while the eutectic reaction, $L \rightarrow \text{C14} + \text{Nb}_2\text{Al}$ shows the fine lamellar morphology that transition to the coarse cellular type. The Class III reaction, $L + \text{C14} \rightarrow \text{Nb}_2\text{Al} + \text{Co}_7\text{Nb}_6$ occurs. The measured phase compositions are given in Table 17.

Table 17 - Average composition (in at.%) of phases present in S8.

Phases	%Al	%Co	%Nb
C14	41.8 ± 0.46	23.1 ± 0.21	35.4 ± 0.17
Nb ₂ Al	29.2 ± 0.45	6.7 ± 0.51	64.2 ± 0.20
Co ₇ Nb ₆	32.1 ± 0.31	21.1 ± 0.29	46.9 ± 0.25

The tie-triangle with respect to the measured compositions is plotted in the isothermal sections at 1250°C and 800°C, in Figure 60. While there is good agreement with the for C14 and Co₇Nb₆ compositions with the vertices of the tie-triangle at 1250°C, the Nb₂Al composition is lower in Nb content and lies outside the single-phase region. This cannot be accounted for by change in solubility during cooling; since a similar situation is observed in the isothermal sections at 800°C. The composition of Nb₂Al differs from that reported in [94].

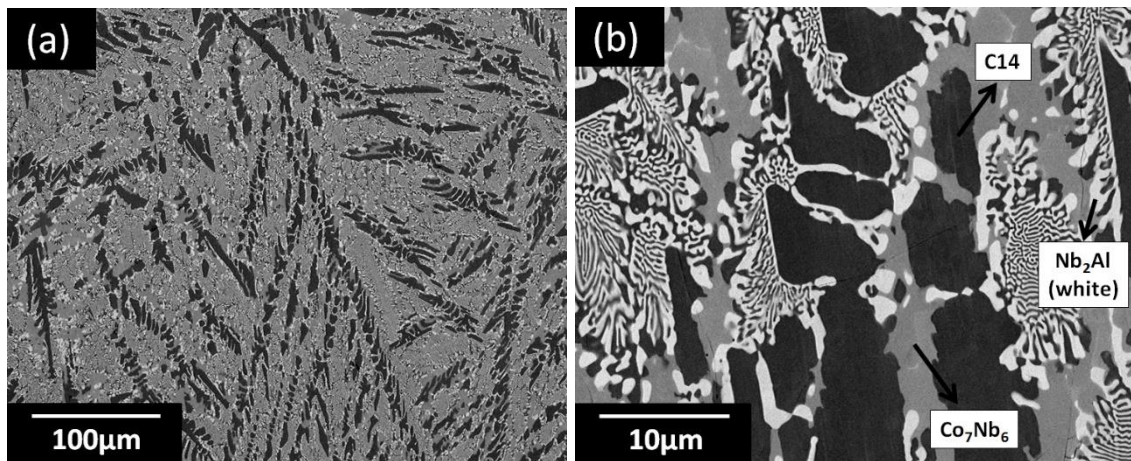


Figure 59 - (a) low magnification BEI for S8, (b) high magnification BEI for S8.

Following from the preceding discussion, below the invariant temperature Co₇Nb₆ arises from either a eutectic reaction, $L \rightarrow \text{Nb}_2\text{Al} + \text{Co}_7\text{Nb}_6$ or peritectic reaction, $L + \text{C14} \rightarrow \text{Co}_7\text{Nb}_6$. There is no evidence that Co₇Nb₆ grows with a eutectic morphology in the channels between the (C14 + Nb₂Al) eutectic below the invariant point [Figure 59(b)]. While (Co₇Nb₆ + Nb₂Al) does show a divorced eutectic morphology [Figure 58(b)], the morphology of Co₇Nb₆ in S8 below the invariant point is more akin to primary growth. This implies that following the eutectic reaction, $L \rightarrow \text{C14} + \text{Nb}_2\text{Al}$, nucleation of Co₇Nb₆ occurs, but it is not clear if nucleation occurs on existing C14 or Nb₂Al phases. However,

solidification will proceed as, $L + C14 \rightarrow Co_7Nb_6$ (peritectic reaction) and terminating in primary growth, $L \rightarrow Co_7Nb_6$, when all liquid has been consumed.

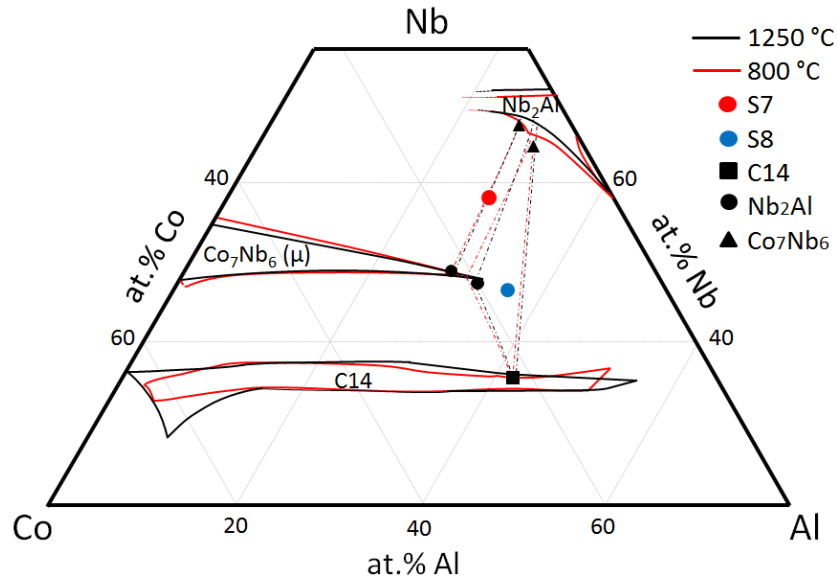


Figure 60 - Isothermal sections at 1250°C and 800°C, showing the phase boundaries in relation to the compositions in the different phases for S7 and S8 [18].

6.3. Nb-Al-Fe system

The nominal composition of the alloys studied and the expected phases according with the diagrams and the actual phases observed is presented in Table 18.

Table 18 - Nominal measured compositions of the alloys studied (in at. %) and phases expected according to liquidus projection.

Sample ID	Composition			Phases observed
	Nb	Al	Fe	
S1	51.8	19.3	28.9	$\mu + Nb_2Al$
S2	35.6	25.9	38.5	$C14 + \mu$
S3	40.8	53.2	6.0	$Nb_2Al + C14 + NbAl_3$
S4	34.0	61.8	4.2	$NbAl_3 + C14 + Nb_2Al$
S5	75.5	17.7	6.8	$(Nb) + Nb_2Al + \mu$
S6	60.1	19.5	20.4	$(Nb) + Nb_2Al + \mu$
S7	37.1	33.4	29.5	$C14 + Nb_2Al + \mu$
S8	39.1	29.9	31.0	$C14 + Nb_2Al + \mu$

The nominal compositions are then plotted in the liquidus projection and isothermal sections at 1300°C and 1000°C, as seen in Figure 61, in order to evaluate the solidification path and phases expected during freezing under equilibrium conditions, and to observe how solubility of the phase regions change with decreasing temperature.

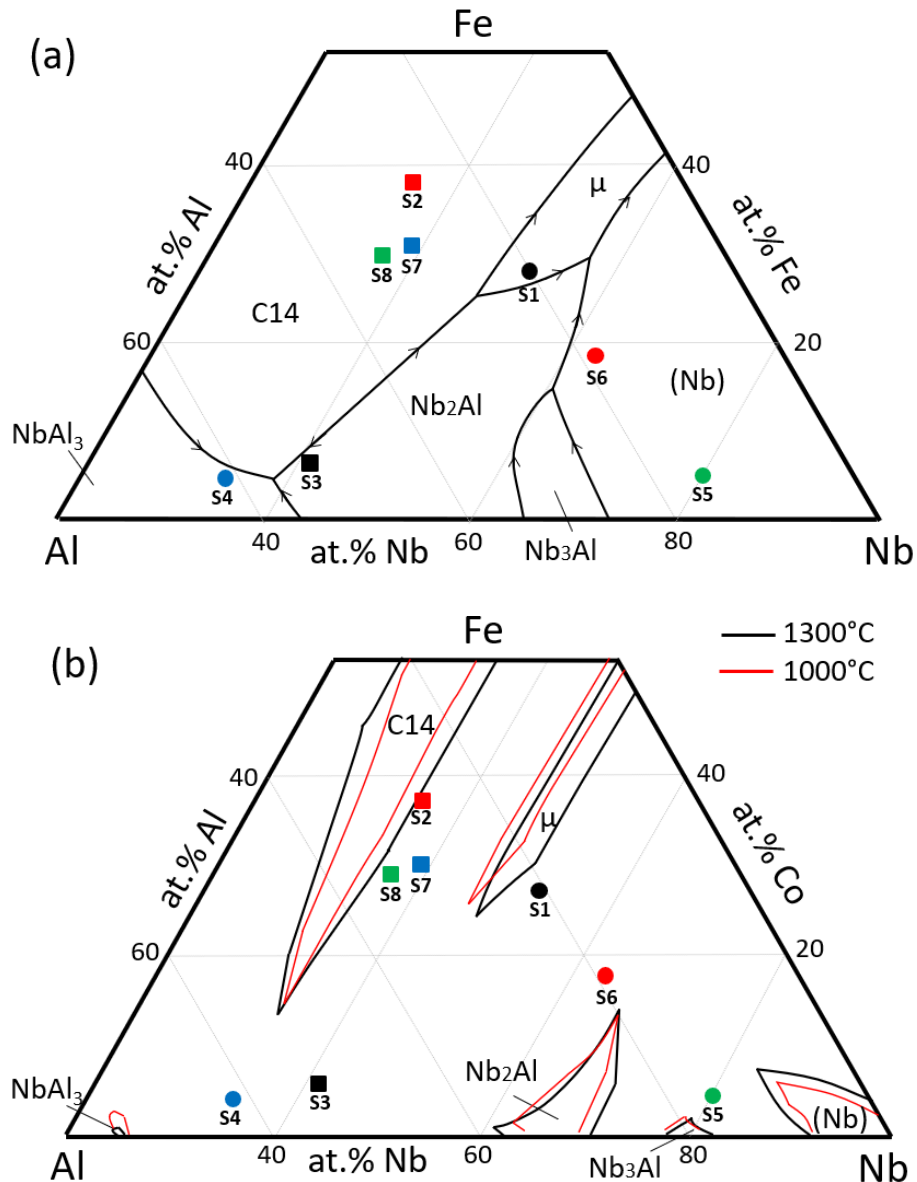


Figure 61 - (a) Liquidus projection, (b) Isothermal section at 1300°C with superimposed limits of solute solubility at 1000°C [26]. The compositions in this study are superimposed in the figures.

6.3.1. Three-phase reaction

Figure 62(a) is a low magnification back-scattered image (BEI) of S1, and in accordance to the liquidus projection in Figure 61(a), the expected phases in the as-cast microstructure are $(\text{Fe,Al})_7\text{Nb}_6$ (also called μ phase), Nb_2Al , and if all the liquid has not yet been consumed, the solid solution (Nb) phase is formed, which was not observed for this case. The compositions of the phases are presented in Table 19. The high magnification BEI, in Figure 62(b), shows a microstructure comprising of the primary dark phase μ dendrites, which are surrounded by the bright Nb_2Al phase, formed eutectically in a divorced morphology with the primary phase. A visible fine connection through the dark dendrites is seen with the presence of Nb_2Al fine stripes.

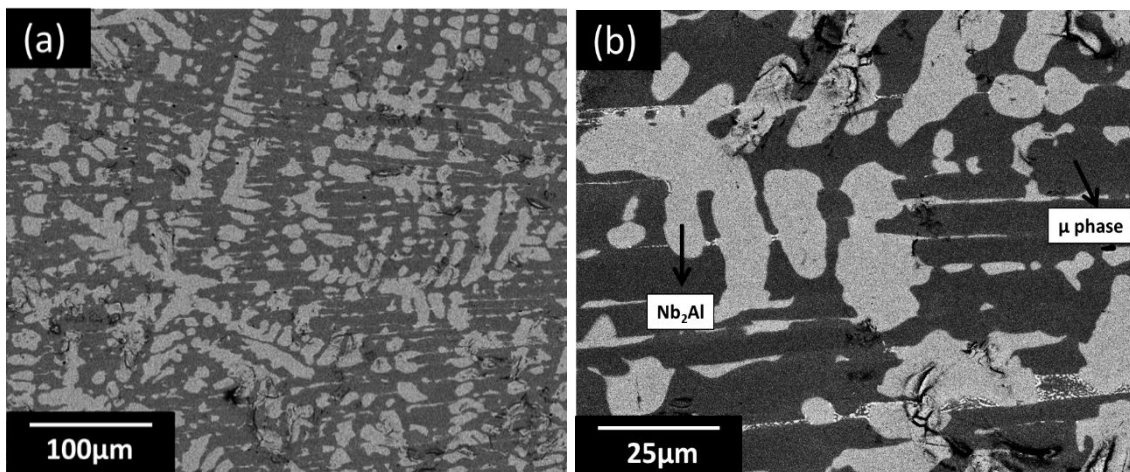


Figure 62 - BEI of microstructure corresponding to S1, (a) low magnification, (b) high magnification.

Figure 63 is a low magnification of S2, which presents a higher amount of Al, and the dark primary phase is $\text{Nb}(\text{Fe,Al})_2$ (C14 Laves phase), and similarly to S1, a second phase, bright μ is formed though peritectically, ending the solidification without the formation of the solid solution (Nb) phase. It can be seen sporadic formations of small circular μ phases within the primary dendrite. The composition of phases measured by EDS is presented in Table 19.

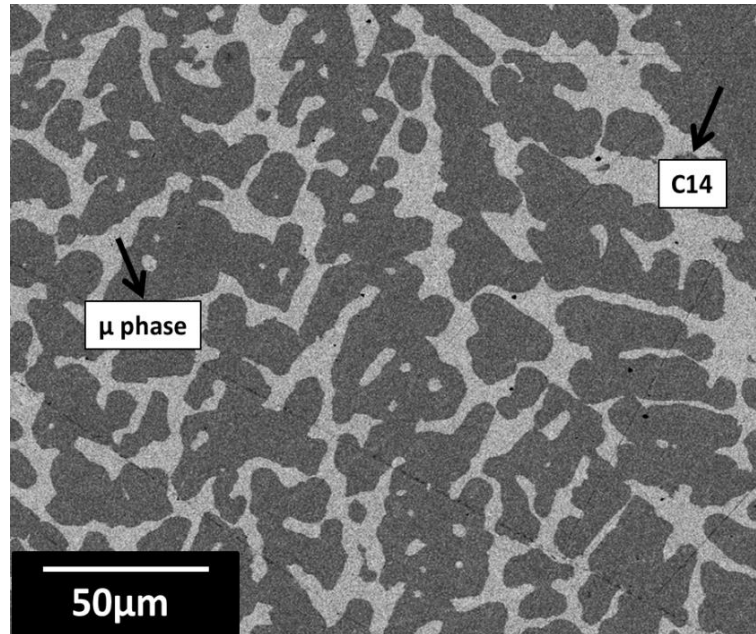


Figure 63 - BEI of microstructure corresponding to S2.

The compositions measured are plotted in the isothermal section at 1000°C and 1300°C, presented in Figure 64, with the section at 1000°C superimposed, in order to show the changes in solubility with further cooling. There is negligible micro-segregation observed in both alloys, and while C14 is in good agreement with the phase boundary in the diagram, both Nb₂Al and μ phases are supersaturated in Fe.

Table 19 - Average measured composition (in at.%) of phases present in S1 and S2.

Phase		Composition		
		Nb	Al	Fe
S1	μ	44.5	19.7	35.8
	Nb ₂ Al	63.7	21.7	14.6
S2	μ	43.3	23.1	33.6
	C14	32.1	27.8	40.1

The formation of Nb₂Al phase in S1 is given by the eutectic $L \rightarrow \text{Nb}_2\text{Al} + \mu$. By drawing a line joining the composition of the primary phase and the nominal composition of S1, it can be seen that such line hits the Nb₂Al - μ valley, which forms the fine acicular pattern of Nb₂Al in the inter-dendritic region.

Similarly, sample S2 presents a fine circular formation of μ phase within the primary C14 Laves phase through the peritectic reaction $L + C14 \rightarrow \mu$. This is confirmed by the fact that when drawing a line joining C14 composition with the nominal composition of S2 it hits the peritectic valley C14 - μ , and here, due to limited diffusion through the solid phase, μ solidifies via primary freezing, $L \rightarrow \mu$, forming the small circular phases indicating a very limited formation.

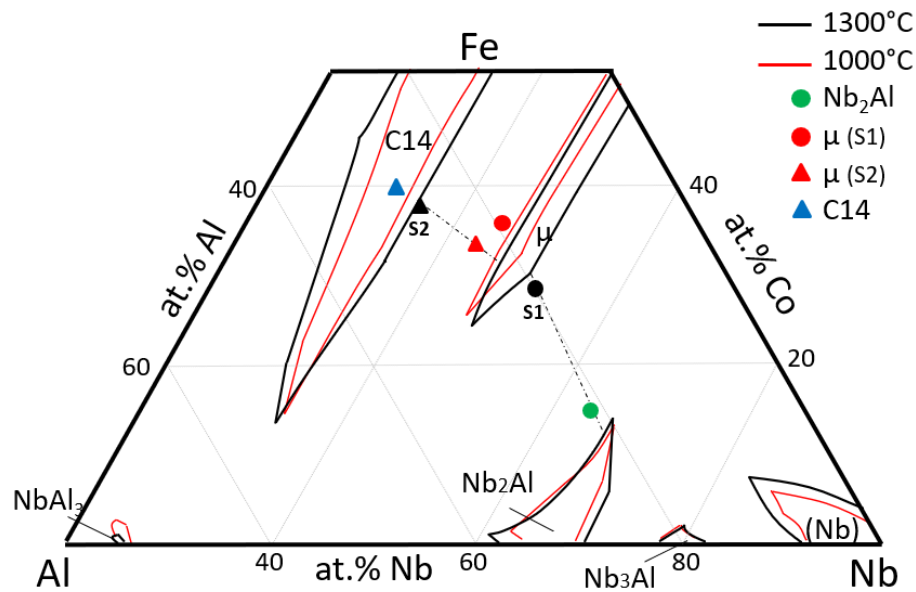


Figure 64 - Isothermal sections at 1300°C and superimposed solute solubility at 1000°C, showing the phase boundaries in relation to the compositions in the different phases for S1 and S2. Dotted lines show tie-lines from [26].

6.3.2. Class I – Ternary eutectic reaction

Figure 65(a) shows a low magnification BEI of sample S3, which presents a white Nb_2Al phase as primary in a dendritic-like morphology. The expected phases in the as-cast microstructure following the primary are C14 and $NbAl_3$ phases, which are indeed observed for this alloy. Figure 65(b) shows a detailed high magnification BEI of S3, where it is observed a formation of a very fine ternary eutectic across the inter-dendritic region, and a cellular two-phase eutectic within the primary phase. Table 20 shows the phase compositions for this alloy, at specific spots so to be possible to measure and to prevent volume averaging.

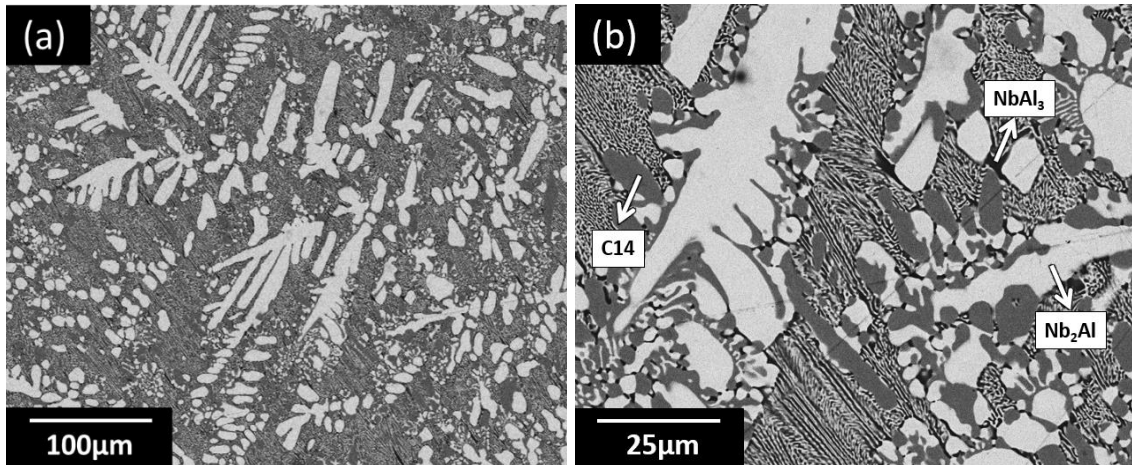


Figure 65 - BEI of microstructure corresponding to S3, (a) low magnification, (b) high magnification.

Table 20 - Average composition (in at.%) of phases present in S3.

Phases	Composition		
	Nb	Al	Fe
C14	31.4	53.5	15.1
Nb ₂ Al	53.8	44.4	1.8
NbAl ₃	28.3	69.8	1.9

The measured and the nominal compositions for S3 and S4 are plotted in the isothermal section at 1000°C and 1300°C in Figure 66. The nominal composition falls very close to the eutectic valley Nb₂Al – C14, and such reaction is observed to occur following the primary freezing of Nb₂Al, $L \rightarrow Nb_2Al + C14$. The formation of a grey C14 phase in cooperation with Nb₂Al occurs within the primary dendrites of Nb₂Al, forming at a larger extension when compared with that of the primary freezing, due to the proximity of the S3 composition with the valley.

Following the formation of the two-phase eutectic, the remaining liquid traverse to the invariant point where the Class I ternary eutectic reaction takes place at the last stage of the solidification, $L \rightarrow Nb_2Al + C14 + NbAl_3$, forming a very fine pattern and consuming the remaining liquid.

While the nominal composition of S3 is in good agreement with the tie-triangle superimposed in Figure 66, the composition of NbAl₃ is super-saturated in Nb, and phase Nb₂Al is rich in Al. This solute enrichment is markedly larger at 1000°C.

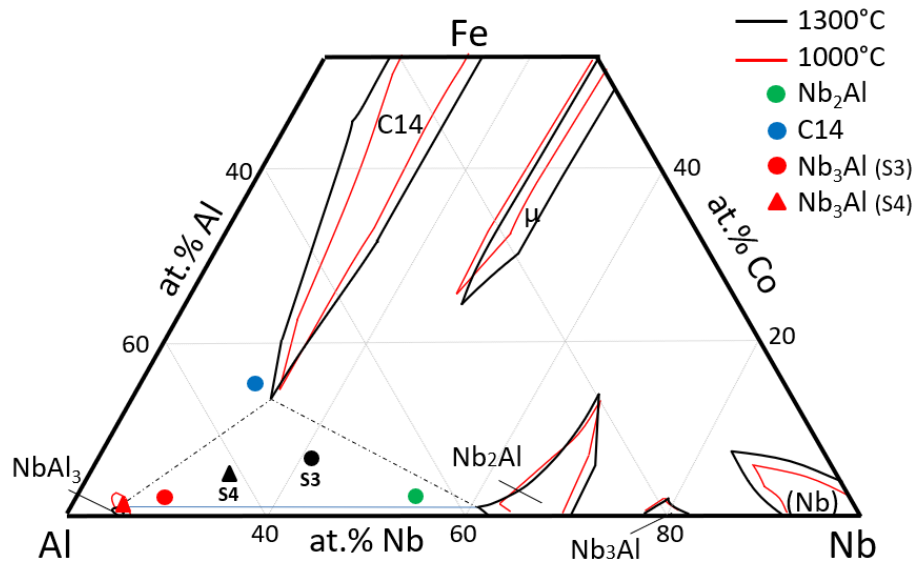


Figure 66 - Isothermal sections at 1300°C and superimposed solute solubility at 1000°C, showing the phase boundaries in relation to the compositions in the different phases for S3 and S4. Dotted lines show tie-lines from [26].

Figure 67(a) and Figure 67(b) present a low and high magnification BEI, respectively, of S4, in which the NbAl_3 phase appears as a dark primary phase in a dendritic-like pattern, followed by a very fine and extended ternary eutectic structure, which is in accordance to the liquidus projection [Figure 61(a)], since the as-cast microstructure should therefore present the $\text{NbAl}_3 + \text{C14} + \text{Nb}_2\text{Al}$ Class I eutectic reaction when freezing terminates.

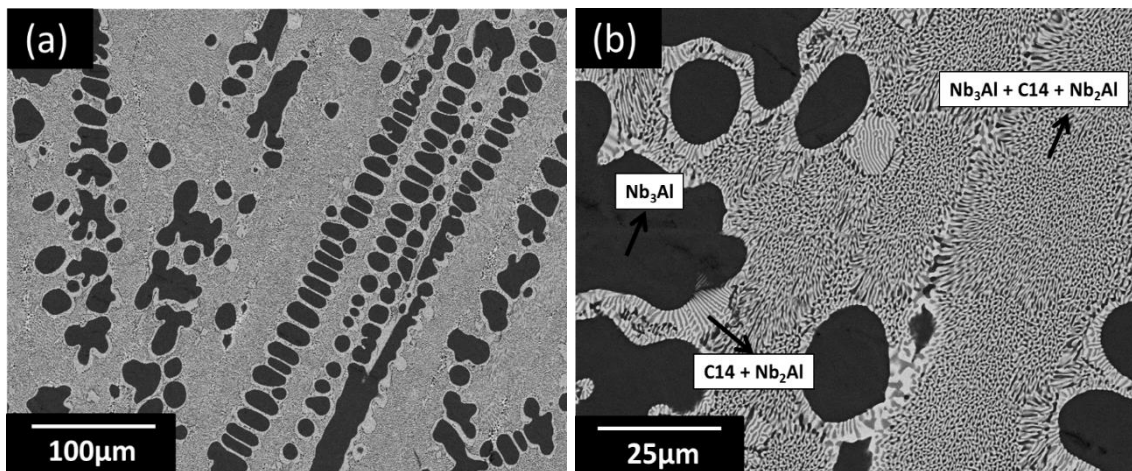


Figure 67 - BEI of microstructure corresponding to S4, (a) low magnification, (b) high magnification.

The measurement of phase compositions (in at.%) was only taken for the primary NbAl_3 phase (Nb = 24.7; Al = 74.7; Fe = 0.6), due to volume averaging of the fine

eutectic strips, which is plotted with the nominal composition in the isothermal sections at 1000°C and 1300°C (Figure 66).

Following primary freezing of NbAl₃, the liquid surface is expected to traverse the eutectic valley of NbAl₃ – C14 phases, before proceeding to the Class I eutectic reaction. A line joining the primary phase composition and the nominal composition of S4 would confirm this affirmation. Although, the detailed microstructure in Figure 67(b) shows no evidence of such eutectic, and instead the remaining liquid undergoes the eutectic formation of phases C14 and Nb₂Al, through the eutectic reaction $L \rightarrow C14 + Nb_2Al$, prior to the occurrence of the Class I reaction, $L \rightarrow NbAl_3 + C14 + Nb_2Al$, and a halo of the binary eutectic Nb₂Al + C14 is formed surrounding the primary globes of NbAl₃, indicating non-equilibrium solidification sequence. This was evidenced by Stein et al. [26] in Al-rich alloys, and accordingly, the NbAl₃ phase should be present in the mixture, either as Nb₂Al + NbAl₃ or C14 + NbAl₃, and according to his evidences, this is related to nucleation failure in the undercooled liquid. A high magnification BEI shown in Figure 68 presents the ternary eutectic formation in detail.

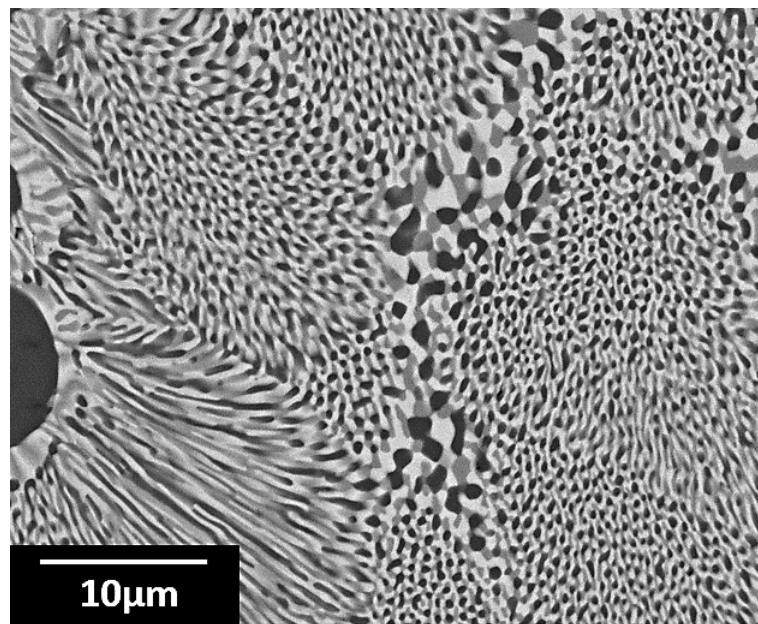


Figure 68 - High magnification image of S4 showing in detail the ternary eutectic formation.

The formation of a halo around the primary phase has been studied for binary alloys, such as Cr-Nb, Fe-Nb and Ni-Nb [57, 81-84], which can be then extended for the ternary system case. Models of halo formation have been proposed in several recent studies [59, 83, 213], following the occurrence of haloes in off-

eutectic binary alloy solidification. Li et al. [82] calculated a coupled growth temperature zone, using the TMK [214] and BCT thermodynamic models [215] to predict this phenomenon, and found that hypoperitectic Cr-Nb alloys, which were out of the couple growth zone, formed haloes of Cr_2Nb around primary Cr dendrites, at high cooling rates. These suggestions raise the following remarks;

- (a) The formation of the eutectic structure requires nucleation, given that not both phases for the binary case, or three phases for the ternary systems precipitate simultaneously, and therefore one phase needs to lead the eutectic growth;
- (b) When the undercooling in the liquid is not large enough for the growth of the eutectic to occur, the secondary or ternary phase can take the place of the leading phase and nucleate on the primary phase to continue the eutectic formation thereafter.

Extending this analysis for the ternary case, it follows that a deviation of equilibrium sequence occurs when the primary phase serves as nucleant for the $\text{C14} + \text{Nb}_2\text{Al}$ eutectic, before forming the ternary eutectic.

Therefore, for the halo formation to occur, both remarks (a) and (b) should also apply for the case of S4. Based on that, and since NbAl_3 phase is absent from the two-phase eutectic halo, the following aspects have to be fulfilled;

- The absence of NbAl_3 phase from the eutectic halo suggests that NbAl_3 is the leading phase during the formation of the eutectic $\text{NbAl}_3 + \text{C14}$;
- The re-nucleation of NbAl_3 requires a larger undercooling than that provided during the solidification, and therefore C14 phase is the first phase to be nucleated from the liquid on the surface of the primary phase;
- Given the non-equilibrium nature of the solidification, C14 leads the formation of a binary eutectic with Nb_2Al , deviating from the equilibrium sequence predicted, and the liquid then traverses the $\text{C14} - \text{Nb}_2\text{Al}$ valley;
- The NbAl_3 phase can then re-nucleate on either C14 or Nb_2Al phases to following the halo to undergo the Class I reaction, terminating the freezing.

The nominal composition of S4 falls close to the invariant point where the Class I reaction takes place. Therefore, the extension of the non-equilibrium eutectic is very limited, before the required undercooling is achieved for NbAl_3 to be re-nucleated and to lead the ternary eutectic reaction.

6.3.3. Class II – Quasi-Peritectic reaction

Figure 69(a) shows the low magnification BEI of S5, which shows a large portion of dendrites of the primary white solid solution phase (Nb). The detailed microstructure in Figure 69(b) shows the formation of a grey phase Nb₂Al forming a rim across the dendrites, characteristic of a peritectic formation, and a dark phase μ forming within Nb₂Al phase when freezing terminates. The data in Table 21 presents the composition of phases measured by EDS.

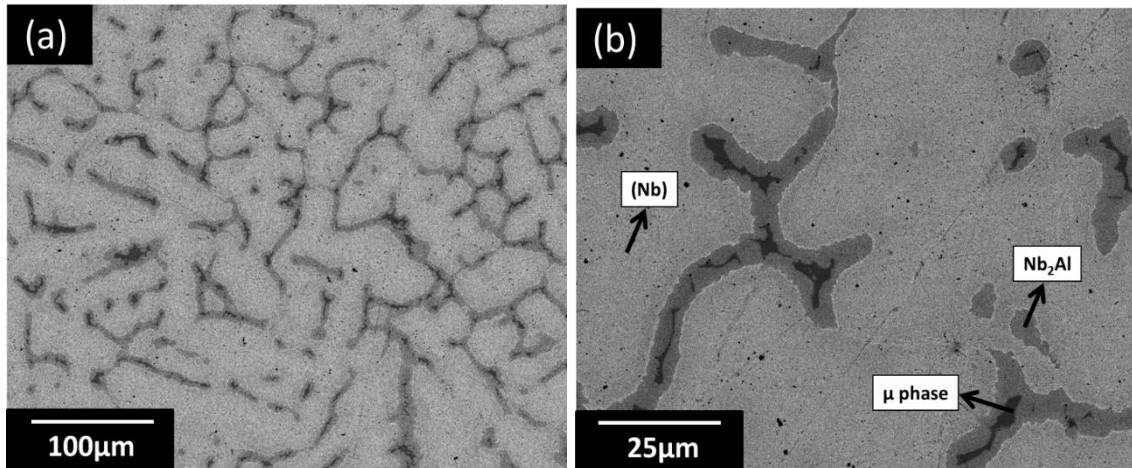


Figure 69 - BEI of microstructure corresponding to S5, (a) low magnification, (b) high magnification.

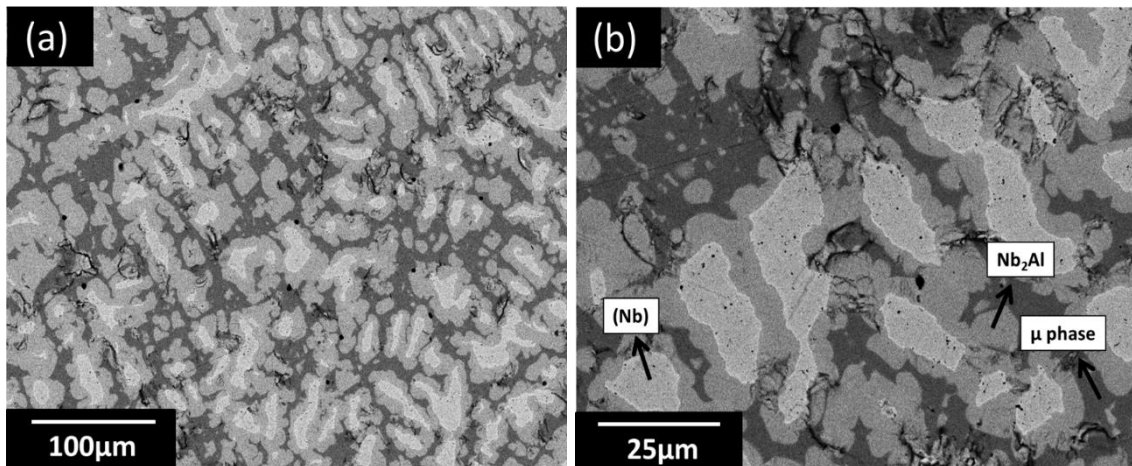


Figure 70 - BEI of microstructure corresponding to S6, (a) low magnification, (b) high magnification.

Figure 70(a) and Figure 70(b) show the low and high magnification images of S6, respectively, in which shows a different aspect from that observed for sample S5, even though the primary phase is still the solid solution (Nb). The formation of a

grey peritectic Nb₂Al forms a rim that surrounds the white primary dendrites of (Nb) phase, and solidification terminates with formation of a dark μ across the peritectic cells. The composition measured is also presented in Table 21.

The phases present in both samples S5 and S6 are expected to present the (Nb) primary phase, according to the liquidus projection presented in Figure 61(a). The compositions measured are plotted in the isothermal section at 1000°C and 1300°C, showed in Figure 71.

Table 21 - Average composition (in at.%) of phases present in S5 and S6.

Phase		Composition		
		Nb	Al	Fe
S5	(Nb)	81.6	15.0	3.4
	Nb ₂ Al	65.4	24.3	10.3
	μ	44.5	22.5	33.0
S6	(Nb)	76.9	14.9	8.2
	Nb ₂ Al	64.2	22.5	13.3
	μ	44.8	20.1	35.1

In S5, the line joining the nominal composition and the composition of the primary (Nb) phase hits the (Nb) – Nb₂Al peritectic valley, which is then confirmed by the formation of the rim across the dendrite as commented, where there is consumption of (Nb) to produce Nb₂Al through the peritectic reaction, $L + (Nb) \rightarrow Nb_2Al$. When the liquid has still not been completely consumed, the liquid surface traverse then the peritectic reaction line and undergoes the Class II quasi-peritectic reaction in which forms μ phase, $L + Nb_2Al \rightarrow (Nb) + \mu$. Due to limited diffusion in the solid, the formation of the eutectic (Nb) + μ is very limited, and μ phase forms mainly from primary freezing $L \rightarrow \mu$.

The composition of S5 falls markedly outside the tie-triangle joining the boundaries of the three expected phases, which indicates that the Class II reaction is not expected to occur at any rate. The composition of (Nb) is significantly rich in Al solute, and this is due to the non-equilibrium solidification observed. The reduced temperature of the isothermal section at 1000°C shows an even more extended solubility of Al in the primary (Nb) phase.

The microstructure of sample S6 shows the formation of the primary (Nb) in an amount much lower than that observed in S5, and this is due to the composition, richer in Fe and Al, falling in the boundary of region of the peritectic valley, $L + (\text{Nb}) \rightarrow \text{Nb}_2\text{Al}$ which occurs in a large extent. Similarly to sample S5, the plot of compositions shows an extensive solubility of Al in the primary phase (Nb). This is markedly higher when superimposed in the isothermal at 1000°C, with solubility limits increasing up to 10 at.%. For both alloys, there is a minor deviation of the single-phase composition boundaries, shifting towards higher Al and Fe concentrations. Reasonable agreement however is observed for Nb_2Al and μ phases.

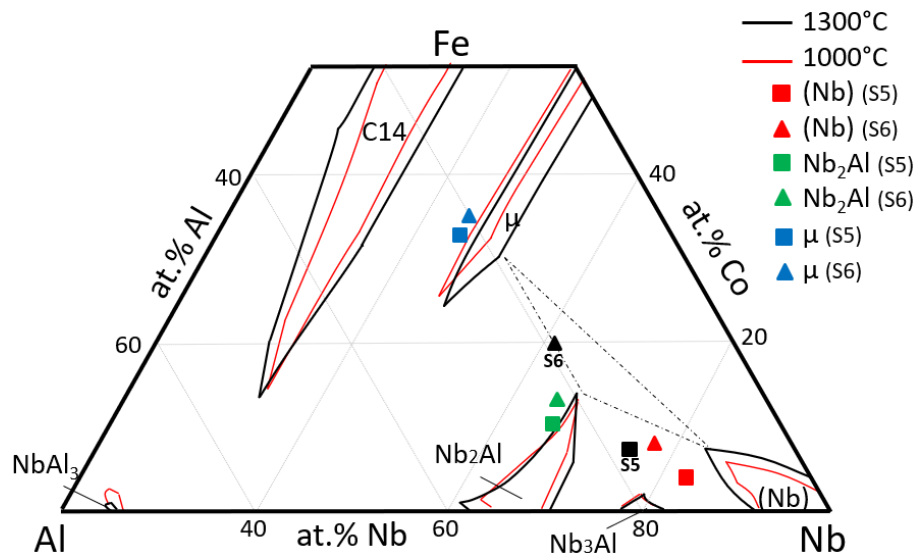


Figure 71 - Isothermal sections at 1300°C and superimposed solute solubility at 1000°C, showing the phase boundaries in relation to the compositions in the different phases for S5 and S6. Dotted lines show tie-lines from [26].

The observance of solute trapping of Al can occur if the formation of (Nb) phase in the subsequent Class II reaction, $L + \text{Nb}_2\text{Al} \rightarrow (\text{Nb}) + \mu$ is suppressed. The Nb and Fe-rich liquid then traverse a metastable solidus reaction, following the formation of the μ phase through the eutectic reaction, $L \rightarrow \text{Nb}_2\text{Al} + \mu$, when the liquid approach the eutectic $\text{Nb}_2\text{Al} - \mu$ valley following the peritectic reaction, instead of terminating at the Class II three-phase reaction as it is expected under equilibrium conditions. From these observations, two points can be considered;

- (a) Under non-equilibrium cooling, there is a shift towards higher Al concentration for the (Nb) solid phase region in the isothermal section and in the tie-triangle;
- (b) The extent of the Class II quasi-peritectic reaction only occurs in a very narrow composition window, and rarely goes to completion under rapid cooling due to limited diffusion in the solid.

Similar behaviour was observed for Ta-rich Ta-Al-Fe ternary alloys [5], where A2 phase is the primary phase and the extended solubility of Ta provoked the suppression of the expected peritectic reaction, $L + A2 \rightarrow \sigma$, and primary freezing is followed by the eutectic reaction, $L \rightarrow A2 + \mu$, shifting the eutectic and peritectic valleys towards “north-west”.

6.3.4. Class III – Ternary Peritectic reaction

Figure 72 shows the microstructure for S7 and S8, in low and high magnification, where C14, Nb₂Al and μ are the expected and observed phases. For both alloys, the primary dark C14 phase presents a dendritic-like morphology, followed by the formation of the eutectic reaction, $L \rightarrow Nb_2Al + C14$ in the inter-dendritic region. Formation of μ occurs through the Class III ternary peritectic reaction, $L + Nb_2Al + C14 \rightarrow \mu$. The measured phase compositions are given in Table 22.

The phase compositions are plotted in the isothermal sections at 1000°C and 1300°C, as observed in Figure 73. While good agreement was observed for C14 and μ , the composition of Nb₂Al is markedly super-saturated in Al solute and lies outside the single phase region, and differs from previous reports [67, 216].

Table 22 - Average composition (in at.%) of phases present in S7 and S8.

Phases		Composition		
		Nb	Al	Fe
S7	Nb ₂ Al	60.9	28.1	11.0
	μ	43.2	27.0	28.8
	C14	32.3	35.4	32.3
S8	Nb ₂ Al	61.7	27.6	10.7
	μ	43.4	28.2	28.4
	C14	32.8	32.6	34.6

For the alloy S7, the primary formation of C14 is followed by the formation of a very fine lamellar eutectic of C14 + Nb₂Al surrounding the primary dendrites. The line joining the nominal composition and the composition of C14 approaches the eutectic valley in the liquidus projection [Figure 61(a)], which is formed in a large extent through the liquid surface. The small portion of liquid remaining traverses then the ternary eutectic point, where the Class III reaction occurs. At this point, the formation of μ requires the consumption of both C14 and Nb₂Al phases, which is very limited due to low diffusion kinetics, forming through the stripes of the eutectic lamellae across the primary dendrites.

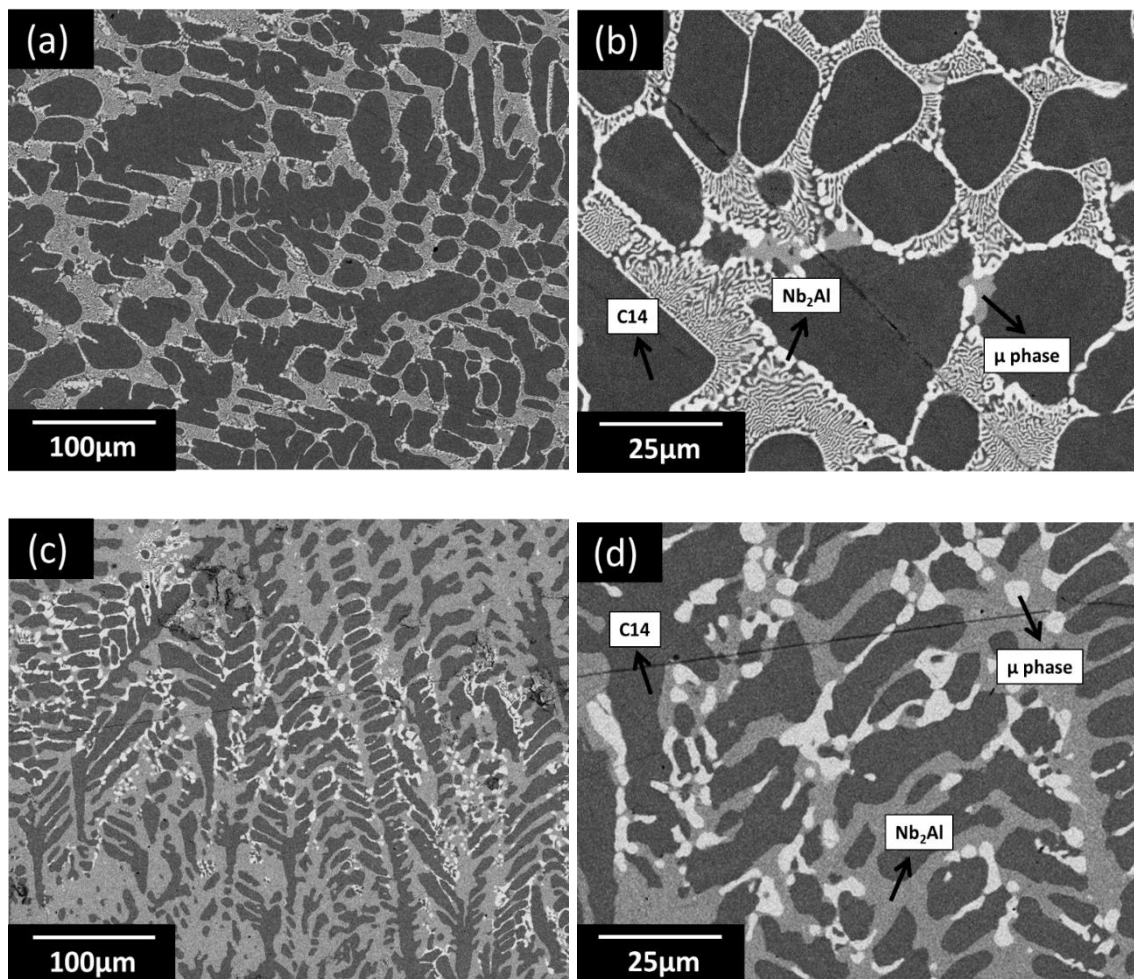


Figure 72 - BEI of microstructure corresponding to S7, (a) low magnification, (c) high magnification; and S8, (b) low magnification, (d) high magnification.

The nominal compositions for S7 and S8 and the measured composition of their respective phases are plotted in the isothermal section observed in Figure 73.

Following similar approach as discussed in previous studies [5], the formation of μ below the invariant temperature occurs from either a two-phase peritectic reaction, $L + C14 \rightarrow \mu$, or a eutectic reaction, $L \rightarrow C14 + \mu$. From Figure 72(a) and Figure 72(c) it is not evidenced a eutectic morphology, which confirms the assumption of a peritectic formation, terminating in primary growth $L \rightarrow \mu$, consuming the remaining liquid.

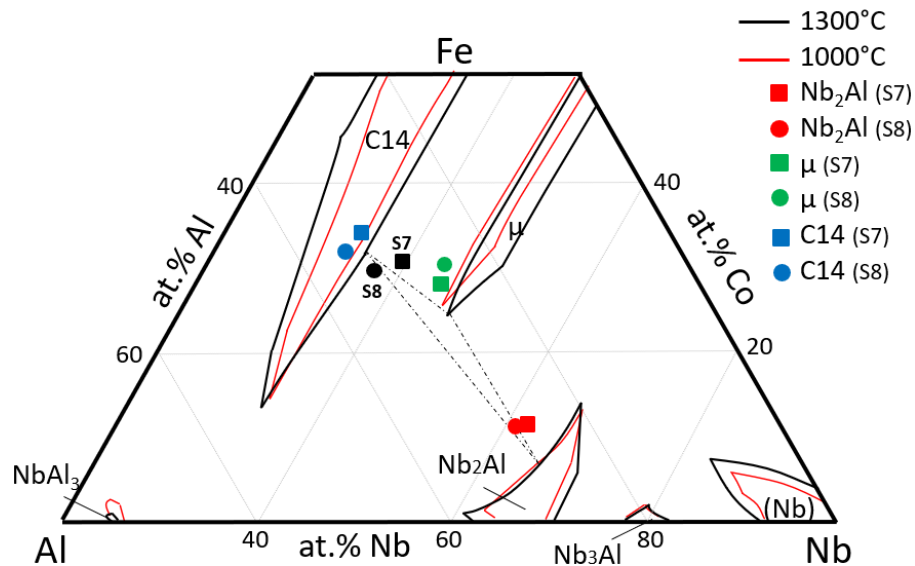


Figure 73 - Isothermal sections at 1300°C and superimposed solute solubility at 1000°C, showing the phase boundaries in relation to the compositions in the different phases for S7 and S8. Dotted lines show tie-lines from [26].

The microstructure observed for S8 in Figure 72(d) indicates a larger extension of μ formation. Similarly to S7, the line joining the nominal composition and the composition of C14 approaches the eutectic valley C14 – Nb₂Al, but in this case there is a much narrower extension of the eutectic formation, before the liquid approaching the invariant Class III reaction temperature, which proceeds to the formation of μ phase. The amount of liquid at this point is still considerably high, and due to limited diffusion the ternary peritectic takes place in a narrow temperature window, and freezing terminates mostly as primary formation, $L \rightarrow \mu$, forming a eutectic-like morphology in most part of the alloy due to the abundant remaining liquid.

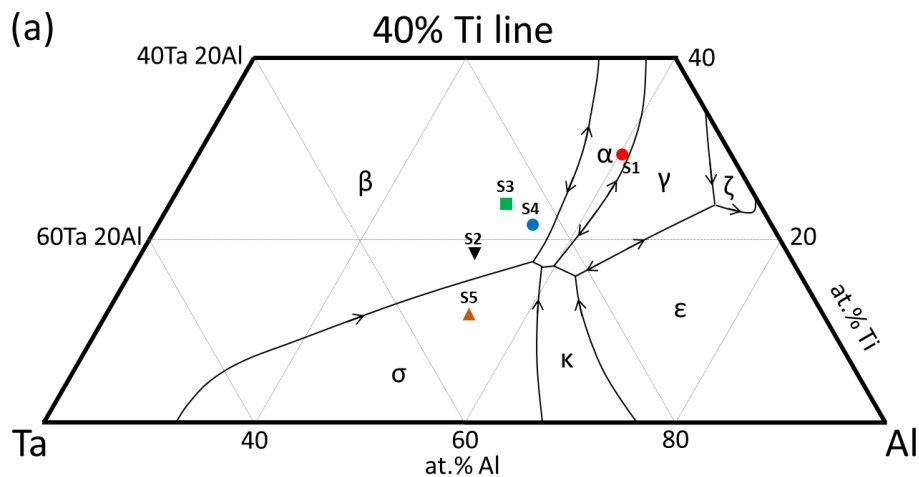
6.4. Ta-Al-Ti system

The average nominal compositions of the alloys studied measured by EDS analysis with the phases observed for each individual alloy, according to the liquidus projection (with the plot of compositions), are presented in Table 23. This allows a comparison between the observed and expected phases.

Table 23 - Nominal measured compositions of the alloys studied (in at. %) and phases expected according to liquidus projection.

Sample ID	Composition			Phases observed
	Ta	Al	Ti	
S1	10.2	61.7	28.1	$\sigma + \gamma$
S2	30.1	51.4	18.5	$\beta + \sigma + \alpha$
S3	24.4	52.1	23.5	$\beta + \sigma + \alpha + \gamma$
S4	31.0	57.0	12.0	$\beta + \alpha + \sigma + \kappa$
S5	27.9	55.6	16.5	$\sigma + \kappa + \epsilon$

The nominal compositions are then plotted in the liquidus and solidus projections and isothermal section at 1350°C, as seen in Figure 74, in order to evaluate the solidification path and phases expected during freezing under equilibrium conditions, and to observe how solubility of the phase regions change with decreasing temperature.



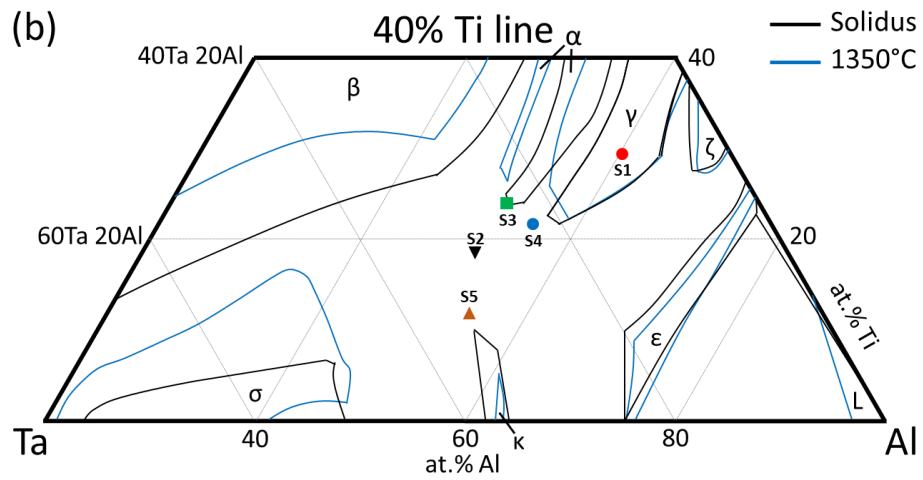


Figure 74 - (a) Liquidus projection, (b) Solidus projection with superimposed limits of solute solubility at 1350°C [28, 30, 63]. The compositions in this study are superimposed in the figures.

6.4.1. Three-phase reaction

Figure 75 shows a low and high magnification BEI of S1, where a coarse dendritic formation can be easily identified followed by a thin inter-dendritic phase solidified between the channels produced by the dendritic arms.

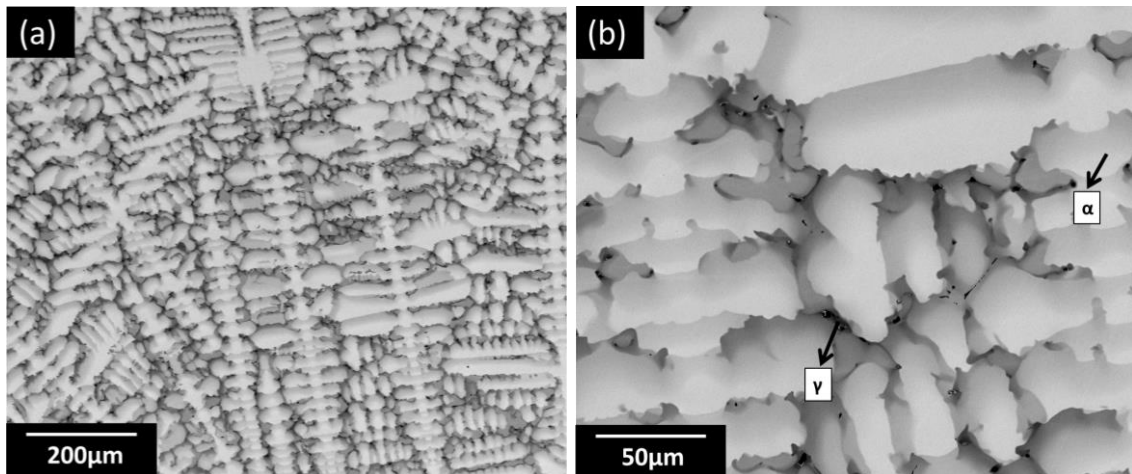


Figure 75 - BEI of microstructure corresponding to S1, (a) low magnification, (b) high magnification.

The expected phases have been measured by EDS and agree well with the phases expected as plotted in the liquidus and solidus projections in Figure 74. According to this analysis, an extensive primary formation of a bright α phase is followed by the solidification of a darker γ phase.

The nominal composition lies within the single-phase region corresponding to α phase, which forms primarily from the liquid, $L \rightarrow \alpha$. As the system cools down the liquid composition follows the path of the peritectic α - γ valley, where γ phase is formed peritectically by the consumption of the primary α phase, via $L + \alpha \rightarrow \gamma$. This is very limited, as observed from the microstructures presented, and since the amount of liquid present is also limited, this reaction does not go to completion but instead forms a very thin γ phase layer around the dendrites, and the remaining liquid transforms directly into γ , from $L \rightarrow \gamma$. Table 24 shows the measured phases compositions for this alloy.

Table 24 - Average measured composition (in at.%) of phases present in S1.

Phase		Composition		
		Ta	Al	Ti
S1	α	13.4	57.3	27.4
	γ	4.3	64.4	31.3

The solidus projection and the superimposed solute solubility at 1350°C, with phase compositions for S1 plotted, is presented in Figure 76, from which it is possible to observe that for both phases α and γ , Al solute is highly trapped.

The high solidification rate involved in the arc melting process would have caused a shift in the boundaries of phase regions corresponding to α and γ phases towards high Al and lower Ti contents.

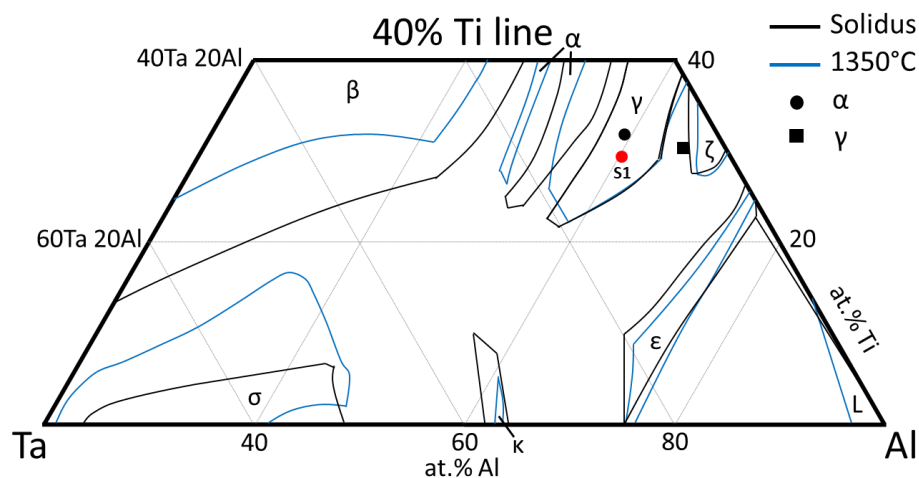


Figure 76 - Solidus projection and superimposed solute solubility at 1350°C, showing the phase boundaries in relation to the compositions in the different phases for S1 [30].

Although the entrapment of Al solute has been observed to occur at considerable levels, the predicted solidification sequence following Figure 74(a) is still observed.

6.4.2. Class II – Quasi-Peritectic reaction

Figure 77 shows a low and high magnification back-scattered electron image (BEI) of S2, where it can be seen a limited formation of a bright primary phase of bcc (β) phase surrounded by very fine eutectic, which has been identified by EDS to be $\beta + \sigma$ followed by a formation of σ phase surrounding the eutectic formation. As the solidification progresses the last remaining liquid is solidified as a dark α Ti phase (henceforth displayed as only α), as expected according to the liquidus projection.

The phases measured and the nominal composition of S2 is plotted in the liquidus and solidus projections showed in Figure 74. A clear solute trapping phenomenon is observed for α and σ phases, where an extended solute solubility towards higher Al and Ti is seen.

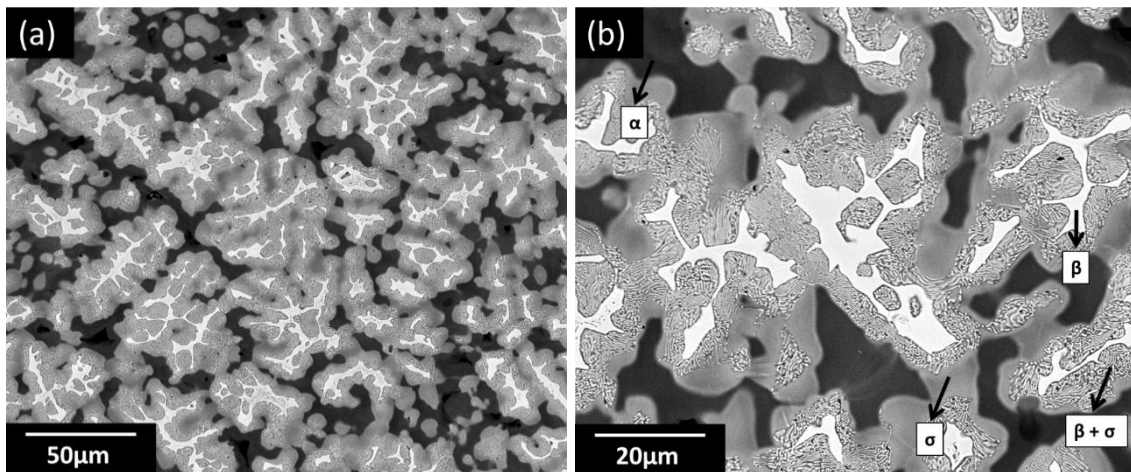


Figure 77 - BEI of microstructure corresponding to S2, (a) low magnification, (b) high magnification.

This is also observed for Ta-Al-Fe alloys discussed previously and is markedly increased when compared to the isothermal section at 1497 $^{\circ}\text{C}$, in which Ti contents in σ phase can be present at a maximum of about 15 at.%, whilst this is

then decreased to roughly 10 at.% for the computed solidus projection. Table 25 shows the measured phases compositions for this alloy.

Table 25 - Average measured composition (in at.%) of phases present in S2.

Phase		Composition		
		Ta	Al	Ti
S2	α	20.7	57.3	22.0
	σ	27.4	53.3	19.3
	β	40.8	44	15.2

The nominal composition falls within β phase, which is the bright primary phase limitedly formed, followed by the intersection of a peritectic valley. However, a fine coupled eutectic structure of $\beta + \sigma$ is observed, which occurs by a solid-state decomposition of $\beta \rightarrow \beta + \sigma$, during the rapid solidification and rarely goes untransformed to room temperature, as also assessed by Witusiewicz et al [63]. Since the cooling rate is at a high rate, this transformation is very limited and precludes the coarsening of the eutectic lamellae that surrounds the primary β phase.

Once the peritectic valley is reached, β is consumed to form σ phase, $L + \beta \rightarrow \sigma$, which can occur at temperatures as high as 2347 K and is also limited by the availability of β phase, producing an irregular morphology surrounding the eutectic compound produced a moment before [63].

The remaining liquid is now enriched in Ti, and the solidification path follows the formation of α Ti phase, after intersection of the Class II four-phase reaction point, in which there is formation of α by the invariant reaction $L + \beta \rightarrow \alpha + \sigma$. Since both β and σ phases are very limited, the remaining liquid forms α phase primarily, as $L \rightarrow \alpha$, where the solidification is completed.

The solidus projection and the superimposed solute solubility at 1350°C, with phase compositions for S2 plotted, is presented in Figure 78. It is possible to observe that there is considerable solute trapping of both Ti and Al solutes. The phase composition corresponding to β phase falls notably far from both the solidus projection and the isothermal projection at 1350°C.

According to D.R.F. West [20], the solidus projection is the most accurate means of presenting the change in solute solubility, however when solid-state transformations take place, it is important to depict an isothermal section at a temperature below the lowest solidus temperature, which for this system corresponds to ϵ phase.

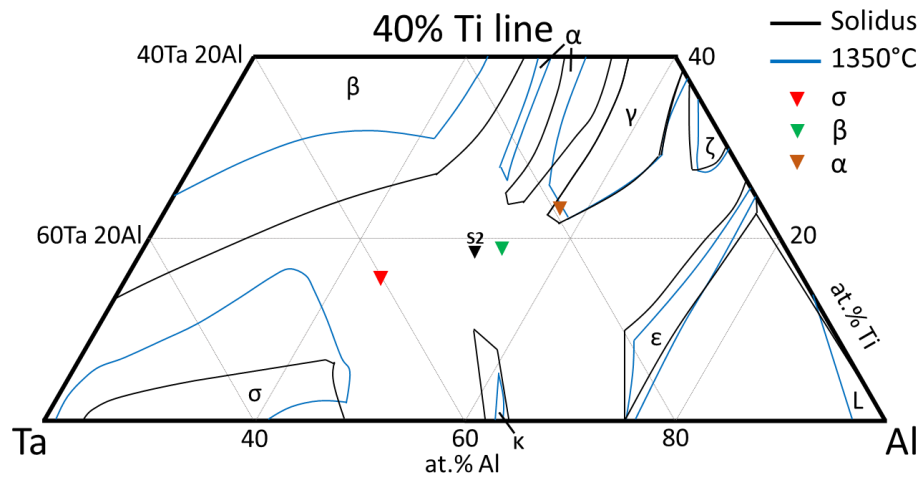


Figure 78 - Solidus projection and superimposed solute solubility at 1350°C, showing the phase boundaries in relation to the compositions in the different phases for S2 [30].

With this in mind, it is possible to observe that the nominal composition of S2 falls outside the tie-triangle of α - β - σ , therefore the Class II invariant reaction never goes to completion.

Once again, a considerable solute trapping of both Al and Ti shifts the boundary of phase regions towards higher Al (for β and α phases) and towards higher Ti (for σ phase), which cannot be accounted for changes in solute solubility during cooling. Micro-segregation is negligible at this stage.

The microstructure produced for S3 is similar to that presented for S2, as shown by the low and high magnification BEI's of microstructures presented in Figure 79.

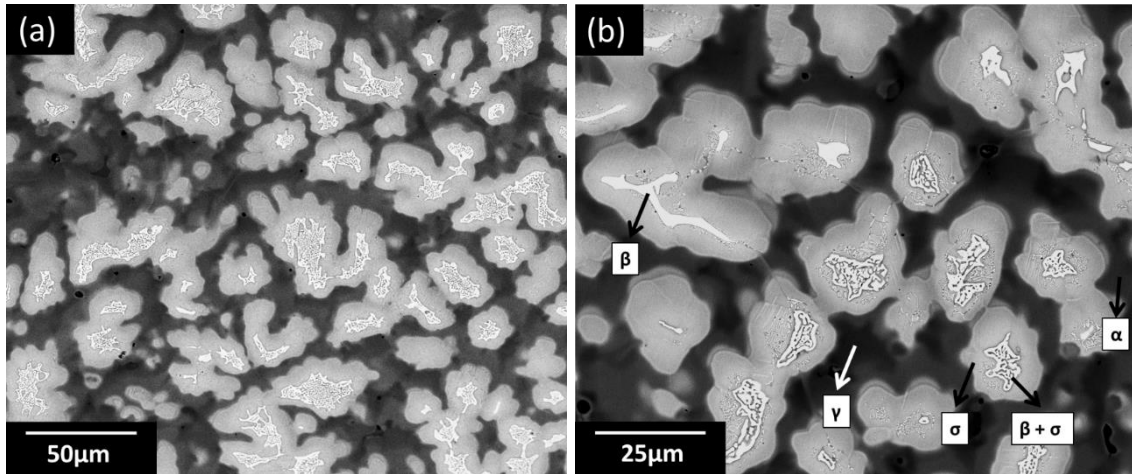


Figure 79 - BEI of microstructure corresponding to S3, (a) low magnification, (b) high magnification.

The expected phases have been measured using EDS analysis and have been identified accordingly. Table 26 shows the measured phases compositions for this alloy. A bright primary β phase is formed in a very limited morphology, followed by a divorced eutectic formation of $\beta+\sigma$ phases surrounded by a very fine and irregular eutectic of the same phases. As cooling takes place the peritectic valley is reached forming the surrounding σ phase. This solidification sequence follows a similar pattern as seen for S2, where now the Al-enriched liquid transforms into α phase, and the solidification is completed by a Ti-rich dark contrast phase identified as γ , formed to a limited extent. The expected phases are plotted with the nominal and phases compositions in the liquidus and solidus projections, presented in Figure 74.

Table 26 - Average measured composition (in at.%) of phases present in S3.

Phase		Composition		
		Ta	Al	Ti
S3	α	17.8	56.4	25.8
	γ	12.3	61.2	26.5
	β	39.4	43.3	17.3
	σ	28.1	50.2	21.7

The nominal composition lies within β phase region, confirming β as primary phase formed very limitedly from the liquid, $L \rightarrow \beta$. The decomposition of β then takes place, in which $\beta \rightarrow \beta + \sigma$, and this is markedly more extensively observed

than that for S2. This is unexpected, since the nominal composition lies at a higher Ti content, providing a considerable distance from the peritectic valley, which then suggests that the high cooling rate associated with this alloy favoured the solid-state decomposition where the eutectic occurs. The morphology of this $\beta+\sigma$ has a divorced and irregular appearance, and as the β phase is transformed, there could be a refinement of this eutectic formation.

The formation of σ phase is observed after the liquid composition reaches the peritectic valley, where a coarser σ phase is formed from $L + \beta \rightarrow \sigma$, which indicates that this could also be a reason for the eutectic refinement, as the β phase is consumed to form the rim of σ phase. The solidification path then reaches the four-phase Class II invariant reaction, $L + \beta \rightarrow \sigma + \alpha$, and similarly to S2, the presence of β phase is extremely limited as is σ phase, and the enriched liquid forms α phase primarily from $L \rightarrow \alpha$.

The formation of γ phase thereafter is observed to occur at small regions entrapped in pockets surrounded by α phase, which suggests that γ is formed primarily from a further enrichment of Al in the remaining liquid, where $L \rightarrow \gamma$. However, this could be an unlikely scenario given the high cooling rate involved and the fact that, since this sample is not expected to follow the formation of γ phase at any rate, this can be attributed as a solid-state precipitation of γ phase from a decomposing and enriched α phase. The enrichment of α phase in this case occurs due to the entrapment of Al solute into α towards the central regions, namely the pockets of enriched phase, which then transforms from $[\alpha]_{ss} \rightarrow \alpha+\gamma$ and is corroborated by the increasing contrast indicated by the difference in Al content.

The solidus projection and the superimposed solute solubility at 1350°C, with the phase compositions for S3 plotted, is presented in Figure 80. Here, there is a better agreement for the compositions of β and α phases, when compared to that of S2, with an observed shift towards higher Al solute.

The composition of γ phase agrees well with the phase boundary predicted in the projections presented. However, there is a further increase in Ti solute trapping for σ phase, with an increase up to 10 at.%. The composition of S3 falls outside

the tie-triangle of σ - β - α , with Class II invariant reaction not being completed, and instead there is formation of a non-equilibrium γ phase.

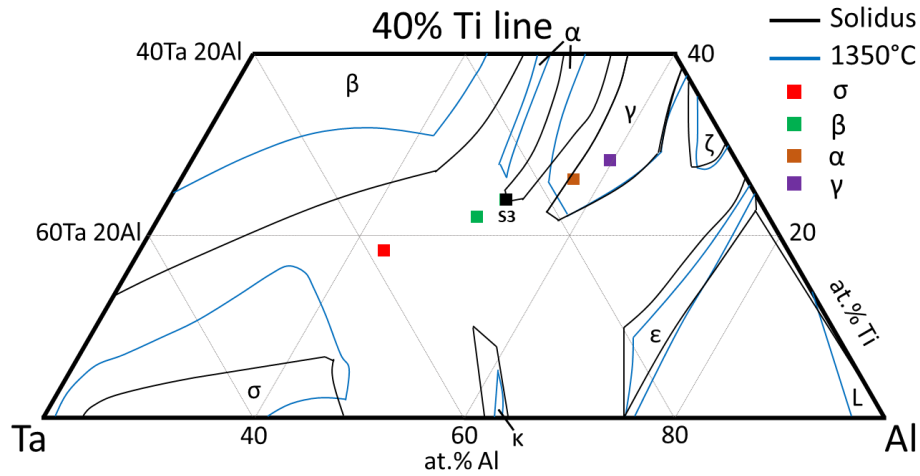


Figure 80 - Solidus projection and superimposed solute solubility at 1350°C, showing the phase boundaries in relation to the compositions in the different phases for S3 [30].

Figure 81 presents a low and high magnification BEI corresponding to S4, where an extended globular grey phase is dominant in the microstructure, with an irregular presence of a bright phase within some globes, forming a characteristic eutectic morphology. A dark grey phase is formed adjacent to the grey phase and is very limited, followed by a black phase formed between the globes presenting a very fine eutectic in the later stages of solidification.

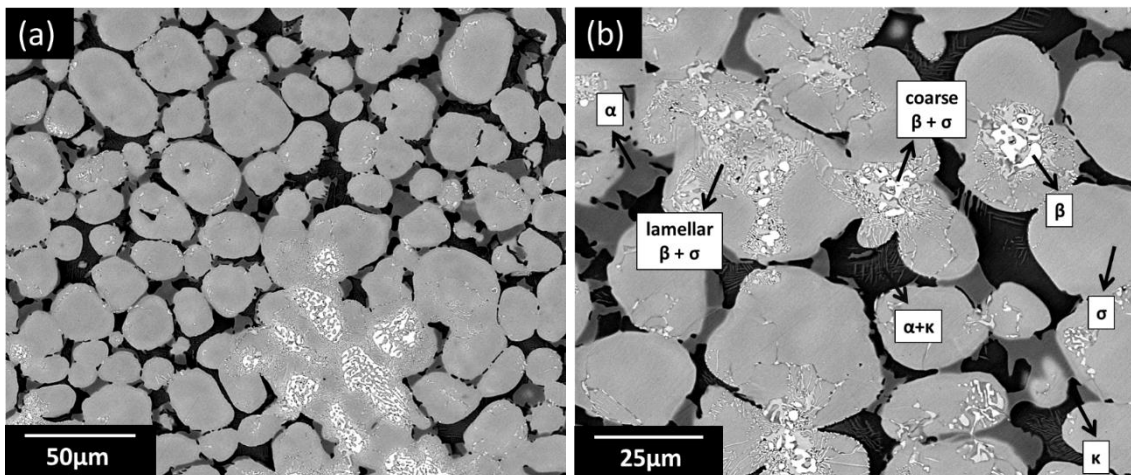


Figure 81 - BEI of microstructure corresponding to S4, (a) low magnification, (b) high magnification.

To avoid volume averaging, a careful analysis by EDS was done in order to identify properly each phase in the microstructure, with a coupled analysis by plotting the measured compositions in the liquidus and solidus projections,

presented in Figure 74, where it can be seen the phases expected and agree well with the expected formation given by where the nominal composition lies. Table 27 shows the measured phases compositions for this alloy.

Table 27 - Average measured composition (in at.%) of phases present in S4.

Phase		Composition		
		Ta	Al	Ti
S4	α	21.1	57.8	21.1
	σ	29.4	53.0	17.6
	κ	18.2	66.2	15.6
	β	45.1	44.9	10.0

The analysis of the solidification path suggests that the primary grey globular phase is σ phase, which has also been expected from EDS measurements, forming directly from the liquid, $L \rightarrow \sigma$, to a large extent as observed by the BEI's. It is important to notice the presence of a bright phase within σ phase, which has been identified as β phase, and was not expected to form given that the liquid follows the peritectic valley where $L + \beta \rightarrow \sigma$. The peritectic reaction cannot be complete when β that should be consumed is not formed in the first place. However, owed to the segregation of Ta and a possible evaporation of Al in the liquid during heating, there could have been present Ta-rich regions that produced small primary β phases at a limited extent, which would follow the decomposition into σ , from $\beta \rightarrow \beta + \sigma$, and intersect the peritectic valley, consuming part of β phase.

A very fine lamellar eutectic of $\beta + \sigma$ is observed thereafter, connecting the pockets of coarse eutectics that are later surrounded by the primary and the peritectic σ phase. As the solidification continues, the invariant four-phase Class II reaction then occurs, where there is consumption of β to produce σ and α phases, $L + \beta \rightarrow \sigma + \alpha$. Since the amount of β is very limited, this reaction never takes place, and instead there is formation of α dark grey phase adjacent to the σ phase globes.

The remaining Al-rich liquid then traverses the to another Class II invariant reaction, consuming σ phase to form a eutectic of α phase with the black κ phase,

from $L + \sigma \rightarrow \alpha + \kappa$. Since the nominal composition lies outside the equilibrium tie-triangle between σ - α - κ , this reaction does not take place, and instead a very fine eutectic of $\alpha + \kappa$ is formed, where a halo of dark κ is observed surrounding the eutectic morphology.

From Figure 81, it is possible to observe that the eutectic of $\alpha + \kappa$ does not go to completion at some places, where only κ phase is observed, and this suggests that (i) the halo formed around σ and the adjacent α phases has been coarsened to a point where the remaining liquid could not have enough space to form the eutectic, or (ii) the composition of the remaining liquid was high enough in Al for the κ phase to form primarily from the liquid, $L \rightarrow \kappa$, where solidification is then completed. The formation of halos will be explained in more details for the other ternary systems in section 6.5.

A curious formation has been noticed regarding to the eutectic formation around the bright β phase, where there is presence of α phase to some extent, which gives the impression of a ternary eutectic with $\alpha + \beta + \sigma$. This is highlighted in the high magnification BEI in Figure 82.

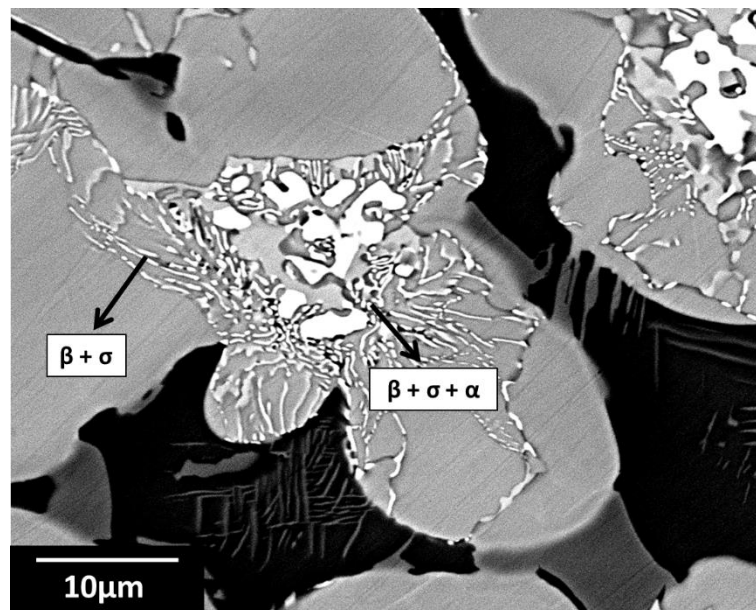


Figure 82 - Detailed high magnification BEI of S4.

At this point, two observations can be made:

- (a) When the temperature is decrease to the point where the Class II invariant reaction, $L + \beta \rightarrow \alpha + \sigma$, should have been achieved, the local composition

of the liquid at that region fell within the tie-triangle of α - β - σ composition and the reaction has taken place, partially consuming β to form the subsequent α + σ adjacent to it.

- (b) Since a peritectic σ has been formed surrounding the eutectic of β - σ phases, the remaining liquid could not have been in contact with β phase for the Class II reaction to take place, which then suggests that α phase forms from a solid-state precipitation from the consumption of β into the observed eutectic, where $[\beta]_{ss} \rightarrow \alpha + \sigma$, giving the appearance of a ternary eutectic.

Though it is important to notice that the extent of formation of α phase adjacent to the β + σ eutectic is very limited and is only observed at specific locations owed to the segregation of Ta, this indicates a clear deviation from the expected equilibrium solidification path.

The solidus projection and the superimposed solute solubility at 1350°C, with phase compositions for S4 plotted, is presented in Figure 83. A similar pattern to that observed for the previous alloys applies for S4.

However, there is a considerable agreement with the composition of σ phase falling markedly closer to its corresponding phase region, whilst α presents a slight enrichment in Al, its composition agrees well to the corresponding phase region. There is a considerable Al solute trapping for β phase.

Phase κ is predicted in the liquidus projection under equilibrium in Figure 73(a), and it is observed to be formed, although its composition presents a higher Ti and Al contents which places it noticeably outside the phase region and shifts κ boundaries towards “north-west”.

The nominal composition of S4 is outside the tie-triangle of σ - β - α , and the Class II invariant reaction never goes to completion. This observed deviation of equilibrium solidification is followed by the formation of κ phase at the latter stages of freezing.

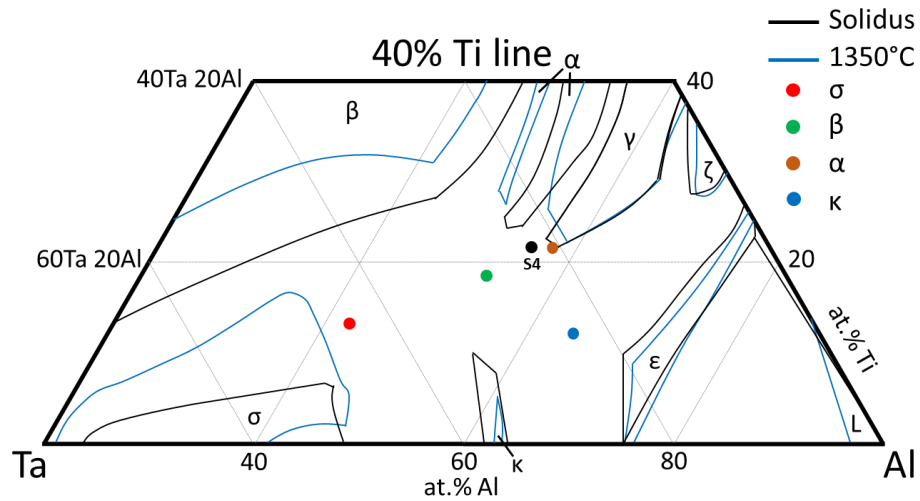


Figure 83 – Solidus projection and superimposed solute solubility at 1350°C, showing the phase boundaries in relation to the compositions in the different phases for S4 [30].

The measure composition of S5 has been observed to be considerably far from that expected when comparing to the nominal composition, as shown in Table 28.

Table 28 - Comparison between nominal and measured composition (in at.%) for S5.

Composition	Ti	Al	Ta
Nominal	20	56	24
Measured	12	57	31

This difference in the composition places this sample at a very close position of S4. However, a peculiar characteristic is observed for this alloy in terms of the microstructure. Figure 84 show a low magnification BEI of this sample, in which can be easily seen a marked segregation forming a “two-sided” microstructure, where one side presents a high amount of a bright phase (Ta-rich) and the other has shown none (Ti-rich). This phenomenon causes the liquid to solidify in two different solidification paths, and since the solidification rate of this occurs at a high rate, the elemental equilibrium at this point can be precluded.

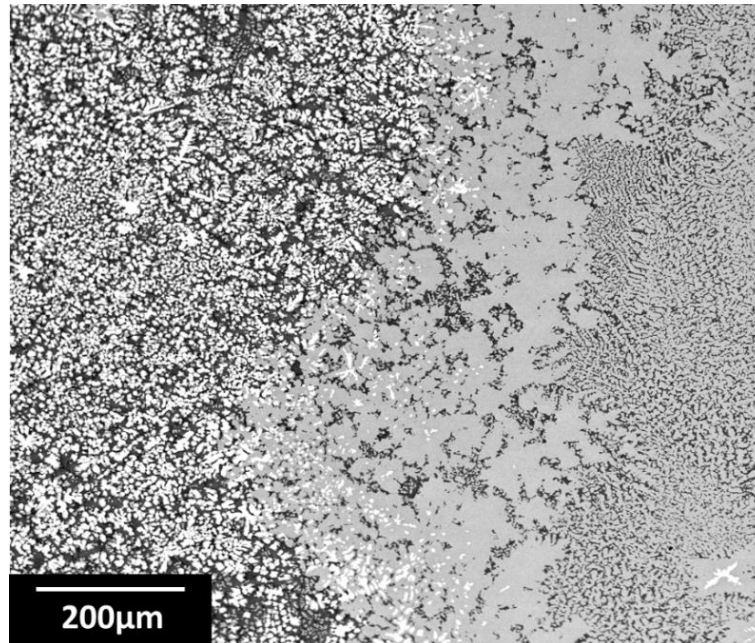


Figure 84 - Low magnification BEI of microstructure corresponding to S5.

Therefore, a closer analysis of each “side” of the microstructure is needed. High magnification BEI’s for these are presented in Figure 85, and the measured composition of each individual phase measured by EDS has been plotted in the liquid and solid projections, in Figure 74. An extended solute solubility of Al is observed.

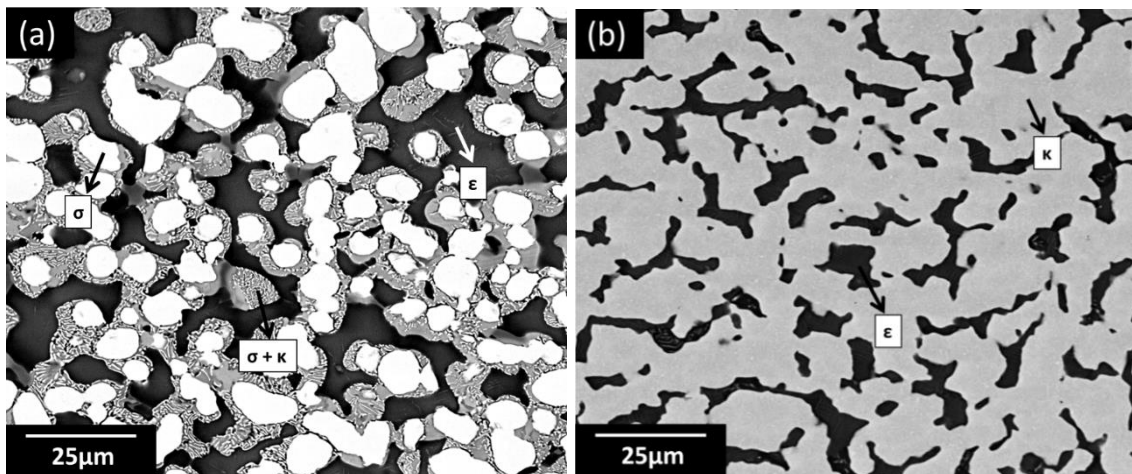


Figure 85 - High magnification BEI of microstructure corresponding to S5, (a) Ta-rich side, and (b) Ti-rich side.

Figure 85(a) shows a Ta-rich portion of the microstructure, where a primary bright β phase forms primarily, followed its dissolution into a non-equilibrium eutectic formation of $\sigma+\kappa$, and when solidification is concluded an Al-rich ϵ phase is identified, following rejection of solute to the remaining liquid.

The morphology of this portion shows an interesting pattern where primary σ phase is formed in a globular characteristic, completely surrounded by the following non-equilibrium $\sigma+\kappa$ eutectic formation. An Al-richer ϵ phase surrounds both components where the final formation of ϵ phase is extensively formed. The formation of non-equilibrium reactions has been explored in more details in section 6.1.

The solidification path of this portion is different from the Ti-rich side of the alloy, following failure of solute mixture during cooling. The primary σ forms from the liquid, from $L \rightarrow \sigma$. The solid-state consumption σ is dissolved through $\sigma \rightarrow \sigma + \kappa$. The following expected peritectic reaction where $L + \sigma \rightarrow \kappa$ is suppressed here or extremely limited. The liquid, now enriched in entrapped Al solute, solidifies into a primarily formed ϵ phase, from $L \rightarrow \epsilon$, which was not expected to occur at any rate. The deviation of solidification path during rapid freezing of Ta and Al containing alloys has also been extensively discussed in section 6.1. Coring is observed towards the edges of the ϵ phase formations.

Figure 85(b) shows the other portion, richer in Ti, of the microstructure, following a simple two-phase solidification path which contains lower Ta and Al and higher Ti contents. The primary phase formed for this part has been observed to be κ phase, formed from $L \rightarrow \kappa$, followed the liquid freezing into ϵ phase whilst consuming κ , from $L + \kappa \rightarrow \epsilon$, where the solidification terminates.

The expected phases have been measured using EDS analysis and have been identified accordingly. Table 29 shows the measured phases compositions for this alloy, where it is clear to observe the difference in solute between the Ta-rich and Ti-rich sides of this alloy.

Table 29 - Average measured composition (in at.%) of phases present in S5.

Phase		Composition		
		Ta	Al	Ti
S5	κ (Ta-rich)	34.1	55.5	10.4
	ϵ (Ta-rich)	20.3	67.1	12.6
	σ (Ta-rich)	49.2	44.1	6.7
	κ (Ti-rich)	31.2	55.3	13.5
	ϵ (Ti-rich)	20.8	65.3	13.9

The solidus projection and the superimposed solute solubility at 1350°C, with phase compositions for S5 plotted, is presented in Figure 86. Although this alloy presented an anomalous solidification pattern, which produced phases with different solute contents, it is possible to observe that all phases agree relatively well with both the solidus projection and the isothermal section at 1350°C.

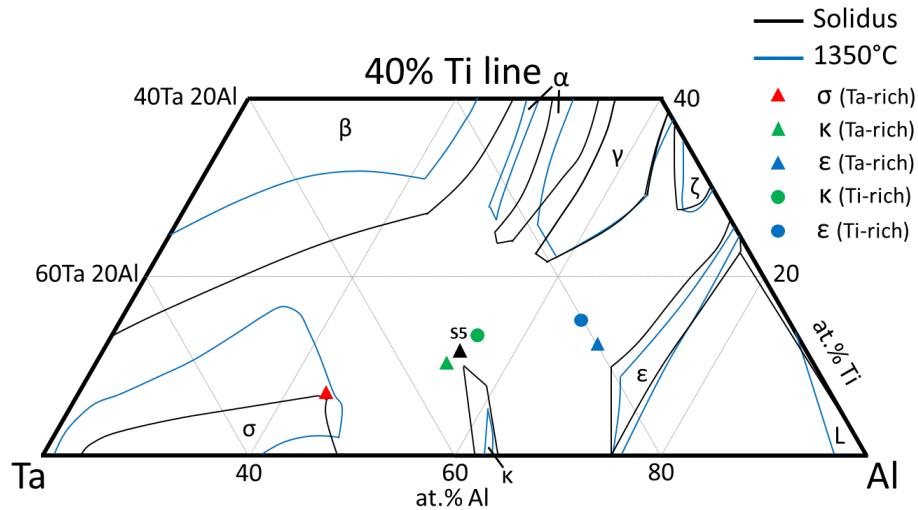


Figure 86 - Solidus projection and superimposed solute solubility at 1350°C, showing the phase boundaries in relation to the compositions in the different phases for S5 [30].

However, for the Ti-rich portion of the alloy, there is noticeable enrichment in Ti solute, as expected given the abnormal nature of the solidification seen, which shifts the boundaries of phase regions towards higher Ti levels.

The Ti-rich side is formed of only two phases, namely κ and ϵ phases. The formation of ϵ phase is not expected under equilibrium conditions, although a tie-line joining κ - ϵ regions can be plotted in agreement with the phases measured.

The Ta-rich portion presents the formation of a primary σ phase in addition to the κ and ϵ phases. As ϵ phase is not expected to form, there is a clear deviation of solidification sequence, which is followed by the suppression of α phase. The nominal compositions of S5 falls inside the tie-triangle joining σ - κ - α regions, but the four-phase reaction involving these phases never takes place, and instead there is a primary formation of ϵ phase from the remaining liquid following the rejection of Al solute.

This is further confirmed by the absence of a tie-triangle of σ - κ - ϵ in the solidus projection. Although there is a very limited window tie-triangle of σ - κ - ϵ for the

isothermal section at 1350°C, this combination is only observed under equilibrium when there is formation of γ phase followed by a solid-state four-phase eutectic reaction where $\gamma + \kappa \rightarrow \sigma + \varepsilon$.

6.5. Halo formation on ternary systems alloys

This section will present the result of anomalous evolution of the different eutectic morphologies during solidification as well as the composition of the various phases in relation to their respective phase boundaries. This analysis will be done based on alloys systems already presented in this chapter, specifically for Ta-Al-Fe, Nb-Al-Co and the Nb-Al-Fe systems, for which the compositions analysed, and the phases observed are presented in Table 30.

Table 30 - List of samples, elemental composition and observed phases in the microstructure.

“p” denotes primary phase.

Sample ID	Composition (at. %)			Phases observed
	Al	Fe	Ta	
S1	20.3	23.0	56.7	σ (p) + μ
S2	29.9	14.7	55.4	σ (p) + μ
	Al	Co	Nb	
S3	41.0	45.2	13.8	CoAl (p) + C14
S4	37.5	38.6	23.9	C14 (p) + CoAl
	Al	Fe	Nb	
S5	61.8	4.3	33.9	NbAl ₃ (p) + Nb ₂ Al + C14

6.5.1. Ta-Al-Fe alloys analysis

Following the liquidus and solidus projections, shown in Figure 87(c) and Figure 87(d) [21, 30], the solidification path of sample S1 can be described as; $L \rightarrow \sigma + L$ and $L \rightarrow \sigma + \mu$, which is identified following low and high magnification BEI analysis presented in Figure 87(a) and Figure 87(b), respectively, from which the following observations can be made;

- (a) A limited extent of primary phase (bright contrast) is observed, which presents an irregular shaped morphology. The inter-dendritic region is formed of a dark matrix phase along with the bright phase showing lamellar morphology. Coarsening of the lamellae is observed to some extent.
- (b) The primary phase corresponds to σ , and its composition has been measured at a number of locations across the primary globular phase (Table 31) and the solidus projection [21, 30]. Primary freezing shows the occurrence of micro-segregation, as shown in the standard deviation in the measured σ composition. An increased solubility of primary Fe is observed in σ from the solidus projection, as presented in Figure 87(d). Due to the fact that the solidus surface of σ enclosed by the $\sigma/[\sigma+\mu]$ and $\sigma/[\sigma+A2]$ boundaries shifts to lower Fe (higher Ta) concentrations with decreasing temperature, it can be inferred that the solute solubility cannot be accounted by solubility changes occurring during cooling.
- (c) The dark inter-dendritic region represents μ phase which has been determined after a number of measurements at various locations within this region (Table 31) and the solidus projection [21, 30]. The fine lamellae have not been measured as expected, due to volume averaging effects [217], but it can be determined that the coarsened island morphology corresponds to σ phase. The measured composition of μ phase falls within the single-phase region in the solidus projection [Figure 87(d)]. However, the change in solute solubility within μ phase during subsequent cooling cannot be neglected, since the $\mu/[\mu+A2]$ phase boundary moves towards *higher* Fe concentration with a decrease in temperature. It is worth mentioning that, as seen in Table 31, the two phases that form in this alloy have Al contents of 16.1 (σ phase) and 20.0 at.% (μ phase), both of which are lower than the expected nominal value, 20.3 at.%, showed in Table 30, with the latter being measured at low magnification, around x50, over a number of locations across the cross-section area. Given that the composition of σ phase (Al-rich) has only been measured in the coarse island type of morphology, it can be inferred that the fine lamellar

morphology has to be enriched in Al compared with the coarse morphology.

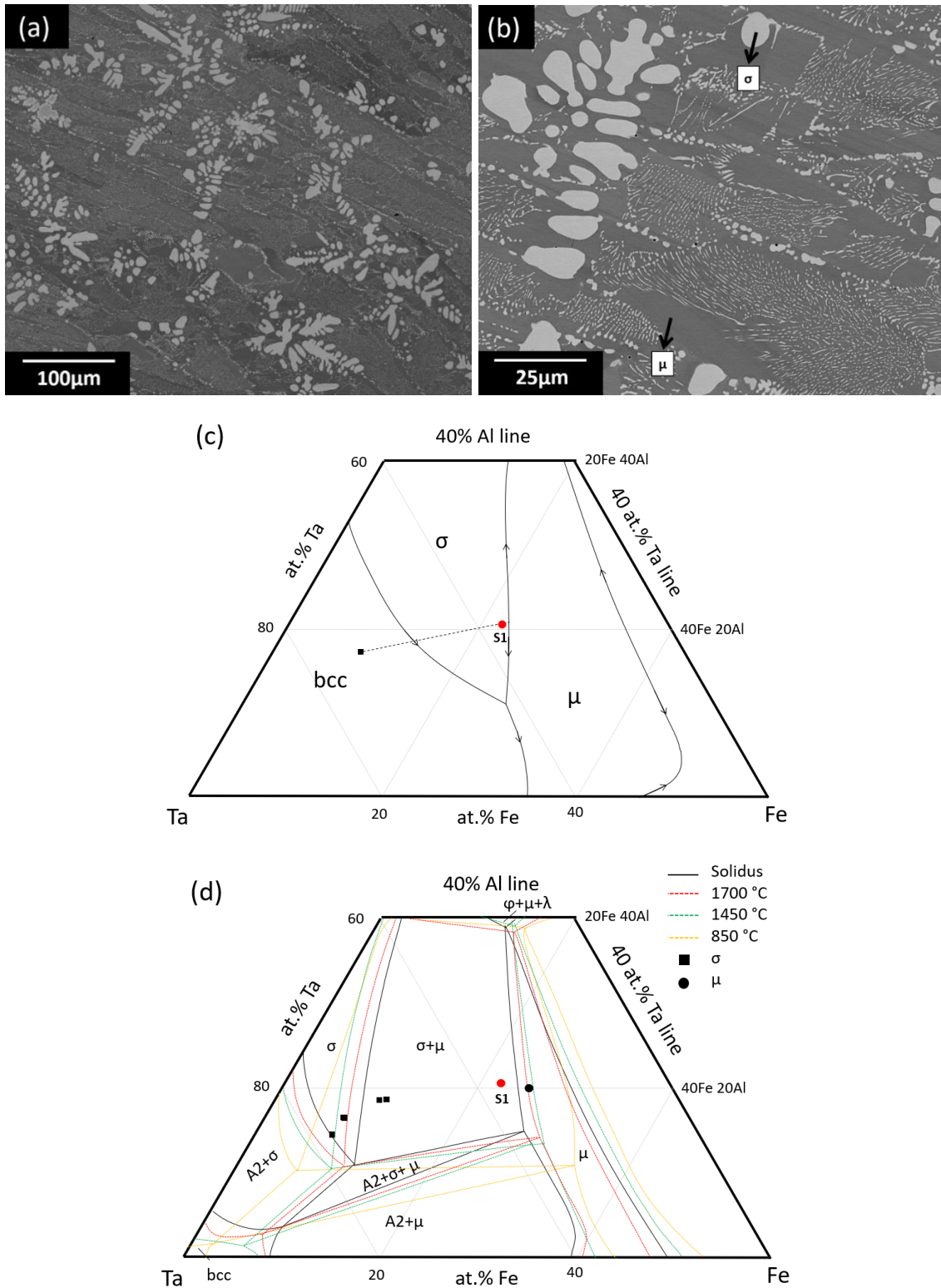


Figure 87 - BEI's for S1, (a) low magnification, (b) high magnification, and (c) liquidus projection and (d) solidus projections at Ta-rich end. Also included are phase boundaries with decreasing temperature and the measured composition in the phases. Adapted from [21, 30].

The solidification path can therefore be written as; $L \rightarrow \sigma + L$ and $L \rightarrow \sigma + \mu$. The extent of primary solidification of σ phase is very limited and followed by a eutectic reaction. An initial eutectic formation is accompanied by a divorced morphology and a coupled growth. The divorced morphology preceding coupled growth corresponds to a halo of μ phase around primary σ phase.

The solidification path of S2 following the analysis of the liquidus and solidus projections [21, 30] is expected to occur as follows; $L \rightarrow \sigma + L$ and $L \rightarrow \sigma + \mu$. Figure 88(a) and Figure 88(b) are low and high magnification BEI's respectively from which the following observations can be made;

- (a) There is the formation of a bright primary phase showing an irregular shaped morphology and the inter-dendritic (ID) region comprising of a dark phase.
- (b) The bright primary phase corresponds to σ , which can be confirmed after the composition analysis measured at various locations across the microstructure of said primary phase (shown in Table 31) and given the plot into the solidus projection [21, 30]. An extended solute solubility of primary Fe is observed in σ phase from the solidus projection, as in Figure 88(d), which in a similar way as in S1 cannot be accounted by solubility changes occurring during cooling.

The inter-dendritic region (dark contrast) has been identified as μ phase following from the composition measured at various locations within this region (shown in Table 31) and the solidus projection [21, 30]. The measured composition of μ phase falls within the single-phase field in the solidus projection [Figure 88(d)]. However, the change in solute solubility within μ phase during subsequent cooling cannot be neglected, given the fact that since the $\mu/[\mu+A2]$ phase boundary moves towards *higher* Fe concentration with decreasing temperature. The solidification path can therefore be written as; $L \rightarrow \sigma + L$ and $L \rightarrow \sigma + \mu$. Primary solidification of σ phase is followed by a eutectic reaction with a divorced morphology. The divorced morphology preceding coupled growth corresponds to a halo of μ phase around primary σ phase, which is more prominent in S2 when compared with S1.

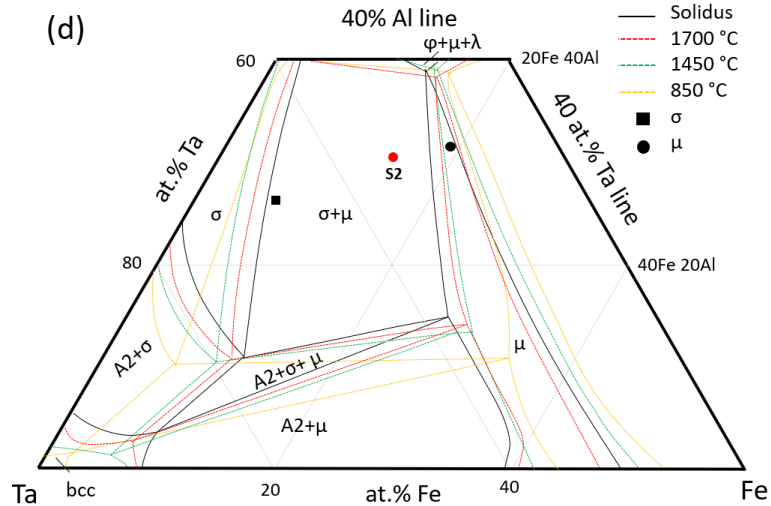
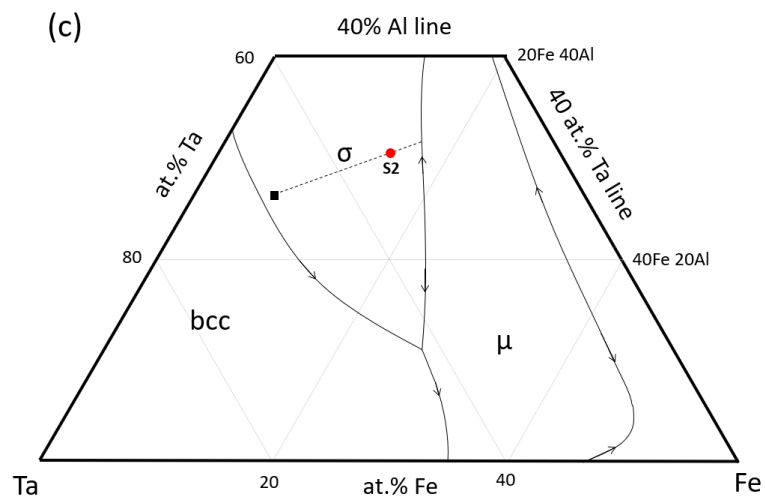
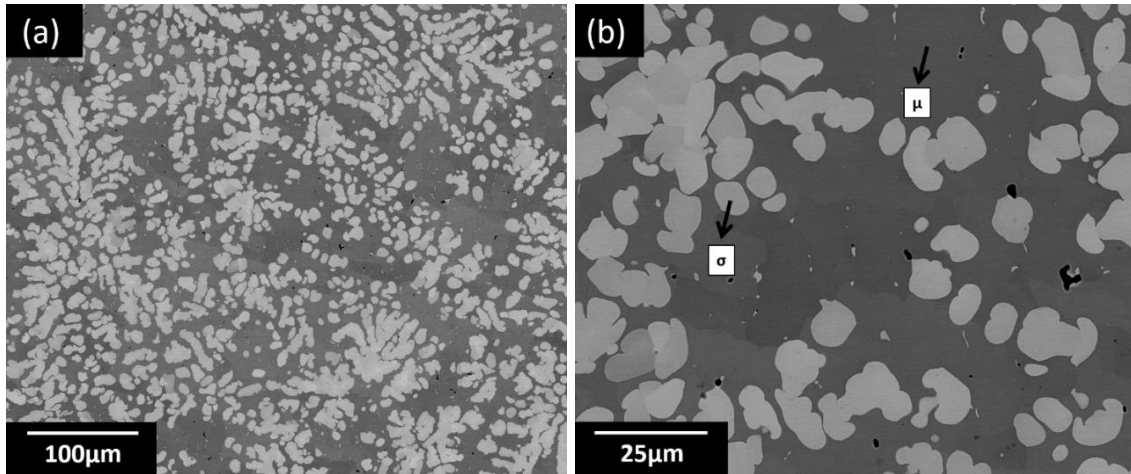


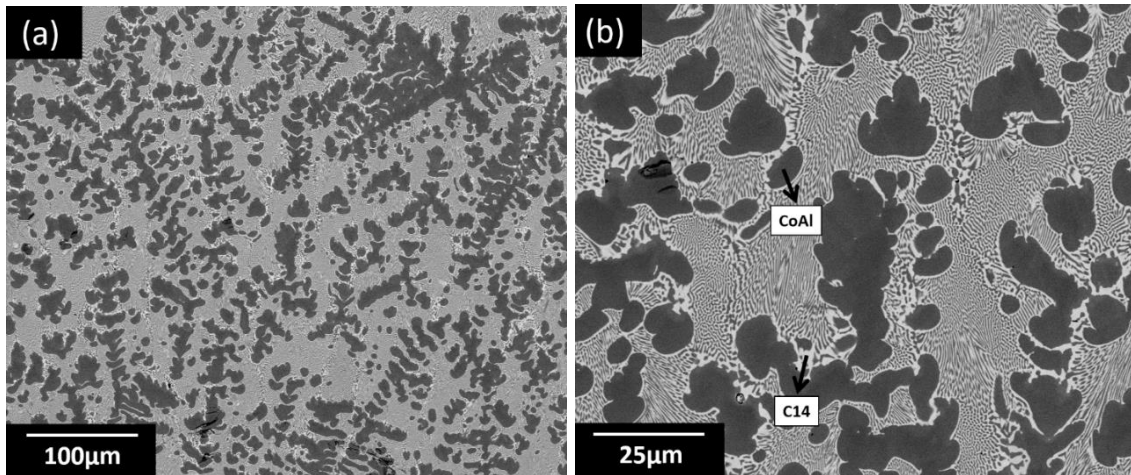
Figure 88 - BEI's corresponding to S2, (a) low magnification, (b) high magnification, and (c) liquidus projection and (d) solidus projections at Ta-rich end. Also included are phase boundaries with decreasing temperature and the measured composition in the phases. Adapted from [21, 30].

Table 31 - Average composition (in at.%) of phases with standard deviation in S1 and S2.

Phase	Al	Fe	Ta
σ (S1)	16.1 ± 1.81	9.4 ± 1.82	74.5 ± 3.63
μ (S1)	20.0 ± 0.10	25.5 ± 0.34	54.6 ± 0.26
σ (S2)	26.4 ± 0.34	6.7 ± 0.26	67.0 ± 0.44
μ (S2)	31.6 ± 0.32	19.2 ± 0.17	49.2 ± 0.15

6.5.2. Nb-Al-Co alloys analysis

The solidification path of S3 after analysis from the liquidus projections and isothermal sections [18, 27, 218] is expected to occur as follows; $L \rightarrow \text{CoAl} + L$ and $L \rightarrow \text{CoAl} + \text{C14}$. Figure 89(a) shows a low magnification BEI of this alloy, while Figure 89(b) and Figure 89(c) are high magnification BEI's from which the following observations can be made;



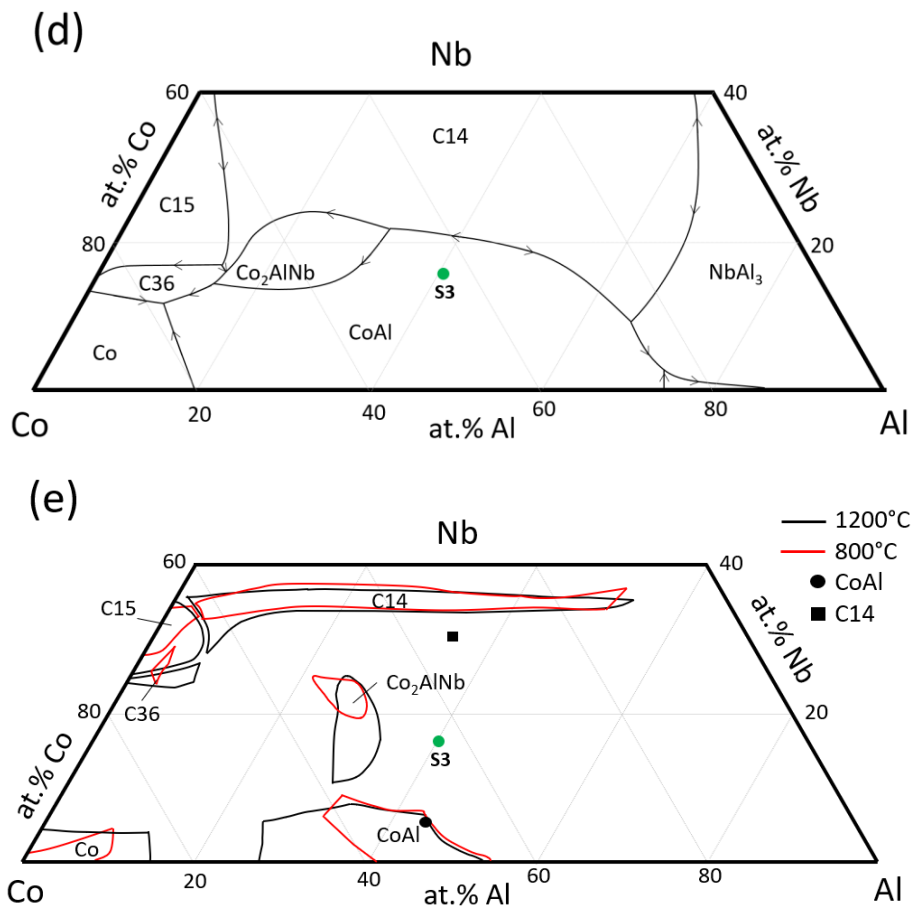
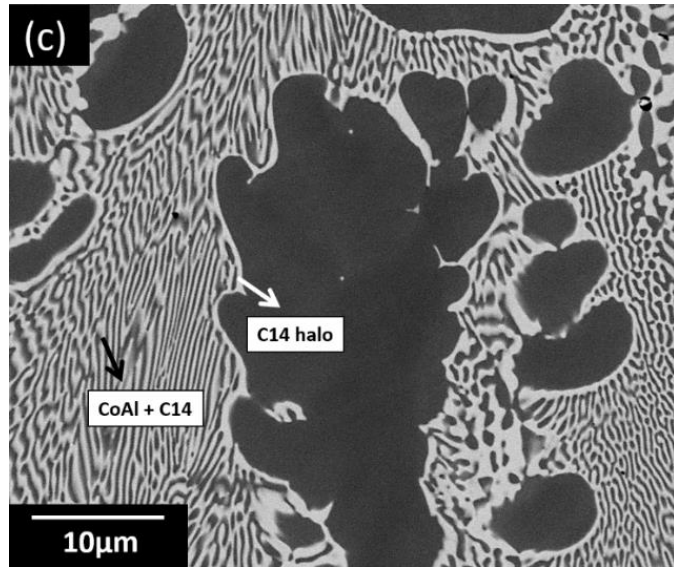


Figure 89 - BEI's corresponding to S3, (a) low magnification, (b) and (c) high magnification, and (d) liquidus projection and (e) isothermal sections showing phase boundaries with decreasing temperature, with the measured phases compositions included. Adapted from [18, 27, 218].

(a) The primary dark CoAl phase has a dendritic or flaky morphology. The inter-dendritic region comprises of a thin rim or halo of the secondary bright C14 phase that surrounds the primary phase and a fine lamellar

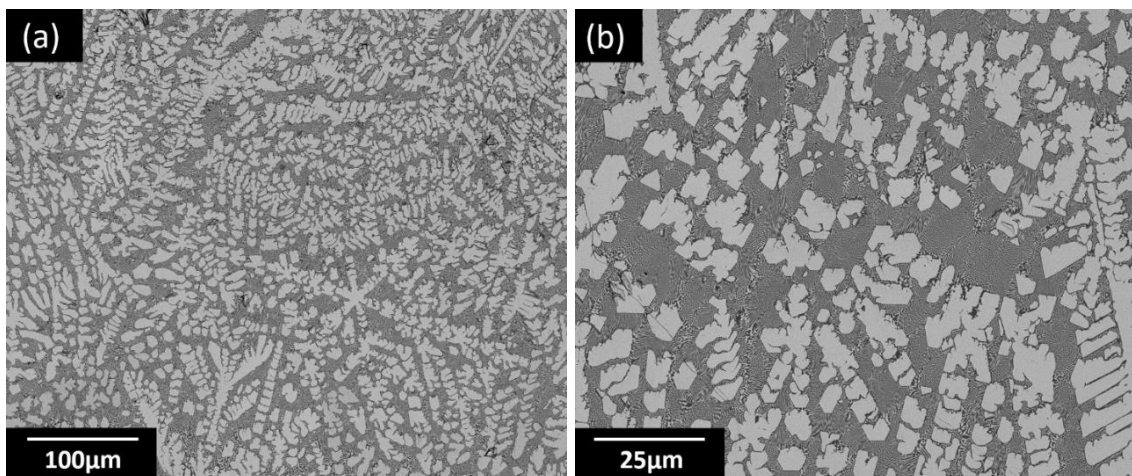
morphology that is originated from the halo. In the terminal stages of the solidification, a progressive coarsening of the lamellar morphology can be observed, specifically at the boundary between two adjacent abutting eutectic cells.

- (b) This primary flaky phase is the CoAl phase that has been identified from the composition measured at various locations (Table 32) and the isothermal projections at a series of decreasing temperatures [18, 27, 218]. The measured composition falls near the CoAl/[CoAl + C14] phase boundary, as it can be seen in the isothermal sections at lower temperatures (800°C and 1200°C) and there is clear evidence of a change in solute solubility during cooling [Figure 89(e)]. In the absence of a solidus projection, neither the change in solute solubility nor the extension of the solute solubility in the primary phase can be determined.
- (c) The measurements of composition in the secondary phase is restricted to the coarser inter-dendritic morphology and the halo to avoid or minimise the effects of volume averaging (Table 32), which corresponds to C14 phase following the analysis from the isothermal projections at a series of decreasing temperatures [18, 27, 218]. However, there will be some degree of volume averaging effects on the measured composition of CoAl, given the fine scale of the C14 phase, which results in a lower measured Nb concentration. Hence, the effects of volume averaging cannot be precluded in the measured composition that falls outside of the phase field corresponding to C14 phase in the isothermal sections presented in Figure 89(e).

The solidification sequence can therefore be written as; $L \rightarrow \text{CoAl} + L$ and $L \rightarrow \text{CoAl} + \text{C14}$. However, prior to the occurrence of the coupled eutectic growth, there is the distinct formation of a halo of C14 phase on primary CoAl solid.

The solidification path of S4 is expected to follow; $L \rightarrow \text{C14} + L$ and $L \rightarrow \text{C14} + \text{CoAl}$, following from the liquidus and isothermal sections [18, 27, 218]. Figure 90(a) is a low magnification, while Figure 90(b) and Figure 90(c) are high magnification BEI's from which the following observations can be made;

- (a) The primary bright phase shows a small degree of faceting. The interdendritic region comprises of a fine lamellar morphology, with nucleation and growth of the dark phase. There is generally the absence of the halo on the primary phase and the lamellar morphology emanates directly from the primary phase. However, in some localised regions as indicated in Figure 90(c), a thin halo of CoAl around primary C14 can be discerned, but it is markedly less prominent compared to the halo of C14 formed around primary CoAl. In the terminal stages of freezing, there is some progressive coarsening of the lamellar morphology, specifically at the boundary between two adjacent abutting eutectic cells.
- (b) The primary phase is C14 following from the measured composition (Table 32) and the isothermal sections [18, 27, 218]. The measured composition lies on the C14/[C14 + CoAl] phase boundary at 1492°C [Figure 90(e)], but in the absence of a solidus projection it is not possible to ascertain the extent of any extended solute solubility in the primary phase.
- (c) The composition measured (Table 32) is restricted to the coarser interdendritic morphology to minimise volume averaging and corresponds to CoAl phase, following from the isothermal projections at many temperatures [18, 27, 218]. The composition lies beyond the single-phase field, but given the fine morphology, volume averaging is always prevalent in CoAl, resulting in a higher measured Nb concentration.



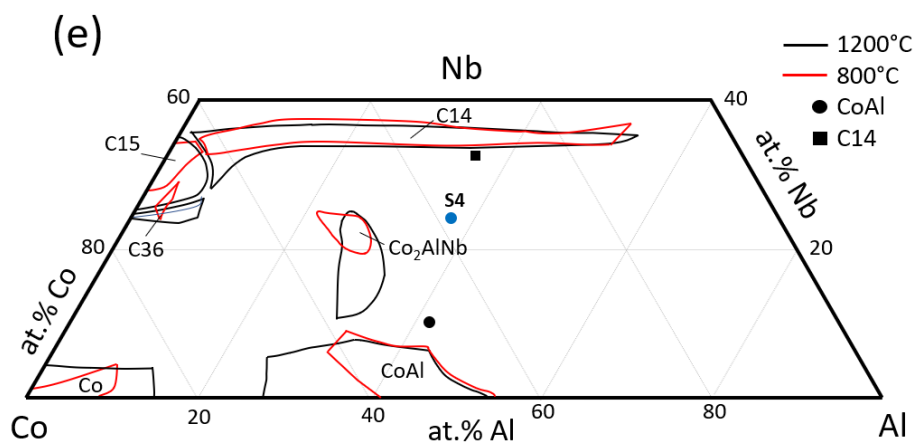
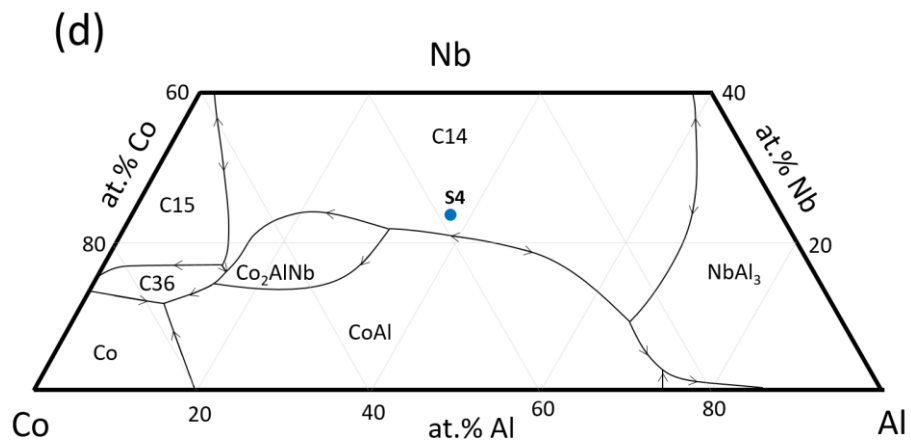
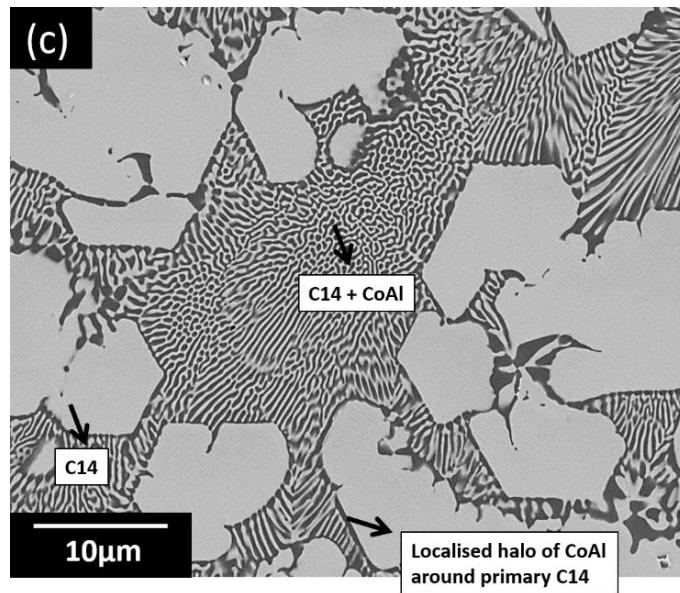


Figure 90 - BEI's corresponding to S4, (a) low magnification, (b) and (c) high magnification, and (d) liquidus projection and (e) isothermal sections showing phase boundaries with decreasing temperature, with the measured phases compositions included. Adapted from [18, 27, 218].

The solidification path can therefore be written as; $L \rightarrow C14 + L$ and $L \rightarrow C14 + CoAl$. Furthermore, there is a notable decrease in the presence of a halo of CoAl phase on primary phase C14.

Table 32 - Average composition of phases (in at.%) with standard deviation in S3 and S4.

Phase	Al	Co	Nb
CoAl (S3)	44.8 ± 0.48	49.6 ± 0.15	5.6 ± 0.33
C14 (S3)	35.0 ± 0.72	35.0 ± 0.82	30.1 ± 1.24
C14 (S4)	35.9 ± 0.13	31.8 ± 0.21	32.3 ± 0.17
CoAl (S4)	41.7 ± 1.43	48.2 ± 1.09	10.1 ± 1.04

6.5.3. Nb-Al-Fe alloys analysis

The solidification path of S5 is expected to follow; $L \rightarrow NbAl_3 + L$, $L \rightarrow NbAl_3 + C14 + L$ and $L \rightarrow NbAl_3 + C14 + Nb_2Al$, following from the liquidus and solidus projections [26, 219, 220]. Figure 91(a) is a low magnification, while Figure 91(b) and Figure 91(c) are high magnification BEI's from which the following observations can be made;

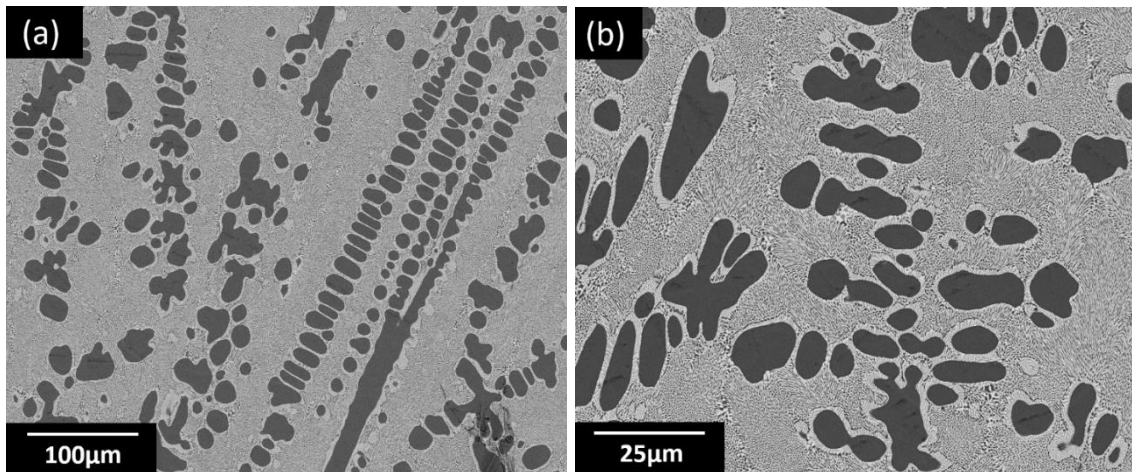
- (a) The dark primary phase is dendritic. The inter-dendritic region comprises of a fine lamellar morphology. The lamellar structure comprises two distinct types;
 - (i) There is a lamellar structure that emanates from the primary solid and constituting a two-phase halo. The halo can be justified on the basis that none of the two lamellar constituents (bright and grey) constitute the primary phase.
 - (ii) Beyond the initial two-phase halo, further growth corresponds to a ternary eutectic with the nucleation and growth of the primary phase, as the third constituent in the eutectic.
- (b) The primary phase corresponds to $NbAl_3$ following composition measurements at a number of locations (Table 33) and the isothermal projections at a series of temperatures, as in Figure 91(d).

(c) The fine lamellar morphology precludes accurate composition measurements. However, given the regular morphology of the eutectic, average compositions were measured within both the two-phase (halo) and three-phase morphologies. The measured composition in the two-phase halo lies in the two-phase Nb₂Al + C14 phase field, indicating that the halo corresponds to coupled growth of Nb₂Al + C14 (Table 33) [26]. The ternary eutectic corresponds very closely to the invariant point in the liquidus projection involving NbAl₃, Nb₂Al and C14 [26, 219, 220], as in Figure 91(d).

The solidification sequence is; L → NbAl₃ + L , followed by L → Nb₂Al + C14 + L and L → Nb₂Al + C14 + NbAl₃, which is not as expected from the phase diagram.

Table 33 - Average composition of phases with standard deviation in S5 (in at. %).

Phase	% Al	% Fe	% Nb
NbAl ₃	74.7 ± 0.05	0.6 ± 0.14	24.7 ± 0.18
Nb ₂ Al + C14	48.3 ± 0.30	8.3 ± 0.25	43.4 ± 0.06
Nb ₂ Al + C14 + NbAl ₃	54.5 ± 0.96	6.1 ± 0.21	39.4 ± 0.76



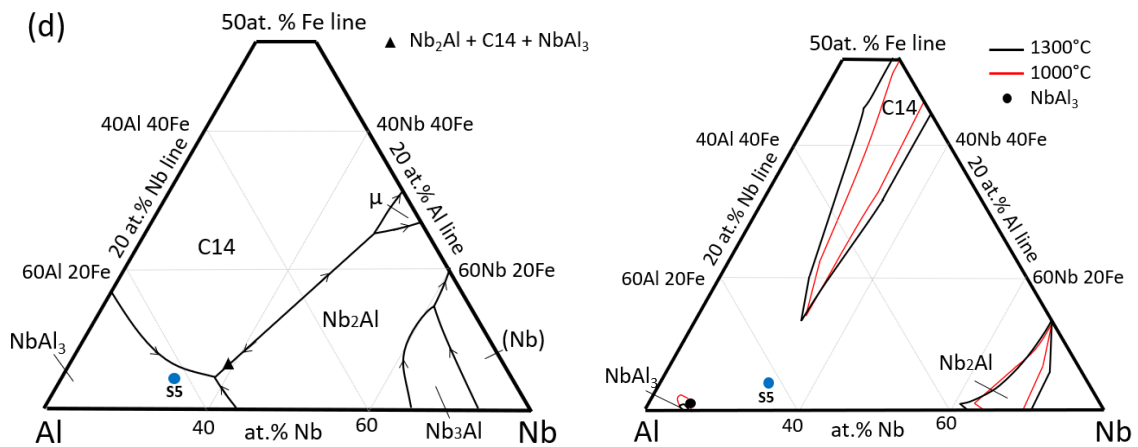
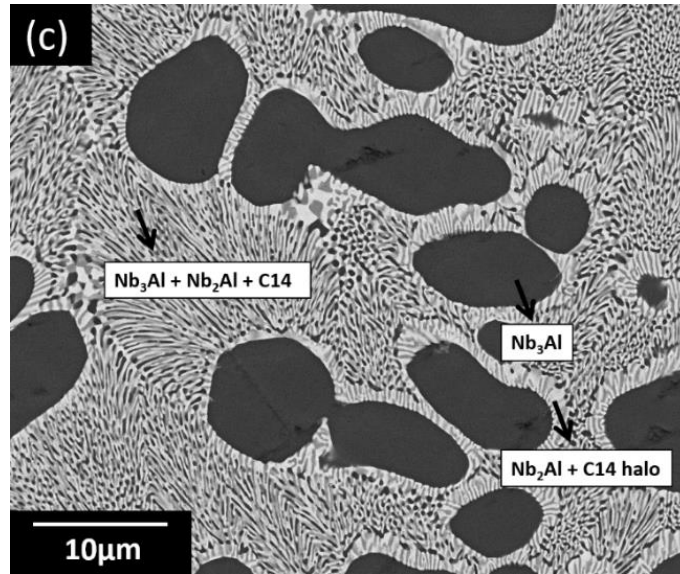


Figure 91 - BEI's corresponding to S5, (a) low magnification, (b) and (c) high magnification, and (d) liquidus projection and isothermal sections showing phase boundaries with decreasing temperature in the Al-rich end, including phases measured compositions. Adapted from [26, 219, 220].

6.5.4. General discussion

Unlike in the binary phase diagram where the “partition coefficient (k)” is fixed at a given temperature during primary freezing, this is not the case in ternary systems since an added degree of freedom exists. For conservation of solute during primary freezing in an incremental temperature interval, dT or time interval dt ,

$$[C_{\infty B} - C_{SB}]df_S = \int D_S \frac{dC_{SB}}{dx} dt + (1 - f_S)dC_{\infty B} \quad (2)$$

$$[C_{\infty C} - C_{sC}]df_s = \int D_s \frac{dC_{sC}}{dx} dt + (1 - f_s)dC_{\infty C} \quad (3)$$

Where the new solute composition in the liquid at $[T - \Delta T]$ is given by $[C_{\infty B} + dC_{\infty B}]$ and $[C_{\infty C} + dC]$, df_s is the incremental fraction solid and D_s is the solute diffusivity in the solid. For small undercooling, S/L interfacial equilibrium exists and therefore there are only two unknowns in Equations 2 and 3, i.e. df_s and $dC_{\infty B}$ (or $dC_{\infty C}$).

Equation (3) is further exemplified in Figure 92, where it is shown the difference in composition of a given solute between a fraction of solid and liquid, given that the interface diffusion will be governed by Fick's diffusion law.

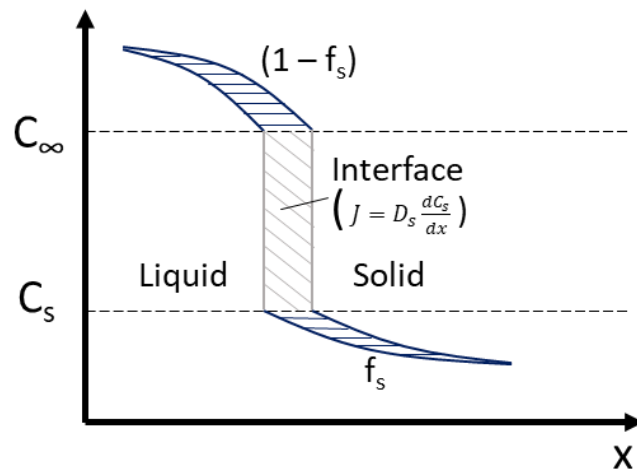


Figure 92 - Liquid and solid interfacial equilibrium during solidification.

Therefore, the extent of back-diffusion will govern the extent of incremental solid growth (df_s) and the composition in the liquid [44, 45, 48]. This is schematically illustrated in Figure 93; where two representative paths taken by the liquid over the liquidus surface during primary freezing is indicated. Accordingly, the liquid composition intersects the eutectic valley (DG) at two different points at the end of primary solidification depending on the path followed, as governed by the kinetics of back-diffusion.

At the end of primary growth, the evolution of the secondary β phase morphology will be determined by the local undercooling. Accordingly, (C_B^e, C_C^e) corresponds to the liquid composition in the eutectic valley at temperature T (at end of primary

growth), and because of undercooling, the composition of the liquid into which β phase grows is $(C_{\infty B}, C_{\infty C})$ and $(C_B^e, C_C^e) \neq (C_{\infty B}, C_{\infty C})$.

Following the approach in [20] in case of three-phase planar eutectic growth (L , α and β), the corresponding undercooling for coupled eutectic growth can also be determined. Like in the binary case for a given undercooling a halo of β phase forms around primary α , if $V > V'$, following the terminology defined previously in section 2.7. Importantly from the preceding arguments in a ternary system, the solidification path will play a prominent role in the formation of halos, since it defines (C_B^e, C_C^e) , as it defines the point where the liquid composition intersects the eutectic valley, as illustrated in Figure 93.

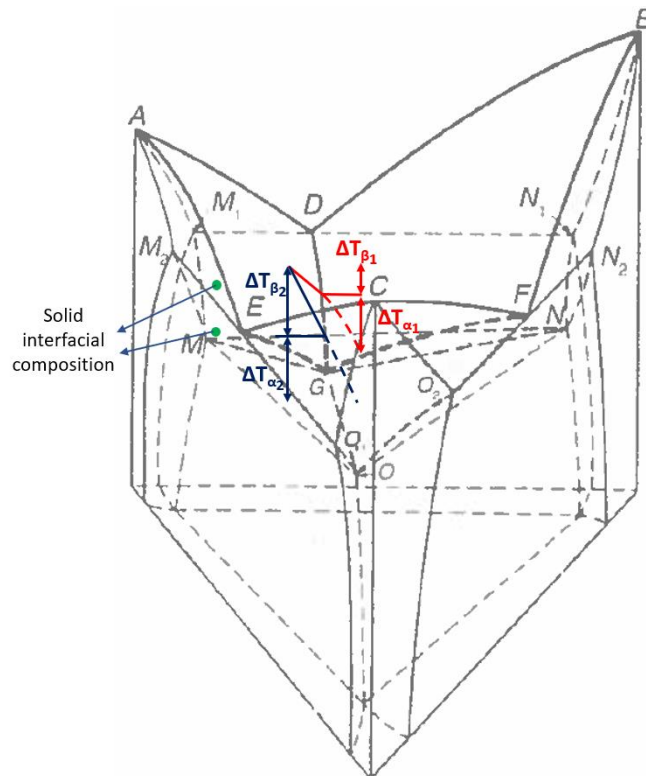


Figure 93 - Schematic of ternary diagram illustrating the liquid and solid compositions during eutectic growth, $L \rightarrow \alpha + \beta$, as a function of the undercooling. Adapted from [20].

In Figure 93, the undercooling associated with growth of halo (β) phase is shown for two representative freezing paths (dotted red and blue lines). Also indicated are the interfacial solid composition for primary (α) phase, which lie beyond solidus line M_1M indicating extended solute solubility. Solute solubility changes during subsequent cooling are neglected.

In the Ta-Al-Fe system, α corresponds to σ phase and β corresponds to μ phase. The liquidus temperature of both S1 and S2 is approximately 1827°C, as deduced from the liquidus projection in [21, 30], but as observed in Figure 87(c) and Figure 88(c) following primary solidification of σ , the path followed by the liquid composition along the σ - μ eutectic valley during the eutectic reaction, $L \rightarrow \sigma + \mu$ is different in the two cases. This is because the line joining the average solid (σ) composition and the nominal composition following primary freezing intersects the σ - μ eutectic valley, on either side of the maximum (e_1) in [21, 30].

When coupled eutectic growth is observed following the formation of an initial halo (S1), the liquid composition intersects the eutectic valley defined by $e_1 U_1$ (where U_1 is the quasi-peritectic point in the Al-lean end), while when there is no coupled growth (S2) the liquid composition intersects the “eutectic valley defined by $e_1 U_2$ (where U_2 is the quasi-peritectic point in the Al-rich end). This confirms that the solidification path;

- (a) Initially dictates the traverse of the liquid composition on the liquidus surface during primary freezing and determines the point of intersection of the liquid composition with the eutectic valley, $[C_B^e, C_C^e]$.
- (b) It also determines the liquid composition, $[C_{\infty B}, C_{\infty C}]$ into which the halo grows, and which determines the phase morphologies that evolve.

Since it is not possible to easily measure the undercooling, it is important to note that since undercooling occurs below the eutectic temperature it must lead to an extended solute solubility within the primary phase through $m_{\sigma Fe}$ and $m_{\sigma Ta}$. It is easier therefore to measure this extended solute solubility in the solid.

However, as a point of caution, it must also be emphasised that changes in solute solubility can also occur during cooling. Nevertheless, it can be observed from Figure 87(d) and Figure 88(d) that an extended solubility of at least ~ 2 at. % Fe is observed in σ phase in both S1 and S2, given that the measured composition lies outside of the single-phase field. It must also be pointed out that the coupled eutectic growth morphology comprises of individual cells, which grow and abut into each other in S1 and arises from a long-range diffusion boundary layer is

built-up above the composite S/L interface. Therefore, coupled eutectic growth does not occur with a planar front, but comprises of cells.

Another point pertaining to primary freezing in S1 and S2 is worth mentioning. In S1 the nominal composition lies almost on the eutectic valley; nevertheless, a noticeable amount of primary σ is observed. A possible explanation is that the location of the σ - μ eutectic valley in the liquidus projection in the vicinity of S1 is inaccurate [21, 30]. It should be slightly displaced to the right in Figure 88(c), so that the nominal composition is further displaced from the eutectic valley.

In the Nb-Al-Co system, a thin halo of C14 is observed around primary CoAl (S3) but very limited vice-versa (S4). The approximate liquidus temperature of S3 is 1545°C and S4 is 1568°C, as deduced from the liquidus projection [27] and solidification must terminate before the peritectic reaction, $L + C14 + CoAl \rightarrow Co_2AlNb$ occurs at 1482°C. There is no reported solidus projection and the highest temperature isothermal projection is 1492°C [218]. Noting that there is very little change in the profile of the CoAl/[CoAl + C14] boundary in the composition range; 35 at. % < Al < 55 at. % and 0 < Nb < 8 at. % and the CoAl composition in S4 lies on the boundary [Figure 89(d)] in the temperature range [800 – 1200]°C, in the absence of a solidus projection and a clear change in solute solubility in the temperature range [1477 – 1492]°C no definitive assertions about the existence of extended solute solubility in CoAl can be made [18, 218].

A similar situation exists when C14 is the primary phase in S5. Although the measured composition of C14 lies outside the single-phase field, in the absence of a solidus projection an extended solute solubility in C14 cannot be definitively confirmed. However, the very thin halo (< 2 μ m) indicates that the halo phase grows at a lower undercooling compared with that in S1 and S2. With progressively decreasing undercooling accompanying growth of C14 halo phase, coupled eutectic growth is rapidly established. Like in the Ta-Al-Fe case, the coupled morphology comprises individual cells, which grow and abut into each other indicating a de-stabilisation of both constituent phases.

In the preceding analysis given the restricted extended solute solubility, it was reasonable to use the assumption of equilibrium at the S/L interface. However, in some cases the eutectic phases grow at large undercooling and there is

departure from equilibrium. This mainly arises from nucleation constraints and is observed in S5 in the Nb-Al-Fe system. The liquidus temperature of S5 is approximately 1873°C, as deduced from the liquidus projection in [26, 219, 220] and the nominal composition is located almost on the NbAl₃-C14 eutectic valley, which indicates very limited primary solidification.

The positioning of the eutectic valley in the vicinity of S5 is also correct, since the measured composition of the 3-phase eutectic [NbAl₃ + C14 + Nb₂Al] corresponds very closely to that of the invariant 4-phase eutectic reaction in the liquidus projection [Figure 91(d)]. Therefore, the notable presence of primary NbAl₃ [Figure 91(a)] indicates that growth of C14 either as a halo or as coupled eutectic requires significant undercooling. This results in the liquid composition departing significantly from the NbAl₃-C14 eutectic valley and continuing on the metastable NbAl₃ liquidus surface.

The continued primary growth of NbAl₃ leads to depletion of Al in the liquid. The corresponding solid compositions will also lie beyond the solidus surface bounded by M₁M, as shown in Figure 93, when the primary phase shows solute solubility. In the case of significant undercooling when the extended liquidus surface lies below the Nb₂Al-C14 eutectic valley for the corresponding liquid composition, either Nb₂Al or C14 or both phases can nucleate on the primary solid.

The coupled growth of Nb₂Al + C14 constituting a two-phase halo implies that Nb₂Al + C14 coupled eutectic must grow at a smaller undercooling than either NbAl₃ + C14 coupled eutectic, NbAl₃ + Nb₂Al coupled eutectic, C14 halo or Nb₂Al halo on primary NbAl₃, as also observed in [26]. The growth of the halo phase is then followed by the invariant eutectic reaction, $L \rightarrow \text{Nb}_2\text{Al} + \text{C14} + \text{NbAl}_3$.

Finally, it is worth emphasising in these experiments because of the small size of sample large thermal gradients are achieved. For larger samples the cooling rates (V) are lower but at the same time there is also a lower directional heat flux (G). Consequently, in the case of halo growth it is not straightforward to qualitatively ascertain the change in G and V . When this term dominates, the halo growth is restricted since for a given velocity, the secondary phase grows with a higher undercooling compared to that for the non-equilibrium coupled eutectic.

Chapter 7 Solidification sequences and microstructure evolution of additive manufactured NbSi-based alloys

7.1. NbSi-based alloys results

The alloys prepared by the laser additive manufacturing process were analysed through SEM before and after HIP and heat treatment stages, to provide comparison and to observe possible formation or dissolution of phases for the given treatment, and XRD was needed in order to confirm the phases present in each case. Figure 94 presents the liquidus projection for the ternary Nb-Si-Ti system with the compositions superimposed.

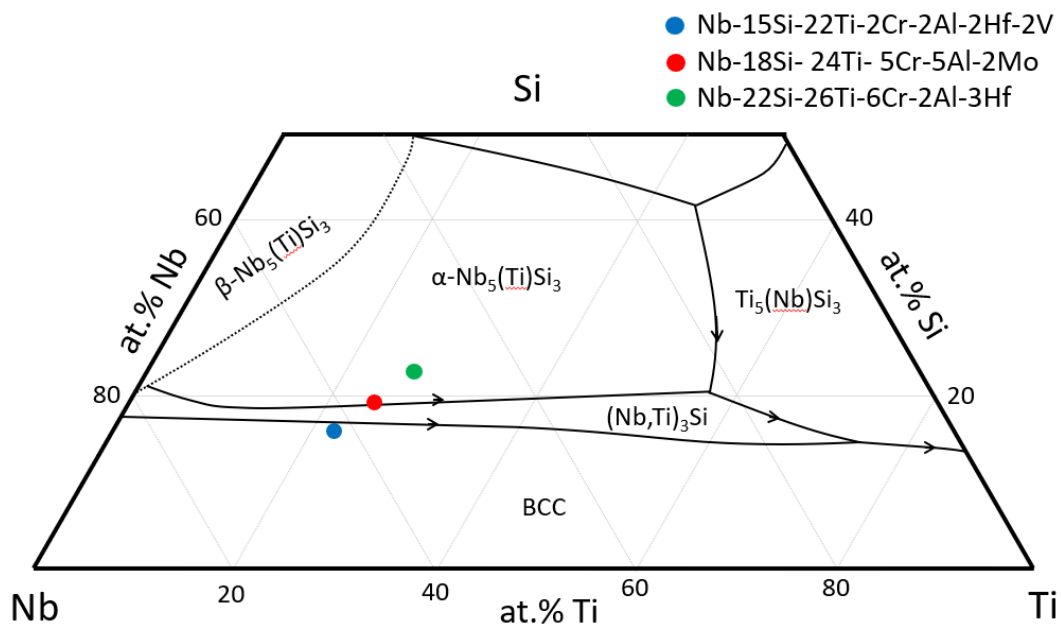


Figure 94 – Liquidus projection of ternary Nb-Si-Ti [70-72].

The choice of compositions has been made aiming to assess the increase in silicide phase formation and its impact on the microstructure evolution, which in turn will dictate the creep behaviour and the oxidation resistance.

7.1.1. Nb-15Si-22Ti-14Cr-2Al-2Hf-2V

No evidence of Nb₃Si phase was found in this alloy. Figure 95 presents the microstructure obtained with a primary bright Nb_{ss} phase, and from which is possible to see different shades of grey phases, suggesting the formation of both Nb₅Si₃ and Nb₃Si phases at first. Instead, the C15 Laves phase was formed (dark phase), which has a high amount of Cr, which cannot be ignored when analysing the ternary Nb-Si-Ti system, as the addition of alloying elements will affect the equilibrium diagrams.

From an approximated plot of composition in the liquidus projection, a detailed analysis of the solidification sequence of this alloy has been made. The nominal composition and the composition of phases observed are plotted in the diagrams in Figure 94.

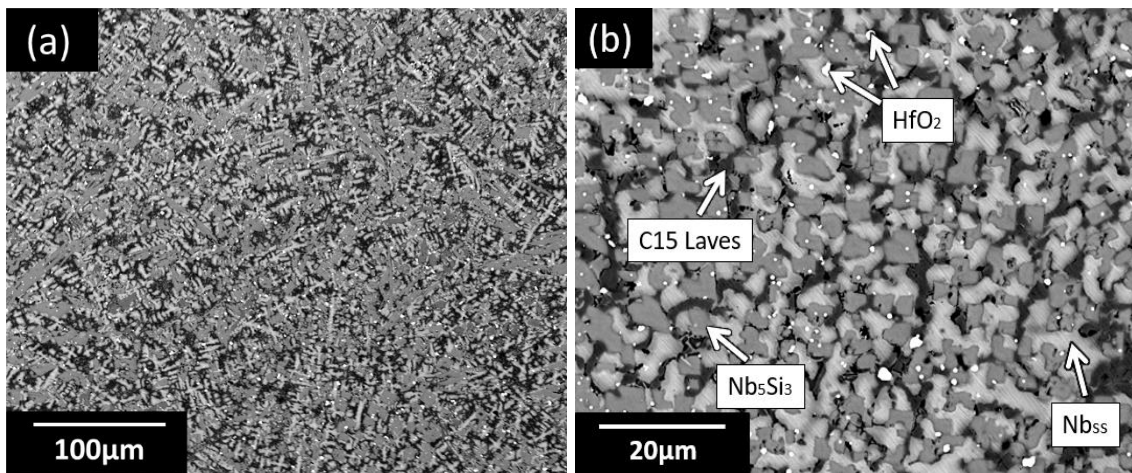


Figure 95 - BEI of Nb-15Si-22Ti-14Cr-2Al-2Hf-2V as-formed alloy, (a) low magnification and (b) high magnification.

The EDS analysis has shown the average composition of the phases found and it is presented in Table 34.

Table 34 - Average compositions (in at.%) of phases present in Nb-15Si-22Ti-14Cr-2Al-2Hf-2V alloy.

Phases	%Phases	Nb	Ti	Si	Cr	Al	Hf	V	O
Nb _{ss}	24.2	57.1	24.1	1.6	13.8	0.9	-	2.5	-
Nb(Ti) ₅ Si ₃	46.3	46.5	13.6	36.8	1.0	-	1.3	0.8	-
C15	20.2	27.7	14.1	10.4	42.4	-	1.6	3.8	-
HfO ₂	2.9	9.2	5.0	-	5.4	-	24.7	-	55.7

The as-formed microstructural analysis shows that the primary phase is Nb_{ss}, formed from $L \rightarrow \text{Nb}_{\text{ss}}$, although this cannot be confirmed without a multicomponent liquidus projection, which then should proceed to intersecting the (Nb_{ss} + Nb₃Si) eutectic surface, which is not observed, since Nb₃Si is not formed. Instead, there is a deviation from the equilibrium path of solidification, and the liquid proceeds to form a Nb(Ti)₅Si₃ phase, through the eutectic non-equilibrium reaction $L \rightarrow \text{Nb}_{\text{ss}} + \text{Nb}(\text{Ti})_5\text{Si}_3$.

Tewari et al. [221] have also observed this phenomenon. The substitution of Ti in Nb₃Si is expected to lower its temperature of formation, which does not affect the Nb₅Si₃ silicide, therefore when this silicide forms there is suppression of Nb₃Si.

The liquidus projection suggests a formation of the α -silicide for the Nb₅Si₃ phase, which was also inferred after EDS measurement. To support that affirmation, an XRD analysis was done, presented in Figure 96.

The characteristic observed in the microstructure then confirms a eutectic-like formation of $L \rightarrow \text{Nb}_{\text{ss}} + \text{Nb}_5\text{Si}_3$ in a cellular pattern with C15 phase forming in the interstices of the dendritic colonies.

The formation of the Laves phase occurs due to the Cr-enriched liquid, as the Cr solute was saturated in the Nb_{ss} and silicide phases, and it freezes as $L \rightarrow \text{C15}$.

The formation of the Laves phase is observed attached to the silicide boundaries, which is due to Cr rejection from the silicide to the solid solution phase [221]. Therefore, Cr solutes accumulated on the boundary led to the formation of a Cr-rich liquid that solidified as C15 Laves phase in the last stage of solidification.

Slight segregation is seen in these alloys, which can influence the composition measurement taken by EDS. Oxygen was found in the overall composition of the alloys, but present a low level as expected (the other were less than 2 at.%), which promoted the formation of HfO₂, seen sporadically throughout the microstructure. The formation of HfO₂ occurs first, when oxygen is consumed. The oxides then take the role of nucleant spots for the solidification to start.

The sequence of solidification under equilibrium conditions is detailed in Table 35, including the invariant reactions and the temperature in which they occur, with Nb₃Si indicated as suppressed (sup.) [70, 73, 222, 223].

Table 35 - Range of temperature for the suggested solidification path of Nb-15Si-22Ti-14Cr-2Al-2Hf-2V alloy.

Reaction	Temperature (°C)
$L \rightarrow Nb_{ss} + Nb_3Si$ (sup.)	1915-1916
$L \rightarrow C15$	1610-1650
$L + Nb_3Si$ (sup.) $\rightarrow Nb_{ss} + Nb_5Si_3$	1350

It is strongly suggested that the other elements (Al, Cr, V, Hf) combined have a great effect in the ternary Nb-Ti-Si phase equilibrium, which confirms the suppression of Nb_3Si , formed through peritectic reaction. For that reason, this alloy can be considered as a multi-component alloy rather than a ternary, given that the influence of the other elements used cannot be ignored having an impact on the solidification path analysed and the deviation caused.

An XRD analysis has been done to confirm the as-formed phases identified by EDS analysis, shown in Figure 96. It is observed that there is a clear formation of Nb_5Si_3 and Nb_{ss} phases, with HfO_2 showing weak peaks due to the small volume fraction which is hardly detected. The Laves phase has been identified as the cubic C15 form.

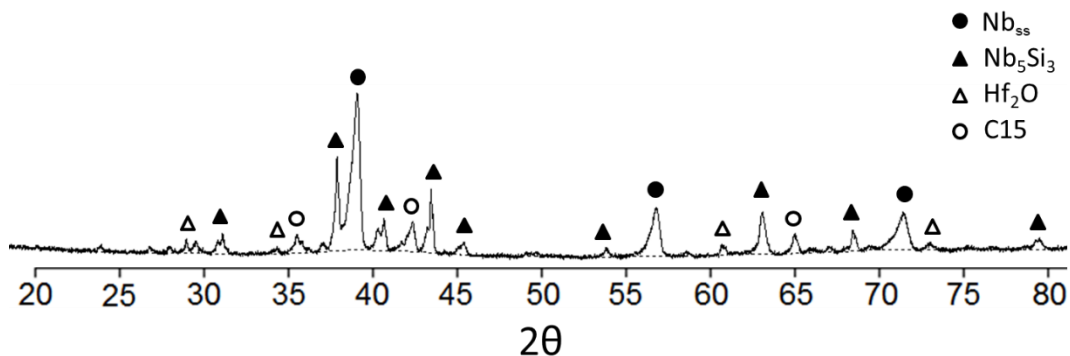


Figure 96 - XRD pattern for the as-formed Nb-15Si-22Ti-14Cr-2Al-2Hf-2V alloy.

As detailed in section 3.2.3, the alloying elements used stabilise and partition to the formation of Nb_5Si_3 -type silicide, and due to the large cooling rate of the LAM process, local equilibrium is lost and therefore the Nb_3Si -silicide region in the diagram is suppressed.

After the HIP processing stage, it is expected that the microstructure will show a slightly different phase composition, which is accounted for with the diffusion at

1200°C for a relative amount of time. This will impact on the microstructure evolution and the final properties of this alloy.

Figure 97 shows a low and high magnification BEI for the HIP processed Nb-15Si-22Ti-14Cr-2Al-2Hf-2V alloy. From Figure 97(a), it is clear that there has been a major change in morphology throughout the new microstructure.

The dendritic formation, for instance, has been observed to assume a cellular (and more regular) shape, with the inter-dendritic Nb₅Si₃ showing a fragmented morphology, when compared to that of the as-formed alloys, in Figure 96.

The presence of HfO₂ has not showed any significant difference, since the volume fraction and availability of elements made the change highly precluded, even at higher temperatures.

The most noticeable change is observed for C15 Laves phase, as the as-formed morphology presented a sporadic formation adjacent the Nb₅Si₃ silicide phase boundaries, which is now located adjacent to both the silicide and the solid solution Nb_{ss} phase, which suggests two possible reasons;

- (i) Diffusion of Cr from the Nb_{ss} solid solution phase takes place, with formation of new C15 phase grains adjacent to the Nb_{ss} phase, in addition to the previous as-formed formations.
- (ii) As C15 Laves phase contains a high amount of Cr (from Table 34), the HIP processing at temperature of 1200°C has nearly achieved the melting temperature of this phase, which would cause a high temperature plastic deformation and change of morphology to a slightly “squeezed” morphology.

Given that a significant diffusion from the Nb_{ss} for only 6 hours at 1200°C would be hardly achieved at a level suggested in (i), it is highly likely that suggestion (ii) is correct. This assumption would then presume that, because the melting temperature of C15 is nearly reached, this would allow the phase to deform around both the Nb₅Si₃ silicide and the Nb_{ss} solid solution phases, which is corroborated in the detailed BEI in Figure 97(b).

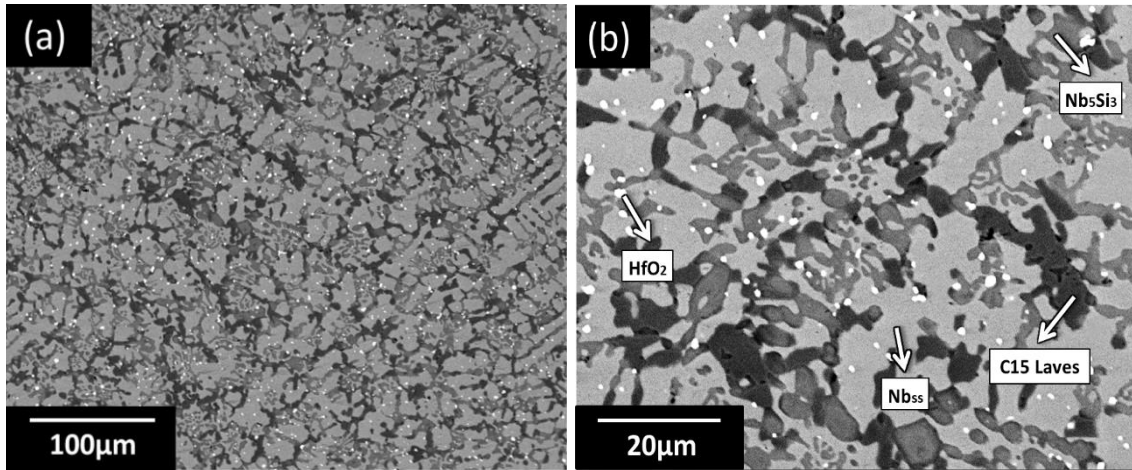


Figure 97 - BEI of Nb-15Si-22Ti-14Cr-2Al-2Hf-2V alloy after HIP process, (a) low magnification and (b) high magnification.

The composition of phases analysed after HIP processing is shown in Table 36, where it can be seen that the diffusion that took place during this process has significantly changed the Ti solute content of Nb_{ss} and C15 phase towards the silicide phase. An increase of Cr content has also seen for C15, when Cr diffuses mainly from the HfO₂, which is not expected to support solid solution.

Table 36 - Average composition (in at.%) of phases present in HIP processed Nb-15Si-22Ti-14Cr-2Al-2Hf-2V alloy.

Phases	%Phases	Nb	Ti	Si	Cr	Al	Hf	V	O
Nb _{ss}	42.4	58.6	23.5	1.3	13.7	-	-	2.6	-
Nb(Ti) ₅ Si ₃	39.1	50.0	15.3	31.2	2.0	-	0.8	0.7	-
C15	16.4	28.0	12.7	11.3	44.1	-	0.8	3.1	-
HfO ₂	2.1	13.2	4.7	-	2.8	-	20.9	0.5	57.9

After heat treatment for 1 hour at 1500°C, a significant coarsening has already taken place for all phases observed, as shown in Figure 98(a). A complete change of morphology of phases is clearly seen and, given that diffusion would be precluded for the period of time tested, a coarsening effect have occurred, for the silicide phases that were entrapped within cellular Nb_{ss} phase to change to a regular and more circular Nb₅Si₃ phase, seen in detail in Figure 98(b).

Moreover, there has been a noticeable change regarding the morphology of C15 Laves phase, which shifted from a “squeezed” morphology (observed in Figure 97(b)). However, as observed in Figure 98(b), the morphology not only changed

but is now placed surrounding the silicide globes. From these observations, three suggestions could be made to explain this phenomenon;

- (i) As suggested previously for both Nb_{ss} and Nb_5Si_3 phases, there has been a clear coarsening of C15 Laves phase adjacent to the Nb_{ss} dendritic pattern. This would mean that, as the Nb_{ss} phase coarses, so does C15 Laves, which then surrounds the silicide blocks.
- (ii) If (i) is true, it means that C15 Laves phase is a nucleant agent for the Nb_5Si_3 silicide phase, which would possibly recrystallise new grains around C15.
- (iii) Differently from (i) and (ii) and given that C15 Laves phase contains a high amount of Cr, there is likely a local re-melting of Laves phase when the temperatures approached 1500°C.

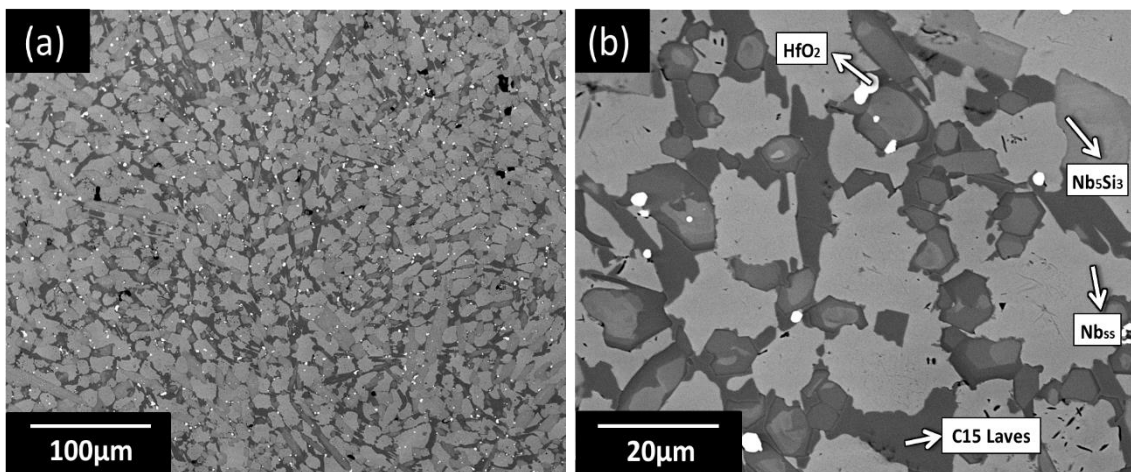


Figure 98 - BEI of Nb-15Si-22Ti-14Cr-2Al-2Hf-2V alloy after heat treatment process, (a) low magnification and (b) high magnification.

Both suggestions (i) and (ii) depend on the diffusion to take place and promote the coarsening throughout the whole microstructure. Besides, it is highly unlikely that Nb_5Si_3 would nucleate adjacent to C15 Laves phase simply because a possible recrystallisation temperature of Nb_5Si_3 would far exceed the melting temperature of C15 Laves.

This conclusion means that, not only suggestion (iii) is correct, but both Nb_{ss} and Nb_5Si_3 coarses as C15 Laves phase re-melts, which would cause the low density Nb_5Si_3 silicide globes to float within a viscous C15 phase. Therefore, as C15 solidifies adjacent to the Nb_{ss} phase, it entraps and surrounds the silicide.

To further analyse this, the isothermal section at 1500°C for the Nb-Ti-Cr system, shown in Figure 99, has been used to provide a theoretical overview of what has been discussed for the re-melting of C15 phase. From the likely position of C15 Laves composition (grey square), it is possible to observe that there could be the presence of a remaining liquid for this system.

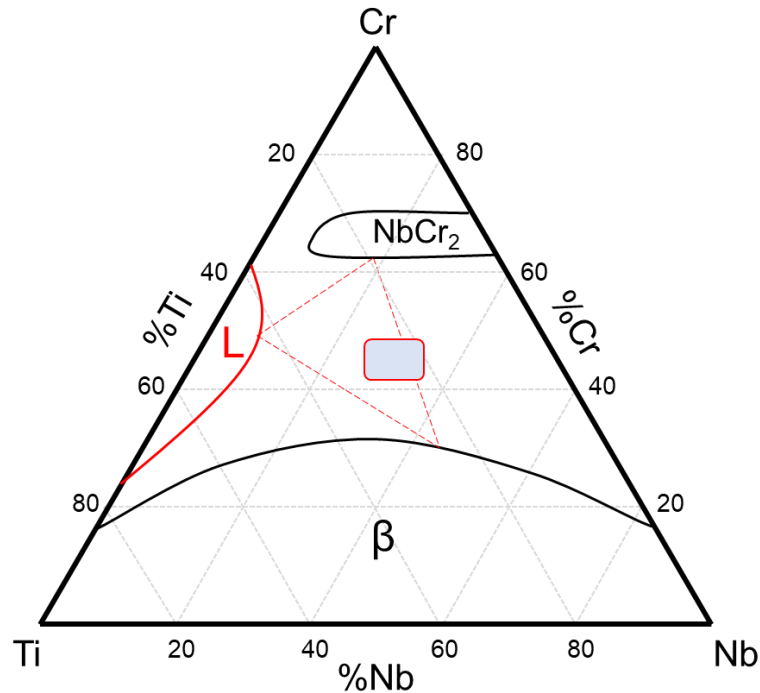


Figure 99 - Isothermal section at 1500°C for the Nb-Ti-Cr system, showing the likely position of the C15 Laves phase composition [224].

To prove this, a DSC (Differential Scanning Calorimetry) analysis has been carried out at 1500°C to verify the possibility of local re-melting of C15 phase. Figure 100 shows the result obtained, where local re-melting of C15 Laves phase, shown by the presence of heat flow peaks, is observed at temperature around 1440°C, which is significantly below the heat treatment temperature. This melting has been further confirmed visually, where the sample tested was glued into the crucible.

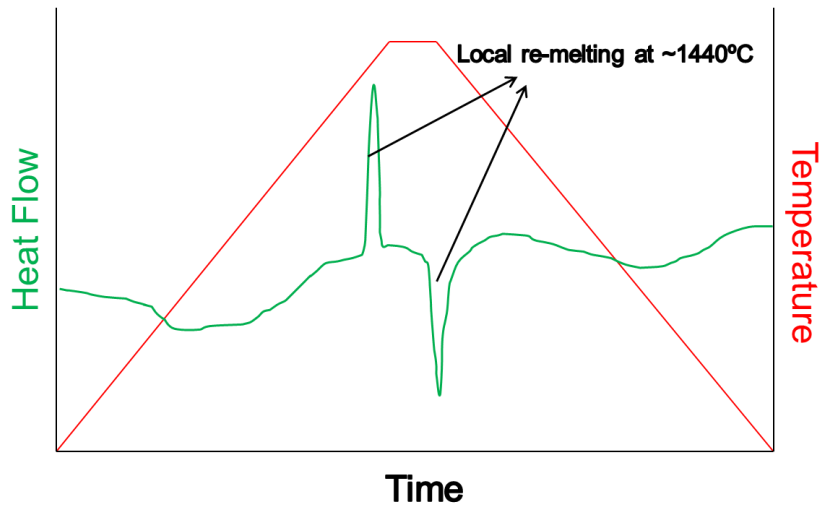


Figure 100 - DSC curve analysis of heat treated Nb-15Si-22Ti-14Cr-2Al-2Hf-2V alloy at 1500°C.

The composition of the phases analysed after heat treatment is shown in Table 37. It is clear that the slight reducing Nb content for the Nb_{ss} phase is due to the increase in Ti diffusion and the fact that Al (not shown for as-formed and HIP processed, since the very small contents cannot always be detected by EDS analysis) has showed to be present at about 3.1 at.%.

It is also noted that the composition of C15 Laves phase has remained fairly constant, since it has been proved that there was local re-melting, which then suggests that the diffusion that took place had no impact on its composition.

Table 37 - Average composition (in at.%) of phases present in heat treated Nb-15Si-22Ti-14Cr-2Al-2Hf-2V alloy.

Phases	%Phases	Nb	Ti	Si	Cr	Al	Hf	V	O
Nb _{ss}	41.7	58.1	22.9	-	12.6	3.3	-	2.9	-
Nb(Ti) ₅ Si ₃	29.2	46.8	16.2	35.5	-	-	1.5	-	-
C15	27.6	27.5	13.1	10.2	44.4	1.5	-	3.4	-
HfO ₂	1.5	13.2	-	-	-	-	31.3	-	68.7

Figure 101 shows the microstructure evolution for the Nb-15Si-22Ti-14Cr-2Al-2Hf-2V alloy through the three stages of processing; namely as-formed, HIP processed, and heat treated.

As the processes take place, a clear phenomenon of coarsening has been observed, which is attributed to the high temperatures involved during the HIP

and heat treatment stages that trigger solute diffusion and coarsening. The pressure applied during HIP, coupled with the fact that the temperature of 1200°C used for this process has reached around 83% of the melting temperature, since re-melting took place at 1440°C, has caused a deformation of the dark C15 Laves phase morphology.

Moreover, the re-melting of C15 observed after heat treatment stage has surrounded the globular Nb₅Si₃ silicide phases, occupying the areas between the solid solution and the silicide phase. This phenomenon can be therefore attributed to the high amount of Cr added to the composition (nominal 14 at.%) promoting the Laves phase.

It is also worth of noticing that, although diffusion is precluded at the tested temperatures and period of times, there has been a balancing of elements, more significantly after 1500°C heat treatment, which has caused a decrease in the contrast of the back-scattered electron images.

The additions of V, Hf, and Al in addition to the high levels of Cr and Ti have caused the suppression of Nb₃Si phase expected under equilibrium conditions. The promotion of Nb₅Si₃ silicide phase has been observed instead, which confirm what has been found from previous studies [13, 96, 99, 101, 102, 131].

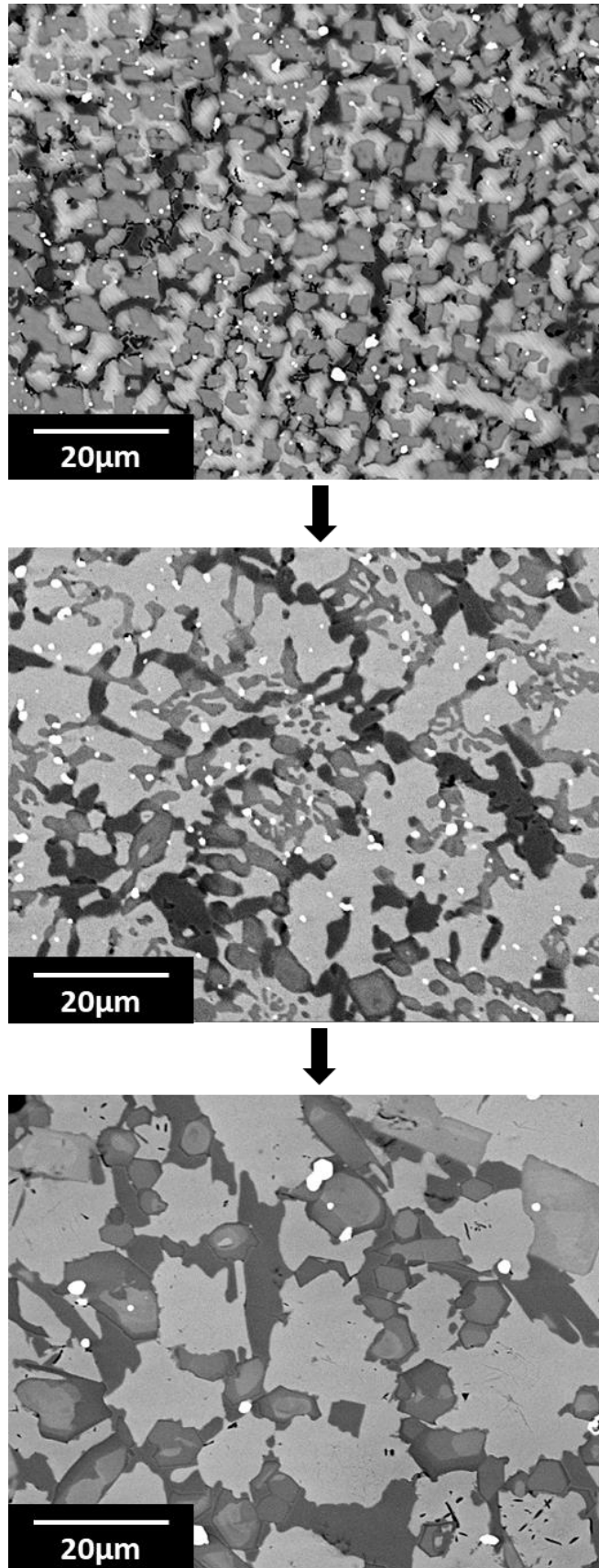


Figure 101 - Microstructure evolution of Nb-15Si-22Ti-14Cr-2Al-2Hf-2V alloy from as-formed to HIP process to heat treatment stages.

7.1.2. Nb-15Si-22Ti-2Cr-2Al-2Hf-2V

Differently from the alloys previously presented (in section 7.1.1.), this composition presents a much lower amount of Cr (nominally 2 at.%). This results in a very different microstructure, especially regarding the notable absence of the C15 Laves phase, with a dendritic characteristic. A BEI of as-formed Nb-15Si-22Ti-2Cr-2Al-2Hf-2V alloy microstructure in low and high magnification is shown in Figure 102.

The low magnification microstructure [Figure 102(a)] shows the formation of the grey primary phase Nb_{ss}, which is highly predominant. A fine eutectic formation is observed in the channels between the dendrites, formed from the liquid remaining during the solidification, seen in detail in Figure 102(b).

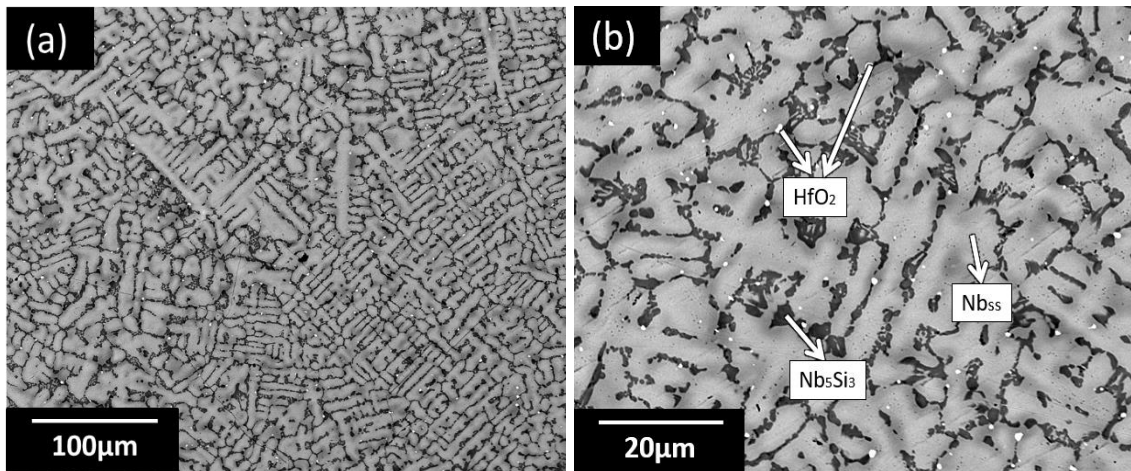
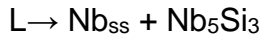
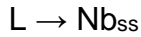


Figure 102 - BEI of as-formed Nb-15Si-22Ti-2Cr-2Al-2Hf-2V alloy, (a) low magnification and (b) high magnification.

The composition plotted in the ternary diagram presented in Figure 94 confirms the primary formation of a solid solution Nb_{ss} phase. Following primary solidification, the liquid composition would traverse the eutectic valley Nb_{ss} + Nb₃Si, which here is also suppressed.

The high magnification image in Figure 102(b) presents a detailed observation of the microstructure of the alloy. Through EDS analysis, it is possible to determine the formation of a fine Nb_{ss} + Nb₅Si₃ eutectic morphology in between the primary dendrites. This reaction follows the suppression of Nb₃Si, when the liquid traverses to the eutectic formation $L \rightarrow \text{Nb}_{\text{ss}} + \text{Nb}_5\text{Si}_3$, therefore the solidification sequence can be described as follows;



Similarly to the Nb-15Si-22Ti-14Cr-2Al-2Hf-2V alloy, the amount of Hf was sufficient to form HfO₂ oxides when in presence of residual oxygen, which are formed in the early stages of solidification and function as nucleation spots for the primary dendrites.

A solute distribution throughout the primary Nb_{ss} phase is noticed, characterised by shadows of light grey tone in the edges of the dendrites, which means that a decreasing amount of Ti and Si is located in their cores.

The extent of Nb_{ss} clearly indicates that the high Cr addition is associated with and extensive change in the liquidus projection, which will most likely shift the equilibrium of the single-phase surfaces.

This reduced Cr seen for the Nb-15Si-22Ti-2Cr-2Al-2Hf-2V alloy shows the closest behaviour possible to a pure ternary Nb-Si-Ti alloy. Other alloying elements only add to 8 at.% of the nominal composition, which results in a suppression of Nb₃Si and were responsible for the large dendritic formation of Nb_{ss} phase.

An analysis made by XRD verified the phases suggestions ascertained from the microstructure and EDS analysis, which is presented in Figure 103. This analysis shows a sharp and predominant presence of Nb_{ss} peaks, with minor presence of Nb₅Si₃ silicide phase and a very small detection of HfO₂ oxide.

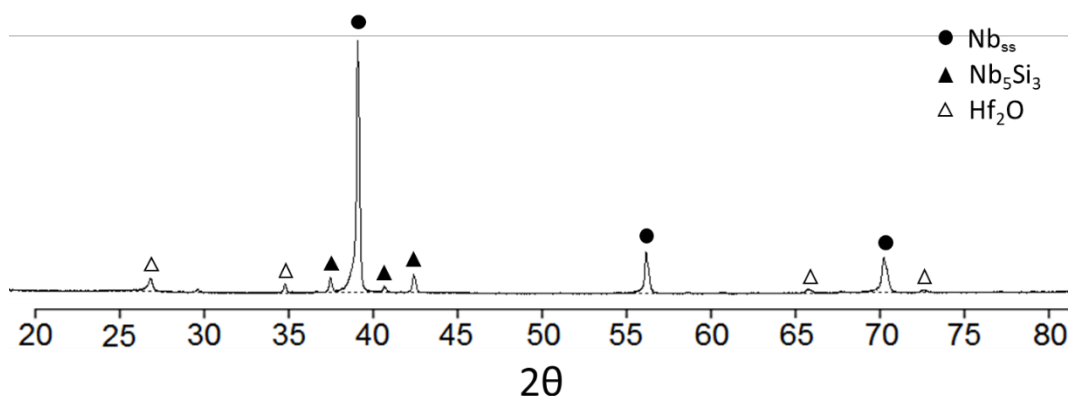


Figure 103 - XRD pattern for the as-formed Nb-15Si-22Ti-2Cr-2Al-2Hf-2V alloy.

Also from EDS analysis, the average composition of the phases and the volume fraction have been found, which are presented in Table 38. The analysis has

been carried out towards the centre of the alloy, where a better homogeneity was found.

Table 38 – Average composition (in at.%) of phases present in Nb-15Si-22Ti-2Cr-2Al-2Hf-2V alloy.

Phases	%Phases	Nb	Ti	Si	Cr	Al	Hf	V	O
Nb _{ss}	79.4	68.4	22.4	2.1	1.9	2.2	1.2	1.8	-
Nb(Ti) ₅ Si ₃	20.1	29.2	29.1	34.7	0.7	1.3	3.9	1.1	-
HfO ₂	0.5	6.8	2.9	-	-	-	26.7	-	63.6

The measure presented in Table 38 shows the discussed disparity between Nb_{ss} phase (and also HfO₂ oxide) volume fraction when compared to the previously discussed Nb-15Si-22Ti-14Cr-2Al-2Hf-2V alloys, shown in Table 34. There is also a noticeable amount of elements in the solid solution with Nb_{ss} phase, whilst the silicide Nb₅Si₃ presented a considerable content of Ti and Hf.

After HIP processing, there is a clear coarsening of the primary dendrites of Nb_{ss} phase, which is expected to occur given the nature of this process involving high temperature and pressure, which triggers diffusion. Figure 104 shows BEI's for the Nb-15Si-22Ti-14Cr-2Al-2Hf-2V alloys.

From Figure 104(b), it is possible to observe that the fine eutectic formation has also coarsened to a significant degree. This is important and can be attributed to the following reasons;

- (a) The inter-dendritic channels that previously showed a formation of a fine Nb_{ss} + Nb₅Si₃ eutectic have been partially dissolved into larger Nb_{ss} formations originating from the secondary dendritic arm branching, which in turn caused the coarsening of Nb_{ss} morphology, changing from a typical dendritic structure to a cellular-like structure, in some parts.
- (b) There is significant diffusion of Ti and Si from the Nb_{ss} towards the Nb₅Si₃ silicide phase, which is observed by the reduced difference in contrast between these two phases. This diffusion would then be responsible for the coarsening of the inter-dendritic Nb₅Si₃ silicide.

Both points (a) and (b) would suggest that there exists a mutual diffusion to and from both the solid solution Nb_{ss} and the Nb₅Si₃ silicide phases, where very fine

eutectic-like formations of the silicide phase would dissolve into the Nb_{ss} solid solution at the same time where there is a coarsening of Nb₅Si₃ from the solute diffused from the Nb_{ss} phase. Therefore, this would cause the coarsening of the whole morphology.

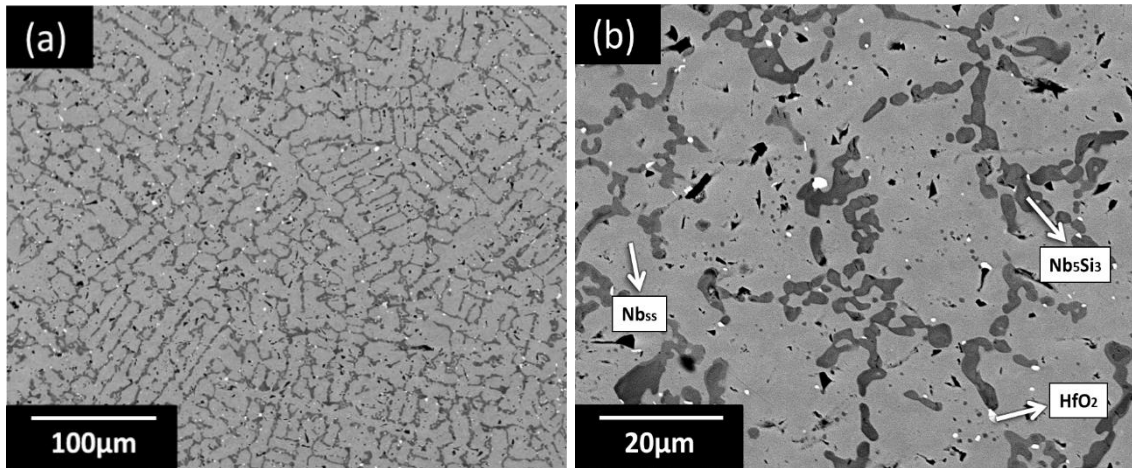


Figure 104 - BEI of Nb-15Si-22Ti-2Cr-2Al-2Hf-2V alloy after HIP process, (a) low magnification and (b) high magnification.

The composition of phases analysed after HIP processing is shown in Table 39, which corroborate the aspects discussed in points (a) and (b) regarding diffusion and balance of composition.

Table 39 - Average composition (in at.%) of phases present in HIP processed Nb-15Si-22Ti-2Cr-2Al-2Hf-2V alloy.

Phases	%Phases	Nb	Ti	Si	Cr	Al	Hf	V	O
Nb _{ss}	75.4	64.0	26.6	-	2.6	3.3	1.0	2.5	-
Nb(Ti) ₅ Si ₃	23.5	31.0	26.7	36.4	-	1.4	3.4	1.1	-
HfO ₂	1.1	5.0	4.6	-	-	-	24.5	-	65.9

There is a clear diffusion of Ti from the Nb₅Si₃ silicide phase to the solid solution Nb_{ss}, which is the main reason for the reduced contrast difference between the two phases. Moreover, part of the Nb and Si solutes is diffused into the silicide. The other alloying elements measure remained relatively constant, with the omission of low content elements that are difficult to detect by the EDS analysis. After the heat treatment stage, coarsening to a limited extent has been observed, as shown in Figure 105(a), which reflects the influence of temperature on

diffusion. Because of that diffusion, the eutectic-like morphology has been transformed to a cellular pattern of $Nb_{ss} + Nb_5Si_3$, as seen in Figure 105(b).

Furthermore, there has been a migration of Ti solute towards the centre of the Nb_5Si_3 silicide phase, indicated by the increasing contrast when compared to the edges of the silicides that are adjacent to the Nb_{ss} phase.

The microstructure obtained is expected under equilibrium conditions, since the composition has a low total of alloying elements, therefore the influence of both HIP and heat treatment stages on the final microstructure will not be significant for the morphology, but for solute diffusion to and from both major phases Nb_{ss} and Nb_5Si_3 , which is contrary to that observed for an alloy with higher Cr addition where coarsening took place.

The composition of phases analysed after heat treatment processing is shown in Table 40, where it can be observed how the Nb_5Si_3 silicide phase has migrated from a single homogenous phase to a dual-phase morphology where there is concentration of Ti towards the centre.

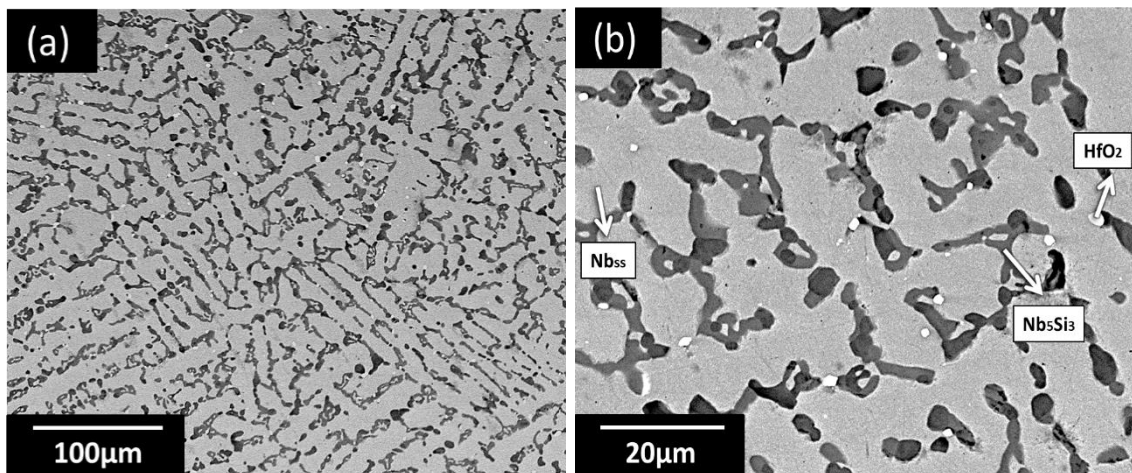


Figure 105 - BEI of the centre of Nb-15Si-22Ti-2Cr-2Al-2Hf-2V alloy after heat treatment, (a) low magnification and (b) high magnification.

The Ti-rich Nb_5Si_3 formation indicates that the high temperature of 1500°C used for heat treatment has impacted on the final microstructure evolution. From this, two possibilities arise;

- 1) The formation of a Ti-rich Nb_5Si_3 will cause the disappearance of the remaining fine silicides located in the channels between the dendrites (and the newly formed cellular) of Nb_{ss} phases, whilst the larger eutectic-

like silicides will transform into globes of Nb₅Si₃ silicides concentrated in Ti, which is similar to a spheroidisation process.

- 2) If the heat treatment is continued for longer periods, it is highly likely that Ti solute will continue the diffusion towards the centre of the silicides, causing a solid-state precipitation into a Ti-rich phase.

The presence of a Ti-rich silicide and its implications will be discussed in section 7.1.3, where a focus is given to this phenomenon. This observance is attributed to the addition of 22 at.% of Ti to the nominal composition, which is considerably high and favours the formation of high Ti phases.

Table 40 - Average composition (in at.%) of phases present in the heat treated Nb-15Si-22Ti-2Cr-2Al-2Hf-2V alloy.

Phases	%Phases	Nb	Ti	Si	Cr	Al	Hf	V	O
Nb _{ss}	66.9	64.1	27.2	1.8	2.0	2.4	-	2.5	-
Nb(Ti) ₅ Si ₃	27.6	42.8	18.4	36.3	-	-	2.4	-	-
Ti-rich Nb ₅ Si ₃	2.1	26.5	33.6	35.5	-	-	3.1	1.3	-
HfO ₂	3.4	5.5	4.1	-	-	-	22.9	-	67.5

Another observation worth mentioning is that, even though the processes of HIP and heat treatment at high temperatures have been carried out, the segregation observed towards the edges of this alloys has not been completely resolved.

Figure 106 shows a back-scattered electron image (BEI) of the edges of Nb-15Si-22Ti-2Cr-2Al-2Hf-2V alloy, which shows the effect of segregation in the final microstructure. When compared to the microstructure presented in Figure 105, it is clear that a significant segregation of Hf is directed towards the edges, evidenced by the high presence of HfO₂ oxide particles.

From Figure 106(a), it is also possible to observe that the coarsening of both the silicide and the solid solution phases are less prominent, given by the presence of untransformed eutectic-like morphology of Nb_{ss} + Nb₅Si₃ located in the interdendritic region, shown in detail in Figure 106(b). Moreover, the diffusion of Ti is not as strongly seen towards the centre of the silicide formations, although some limited Ti-rich characteristics are observed.

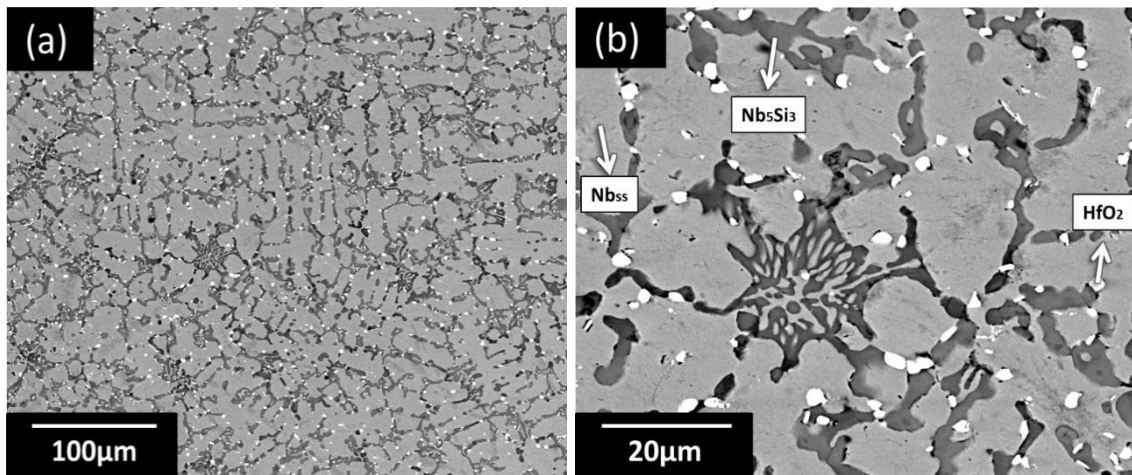


Figure 106 - BEI of the edge of Nb-15Si-22Ti-2Cr-2Al-2Hf-2V alloy after heat treatment, (a) low magnification and (b) high magnification.

Figure 107 shows the microstructure evolution for the Nb-15Si-22Ti-2Cr-2Al-2Hf-2V alloys through the stages of processing; as-formed, HIP and heat treated.

The as-formed alloy presents a dendritic structure of primary Nb_{ss} solid solution phase followed by an inter-dendritic formation of a eutectic Nb_{ss} + Nb₅Si₃ showing a cellular morphology, and the presence of bright HfO₂ oxide particles, which have been produced by oxygen contamination during the laser formation.

Limited micro-segregation is observed from the core to the edges of the Nb_{ss} dendrites, when Ti is shown to be adjacent to the silicide formations. This is confirmed when further segregation is observed at the edges of the alloy after post processing, showing a significant presence of HfO₂ particles and a weak dissolution of the pockets of cellular eutectics, shown in Figure 106(a).

When HIP is completed, there is coarsening of the solid solution and the silicide phases, with the dissolution of silicide “branches” and thickening of larger Nb₅Si₃ particles, likely from the movement of Ti and Si solute between both phases.

The heat treatment stage has accentuated the Ti diffusion towards Ti-rich localised spots, where there is the possibility of a new Ti-rich phase formation, and at this point, the morphology changes to a cellular/globular structure.

The difference in Cr addition by reducing this element from 14 to 2 at.% has proved to play a key role into changing the microstructure, which has approached the predicted structure under equilibrium formation, while maintaining the remaining elements at low levels.

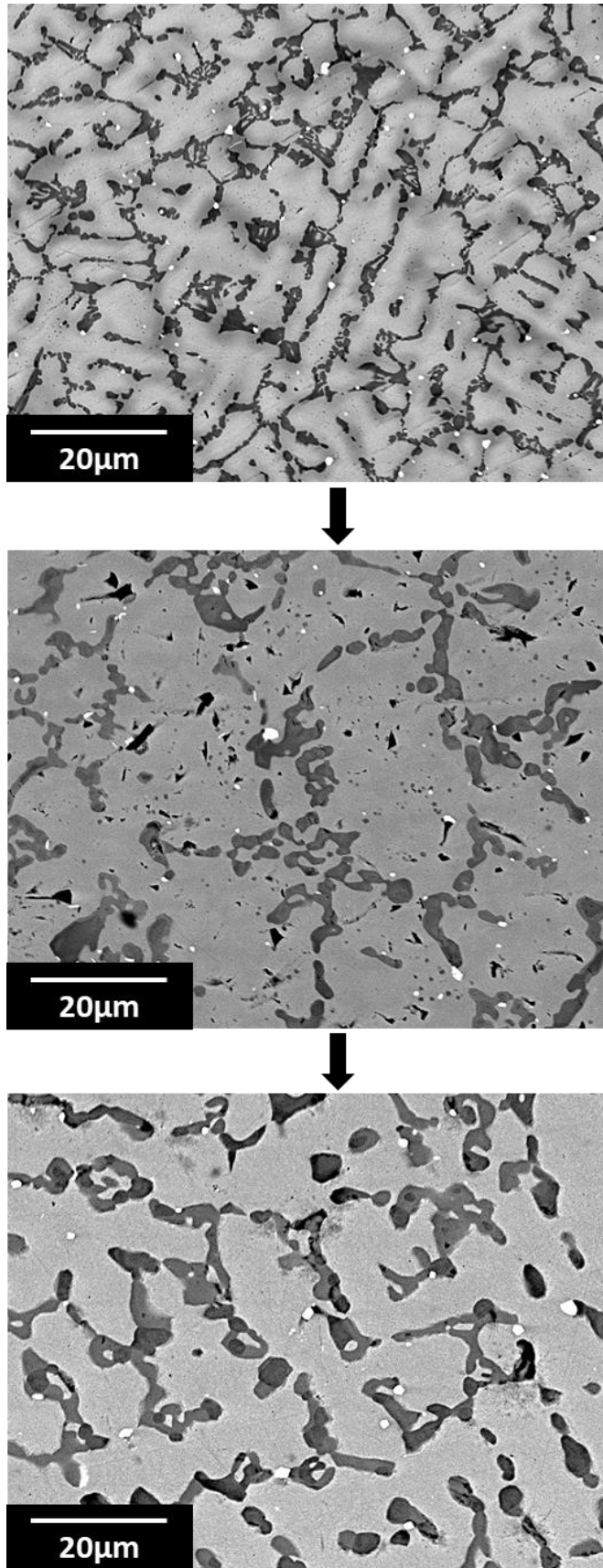


Figure 107 - Microstructure evolution of Nb-15Si-22Ti-2Cr-2Al-2Hf-2V alloy from as-formed to HIP process to heat treatment stages.

7.1.3. Nb-18Si-24Ti-5Cr-5Al-2Mo

Alloys prepared with this composition have been prepared using different scanning speeds in the LAM machine and different powder conditions (new or recycled). It was found that those different conditions have not changed the phases presented, although faster scan speeds and recycled powder showed finer the microstructure.

The composition plotted in Figure 94 suggests a formation of Nb_5Si_3 as primary phase close to the peritectic valley, and the sequence of freezing expected, including the invariant reactions and the temperature in which they occur, is describe as follows;

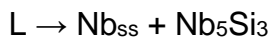


Figure 108 presents the BEI of as-formed Nb-18Si-24Ti-5Cr-5Al-2Mo alloy microstructure in low and high magnification. A dendritic primary Nb_{ss} structure forming a eutectic pattern of $Nb_{ss} + Nb_5Si_3$ throughout the alloy, and a dark formation is observed in the eutectic channels. Moreover, a layer richer in Ti can be seen forming in the boundaries between Nb_{ss} and Nb_5Si_3 phases.

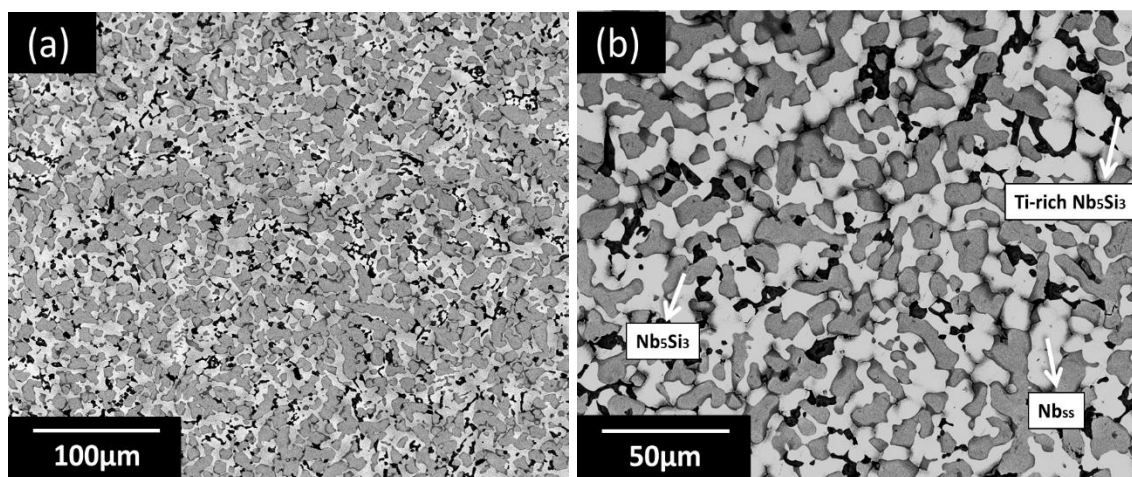


Figure 108 - BEI of as-formed Nb-18Si-24Ti-5Cr-5Al-2Mo alloy, (a) low magnification and (b) high magnification.

From EDS analysis, the composition of phases can be observed in Table 41, also plotted with the nominal composition seen in Figure 94, in order to determine the

path of solidification of this alloy. The bright phase is the primary Nb(Ti)₅Si₃ containing a high number of elements in solid solution, growing in a dendritic pattern and forming eutectics with a light grey Nb_{ss} phase [Figure 108(b)], which is stabilised by the addition of Ti. A third dark colour is also identified, and at first glance it can be considered as a new phase. Although, EDS suggests a composition similar to Nb₅Si₃ phase, this is possible due to the large extent of the Nb₅Si₃ phase region with varying Ti contents.

Table 41 – Average composition (in at.%) of phases in the as-formed Nb-18Si-24Ti-5Cr-5Al alloy.

Phases	%Phase	Nb	Ti	Si	Al	Cr	Mo
Nb _{ss}	38.4	55.4	28.4	1.8	5.6	6.1	2.6
Nb ₅ Si ₃	39.2	48.0	15.7	29.9	2.5	0.8	1.1
Ti-rich Nb ₅ Si ₃	22.4	33.7	28.5	32.1	3.3	1.1	0.9

A initial observance of this phenomena was made when first comparing the composition of such phases with that tested by Li et al. [109], it can be seen that they can be, in fact, the same phase with different Ti content, and this occurs due to the Nb₅Si₃ region in the ternary diagram extending throughout a high range of Ti solubility, hence raising the possibility to obtain the same Nb₅Si₃ phase with 10 and 30 at.%, namely a large miscibility gap, which is also influenced by the rapid solidification rate proportioned by this processing method.

As temperature decreases rapidly, there is also a decrease of solubility of Ti in the silicide that follows, hence the rejection of solute to the freezing liquid that solidifies as the Ti-rich silicide. This is evidenced from the microstructure pattern observed, with the dark silicide phase forming adjacent to the eutectic cellules.

Figure 109 presents the isothermal section at 1200°C with the measured composition of phases superimposed. A clearly seen the formation of separated Nb₅Si₃ silicides is seen, according to compositions shown in Table 41. A three-phase tie-triangle region is replaced by a two-phase tie-line with Nb₅Si₃ + Nb_{ss}.

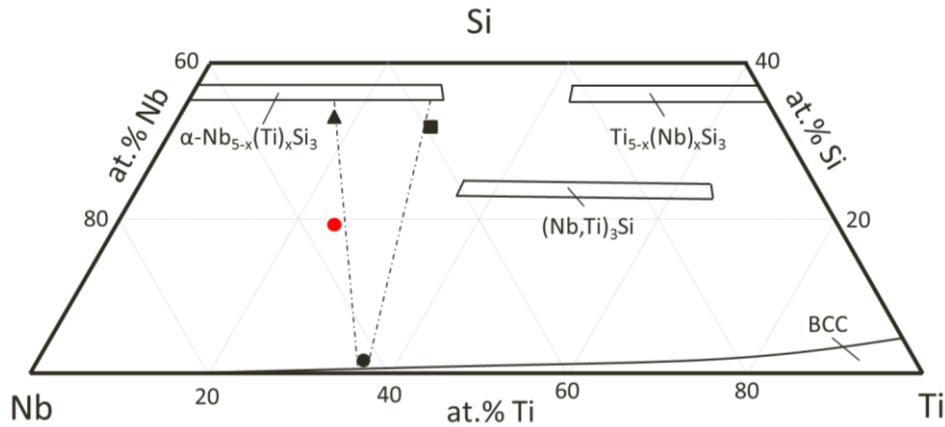


Figure 109 - Isothermal section at 1200°C with measured compositions of phases present in the Nb-18Si-24Ti-5Cr-5Al-2Mo alloy [73]. Solid triangle and square represent Nb₅Si₃ phase; solid circle represents solid solution phase.

The Nb₅Si₃ phase indeed forms a second time, with different contents of Ti, which is clearly seen from Figure 109, where two compositions fall within the Nb₅Si₃ silicide phase region. Because of that, the solidification path was analysed in detail and it is concluded that the solidification pattern forms a eutectic like structure from the liquid giving the primary silicide and the solid solution phase through $L \rightarrow \text{Nb}_5\text{Si}_3 + \text{Nb}_{\text{ss}}$, at this point not all liquid has been consumed, which contains a higher content of Ti solute, hence the liquid solidifies as $L \rightarrow \text{Nb}_5\text{Si}_3$ once more with a different composition in the last stage of solidification. This phenomenon produces the characteristic observed in Figure 108, where a higher Ti containing Nb₅Si₃ is present in channels between the eutectic Nb(Ti)₅Si₃ + Nb_{ss} eutectic.

From that, the role of elemental addition arises. The combined amount of Cr + Al is as high as 10 at.%, and it is known that both elements promote and stabilise formation of Nb₅Si₃ phase. This remark supports the conclusion of suppression of Nb₃Si, which is also influenced by the freezing velocity. Cr also promotes the formation of the C15 Laves phases, but at higher amounts, thus all the Cr is in solid solution with Ti in the Nb_{ss} phase.

The high amount of Ti is still not enough to promote the formation of Ti-silicide, which is due to a higher amount of Nb and lower amount of Si, as it can be seen in the diagrams in Figure 94. Therefore, Ti substitutes Nb in the solid solution phase Nb_{ss} and the Nb-silicide phases.

Under equilibrium conditions, and according to the liquids projection, Nb_3Si phase would not have been suppressed and the formation of the eutectic phases would follow the formation of $\text{Nb}_5\text{Si}_3 + \text{Nb}_3\text{Si}$, where the Nb_3Si would be decomposed into the eutectoid reaction $\text{Nb}_3\text{Si} \rightarrow \text{Nb}_{\text{ss}} + \text{Nb}_5\text{Si}_3$.

Figure 110 shows the microstructure obtained after HIP stage, where it is observed that there has been a decrease in the overall difference in contrast, especially regarding the difference in Ti from both Nb_5Si_3 silicide phases. This indicates that diffusion, even though it can be restricted, takes place at temperature of 1200°C and above, where Ti solute is distributed between both silicides.

Coarsening is not significant, unlike previously observed for alloys containing lower Ti contents. The increase in Ti from 22 to 24 at.% has been responsible for the promotion of the Ti-rich silicide phase in the as-formed alloy, which has only been observed for heat treated alloys with 22 at.% of Ti, in section 7.1.2. It is clear then that this increase in Ti will govern the final microstructure of this alloy, throughout all stages of processing.

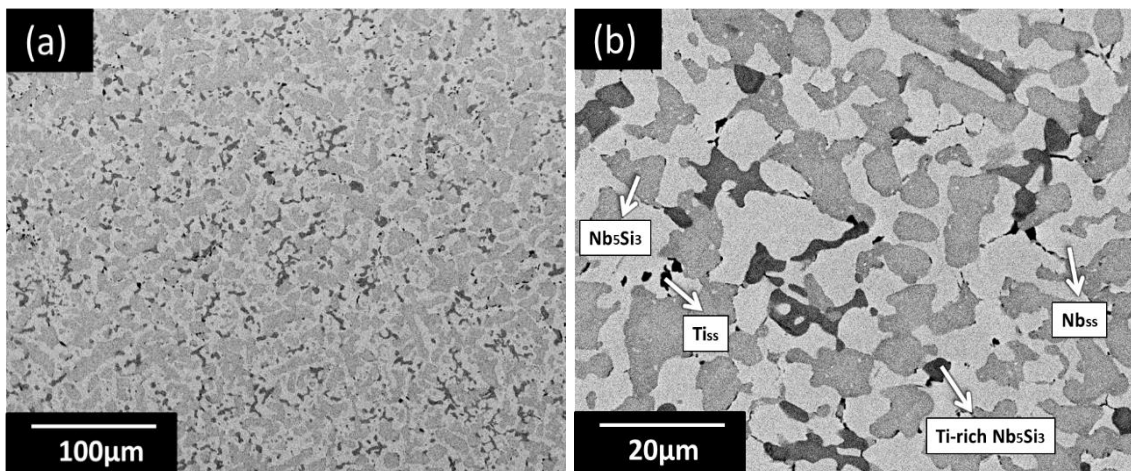


Figure 110 - BEI of HIP processed Nb-18Si-24Ti-5Cr-5Al-2Mo alloy, (a) low magnification and (b) high magnification.

This is confirmed by the presence of a Ti-rich dark phase formations seen in detail in Figure 110(b). As Ti diffuses from the Ti-rich silicide towards the lower Ti-containing silicide, there is a movement of Ti solute to the centre of the Ti-rich Nb_5Si_3 phase. With heat treatment at 1500°C, it is highly likely that this observance will be accentuated, as a higher temperature will trigger a higher

diffusion of solute. The difference in solute observed by the measured phases compositions are presented in Table 42.

The analysis of phases compositions can reveal that diffusion in fact takes place, when there is a decrease of Ti in the Ti-rich Nb₅Si₃ silicide that diffuses to the major Nb₅Si₃ phase, shown by the increase of Ti for this phase. The formation of Ti_{ss} is still very limited, restricted to a volume fraction of only 0.8%, and a very high concentration of Ti solute.

Table 42 - Average compositions (in at.%) of phases present in Nb-18Si-24Ti-5Cr-5Al-2Mo alloy after HIP process.

Phases	%Phase	Nb	Ti	Si	Al	Cr	Mo
Nb _{ss}	41.3	52.7	27.6	3.4	5.7	8.1	2.4
Nb ₅ Si ₃	42.5	44.5	18.6	30.1	3.2	2.6	0.8
Ti-rich Nb ₅ Si ₃	15.4	38.4	27.5	29.3	2.1	1.2	0.8
Ti _{ss}	0.8	8.7	88.1	0.5	1.0	1.7	-

Figure 111 presents the BEI of heat treated Nb-18Si-24Ti-5Cr-5Al alloy. The microstructure observed does not vary significantly from the pre-heat-treated alloy, which suggests that;

- (1) The heat treatment temperature and time used were not high/long enough to promote the dissolution of the Ti-rich Nb₅Si₃ phases;
- (2) Due to the high amount of additional alloy elements, a large occupation of interstitial space has been promoted, which then induces to a much lower diffusion coefficient of Ti, hence the solid-state reaction is difficult to achieve at these circumstances;

From suggestions (1) and (2), it is possible to infer that a longer period of heat treatment would increase diffusion and that the alloy at 1500°C would have increased the solute solubility of the silicide. However, suggestion (2) is contrary to the fact that diffusion is higher, as a high Ti diffusion has been observed for the HIP processed alloy, but solid-state reaction is in fact difficult. This means that, even though interstitial space is largely occupied, the increase in solute solubility promotes diffusion at high temperatures.

It can be seen a relative coarsening of the Nb_{ss} and the Nb_5Si_3 phases, as well as the decrease in contrast of the Ti-rich Nb_5Si_3 phase, which shows a reduced amount of Ti, due to diffusion occurred to equilibrate the unbalanced solute concentration. A new formation is then observed, where small volume fraction of a punctual growth has taken place forming a Ti-rich solid solution.

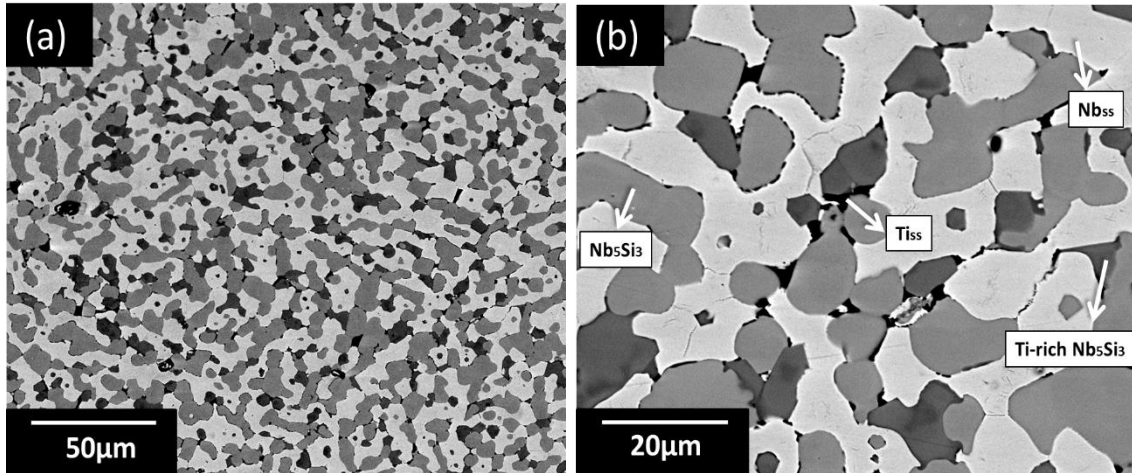


Figure 111 - BEI of Nb-18Si-24Ti-5Cr-5Al-2Mo alloy after heat treatment, (a) low magnification and (b) high magnification.

The formation of Ti_{ss} phase can be seen to form at the boundaries of the Nb_5Si_3 silicide phases, which is an indication that precipitation has occurred by diffusion during the heat treatment stage.

The microstructure presented in Figure 111, indicates that there has been diffusion of Ti from the Ti-rich silicide into both the Nb_{ss} and the Nb_5Si_3 phases by the reduced contrast of the Ti-rich silicide, which triggered small scales of Ti segregation that formed Ti_{ss} solid solution phase under equilibrium circumstances. This is further confirmed by the decrease of Ti in both phases after heat treatment.

With reduced temperature during the furnace cooling stage, a decreasing Ti diffusion restricts the coarsening of the Ti_{ss} phases, confirmed by the observance of the punctual-type phase formation, which relates to shorter distances for the Ti solute to diffuse.

Table 43 shows the compositions measured for the Nb-18Si-24Ti-5Cr-5Al-2Mo alloy after heat treatment. An increase of approximately 2 at.% of Ti in the Nb_5Si_3 phase can be seen, which indicates the diffusion of Ti from the Ti-rich silicide.

Furthermore, there is a decrease of Ti seen for the Nb_{ss} phase, responsible for forming the relatively small volume fraction of Ti_{ss} phases (~2.9%). It can also be observed a decrease of the gap between the Nb solubility of the Nb₅Si₃ silicides, indicating a higher diffusive equilibrium, with Ti solute diffusing to form the Ti_{ss} solid solution phase. The alloy composition of Mo could not be measured precisely by EDS methods, however X-ray fluorescence methods confirmed its presence, though in very small amounts.

Table 43 – Average measured compositions of phases present in Nb-18Si-24Ti-5Cr-5Al-2Mo alloy after heat treatment.

Phases	%Phase	%Nb	%Ti	%Si	%Al	%Cr	%Mo
Nb _{ss}	41.3	54.4	26.0	1.9	5.4	8.6	3.5
Nb ₅ Si ₃	40.9	45.0	17.5	31.7	2.7	2.1	1.3
Ti-rich Nb ₅ Si ₃	13.9	35.1	26.6	33.3	2.6	1.3	1.1
Ti _{ss}	2.9	8.7	88.1	0.5	1.0	1.7	-

There is a notable decrease in the volume fraction of Ti-rich Nb₅Si₃, from 22.4% in the as formed microstructure to approximately 13.9% after heat treatment. A heat treatment at higher temperature is then suggested in order to promote diffusive energy to eliminate the formation of the Ti-rich silicide. A slight increase in the amount of both Nb_{ss} and Nb₅Si₃ phases is noticed, which occurs as a natural phase coarsening due to the diffusion.

The formation of a new solid solution phase during heat treatment has also been observed by Tewari et al. [221], when analysing low temperature aging of multi-component Nb-Si-Ti alloys. In his study, the Nb_{ss} phase was split into another Ti-rich phase. Due to a high concentration of several other elements in solid solution within the phases, the same behaviour can be inferred to the silicide phase in this study during freezing, as commented previously.

Given the multicomponent diagrams such as Nb-Si-Cr and Nb-Si-Al, the effect of Cr and Al has little impact in reducing the miscibility gap of both the BCC solid solution and the Nb₅Si₃ silicide phases, which leads to a strong tendency for the separation of phases due to spinodal decomposition and for the formation of Ti_{ss}.

This can be derived as $[\text{Nb}(\text{Ti})_5\text{Si}_3]_{\text{ss}} \rightarrow \text{Nb}(\text{Ti})_5\text{Si}_3 + \text{Ti}_{\text{ss}}$, where the focus of the following discussion will be given.

Chandrasekaran et al. [225] have demonstrated, in early studies of Ti-Mo alloys, that a phase split is observed following aging treatment at 450°C for 15 minutes. The split was identified as a new precipitation of the solid solution β phase, when two identical crystal structures coexist with different lattice parameters, which is attributed to the presence of composition fluctuation in a material of a given composition [226].

A similar approach can be seen for Ti-X alloys [227], where it has been highlighted that the formation of a new solid solution phase can follow the supersaturation of parts of the original silicide, which means that a Nb_{ss} saturated in Ti has been shown to relieve its saturation by forming a phase more stable with local equilibrium [228].

A high magnification image detailing the Ti-rich solid solution phase formation is shown in Figure 112. It is possible to see the Ti solute located at the boundaries of Nb_{ss} solid solution phase, forming a halo of Ti. This halo confirms the diffusion of Ti from the high Ti containing phases towards a more stable phase with reduced free energy, showing a higher concentration of Ti solute in the vicinity of the already formed Ti_{ss} phase.

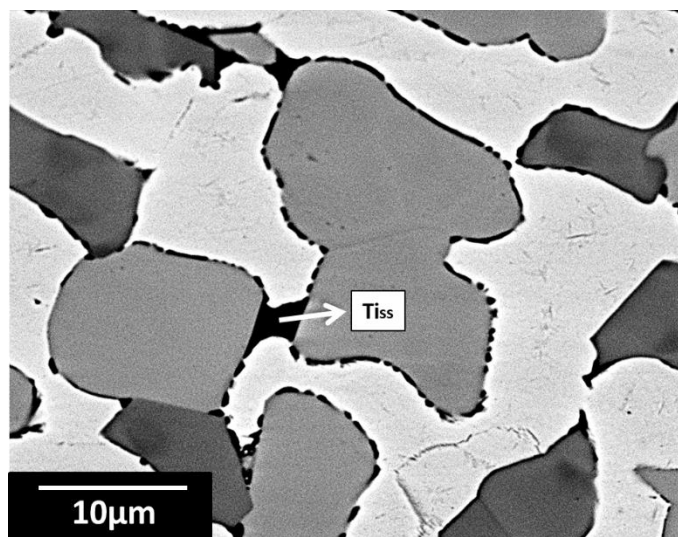


Figure 112 - Detail of formation of Ti_{ss} phase.

Phase separation is governed by changes in a stress-free molar volume. A dependence of the Gibbs free energy for this case arises, given the composition

fluctuation and the free energy density, or free energy gradient for segregated solutions [226, 229]. And it has been shown that the mechanism for the split of phases approaches that of nucleation [230].

The kinetics of decomposition for a new solid solution formation must, therefore, consider the effect of diffusion as it approaches the nucleation stage [231]. Analysing the initial stages of the decomposition mechanism by taking into account linear components to a given crystallography direction, considering the change in free energy and the chemical potential [226, 231], the local change in composition is directly dependant on an inter-diffusion coefficient related to the thermodynamic correction factor for incipient surfaces.

The relation of compositional change also shows a direct dependence on the free energy and the diffusional component into the formation of a new more stable split phase from the existing solid solution. Because of this, it is necessary to evaluate the diffusivity of Ti and Nb solutes in the phases present. Pontau et al. [232] measured the diffusion coefficient of both Ti and Nb solute in Ti-Nb alloys slowly cooled from high temperatures (~1500°C to ~950°C). Table 44 highlights these findings for four different compositions.

Table 44 - Diffusivity of Ti and Nb solute as a function of Nb content and temperature.

Nb content (at.%)	Temperature (°C)	D_{Ti} (cm²/sec)	D_{Nb} (cm²/sec)
0	1511	7.7 x 10 ⁻⁸	4.9 x 10 ⁻⁸
5.4	959	5.9 x 10 ⁻¹⁰	2.8 x 10 ⁻¹⁰
19.6	1292	4.9 x 10 ⁻⁹	3.6 x 10 ⁻⁹
35.7	1384	4.1 x 10 ⁻⁹	2.0 x 10 ⁻⁹

Given that the diffusivity of Ti into Ti_{ss} has been shown to be much greater than that of Ti in a Nb-doped alloy, and also greater than the diffusion of Nb into the same two phases for all temperatures, this can be expanded for the multi-component case, which it confirms the preference of Ti to diffuse into Ti-rich phase rather than into the Nb-rich solid solution phase. It is also noticed that the increase of Nb and the decrease of temperature negatively affects the diffusivity of both elements. Therefore, Ti will diffuse easily when compared to Nb solute.

The XRD analysis for the alloys throughout all stages of processing is shown in Figure 113, which confirms the formation of the phases Nb_{ss} and Nb_5Si_3 expected after analysis from the liquidus and solidus projections.

However, the Ti-rich Nb_5Si_3 formation and the split formation of Ti_{ss} cannot be detected as new separate phases, since they present the same crystal structures as the Nb_5Si_3 and Nb_{ss} , respectively.

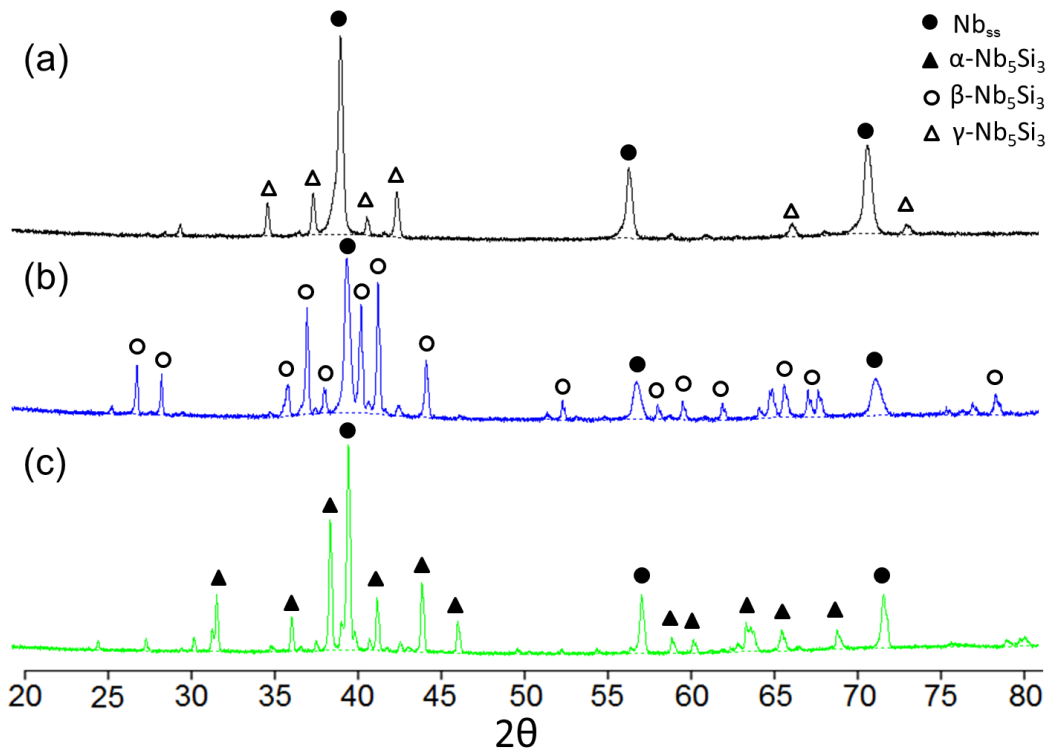


Figure 113 - XRD pattern for Nb-18Si-24Ti-5Cr-5Al-2Mo alloy, (a) as-formed, (b) HIP processed and (c) heat treated.

The main observation from Figure 115 is the evolution of the Nb_5Si_3 silicide phase from the as-formed stage to HIP processing and to heat treatment, which is transformed in the following sequence; $\gamma-Nb_5Si_3 \rightarrow \beta-Nb_5Si_3 \rightarrow \alpha-Nb_5Si_3$.

Zelenitsas et al. [13, 100] and Tsakirooulos [233] have reported on these different structures of Nb_5Si_3 silicide phase. The metastable hexagonal γ -type silicide is presented in the as-formed structure due to the addition of alloying elements that deviate the solidification sequence from equilibrium conditions and the rapid solidification involved during the additive manufacturing processing of these alloys.

After HIP processing, due to the high temperature and time provided, there is a crystal structure transformation to a tetragonal β -type silicide, which is stable at high temperatures and is stabilised by the addition of Al, Cr and Mo, as showed in section 3.2.3. The temperature of 1200°C used for HIP processing contributed to the transformation, however it was not sufficient for the complete transformation to the low temperature α -type silicide, which is predicted under equilibrium.

The heat treatment stage reached a temperature high enough for the desired tetragonal α -silicide to be stabilised, even though processing has been performed within a relatively short period of time.

Finally, the microstructure evolution is analysed by the comparison shown in Figure 114. The most noticeable change observed through the stages of processing is the decrease of Ti concentration in the Ti-rich Nb_5Si_3 silicide phase, which is caused by diffusion to balance the difference in composition between the “stable” Nb_5Si_3 silicide and the Nb_{ss} solid solution.

The Nb_{ss} phase maintains a regular composition regardless of the stage, which is seen by the lack of segregation in its morphology. As diffusion takes place at 1200°C for the HIP stage, there is diffusion of Ti towards a high concentration area that will later, after heat treatment at 1500°C, be consolidated in Ti_{ss} areas, from a split formation to reduce local free energy.

Coarsening of the phases is slightly observed after heat treatment, which is very limited. The eutectic cellular-like formation of $\text{Nb}_{\text{ss}} + \text{Nb}_5\text{Si}_3$ is kept, even after heat treatment. At this stage, it is impossible to predict if the Ti-rich silicide phase will be decomposed.

When compared to the alloys presented in sections 7.1.1 and 7.1.2, it is noticed that a balance of Cr addition to 5 at.% has not promoted formation of C15 Laves phase, although the increase in Ti has been the responsible for the undesirable formation of a Ti-rich silicide phase.

It is expected that, after a heat treatment undertaken for longer periods of time, Ti_{ss} phase will be located at specific points, with the disappearance of the halo observed in Figure 112.

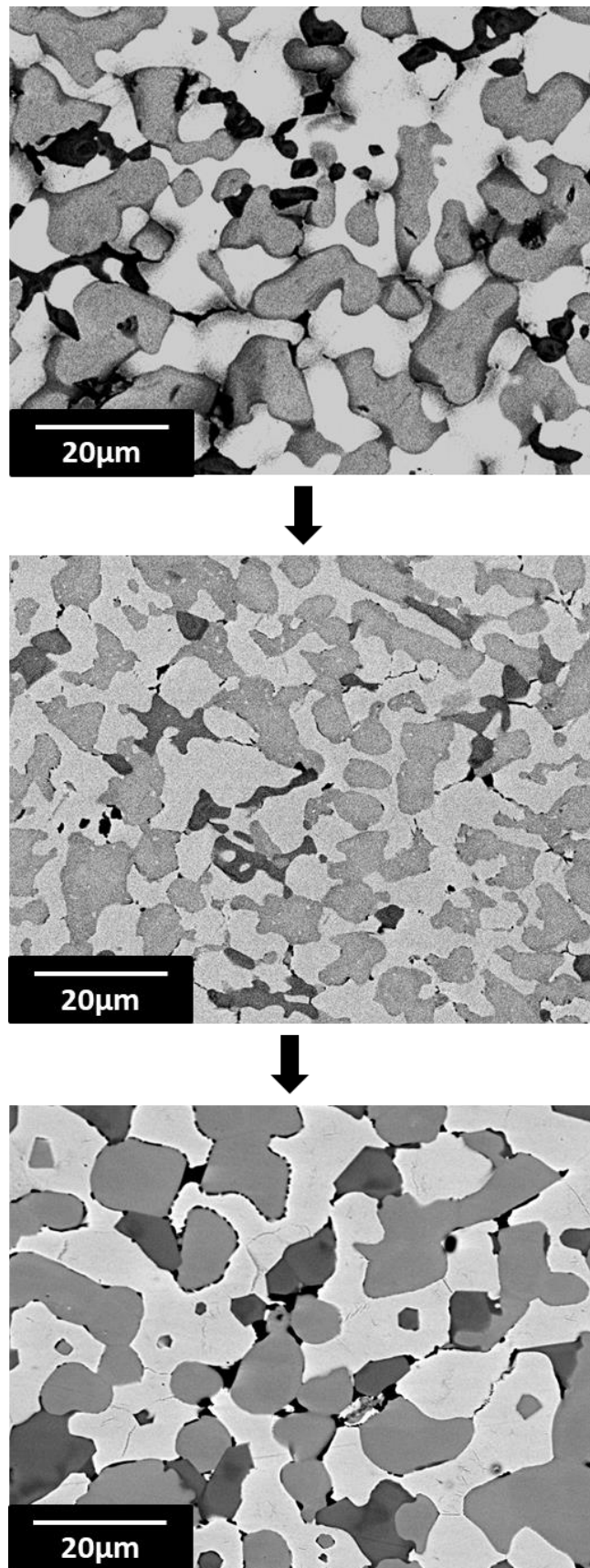


Figure 114 - Microstructure evolution of Nb-18Si-24Ti-5Cr-5Al-2Mo alloy from as-formed to HIP process to heat treatment stages.

7.1.4. Nb-22Si-26Ti-6Cr-2Al-3Hf

The composition of this alloy presents an increase in Si and Ti when compared with the previous alloys presented. The relatively high amount of Cr is responsible for forming C15 Laves phase, even though in small volume fraction, which confers this alloy a similar microstructure to that observed for Nb-15Si-22Ti-14Cr-2Al-2Hf-2V alloy.

Figure 115 presents the back-scattered electron image of the microstructure for Nb-22Si-26Ti-6Cr-2Al-3Hf alloys, where large formations of a non-uniform grey primary phase can be seen [Figure 115(a)], which is identified as Nb₅Si₃ according to the liquidus projection presented in Figure 94 and further confirmed with EDS analysis.

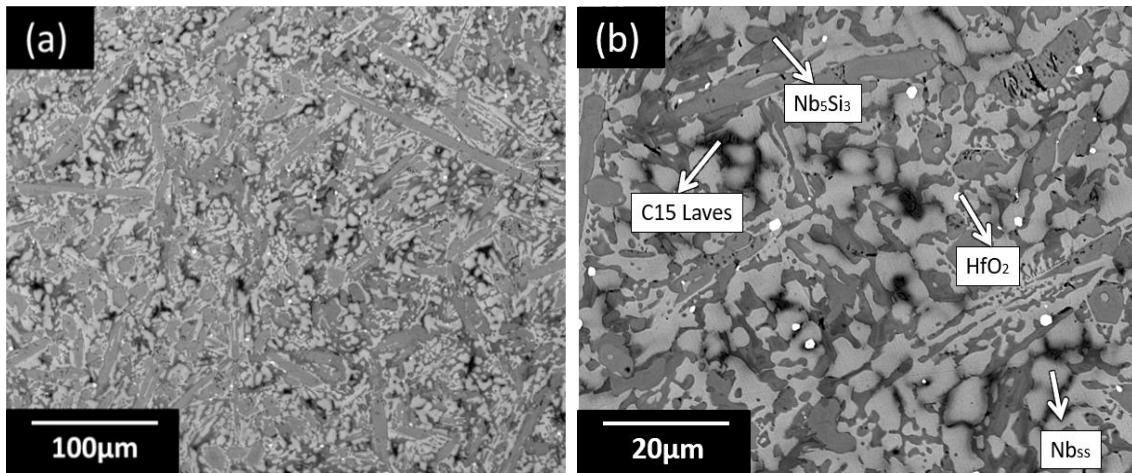


Figure 115 - BEI of as-formed Nb-22Si-26Ti-6Cr-2Al-3Hf alloy, (a) low magnification and (b) high magnification.

The high magnification image in Figure 115(b) shows a detailed formation of lath-like formation of primary silicide from liquid, $L \rightarrow \text{Nb}_5\text{Si}_3$, which is then followed by a cellular eutectic formation with a light grey Nb_{ss} phase, through the invariant reaction, $L \rightarrow \text{Nb}_5\text{Si}_3 + \text{Nb}_{ss}$. For this alloy, it is also observed the suppression of Nb₃Si phase, which is expected, given the similarity of its composition to the previous alloys presented.

The formation of C15 Laves phase is noticed to form in the edges of the Nb_{ss} phase, which suggests a formation in the last stage of solidification, when Nb_{ss} expels Cr to the liquid remaining, finally solidifying primarily, $L \rightarrow \text{C15}$. The

solidification path can therefore be presented as: $L \rightarrow \text{Nb}_5\text{Si}_3$; $L \rightarrow \text{Nb}_{\text{ss}} + \text{Nb}_5\text{Si}_3$; $L \rightarrow \text{C15}$.

Small scattered formations of HfO_2 can be observed, due to residual oxygen contamination during freezing. The EDS analysis has shown the average composition of phases found, which are presented in Table 45.

Table 45 - Average composition (in at.%) of phases present in as-formed Nb-22Si-26Ti-6Cr-2Al-3Hf alloy.

Phases	%Phases	Nb	Ti	Si	Cr	Al	Hf	O
Nb _{ss}	44.6	55.0	29.5	2.9	9.3	1.9	1.4	-
Nb ₅ Si ₃	50.3	35.7	23.4	35.4	1.6	0.9	3.0	-
C15	4.7	19.9	24.1	9.0	43.7	-	3.2	-
HfO ₂	0.4	1.4	0.9	-	-	-	30.2	67.5

The absence of a Ti-rich Nb₅Si₃ phase for increasing Ti of this alloy, suggests that;

- (1) The high amount of Ti is responsible for the formation of Ti-rich Nb₅Si₃ phase only when not accompanied by increased Si level, thus if the amount of Si was kept at 18 at.% as observed previously, it is suggested that Ti-rich Nb₅Si₃ would be present in the as-formed stage;
- (2) Increasing Si contents stabilises Nb₅Si₃ phase and increases the solubility of Ti into Nb_{ss};
- (3) The formation of C15 Laves phase consumes part of the Ti responsible for forming a new Ti-rich silicide.

It can be observed that a high amount of eutectic Nb₅Si₃ + Nb_{ss} is formed throughout the microstructure, which confirms the suggestion proposed in (1) and (2). When the liquid traverses the eutectic valley surface, the reaction consumes most of Ti and Si to form the eutectic phases rather than segregating and expelling the solutes into the liquid, and because of that the liquid remaining possess low Ti and Si and freezes with formation C15 Laves phase.

Figure 116 presents the XRD analysis for the Nb-22Si-26Ti-6Cr-2Al-3Hf alloy in the as-formed condition. The phases suggested by the microstructure and EDS

analysis are confirmed, with relatively small peaks of HfO_2 and C15 phases as expected.

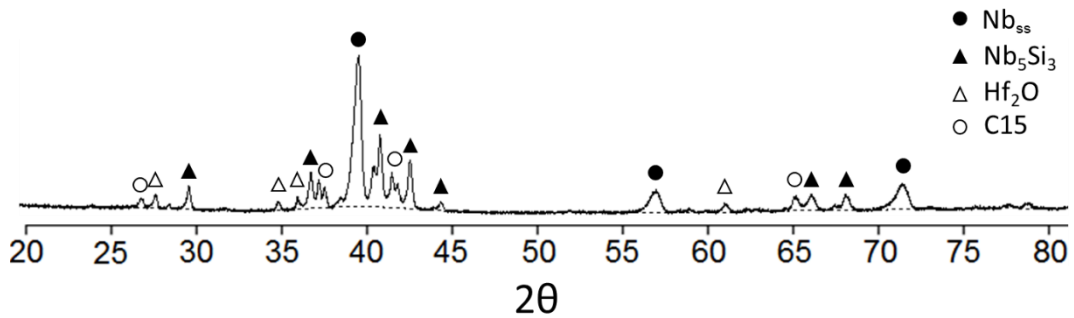


Figure 116 - XRD pattern for the as-formed Nb-22Si-26Ti-6Cr-2Al-3Hf.

After HIP processing, a significant change is observed throughout the microstructure, as presented in the low magnification image in Figure 117(a). The high magnification detailed image in Figure 117(b) shows the different phases encountered for this alloy.

The HfO_2 oxide formation is seen to be agglomerated in a cellular-like morphology at specific spots, and at this stage it is still unclear the exact reason for this observation. However, it can be suggested that a morphology change could have occurred due to diffusion of elements during HIP processing, or a further contamination has occurred. This would cause the solute solubility in the oxide to vary and potentially change its morphology.

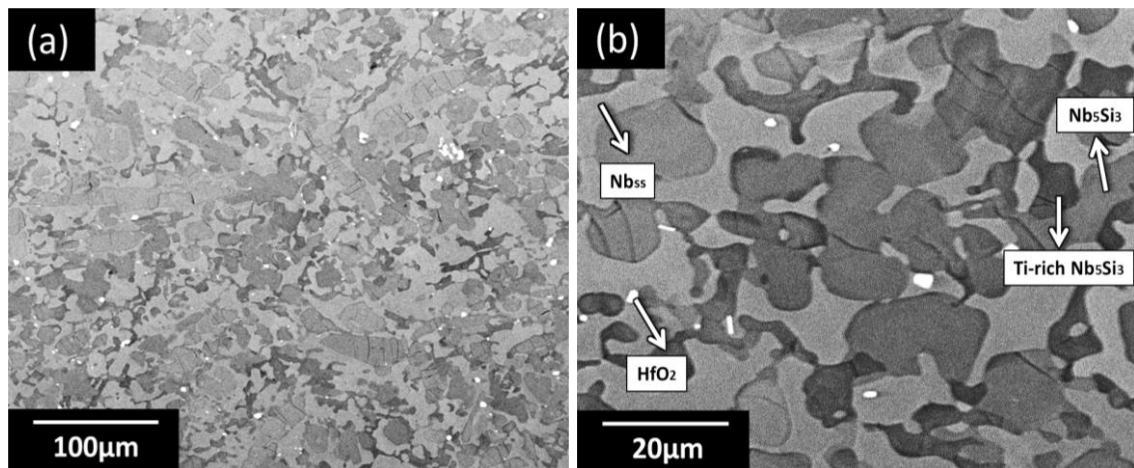


Figure 117 - BEI of HIP processed Nb-22Si-26Ti-6Cr-2Al-3Hf alloy, (a) low magnification and (b) high magnification.

There is a noticeable coarsening of the Nb_5Si_3 silicide phase, which becomes very prominent and forms blocks of silicide phase as a eutectic-like structure with

the Nb_{ss} phase formations, as seen before the HIP process. The eutectic-like structure is seen to start to change as the coarsening of phases takes place to allow the both phases to become more regular and globular, which is evidenced by the morphology of Nb_{ss} phase being transformed to a more continuous formation.

The increase in formation of dark spots is also noticed, which have been identified as a Ti-rich Nb₅Si₃ silicide phase, and this is followed by the disappearance of C15 Laves phase. The average composition of phases observed for this alloy after HIP processing is presented in Table 46.

Table 46 - Average composition (in at.%) of phases present in HIP processed Nb-22Si-26Ti-6Cr-2Al-3Hf alloy.

Phases	%Phases	Nb	Ti	Si	Cr	Al	Hf	O
Nb _{ss}	51.1	55.2	29.9	-	11.8	2.2	0.8	-
Nb ₅ Si ₃	41.3	36.7	21.2	37.3	1.4	-	3.3	-
Ti-rich Nb ₅ Si ₃	16.1	23.7	34.3	35.8	-	1.7	4.5	-
HfO ₂	0.5	22.7	7.5	-	2.3	-	18.7	48.8

The volume fraction of Ti-rich Nb₅Si₃ phase is relatively high, with levels compared to that from the split formation for the Nb-18Si-24Ti-5Cr-5Al-2Mo alloy, presented in section 7.1.3. This can lead to a few conclusions;

- a) C15 is formed adjacent to Nb_{ss} solid solution phase during the laser forming, thus the phase is dissolved into the Nb_{ss} phase, which can take extra Cr into solid solution. This is evidenced by the increase in Cr content of the Nb_{ss} phase and the increase in its volume fraction.
- b) As the C15 Laves phase is dissolved, there is significant solute movement governed by diffusion to and from both Nb_{ss} and Nb₅Si₃ phases. This leads to local super-saturation that follows the split of the Nb₅Si₃ silicide phase.
- c) The silicide phase split reduces the overall Ti content of the Nb₅Si₃ silicide and from the Nb_{ss} phase that is directed towards the newly formed Ti-rich silicide phase, which is formed adjacent to the Nb_{ss} phase.
- d) The formation of the Ti-rich phase is located at the extinct eutectic-like structure of Nb_{ss} + Nb₅Si₃ phases, where there is a local solid-state phase

transformation, which led to the dissolution of C15 Laves phase and formed a Ti-rich silicide phase.

The formation of Ti-rich phases at this stage is unexpected, as a HIP process at 1200°C does not usually attain these levels of transformations and diffusion. However, the dissolution of C15 phase, formed adjacent to the eutectic-like structure, certainly led to a deviation of solute equilibrium and caused local supersaturation that is a precursor to a spinodal composition.

Since the formation of Ti-rich silicide is followed by deviation of local equilibrium conditions, it is likely that it will persist after heat treatment stage, since the high temperature that is provided for dissolution and balance of solute is kept at short periods of time. This observation is confirmed as heat treatment takes place, as observed in Figure 118, where a more stable structure is seen, comprised of Nb_{ss} + Nb₅Si₃ phases, following partial dissolution of the Ti-rich Nb₅Si₃ phase.

However, the movement of Ti solute that occurs by the dissolution of the Ti-rich silicide phase is precluded. The restricted period of time provided for the heat treatment did not suffice for Ti solute to be equally distributed to both Nb_{ss} and Nb₅Si₃ phases, which caused a formation of a Ti-rich halo surrounding the Nb₅Si₃ silicide blocks. It is also observed that a clear coarsening of phases occurs that changes the morphology of the silicide phase into longer and more irregular shaped formations. Ti-rich Nb₅Si₃ phase formations are seen in Figure 118(b) where Ti solute diffusion has been precluded.

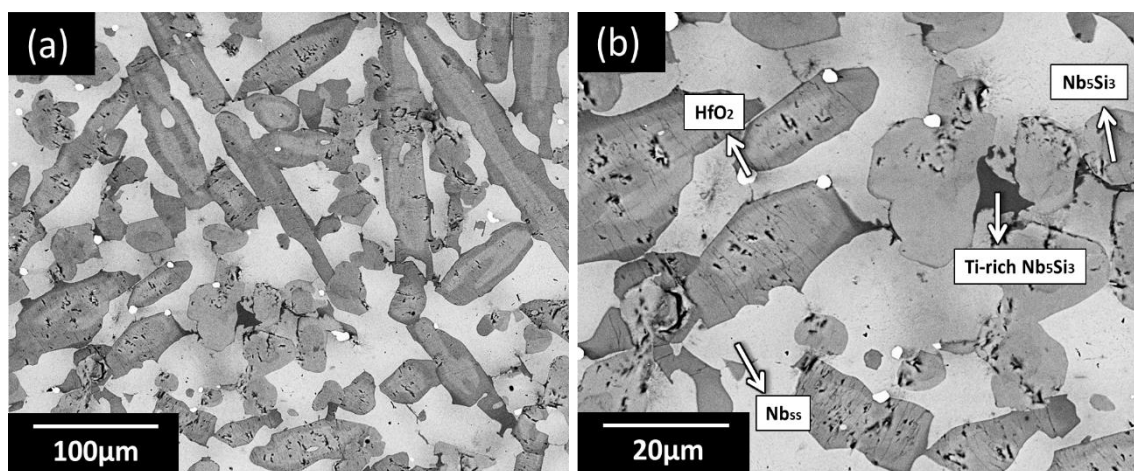


Figure 118 - BEI of Nb-22Si-26Ti-6Cr-2Al-3Hf alloy after heat treatment, (a) low magnification and (b) high magnification.

The previous formation of Ti-rich silicide phase adjacent to the Nb_{ss} phase has been partially dissolved into the Nb₅Si₃ silicides, which surrounds these phases and caused a local enrichment of Ti solute.

An analysis made by EDS has been carried out, and an average composition of phases identified has been drawn, which is presented in Table 47.

Table 47 - Average composition (in at.%) of phases present in heat treated Nb-22Si-26Ti-6Cr-2Al-3Hf alloy.

Phases	%Phases	Nb	Ti	Si	Cr	Al	Hf	O
Nb _{ss}	39.1	55.2	29.2	2.7	9.5	2.2	1.1	-
Nb ₅ Si ₃	37.3	40.9	20.5	35.3	0.4	0.5	2.4	-
Ti-rich Nb ₅ Si ₃	21.3	28.8	27.1	37.3	1.4	1.5	4.7	-
HfO ₂	2.3	-	-	-	-	-	33.9	66.1

From the analysis of Table 47, it is seen that there is no correlation for the phase transformation observed. There has been an increase in the volume fraction of Nb_{ss} following the partial dissolution of Ti-rich Nb₅Si₃ phase, whilst Nb₅Si₃ remains constant.

The microstructure evolution is finally evidenced in Figure 119, from which it is clear that this composition has produced an alloy of difficult homogeneity and of unpredictable microstructure transformation pattern. This is undesirable for turbine engine applications, which are subject of numerous cycles of temperature and pressure increase.

The final microstructure provided by heat treatment showed a more stable formation and distribution of phases, when compared to the HIP process stage. The increase in Cr from 5 to 6 at.% caused the promotion of Laves phase, and the decrease of Nb caused by the increase in Si and Ti has destabilised the formation of Nb_{ss}, by formation of a Ti-rich Nb₅Si₃ silicide phase that persisted after heat treatment.

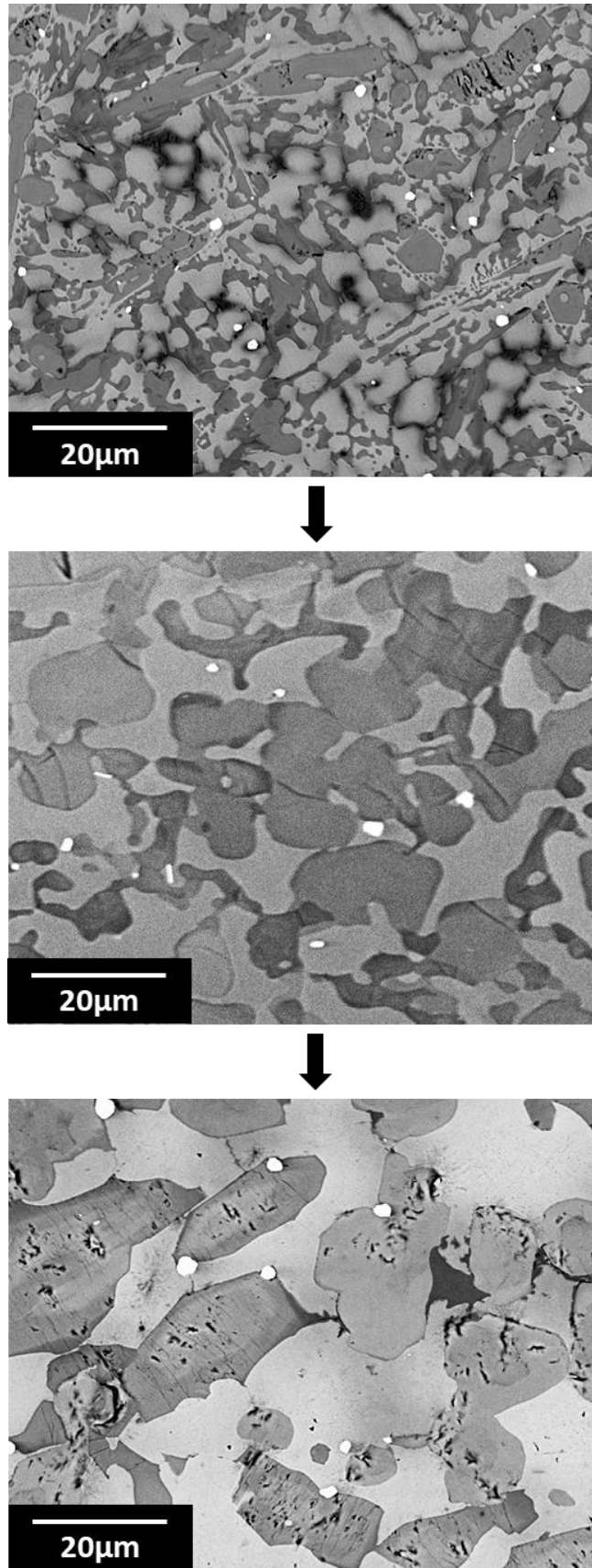


Figure 119 - Microstructure evolution of Nb-22Si-26Ti-6Cr-2Al-3Hf alloy from as-formed to HIP process to heat treatment stages.

Chapter 8 Conclusions and Future Work

8.1. Cast refractory metals-based alloys conclusions

The reaction sequence of Ta-Al-Fe system in the Ta-rich corner under rapid solidification condition was investigated with the following conclusions:

- Primary solidification of A2 (Ta) is accompanied by loss of interfacial equilibrium resulting in extended solubility of primarily Al and to a lower extent Fe in A2 for samples made via arc melting.
- Non-equilibrium solidification leads to deviation of the solidification path from that predicted by equilibrium liquid and solidus projections following primary freezing.
- For less than 10 at. % Al and less than 4 at. % Fe, the peritectic reaction, $L + A2 \rightarrow \sigma$ is suppressed and instead the eutectic reaction, $L \rightarrow A2 + \mu$ was observed following primary freezing, $L \rightarrow A2$. Extended solubility of Al within A2 up to 15 at. % was observed even when the peritectic reaction occurred.
- Non-equilibrium freezing occurs because of increased cooling rates that arose from higher melt superheat for alloys with higher liquidus temperature. Additionally under splat cooling conditions, non-equilibrium freezing was exhibited not only during primary freezing, but also during the $A2 + \mu$ eutectic reaction.

The freezing sequence in the Nb-Al-Co ternary system in the Co-rich corner with emphasis on the Laves and Heusler phases was examined. The following conclusions can be drawn:

- In the case of the (α -Co + CoAl + C36) ternary eutectic, the measured compositions for α -Co and C36 phases show good agreement with the corresponding vertices of the tie-triangle in the 1200°C isothermal section. Negligible solute solubility occurs during cooling, and the measured phase compositions of α -Co and C36 can be taken as the corresponding vertices for the tie-triangle.

- Care must be taken in the interpretation of the microstructure, because there is a narrow composition window that permits the Class II reaction. When not all liquid has been consumed, the liquid composition re-intersects the (C14-Co₂AlNb) valley and forms a new and finer eutectic. The measured composition of C36 is in good agreement with the corresponding vertex of the tie-triangle in the 1250°C isothermal section.
- When the quasi-peritectic reaction does not occur, depending on the initial composition, solid-state precipitation of C36 and CoAl does occur within supersaturated Co₂AlNb and C36 phases, respectively. The resultant microstructure in this instance is markedly different from the quasi-peritectic case.

The solidification sequence of Nb-Al-Fe ternary alloys has been examined under rapid freezing conditions, and the following conclusions can be drawn:

- Under rapid freezing conditions, a large super-saturation of Nb and Al solutes has been observed for phases NbAl₃ and Nb₂Al, respectively, followed by trapping of Al into (Nb) solid solution phase, after analysis of isothermal sections at 1300 and 1000°C.
- For the Al-rich Nb-Al-Fe alloy, the absence of NbAl₃ from the subsequent eutectic suggests that NbAl₃ is the leading phase during the formation of the eutectic NbAl₃ + C14, which fails to re-nucleate if the undercooling is not large enough, which then forms a halo of Nb₂Al + C14 that surrounds the primary phase.
- The extension of the halo formed is related to the ability of the nucleant phase, which suggests that C14 and Nb₂Al phases have similar nucleation tendencies, when there is formation of a halo of Nb₂Al phase around primary C14 phase.
- Suppression of the Class II reaction $L + Nb_2Al \rightarrow (Nb) + \mu$ is observed, which deviates from equilibrium and forms a eutectic (Nb₂Al + μ) structure, and of the Class III reaction $L + C14 + Nb_2Al \rightarrow \mu$, which takes place as $L + C14 \rightarrow \mu$ and $L \rightarrow \mu$.

The solidification sequence of Ti-Al-Ta ternary alloys, with focus on the formation of Class II quasi-peritectic reactions, has been examined under rapid freezing conditions, and the following conclusions can be drawn:

- For the Ti-rich Ti-Al-Ta alloy, solidification takes place as expected under equilibrium, with a three-phase reaction resulting $\alpha + \gamma$ dendritic structure.
- Although there is good agreement of γ and ϵ phases compositions with reducing temperature, it is noticed a significant solute trapping of Al, Ta and Ti, shifting the phase boundary regions.
- Following precluded diffusion at high cooling rates, the Class II reactions, $L + \beta \rightarrow \alpha + \sigma$ and $L + \sigma \rightarrow \alpha + \kappa$, do not take place, leading to the formation of α phase and a eutectic formation of $\alpha + \kappa$ respectively.
- Significant Ta solute segregation is observed for the low Ti alloy, which led to the formation of segregated phases and divergent solidification reaction sequence across the microstructure.

Secondary phase morphologies following primary solidification have been studied in the Ta-Al-Fe, Nb-Al-Co, and Nb-Al-Fe ternary systems. The following conclusions can be made:

- The undercooling accompanying solid growth is related to the extended solute solubility in the primary and secondary phases and can be used to account for the evolution of phase morphologies during ternary eutectic solidification.
- In Ta-Al-Fe system, there occurs an extended solubility of Fe in σ phase, which was consistent with the formation of a halo of μ phase on primary σ phases.
- In Nb-Al-Co system, halo of C14 is formed on primary CoAl, but very limited vice versa. In the absence of a solidus projection it was not possible to definitively determine the extended solute solubility in the primary phase.
- Nucleation constraints result in large undercooling and departure from equilibrium conditions and leading to the occurrence of halos. In Nb-Al-Fe system, extended primary freezing of NbAl₃ is followed by a two-phase halo of C14+Nb₂Al on primary NbAl₃, before the ternary eutectic reaction.

8.2. AM processed NbSi-based alloys conclusions

The analysis of a range of AM processed Nb-Si-Ti alloys focus on the solidification sequence and microstructure evolution through stages of forming, hot isostatic pressing and heat treatment has been done. From this study, a few conclusions can be made:

- The combination of the additions of Al, V, Mo and Hf has had significant effect on the ternary Nb-Ti-Si solidus and liquidus projections under equilibrium. Such elements promote and stabilise the formation of Nb₅Si₃ silicide phase, following suppression of Nb₃Si silicide.
- Formation of C15 Laves phase occurs due additions of Cr > 6 at.%, and Hf consumed residual oxygen forming HfO₂ oxides. For a combined addition of Cr + Al as high as 10 at.% with increasing additions of Ti and Si, there is the formation of an atypical Ti-rich Nb₅Si₃ silicide phase, which is due to solute solubility and solute rejection during cooling.
- Post processing methods, such as hot isostatic pressing and solution heat treatment, have been responsible for the coarsening of phases and a phase transformation when the metastable γ -Nb₅Si₃ has transformed into the α -Nb₅Si₃ silicide, predicted under equilibrium.
- Local micro-segregation and super-saturation of Ti in the Nb-rich solid solution phase boundaries led to a spinodal decomposition and formation of a Ti_{ss} phase, following diffusion of Ti into a more energetically stable and homogeneous composition.

8.3. Future Work

The study of AM processed NbSi-based alloys has shown to be significant, and given the advances made by technology and knowing the effects of alloying elements, it is possible to say that these are interesting results.

However, much is yet to be understood and studied, if these alloys are to be used under high pressure and at high temperature environments, with a detailed analysis focused on structural tests and applications. Having this in mind, a few

suggestions can be made for future work and projects aiming to study NbSi-based alloys processed via additive manufacturing:

- The study of the mechanisms of pores closure during HIP process would be fundamental to understand how the elemental additions and the processing parameters affect the densification of these alloys after post processing methods. A detailed review on how the porosity is formed can help defining the ideal environment conditions for these alloys to achieve the best as-formed properties.
- A separate and detailed study of processing parameters, such as scanning speed and scanning pattern, can lead to the development of bespoke processing of best performing alloys, with reduced shrinkage during cooling and oxygen contamination, as well as with the necessary microstructure, in terms of grains/phases size and the prediction of previously unexpected phases.
- For these alloys to be used at high temperature applications, a thorough study on the oxidation behaviour is needed, as to evaluate the formation of oxidation layers and probable oxidation protection mechanisms (passivation). This study would lead to a direct comparison between AM and cast processing techniques, providing a general idea on whether AM processed alloys can achieve the necessary requirements for high temperature applications.
- Finally, a study on the mechanical properties is of utmost importance for alloys to be used on aerospace applications and would lead to a detailed conclusion of the viability of the AM process.

References

1. N. Sekido, Y. Kimura, S. Miura, Fu-Ga Wei, Y. Mishima. Fracture toughness and high temperature strength of unidirectionally solidified Nb-Si binary and Nb-Ti-Si ternary alloys. *Journal of Alloys and Compounds*, 2006(425): p. 223-229.
2. B.P. Bewlay, M.R. Jackson, P.R. Subramanian. Processing High-Temperature Refractory-Metal Silicide in-situ Composites. *JOM*, 1999: p. 32-36.
3. J.C. Zhao, B.P. Bewlay, M.R. Jackson, L.A. Peluso. Alloying and Phase Stability in Niobium Silicide In-situ Composites. GE Technical Report no. 2001 CRD090, 2001a.
4. M. Cervenka. Trent 800 breakdown with pressure and temperature considerations. Rolls-Royce Group plc: Derby UK.
5. N. D'Souza, L.M. Feitosa, G.D. West, N.G. Jones, H.B. Dong. Effects of Solute Trapping on Solidification Path in Ta-rich Ta-Al-Fe Ternary Alloys under Rapid Freezing. *Journal of Alloys and Compounds*, 2017. 698: p. 375-383.
6. P. Cerba, M. Vilasi, B. Malaman, J. Steinmetz, *Journal of Alloys and Compounds*, 1993. 201: p. 57-60.
7. B.P. Bewlay, M.R. Jackson, J.C. Zhao, P.R. Subramanian, M.G. Mendiratta, J.J. Lewandowski. Ultrahigh-Temperature Nb-Silicide-Based Composites. *Mrs Bulletin*, 2003: p. 646-653.
8. N. D'Souza, B. Kantor, G.D. West, L.M. Feitosa, H.B. Dong. Key aspects of carbide precipitation during solidification in the Ni-base superalloy, MAR M002. *Journal of Alloys and Compounds*, 2017. 702: p. 6-12.
9. B.P. Bewlay, M.R. Jackson, J.C. Zhao, P.R. Subramanian. A Review of Very-High-Temperature Nb-Silicide-Based Composites. *Metallurgical and Materials Transactions A*, 2003. 34: p. 2043-2052.
10. P. Tsakirooulos. On the macrosegregation of silicon in niobium silicide based alloys. *Intermetallics*, 2014. 55: p. 95-101.

11. I. Grammenos, P. Tsakiroopoulos. Study of the role of Mo and Ta additions in the microstructure of Nb-18Si-5Hf silicide based alloy. *Intermetallics*, 2010. 18(1524-1530).
12. Z. Li, P. Tsakiroopoulos. The microstructure of Nb-18Si-5Ge-5Al and Nb-24Ti-18Si-5Ge-5Al in situ composites. *Journal of Alloys and Compounds* 2013. 550: p. 553-560.
13. K. Zelenitsas, P. Tsakiroopoulos. Study of the role of Ta and Cr additions in the microstructure of Nb-Ti-Si-Al in situ composites. *Intermetallics*, 2006. 14: p. 639-659.
14. M. Attaran. The rise of 3-D printing: The advantages of additive manufacturing over traditional manufacturing. *Business Horizons*, 2017. 60: p. 677-688.
15. L. Machon, G. Sauthoff. Deformation Behaviour of Al-containing C14 Laves Phase Alloys. *Intermetallics*, 1996. 4: p. 469-481.
16. G. Sauthoff. Multi-phase Intermetallic Alloys for High-temperature Applications. *Intermetallics*, 2008. 8:1: p. 1101-1109.
17. P. Hanus, E. Bartsch, M. Palm, R. Krein, K. Bauer-Partenheimer, P. Janschek. Mechanical Properties of a Forged Fe-25Al-2Ta Steam Turbine Blade. *Intermetallics*, 2010. 18: p. 1379-1384.
18. O. Dovbenko, F. Stein, M. Palm, O. Prymak. Experimental determination of the ternary Co-Al-Nb phase diagram. *Intermetallics*, 2010. 18(2191-2207).
19. C.A. Nunes, R. Sakidja, Z. Dong, J.H. Perepezko. Liquidus Projection for the Mo-rich Portion of the Mo-Si-B Ternary System. *Intermetallics*, 2000. 8: p. 327-337.
20. D.R.F. West, N. Saunders, Ternary Phase Diagrams in Materials Science. *Inst. of Met.*, 2002. 3rd ed.: p. 49-52.
21. V.T. Witusiewicz, A.A. Bondar, U. Hecht, V.M. Voblikov, N.I. Tsyganenko, O.S. Fomichov, M.V. Karpets, V.M. Petyukh, T.Y. Velikanova. Experimental Study and Thermodynamic Modeling of the Ternary Al-Fe-Ta System. *J. Mater. Sci.*, 2013. 48: p. 377-412.
22. L. M. Feitosa, N. D'Souza, G.D. West, H.B. Dong, Solidification Path in Co-rich Nb-Al-Co Ternary Alloys. *Journal of Alloys and Compounds*, 2017. 48: p. 3814-3822.

23. M. Hillert. *Solidification and Casting of Metals*. The Metals Society, 1979.
24. K. Das, S. Das. A Review of the Ti-Al-Ta (Titanium-Aluminium-Tantalum) System. *Journal of Phase Equilibria and Diffusion*, 2005. 26: p. 322-329.
25. S. Das, J.H. Perepezko. Ternary Phase Development in the Ti-Al-Ta System. *Scripta Metallurgica et Materialia*, 1991. 25: p. 1193-1198.
26. F. Stein, C. He, O. Prymak, S. Voß, I. Wossack. Phase equilibria in the Fe-Al-Nb system: Solidification behaviour, liquidus surface and isothermal sections. *Intermetallics*, 2015. 59: p. 43-58.
27. M. Palm, C. He, O. Dovbenko, F. Stein, J.C. Schuster. Liquidus Projection and Reaction Scheme of the Co-Al-Nb System. *Journal of Phase Equilibria and Diffusion*, 2012. 33: p. 210-221.
28. V. Raghavan. Al-Ta-Ti (Aluminum-Tantalum-Titanium). *Journal of Phase Equilibria and Diffusion*, 2005. 26: p. 629-634.
29. V. Raghavan. Al-Co-Nb (Aluminum-Cobalt-Niobium). *Journal of Phase Equilibria and Diffusion*, 2012. 33: p. 472-473.
30. V. Raghavan. Phase Diagram Updates and Evaluations of the Al-Fe-Ta, Al-Ge-Ni, Al-Li-Zn, Al-Sc-Si and Al-Ta-Ti Systems. *Journal of Phase Equilibria and Diffusion*, 2013. 34: p. 328-349.
31. H.W. Kerr, W. Kurz. Solidification of peritectic alloys. *International Materials Reviews*, 1996. 41(4): p. 129-164.
32. T.S. Lo, S. Dobler, M. Plapp, A. Karma, W. Kurz. Two-phase microstructure selection in peritectic solidification: from island banding to coupled growth. *Acta Materialia*, 2003. 51: p. 599-611.
33. Y.Z. Chen, F. Liu, G.C. Yang, N. Liu, C.L. Yang, Y.H. Zhou. Suppression of peritectic reaction in the undercooled peritectic Fe–Ni melts. *Scripta Materialia*, 2007. 57: p. 779-782.
34. S. Dobler, T.S. Lo, M. Plapp, A. Karma, W. Kurz. Peritectic couple growth. *Acta Materialia*, 2004. 52: p. 2795-2808.
35. L.S. Luo, Y.Q. Su, J.J. Guo, X.Z. Li, S.M. Li, H. Zhong, L. Liu, H.Z. Fu, Peritectic reaction and its influences on the microstructures evolution during directional solidification of Fe–Ni alloys. *Journal of Alloys and Compounds*, 2008. 461: p. 121-127.
36. ASM Handbook - Alloy Phase and Diagrams. 1992. 3: p. 845.

37. W. Kurz, D.J. Fisher, *Fundamentals of Solidification*. Aedormannsdorf, Switzerland: Trans Tech. Publications, 1986.
38. R. Trivedi. *Metallurgical and Material Transactions A*, 1995. 26A: p. 1583-1590.
39. W.J. Boettinger. *The Structure of Directional Solidified Two-Phase Sn-Cd Peritectic Alloys*. *Metallurgical Transactions*, 1974. 5: p. 2023-2031.
40. K.A. Jackson, J.D. Hunt, *Trans. Met. Soc. AIME*, 1966. 236: p. 1129.
41. B. Chalmers. *Physical Metallurgy*, 1959: p. 271-272.
42. Z. Feng, J. Shen, Z. Min, L. Wang, H. Fu. *New initiating mechanism of coupled growth in directionally solidified Fe–Ni peritectic system in diffusive regime*. *Materials Letters*, 2012. 67: p. 14-16.
43. M. Vandyoussefi, H.W. Kerr, W. Kurz. *Two-phase growth in peritectic Fe-Ni alloys*. *Acta Materialia*, 2000. 48: p. 2297-2306.
44. E.C. Kurum, H.B. Dong, J.D. Hunt, *Metall. Mater. Trans. A*, 2005. 36: p. 3103-3110.
45. W.J. Boettinger, U.R. Kottner, D.K. Banerjee. *Modelling and Casting of Advanced Solidification Processes (MCWASP)*. B. G. Thomas, C. Beckermann, TMS, 1998. VIII Eds: p. 159-170.
46. Y. Ruan, W.J. Xie. *Intermetallics*, 2012. 31: p. 232-241.
47. X. Zhang, Y. Ruan, W. Wang, B. Wei. *Rapid solidification and dendrite growth of ternary Fe-Sn-Ge and Cu-Pb-Ge monotectic alloys*. *Science in China Series G: Physics, Mechanics and Astronomy*, 2007. 50: p. 472-490.
48. N. D'Souza, H.B. Dong. *Solidification path in third-generation Ni-based superalloys, with an emphasis on last stage solidification*. *Scripta Materialia*, 2007. 56: p. 41-44.
49. G. Ghosh, I.G. Effenberg, S. Ilyenko. *Bornstein numerical data and functional relationships in materials science and technology, Group IV*. Martinsen (ed) *Physical chemistry, ternary alloy systems, Phase diagrams, crystallographic and thermodynamic data critically evaluated by MSIT*, 2008. 11(Springer Berlin): p. 213.
50. K.S. Kumar. *Int. Mater. Rev.*, 1990. 35: p. 293-327.

51. V. Raghavan. The Al-Fe-Ta (Aluminium-Iron-Tantalum) System. Phase Diagrams of Ternary Iron Alloys, 1992. 6A (Indian Institute of Metals, Calcutta, India): p. 187-190.
52. C.R. Hunt, A. Raman, Z. Metallkde, 1968. 59: p. 701-707.
53. F. Stein, D. Jiang, M. Palm, G. Sauthoff, D. Grüner, G. Kreiner. Experimental reinvestigation of the Co–Nb phase diagram. Intermetallics, 2008. 16: p. 785-792.
54. K.C. Hari Kumar, I. Ansara, P. Wollants, L. Dalaey. Thermodynamic Optimisation of the Co-Nb System. J. Alloys and Compounds, 1998. 267: p. 105-112.
55. V. Raghavan. Al-Fe-Nb (Aluminium-Iron-Niobium). J. Phase Equilib Diffus, 2011. 32: p. 55-56.
56. K. Wang, M. Wei, L. Zhang. Anomalous Halo Formation in an Arc-Melted ScNi-Sc₂Ni Off-Eutectic Binary Alloy. Materials MDPI, 2016. 9(589): p. 1-7.
57. B.E. Sundquist, R. Bruscatto, L.F. Mondolfo. Journal of Australian Institute of Metals, 1963. 91: p. 204.
58. A. Kofler. Precipitation anomalies during isothermal crystallization from undercooled binary organic melts. J. Aust. Inst. Met., 1965. 10: p. 132.
59. M.F.X. Gigliotti, G.A. Colligan, G.L.F. Powell. Halo formation in eutectic alloy systems. Metall. Mater. Trans., 1970. 1: p. 891-897.
60. C. McCullough, J.J. Valencia, C.G. Levi, R. Mehrabian. Peritectic solidification of Ti-Al-Ta alloys in the region of γ -TiAl. Materials Science and Engineering A, 1992. 156(2): p. 153-166.
61. O. Shuleshova, D. Holland-Moritz, A. Voss, W. Löser. In situ observations of solidification in Ti-Al-Ta alloys by synchrotron radiation. Intermetallics, 2011. 19: p. 688-692.
62. X. Wu. Intermetallics, 2006. 14: p. 1114-22.
63. V.T. Witusiewicz, A.A. Bondar, U. Hecht, V.M. Voblikov, O.S. Fomichov, V.M. Petyukh, S. Rex. Experimental study and thermodynamic modelling of the ternary Al-Ta-Ti system. Intermetallics, 2011. 19: p. 234-259.
64. C. McCullough, J.J. Valencia, C.G. Levi, R. Mehrabian, M. Maloney, R. Hecht. Solidification Paths of Ti-Ta-Al alloys. Acta Metall. Mater., 1991. 39(11): p. 2745-2758.

65. M.L. Weaver, S.L. Guy, R.K. Stone, M.J. Kaufman. An Investigation of Phase Equilibria in the Ternary Al-Ti-Ta System. *Mat. Res. Soc. Symp. Proc.*, 1991. 213: p. 163-168.
66. V.T. Witusiewicz, A.A. Bondar, U. Hecht, S. Rex, T.Ya. Velikanova. The Al-B-Nb-Ti system: III. Thermodynamic re-evaluation of the constituent binary system Al-Ti. *Journal of Alloys and Compounds*, 2008. 465: p. 64-77.
67. A. Raman. *Z. Metallkde*, 1966. 57: p. 535-540.
68. S.S.H. Nowotny. Studies in the Ternary System Ti-Ta-Al and in the Quaternary System Ti-Ta-Al-C. *Z. Metallkde*, 1983. 74: p. 468-472.
69. H. Nowotny, C. Brukl, F. Benesovsky, *M Schr. Chem.*, 1961. 92: p. 116.
70. B.P. Bewlay, M.R. Jackson. The Nb-Ti-Si Ternary Phase Diagram: Evaluation of Liquid-Solid Phase Equilibria in Nb- and Ti-Rich Alloys. *Journal of Phase Equilibria*, 1997. 18: p. 264-278.
71. B. Jing, H. Qiang, T. Liang, G. Tai, Z. Xinqing, Ma Chaoli. Liquid-Solid Phase Equilibria of Nb-Si-Ti Ternary Alloys *Chinese Journal of Aeronautics*, 2008. 21: p. 275-280.
72. H. Liang, Y.A. Chang. Thermodynamic modeling of the Nb-Si-Ti ternary system. *Intermetallics*, 1999. 7: p. 561-570.
73. T. Geng, C. Li, J. Bao, X. Zhao, Z. Du, C. Guo. Thermodynamic assessment of the Nb-Si-Ti system. *Intermetallics*, 2009. 17: p. 343-357.
74. B.P. Bewlay, M.R. Jackson. The Nb-Ti-Si Ternary Phase Diagram: Determination of Solid-State Phase Equilibria in Nb- and Ti-Rich Alloys *Journal of Phase Equilibria*, 1998. 19: p. 577-586.
75. J.C. Zhao, M.R. Jackson, L.A. Peluso. Mapping of the Nb-Ti-Si phase diagram using diffusion multiples. *Materials Science and Engineering A*, 2004. 372: p. 21-27.
76. Y. Li, C. Li, Z. Du, C. Guo, X. Zhao. As-cast microstructures and solidification paths of the Nb-Si-Ti ternary alloys in Nb₅Si₃-Ti₅Si₃ region. *Rare Metals*, 2013. 32: p. 502-511.
77. M. McLean. *Directionally Solidified Materials for High Temperature Service*. The Metals Society, Pittsburgh, 1983: p. 55.
78. W. Kurz, D.J. Fisher. *Fundamentals of Solidification*. *Trans. Tech. Publ.*, 1986. 1: p. 134 and 221.

79. M.H. Burden, J.D. Hunt. *J. Cryst. Growth*, 1974. 22: p. 109-116.
80. J.D. Hunt, S. Lu. *Handbook of Crystal Growth*, 1994. 2(Ed. D. T. J. Hurle): p. 1113-66.
81. M.D. Nave, A.K. Dahle, D.H. StJohn. *Acta Metallurgica*, 2002. 50: p. 2837.
82. K.W. Li, S.M.L., Y.L. Xue, H.Z. Fu. Halo formation in arc-melted Cr–Nb alloys. *Journal of Crystal Growth*, 2012. 357: p. 30-34.
83. K.W. Li, X.B. Wang, S.M. Li, W. Wang, S. Chen, D. Gong, J. Cui. Halo Formation in Binary Fe-Nb Off-eutectic Alloys. *High Temp. Mat. Proc.*, 2015. 34: p. 479-485.
84. S.M. Li, B.L. Jiang, B.L. Ma, H.Z. Fu. Halo formation in directional solidification of Ni–Ni₃Nb hypereutectic alloy. *Journal of Crystal Growth*, 2007. 299: p. 178.
85. D. Welton, N. D'Souza, J. Kelleher, S. Gardner, Z.H. Dong, G.D. West, H.B. Dong. *Metallurgical and Materials Transactions A.*, 2015. 46A: p. 4298-15.
86. R.C. Reed. *The Superalloys - Fundamentals and Applications*. Cambridge University Press, 2006.
87. H.J. Dai. *A Study of Solidification Structure Evolution during Investment Cast of Ni-based Superalloy for Aero-Engine Turbine Blades*. PhD Thesis. University of Leicester, 2008.
88. N. Das. *Advances in nickel-based cast superalloys*. *Transactions of The Indian Institute of Metals*, 2010. 63(2-3): p. 265-274.
89. T.M. Pollock. *Nickel-Based Superalloys for Advanced Turbine Engines: Chemistry, Microstructure, and Properties*. *Journal of Propulsion and Power*, 2006. 22(2): p. 361-374.
90. C. Small. *Strategic Metals Use in the Gas Turbine Industry – Challenges and Opportunities*. Rolls-Royce plc., 2011.
91. H.J. Dai, H.B. Dong, N. D'Souza, J.C. Gebelin, R.C. Reed. Grain Selection in Spiral Selectors During Investment Casting of Single-Crystal Components: Part II. Numerical Modeling. *The Minerals, Metals & Materials Society and ASM International*, 2011. 42A: p. 3439-3446.
92. N. D'Souza, H.B. Dong. *An Analysis Of Solidification Path In The Ni-Base Superalloy, CMSX10K*. *Superalloys*, 2008: p. 261-269.

93. L. Zhu, C. Wei, H. Qi, L. Jiang, Z. Jin, J.C. Zhao, *J. Alloys and Compounds*, 2017. 691: p. 110-118.
94. N. D'Souza, M. Lekstrom, H.B. Dong. *Mater. Sci. Eng. A*, 2008. 490: p. 258-265.
95. J.R. Davis. *ASM Specialty Handbook: Nickel, Cobalt, and Their Alloys*, ASM International. 2000.
96. I. Grammenos, P. Tsakiroopoulos. Study of the role of Hf, Mo and W additions in the microstructure of Nb-20Si silicide based alloys. *Intermetallics*, 2011. 19: p. 1612-1621.
97. W.Y. Kim, H. Tanaka, S. Hanada. Microstructure and High-Temperature Strength at 1773K of Nbss/Nb₅Si₃ Composites Alloyed with Molybdenum. *Intermetallics*, 2002. 10: p. 625-634.
98. N. Sekido, Y. Kimura, S. Miura, Y. Mishima. Solidification Process and Mechanical Behavior of the Nb/Nb₅Si₃ Two Phase Alloys in the Nb-Ti-Si System. *Materials Transactions*, 2004. 45(12): p. 3264 - 3271.
99. J. Geng, P. Tsakiroopoulos, G. Shao. A study of the effects of Hf and Sn additions on the microstructure of Nbss/Nb₅Si₃ based in situ composites. *Intermetallics*, 2007(15): p. 69-76.
100. K. Zelenitsas, P. Tsakiroopoulos. Effect of Al, Cr and Ta additions on the oxidation behaviour of Nb-Ti in situ composites at 800°C. *Materials Science and Engineering A* 2006. 416: p. 269-280.
101. W.Y. Kim, I.D. Yeo, T.Y. Ra, G.S. Cho, M.S. Kim. Effect of V addition on microstructure and mechanical property in the Nb-Si alloy system. *Journal of Alloys and Compounds*, 2004. 364: p. 186-192.
102. Z. Sun, X. Guo, B. Guo. Effect of B and Ti on the directionally solidified microstructure of the Nb-Si alloys. *International Journal of Refractory Metals and Hard Materials* 2015. 51: p. 243-249.
103. B.P. Bewlay, M.R. Jackson, M.F.X. Gigliotti. Niobium Silicide High Temperature In Situ Composites, in *Intermetallic Compounds*, ed. Westbrook and Fleisher. Vol. 3. 2002: John Wiley and Sons, Ltd. 541-560.
104. W. Jun, G. Xiping, G. Jinming. Effects of B on Microstructure and Oxidation Resistance of Nb-Ti-Si-based Ultrahigh-temperature Alloy. *Chinese Journal of Aeronautics*, 2009. 22: p. 544-550.

105. Y. Kang, Y. Tan, J. Song, H. Ding. Microstructures and mechanical properties of Nbss/Nb₅Si₃ in-situ composite prepared by electromagnetic cold crucible directional solidification. *Materials Science and Engineering A*, 2014. 559: p. 87-91.
106. Y. Li, S. Miura, K. Ohsasa, C. Ma, H. Zhang. Ultrahigh-temperature Nbss/Nb₅Si₃ fully-lamellar microstructure developed by directional solidification in OFZ furnace. *Intermetallics*, 2011. 19: p. 460-469.
107. S. Miura, K. Ohkubo, T. Mohri. Microstructural control of Nb-Si alloy for large Nb grain formation through eutectic and eutectoid reactions. *Intermetallics*, 2007. 15: p. 7.
108. H. Okamoto. Phase diagrams for binary alloys. Materials Park, OH: ASM International, 2000.
109. Z. Li, L.M. Peng. Microstructural and mehcanical characterisation of Nb-based in situ composites from Nb-Si-ti ternary system. *Acta materialia*, 2007. 55: p. 6573-6585.
110. S. Zhang, X. Shi, J. Sha. Microstrucural evolution and mechanical properties of as-cast and direcionally solidified Nb-15Si-22Ti-2Al-2Hf-2V-(2,14) Cr alloys at room and high temperatures. *Intermetallics*, 2015(56): p. 8.
111. B.P. Bewlay, J.A. Sutliff, M.R. Jackson, H.A. Lipsitt. Microstructural and Crystallographic Relationships in Directionally Solidified Nb-Cr₂Nb and Cr-Cr₂Nb Eutectics. *Acta Matallurgica et Materialia* 1994. 42(8): p. 2869-2878.
112. Q. Huang, X. Guo, Y. Kang, J. Song, S. Qu, Y. Han. Microstructures and mechanical properties of directionally solidified multi-element Nb-Si alloy. *Progress in Natural Science: Materials International*, 2011. 21: p. 146-152.
113. N. Sekido, Y. Kimura, S. Miura, Y. Mishima. Microstructure development of unidirectionally solidified (Nb)/Nb₃Si eutectic alloys. *Materials Science and Engineering*, 2007(444): p. 7.
114. B.P. Bewlay, M.R. Jackson, H.A. Lipsitt. *Metall. Trans.*, 1996. 27A: p. 3801.
115. J.A. Sutliff, B.P. Bewlay. 53rd Annual Meeting of the Microscopy Society of America. 1995. San Francisco, CA: San Francisco Press.

116. S. Drawin, J.F. Justin. Advanced Lightweight Silicide and Nitride Based Materials for Turbo-Engines Applications. *Journal AerospaceLab* 2011(3): p. 1-13.
117. D.M. Herman, B.P. Bewlay, L. Creteigny. R. DiDomizio. Fracture and Fatigue of Niobium silicide Alloys. *Materials Research Society*, 2009. 1128.
118. W.-Y. Kim, H. Tanaka. High temperature strength at 1773K and room temperature fracture toughness of Nbss/Nb5Si3 in situ composites alloyed with Mo. *Journal of Materials Science*, 2002. 37: p. 2885-2891.
119. S. Kashyap, C.S. Tiwary, K. Chattopadhyay. Effect of Gallium on microstructure and mechanical properties of Nb-Si eutectic alloy. *Intermetallics*, 2011. 19: p. 1943-1952.
120. P.R. Dicks. The development of niobium-silicide based materials for high temperature applications. PhD Thesis. University of Birmingham, 2002.
121. G.A. Henshall, P.R. Strum, M.J. Strum, M.G. Mendiratta. Continuum Predictions of Deformation in Composites with Two Creeping Phases-II. Nb5Si3/Nb Composites. *Acta Materialia*, 1997. 45: p. 3135-3142.
122. P.R. Subramanian, T.A. Parthasarathy, M.G. Mendiratta, D.M. Dimiduk. Compressive Creep Behavior of Nb5Si3. *Scripta Metallurgica et Materialia*, 1995. 32: p. 1227-1232.
123. R.A. Perkins, G.H. Meier. The Oxidation Behavior and Protection of Niobium. *JOM*, 1990: p. 17-21.
124. J. Geng, P. Tsakirooulos, G. Shao. Oxidation of Nb-Si-Cr-Al in situ composites with Mo, Ti and Hf additions. *Materials Science and Engineering A*, 2006. 441: p. 26-38.
125. J. Geng, P. Tsakirooulos, G. Shao. Oxidation of Nb-Si-Cr-Al in situ composites with Mo, Ti and Hf additions. *Materials Science and Engineering*, 2006. 441: p. 26-38.
126. L.N. Jia, J.F. Weng, Z. Li, Z. Hong, L.F. Su, H. Zhang. Room temperature mechanical properties and high temperature oxidation resistance of a high Cr containing Nb-Si based alloy. *Materials Science and Engineering A*, 2015. 623: p. 32-37.

127. Y. Qiao, X. Guo, X. Li. Hot corrosion behavior of silicide coating on an Nb-Ti-Si based ultrahigh temperature alloy. *Corrosion Science*, 2015. 91: p. 75-85.
128. E.J. Felten. The Oxidation Behavior of a Niobium (Colombium) Alloy, Cb-132. *Journal of Less Common Metals*, 1972. 26: p. 105-115.
129. C. Wagner. *Z. Elektrochem.*, 1959. 63: p. 772.
130. N. Vellios, P. Tsakirooulos. Study of the role of Fe and Sn additions in the microstructure of Nb-24Ti-18Si-5Cr silicide based alloys. *Intermetallics*, 2010. 18: p. 1729-1736.
131. S. Zhang, X. Guo. Microstructure, mechanical properties and oxidation resistance of Nb silicide based ultrahigh temperature alloys with Hf addition. *Materials Science and Engineering A*, 2015. 645: p. 88-98.
132. Y. Qiao, M. Li, X. Guo. Development of silicide coatings over Nb-NbCr2 alloy and their oxidation behavior at 1250°C. *Surface and Coatings Technology*, 2014. 258: p. 921-930.
133. W.Y. Kim, H. Tanaka, A. Kasama, R. Tanaka, S. Hanada. Microstructure and room temperature deformation of Nbss/Nb5Si3 in situ composites alloyed with Mo. *Intermetallics*, 2001. 9: p. 521.
134. L. Feng, W. Huang, X. Lin, H. Yang, Y. Li, J. Yang. Laser Multi-layer Cladding Experiment on the DD3 Single Crystal Using FGH95 Powder: Investigation on the Microstructure of Single Crystal Cladding Layer. *Chinese Journal of Aeronautics*, 2002. 15: p. 421-427.
135. X. Lin, T.M. Yue, H.O. Yang, W.D. Huang. Laser rapid forming of SS316L/Rene88DT graded material. *Materials Science and Engineering A*, 2005. 391: p. 325-336.
136. F. Zhang, J. Chen, H. Tan, X. Lin, W. Huang. Composition control for laser solid forming from blended elemental powders. *Optics & Laser Technology*, 2009. 41: p. 601-607.
137. X. Xu, X. Lin, M. Yang, J. Chen, W. Huang. Microstructure evolution in laser solid forming of Ti-50 wt% Ni alloy. *Journal of Alloys and Compounds*, 2009. 480: p. 782-787.
138. M. Margulies, P. Witomski, T. Duffar. Optimization of the Bridgman crystal growth process. *Journal of Crystal Growth*, 2004. 266: p. 175-181.

139. L. Ma, X. Tang, B. Wang, L. Jia, S. Yuan, H. Zhang. Purification in the interaction between yttria mould and Nb-silicide-based alloy during rdirectional solidification: A novel effect of yttrium. *Scripta Materialia*, 2012(67): p. 4.
140. R. Dicks, F. Wang, X. Wu. The manufacture of a niobium/niobium-silicide-based alloy using direct laser fabrication. *Journal of Materials Processing Technology*, 2009. 209: p. 1752-1757.
141. C.H. Shang, D. Van Heerden, A.J. Gavens, T.P. Weihs. An X-ray study of residual stresses and bending stresses in free-standing Nb/Nb₅Si₃ microlaminates. *Acta Materialia*, 2000. 48: p. 3533-3543.
142. R. Bogue. 3-D printing: The dawn of a new era in manufacturing? *Assembly Automation*, 2013. 33(4): p. 307-311.
143. L. Xue. Laser Consolidation - A Rapid Manufacturing Process for Making Net-Shape Functional Components. *Advances in Laser Materials Processing*, 2018: p. 461-505.
144. Z. Fan, F. Liou. Numerical Modeling of the Additive Manufacturing (AM) Processes of Titanium Alloy. *Titanium Alloys - Towards Achieving Enhanced Properties for Diversified Applications*, 2012.
145. H. Sahasrabudhe. Characterization of Ti and Co based biomaterials processed via laser based additive manufacturing (Ph.D. Thesis). Washington State University, 2016.
146. H. Sahasrabudhe, S. Bose, A. Bandyopadhyay. Laser-Based Additive Manufacturing Processes. *Advances in Laser Materials Processing*, 2018: p. 507-539.
147. C. Emmelmann, D. Herzog, J. Kranz. Design for laser additive manufacturing. *Laser additive manufacturing*, 2017: p. 259-279.
148. A. Gebhardt. *Understanding Additive Manufacturing*. Carl Hanser, Munich, 2011: p. 89.
149. I. Gibson, D. Rosen, B. Stucker. *Additive Manufacturing Technologies*. Springer, New York, 2010.
150. B.P. Conner, G.P. Manogharan, A.N. Martof, L.M. Rodomsky, C.M. Rodomsky, D.C. Jordan, J.W. Limperos. Making sense of 3-D printing: creating a map of additive manufacturing products and services. *Additive Manufacturing*, 2014. 1-4: p. 64-76.

151. W.R. Morrow, H. Qi, I. Kim, J. Mazumder, S. J. Skerlos. Environmental aspects of laser-based and conventional tool and die manufacturing. *Journal of Cleaner Production* , 2007. 15: p. 932-943.
152. D.S. Thomas, S.W. Gilbert. *Costs and Cost Effectiveness of Additive Manufacturing*. National Institute of Science and Technology, 2014.
153. E. Atzeni, A. Salmi. Economics of additive manufacturing for end-usable metal parts. *The International Journal of Advanced Manufacturing Technology* , 2012. 62(9-12): p. 1147-1155.
154. C. Achillas, D. Aidonis, E. Iakovou, M. Thymianidis, D. Tzetzis, A methodological framework for the inclusion of modern additive manufacturing to the production portfolio of a focused factory. *Journal of Manufacturing Systems*, 2014. 37(Part 1): p. 328-339.
155. N. Hopkinson, P. Dicknes. Analysis of rapid manufacturing — using layer manufacturing processes for production. *Proceedings of the Institution of Mechanical Engineers, Part C: Journal of Mechanical Engineering Science*, 2013. 217: p. 31-39.
156. M. Ruffo, C. Tuck, R. Hague. Cost estimation for rapid manufacturing laser sintering production for low to medium volumes. *Proc. Inst. Mech. Eng. Part B: J. Eng. Manuf*, 2006. 220(9): p. 1417-1427.
157. C. Lindemann, U. Jahnke, R. Koch. Analyzing Product Lifecycle Costs for a Better Understanding of Cost Drivers in Additive Manufacturing. *Solid Freeform Fabrication Symposium*, 2012. Vol. 23: University of Texas, TX.
158. A.J. Pinkerton. Lasers in additive manufacturing. *Optics & Laser Technology* 2016. 78: p. 25-32.
159. H. Lipson, M. Kurman. *Fabricated: The New World of 3D Printing*. Indianapolis, John Wiley & Sons, 2013.
160. S.H. Huang, P. Liu, A. Mokasdar, L. Hou. Additive manufacturing and its societal impact: a literature review. *The International Journal of Advanced Manufacturing Technology*, 2013. 67: p. 1191-1203.
161. V. Petrovic, J.V.H. Gonzalez, O.J. Ferrando, J.D. Gordillo, J.R.B. Puchades, L.P. Griñan. Additive layered manufacturing: sectors of industrial application shown through case studies. *International Journal of Production Research*, 2010. 49(4): p. 1061-1079.

162. G.D. Janaki Ram, C.K. Esplin, B.E. Sticker. Microstructure and wear properties of LENS® deposited medical grade CoCrMo. *Journal of Materials Science: Materials in Medicine*, 2008. 19: p. 2105-2111.
163. K.B. Hazlehurst, C.J. Wang, M. Stanford. An investigation into the flexural characteristics of functionally graded cobalt chrome femoral stems manufactured using selective laser melting. *Materials & Design*, 2014. 60: p. 177-183.
164. K. Monroy, J. Delgado, J. Ciurana. Study of the pore formation on CoCrMo alloys by selective laser melting manufacturing process. *Procedia Engineering*, 2013. 63: p. 361-369.
165. M.L. Griffith, D.M. Keicher, C.L. Atwood, J.A. Romero, J.E. Smugeresky, L.D. Harwell, D.L. Greene. Free form fabrication of metallic components using laser engineered net shaping (LENS™). *Proceedings of the Solid Freeform Fabrication Symposium, University of Texas at Austin, Austin, TX*, 1996: p. 125-131.
166. J. Mazumder, J. Choi, K. Nagarathnam, J. Koch, D. Hetzner. The direct metal deposition of H13 tool steel for 3-D components. *JOM*, 1997. 49: p. 55-60.
167. R.S. Amano, P.K. Rohatgi. Laser engineered net shaping process for SAE 4140 low alloy steel. *Materials Science and Engineering: A* 2011. 528(22): p. 6680-6693.
168. A.J. Pinkerton, L. Lin. Multiple-layer laser deposition of steel components using gas and water-atomised powders: the differences and the mechanisms leading to them. *Applied Surface Science*, 2007. 247(1): p. 175-181.
169. B.V. Krishna, S. Bose, A. Bandyopadhyay. Laser processing of net-shape NiTi shape memory alloy. *Metallurgical and Materials Transactions A*, 2007. 38: p. 1096-1103.
170. S. Das, M. Wohlert, J.J. Beaman, D.L. Bourell. Processing of titanium net shapes by SLS/HIP. *Materials & Design*, 1999. 2: p. 115-121.
171. W.L. Mankins, S. Lamb. Nickel and nickel alloys. *ASM Handbook: Properties and Selection: Nonferrous Alloys and Special-Purpose Materials*, 1990. 2(ASM International, Ohio): p. 438.

172. F.R. Morral. Wrought superalloys. *Metals Handbook: Properties and Selection: Stainless Steels, Tool Materials and Special-purpose Metals*, 1980. 3: p. 219.
173. S. Azadian. *Aspects of Precipitation in the Alloy Inconel 718* (Doctoral thesis). Lulea University of Technology, Lulea, Sweden, 2004: p. 15.
174. J.R. Newman. ASM Handbook Committee (Ed.), *Metals Handbook*, ninth ed. *Properties and Selection: Stainless Steels, Tool Materials and Special-Purpose Metals*. American Society for Metals, Ohio, 1980. 3: p. 409.
175. J.R. Davis. *ASM Specialty Handbook: Heat-Resistant Materials*. ASM International, Ohio, 1997: p. 347-360.
176. S. Mathieu, S. Knittel, M. François, L. Portebois, S. Mathieu, M. Vilasi, Towards the improvement of the oxidation resistance of Nb-silicides in situ composites: A solid state diffusion approach. *Corrosion Science*, 2014. 79: p. 119-127.
177. P. Zhang, X. Guo, Improvement in oxidation resistance of silicide coating on an Nb-Ti-Si based ultrahigh temperature alloy by second aluminizing treatment. *Corrosion Science*, 2015. 91: p. 101-107.
178. R.O. Suzuki, M. Ishikawa, K. Ono, NbSi₂ coating on niobium using molten salt. *Journal of Alloys and Compounds*, 2002. 336: p. 280-285.
179. L. Shichao. *Development of TiAl-Based Alloys Using Suspended Droplet Alloying*. PhD thesis, University of Birmingham, 2017: p. 47-50.
180. J.-P. Delplanque, R.H. Rangel. An improved model for droplet solidification on a flat surface. *Journal of Materials Science*, 1997. 32: p. 1519-1530.
181. R. Tiwari, H. Herman, S. Sampath, B. Gudmundsson. Plasma spray consolidation of high temperature composites. *Materials Science and Engineering A*, 1991. 144: p. 127.
182. T. Bennett, D. Poulikakos. Splat-quench solidification: estimating the maximum spreading of a droplet impacting a solid surface. *Journal of Materials Science*, 1993. 28: p. 963.
183. D. Poulikakos, J. Waldvogel. Transport phenomena relevant to the impact regime of the process of spray deposition. Presented at the 24th National Heat Transfer Conference, Heat Transfer division of the ASME Portland, OR, 1995. 306: p. 151-170.

184. J. Madejski. Solidification of droplets on a cold surface. *International Journal of Heat and Mass Transfer*, 1976, 19: p. 1009-1013.
185. C. San Marchi, H. Liu, E.J. Lavernia, R.H. Rangel, A. Sickinger, E. Muehlberger. Numerical analysis of the deformation and solidification of a single droplet impinging onto a flat substrate. *Journal of Materials Science*, 1993. 28(12): p. 3313-3321.
186. R.H. Rangel, X. Bian. The Inviscid Stagnation-Flow Solidification Problem. *International Journal of Heat and Mass Transfer*, 1996. 39: p. 1591.
187. R.H. Rangel, X. Bian. Numerical Solution Of The Inviscid Stagnation-Flow Solidification Problem. *Numerical Heat Transfer, Part A: Applications*, 1995. 28: p. 589-603.
188. J. Madejski. Droplets on Impact With a Solid Surface. *International Journal of Heat and Mass Transfer*, 1983. 26: p. 1095-1098.
189. H.M. Cobb. *Dictionary of Metals, Appendix I: Metals History Timeline*. ASM International, Materials Park, OH, USA., 2012: p. 304.
190. J. Madias. *Treatise on Process Metallurgy*. 2014. 3(Chapter 1.5): p. 271-300.
191. S.A. Billings, F.M. Boland, H. Nicholson. Electric Arc Furnace Modelling and Control. *Automatica*, 1979. 15: p. 137-148.
192. H. Driller. Present status and development of electrical regulation for electric arc steel furnaces. *Stahl und Eisen*, 1954. 74(Pt. 2): p. 82-85.
193. L. Kolkwiewicz. Arc furnace electrode control. *Elec. Eng. in the Metal Ind., (Supplement to AEI Eng.)*, 1967: p. 30-33.
194. R. Roebuck. Modelling and control of an electric arc furnace. M.Sc. Thesis, Dept. Control Eng., University of Sheffield, 1969.
195. A.S. Morris, M.J.H. Sterling, Analysis of electrode position controllers for electric arc steelmaking furnace. *Iron Steel Int.*, 1975. 48(4): p. 291-298.
196. L. McGee, J. Ravenscroft. Heat transfer investigations and development of the automatic control of power input on the BISRA 10-cwt arc furnace. *J. Iron Steel Inst.*, 1959(34-39).
197. W.E. Schwabe. Arc heat transfer and refractory erosion in electric steel furnaces. *Proc. Electr. Arc Furnace Conf.*, 1962: p. 195-206.
198. W.E. Schwabe. Lighting flicker caused by electric arc furnaces. *Iron Steel Eng.*, 1958: p. 93-100.

199. J.W.S. Payne. The control of a large electric arc furnace in relation to their effect on the supply system. *Instrument Practice*, 1959: p. 808-814.
200. B.C. Robinson. Excess voltage in transformers and reactors connected to 3-phase electric arc furnaces. *Proc. IEE*, 1952. 99: p. 271-287.
201. H.-B. Lungen, M. Peters, P. Schmole, *AISTech 2012 Proceedings*, 2012: p. 109-119.
202. B. Bowman, K. Kruger. *Electric Arc Furnace Physics*. Stahleisen Communications. Verlag Stahleisen: Düsseldorf, Germany, 2009.
203. H.-J. Odenthal, A. Kemminger, F. Krause, L. Sankowski, N. Uebber, N. Vogl. Review on Modeling and Simulation of the Electric Arc Furnace (EAF). *Steel Research International*, 2017: p. 1-36.
204. M.H. Bocanegra-Bernal. Hot Isostatic Pressing (HIP) technology and its applications to metals and ceramics. *Journal of Materials Science*, 2004. 39(21): p. 6399–6420.
205. S.Tammas-Williams, P.J. Withers, I.Todd, P.B.Prangnell, Porosity regrowth during heat treatment of hot isostatically pressed additively manufactured titanium components. *Scripta Materialia*, 2016. 122: p. 72-76.
206. H.V. Atkinson, S. Davies, Fundamental aspects of hot isostatic pressing: An overview. *Metallurgical and Materials Transactions A*, 2000. 31(12): p. 2981–3000.
207. G.J. Bonami. *Heat treatment: theory, techniques, and applications*. Hauppauge, N.Y. : Nova Science Publishers, 2010.
208. J.R. Davis. *Aluminum and Aluminum Alloys. Alloying: Understanding the Basics*. *Light Metals and Alloys*, 2001: p. 351–416.
209. M.A. Mutalib, M.A. Rahman, M.H.D. Othman, A.F. Ismail, J. Jaafar, Scanning Electron Microscopy (SEM) and Energy-Dispersive X-Ray (EDX) Spectroscopy. *Membrane Characterization*, 2017. Chapter 9: p. 163.
210. S. Hashimoto, K.F. Kobayashi, S. Miura. Roles Of Lattice Coherency To The Heterogeneous Nucleation In The Al-Ti System. *Z. Metallkunde*, 1983. 74: p. 787-792.
211. H. Assadi, A.L. Greer. The interfacial undercooling in solidification. *Journal of Crystal Growth*, 1997. 172: p. 249-258.

212. K.H.J. Buschow, P.G. van Engen, R.J. Jongebreur. *Magn. Magn. Mater.*, 1983. 38: p. 1-22.
213. R.S. Barclay, P. Niessen, H.W. Kerr. Halo Formation During Unidirectional Solidification of Off-eutectic Binary Alloys. *Journal of Crystal Growth*, 1973. 20: p. 175-182.
214. R. Trivedi, P. Magnin, W. Kurz. Theory of eutectic growth under rapid solidification conditions. *Acta Metallurgica*, 1987. 35: p. 971.
215. W.J. Boettinger, S.R. Coriell, R. Trivedi in R. Mehrabian and P. A. Parrish (eds.), *Rapid Solidification Processing: Principles and Technologies IV*, Claitor's, Baton Rouge, LA, 1988, pp. 13-25.
216. S.K. Bataleva, V.V Kuprina., V.Y. Markiv, V.V. Burnashova, G.N. Ronami, S.M. Kusnetsova, *Vest. Moskovskogo Universiteta Khimiya*, 1970. 11: p. 432.
217. N. D'Souza, R. Beanland, C. Hayward, H.B. Dong. Accuracy of composition measurement using X-ray spectroscopy in precipitate-strengthened alloys: Application to Ni-base superalloys. *Acta Materialia*, 2011. 59: p. 1003-1013.
218. C. He, F. Stein, M. Palm. Thermodynamic description of the systems Co-Nb, Al-Nb and Co-Al-Nb. *Journal of Alloys and Compounds*, 2015. 637: p. 361-375.
219. C. He, Y. Qin, F. Stein. Thermodynamic Assessment of the Fe-Al-Nb System with Updated Fe-Nb Description. *Journal of Phase Equilibria and Diffusion*, 2017. 38: p. 771-787.
220. C. Guo, T. Wu, C. Li, Z. Du. Thermodynamic description of the Al-Fe-Nb system. *Calphad*, 2017. 57: p. 78-87.
221. R. Tewari, H.J. Song, A. Chatterjee, V.K. Vasudevan. Microstructural Characterization of Multicomponent Nb-Ti-Si-Cr-Al-X Alloys. *Metall. Mater. Trans. A*, 2006. 37A: p. 2669-2682.
222. N. David, Y. Cartigny, T. Belmonte, J.M. Fiorani, M. Vilasi. Thermodynamic description of the Cr-Nb-Si isothermal section at 1473 K. *Intermetallics*, 2006. 14: p. 464.
223. H.J. Goldschmidt, J.A. Brand. The Constitution of the Chromium-Niobium-Silicon System. *Journal of the Less-Common Metals*, 1961. 3: p. 34-43.

224. MSIT®, M.S.I.T., Light Metal Ternary Systems: Phase Diagrams, Crystallographic and Thermodynamic Data. Cr-Nb-Ti (Chromium - Niobium - Titanium). Light Metal Systems. Part 4. vol 11A4: p. 1-17.
225. V. Chandrasekaran, R. Taggart, D.H. Polonis. Phase Separation Processes in the Beta Phase of Ti-Mo Binary Alloys. *Metallography*, 1972. 5: p. 393-398.
226. J.W. Cahn. On Spinodal Decompositions in Cubic Crystals. *Acta Metallurgica*, 1962. 10: p. 179-183.
227. R.F. Bunshah. *T.M.S.-A.I.M.E.*, 1958. 212: p. 424.
228. E.S.K. Menon, H.I. Aaronson. "Black Plate" Formation in Ti-X Alloys. *Acta Metallurgica*, 1986. 34: p. 1963-1973.
229. J.W. Gibbs. *Collected Works*. Yale University Press, New Haven, Connecticut, 1948. 1: p. 105-115, 252-258.
230. M. Hillert. *Acta Metallurgica*, 1961. 9: p. 525.
231. J.W. Cahn. On Spinodal Decomposition. *Acta Metallurgica*, 1961. 9: p. 795-801.
232. A.E. Pontau, D. Lazarus. Diffusion of titanium and niobium in bcc Ti-Nb alloys. *Physical Review B*, 1979. 19(8): p. 4027-4037.
233. P. Tsakiroopoulos. On the Alloying and Properties of Tetragonal Nb₅Si₃ in Nb-Silicide Based Alloys. *Materials*, 2018. 11, 69: p. 1-19.